

Doctor Thesis

Studies on Extended Higgs Sectors as a Probe of New Physics Beyond the Standard Model

Kei Yagyu

*Department of Physics, University of Toyama,
3190 Gofuku, Toyama 930-8555, Japan*

March 2012



ACKNOWLEDGMENTS

I would like to express my sincere gratitude to my supervisor, Prof. Shinya Kanemura for providing me much instruction in particle physics and its philosophy. I am very grateful to Prof. Mayumi Aoki, Prof. Tetsuo Shindou, Prof. Stefano Moretti, Prof. Rui Santos, Dr. Koji Tsumura, Dr. Renato Guedes, Mr. Kazuya Yanase and Mr. Yuki Mukai for the fruitful collaborations. I am also grateful to the other faculty members of the laboratory, Prof. Takeshi Kurimoto and Prof. Mitsuru Kakizaki for useful discussions. I would like to thank Prof. Yasuhiro Okada, Prof. Fusakazu Matsushima and Prof. Yoshiki Moriwaki for careful reading of this thesis. I would also like to thank all the members in my laboratory, Dr. Makoto Nakamura, Mr. Takehiro Nabeshima, Mr. Hiroyuki Taniguchi, Mr. Tsutomu Kaburagi, Mr. Hiroyasu Nakahori, Ms. Mariko Kikuchi, Mr. Naoki Machida and Mr. Toshinori Matsui for their hospitality.

Abstract

It is the most important issue in particle physics to understand the mechanism of electroweak symmetry breaking. In the standard picture for elementary particles based on the quantum field theory, the vacuum expectation value (VEV) of the Higgs scalar field triggers the spontaneous breakdown of the electroweak gauge symmetry. Although the Standard Model (SM) for elementary particles has been successful in describing high-energy phenomena at colliders, the Higgs boson has not been discovered yet. Currently, Higgs boson searches are underway at the CERN Large Hadron Collider (LHC). The Higgs boson is strongly expected to be discovered in near future as long as the SM is effectively correct. The discovery of the Higgs boson does not mean the end of particle physics, because there remain problems which cannot be explained within the framework of the SM. First of all, it is well known that the Higgs scalar boson causes so-called the hierarchy problem, in which the quadratic ultraviolet divergence appears in the renormalization of the Higgs boson mass. The renormalization of such quadratic divergences leads to a huge unnatural fine tuning. Second, neutrino oscillation has been established by experiments. Tiny masses of neutrinos are necessary to explain such phenomena, while neutrinos are massless in the SM. Therefore, we need to extend the SM so as to have tiny but nonzero neutrino masses. Third, there is no candidate for dark matter in the particle content in the SM, although the existence of dark matter has been confirmed at the experiment. Finally, it has been clarified that the baryon asymmetry of the Universe cannot be realized in the SM. To solve these problems, new physics models beyond the SM have been proposed. In such new models, the Higgs sector is often extended from that of the SM, where it takes the minimal form with only one isospin doublet Higgs field. The structure of a Higgs sector strongly depends on the property of the corresponding new physics model at the high energy scale. Therefore, by comparing predicted observables with future experimental data such as the Higgs boson mass, the width, decay branching ratios and so on, we can determine new paradigm for physics beyond the SM. In this thesis, we discuss theoretical properties of various Higgs sectors, and we analyze constraints from current experimental data, and then we study collider signatures in each Higgs sector from this view point.

In Part I, we focus on the phenomenology of various extended Higgs sectors.

First, as a simple but important extended Higgs sector, we discuss the two Higgs doublet model (THDM). The THDM appears in several classes of new physics models such as the CP-violation, the minimal supersymmetric standard model (MSSM), radiative seesaw models and so on. In the THDM, the softly-broken discrete Z_2 symmetry is often imposed to avoid the flavor changing neutral current at the tree level. Under the Z_2 symmetry, there are four types of the Yukawa interaction (type-I, type-II, type-X and type-Y). The type of Yukawa interaction can be related to each new physics scenarios. For example, the type-II THDM is predicted in the Higgs sector of the MSSM, while so-called the type-X THDM appears in some TeV scale models which can explain neutrino masses, dark matter and baryon symmetry of the Universe. We investigate the phenomenological differences among these THDMs at the LHC and the International Linear Collider (ILC) to discriminate new physics models. We find that in the type-II THDM, additional Higgs bosons such as the CP-odd Higgs boson and the heavier CP-even Higgs boson can dominantly decay into $b\bar{b}$, while in the type-X THDM, those mainly decay into $\tau^+\tau^-$. By using this difference the Higgs sector in the MSSM and the type-X THDM may be able to be distinguished at colliders.

Second, we consider the Higgs model with the $Y = 1$ triplet Higgs field so-called the Higgs triplet model (HTM) which is motivated by generating tiny neutrino masses. In this model, the rho parameter ρ can deviate from unity at the tree level, since the custodial symmetry is broken in the kinetic term of Higgs fields. Thus, the electroweak parameters are described by the four input parameters such as α_{em} , G_F , m_Z and $\sin \theta_W$ instead of three parameters α_{em} , G_F and m_Z with the relation of $\cos \theta_W = m_W/m_Z$ in models with $\rho = 1$ at the tree level. We calculate the one-loop correction to the W boson mass as well as the rho parameter in order to clarify the possible mass spectrum of extra scalar bosons under the constraint from the electroweak precision data. We find that the hierarchical mass spectrum among the scalar bosons mainly originated from the triplet field is favored by the data, especially in the case where doubly-charged scalar bosons are the lightest of all them. We then discuss the phenomenology of the HTM in light of the case with the mass splitting among the triplet-like scalar bosons. We outline that all the masses of these scalar bosons would be reconstructed by using the transverse mass distribution and the invariant mass distribution at the LHC. We also calculate the deviation of the decay rate of the Higgs boson decay into two photons in the HTM from that in the SM.

Third, we study properties of charged Higgs bosons H^\pm , especially focusing on the $H^\pm W^\mp Z$ vertex. This vertex strongly depends on the structure of Higgs sectors depending on the breakdown of a custodial symmetry of the model, so that we can constrain Higgs sectors with custodial symmetry breaking. We study the possibility of measuring the $H^\pm W^\mp Z$ vertex via single charged Higgs boson production associated with the W^\pm boson at the ILC by using the recoil method. We find that the $H^\pm W^\mp Z$ vertex would be testable with the similar accuracy to the rho parameter at the ILC.

Finally, we discuss various supersymmetric (SUSY) Higgs sectors, where extra chiral superfields are added to the MSSM, which are motivated to solve several physics problems. For example, the next-to-MSSM in which a neutral singlet superfield is added to the MSSM is motivated to solve the μ -problem, models with extra triplet superfields can be used to explain neutrino masses and so on. In particular, we focus on decoupling properties of extended SUSY Higgs sectors. When masses of new particles are heavy then effects of new physics to the low energy observables decouple which is well known as the Appelquest's theorem. However, if masses of new particles are mainly determined by the VEV of the Higgs field then this theorem does not hold. In such a case, nondecoupling effects appear in the low energy observables. We investigate such effects in various SUSY Higgs sectors with additional interaction terms from the F-term contribution in the Higgs potential at the tree level. We also discuss extended SUSY Higgs sectors without such F-term contributions. As a concrete example, we consider the model with four Higgs doublet fields. In this model, if there are mixings between the MSSM-like doublet fields and the extra doublet fields due to a large soft-breaking B-term, nonvanishing effects can appear in the MSSM observables such as the masses of the CP-even scalar bosons, those of charged Higgs bosons and the mixing angle between the CP-even scalar states.

In Part II, we discuss new physics models at the TeV scale, where neutrino masses, dark matter and/or baryon asymmetry of the Universe can be explained.

First, we discuss a model proposed by M. Aoki, S. Kanemura and O. Seto (2009), in which neutrino oscillation, dark matter, and baryon asymmetry of the Universe would be simultaneously explained by the TeV scale physics without fine tuning. The Higgs sector of this model is composed of the two Higgs doublet fields with the singlet neutral and charged scalar fields where

singlet fields are odd under an unbroken Z_2 symmetry. We discuss not only the constraints on the parameter space from the current experimental data but also theoretical bounds from the triviality and the vacuum stability. We find that the model can be consistent up to the scale above 10 TeV in the parameter region where the neutrino data, the lepton flavor violation data, the thermal relic abundance of dark matter as well as the requirement from the strongly first order phase transition are satisfied.

Second, we investigate a SUSY extension of the radiative seesaw model proposed by A. Zee (1986) and K. S. Babu (1988) independently, in which neutrino masses are induced at the two-loop level by addition to charged singlet fields. One of the problem in the original Zee-Babu model is absence of the dark matter candidate. By the SUSY extension of the model, the lightest superpartner particle can be a dark matter candidate. We show that the neutrino data can be reproduced with satisfying current data from lepton flavour violation even in the scenario where not all the superpartner particles are heavy. In this model, in addition to the doubly-charged isospin singlet scalar bosons, their SUSY partner fermions appear. We also discuss the outline of phenomenology for these particles at the LHC.

Finally, we consider models which contain the isospin doublet scalar fields with $Y = 3/2$. Such a doublet field $\Phi_{3/2}$ is composed of a doubly charged scalar boson as well as a singly charged one. We discuss a simple model with $\Phi_{3/2}$, and we study its collider phenomenology at the LHC. We then consider a new model for radiatively generating neutrino masses with a dark matter candidate, in which $\Phi_{3/2}$ and an extra $Y = 1/2$ doublet as well as vector-like singlet fermions carry the odd quantum number for an unbroken discrete Z_2 symmetry.

Contents

1	Introduction	1
1.1	Overview	1
1.2	The Two Higgs Doublet Model	4
1.3	The Higgs Triplet Model	5
1.4	Supersymmetric Higgs sectors	6
1.5	Extended Higgs sectors and the phenomena beyond the SM	7
1.6	Organization of this thesis	7
I	Phenomenology of Higgs sectors	9
2	The Standard Model Higgs sector	11
2.1	The masses of particles	11
2.1.1	The masses for the Higgs boson and the gauge bosons	11
2.1.2	The fermion masses	12
2.2	Bounds for the Higgs boson mass	13
2.2.1	Perturbative unitarity bound	14
2.2.2	Triviality and vacuum stability bounds	15
2.3	Decay of the Higgs boson	15
3	Extended Higgs sectors	17
3.1	The Two Higgs Doublet Model	17
3.1.1	Model	17
3.1.2	Decay	22
3.1.3	Constraints from the current experimental data on THDMs	22
3.1.4	Collider signals in the Type-X THDM at the LHC and the ILC	28
3.2	The Higgs Triplet Model	36
3.2.1	Tree level formulae	36
3.2.2	One-loop corrections to electroweak parameters	39

3.2.3	Decay of the triplet-like scalar bosons	48
3.2.4	Mass determination of the triplet-like scalar bosons at the LHC	51
3.2.5	The two photon decay of the SM-like Higgs boson	57
3.3	Testing Higgs models via the $H^\pm W^\mp Z$ vertex	61
3.3.1	The $H^\pm W^\mp Z$ vertex	62
3.3.2	The $e^+e^- \rightarrow H^\pm W^\mp$ process	63
3.3.3	Recoil method and the assumption for the ILC performance	64
3.3.4	Signal and Backgrounds	66
4	Decoupling property of SUSY Higgs sectors	75
4.1	The Higgs sector of the Minimal Supersymmetric Standard Model	76
4.2	Nondecoupling effects in supersymmetric Higgs sectors	80
4.3	SUSY Higgs sectors with nondecoupling effects	82
4.3.1	The next-to-MSSM	82
4.3.2	Model with extra triplet superfields	83
4.3.3	Model with four Higgs doublets and charged singlet superfields	85
4.3.4	Possible allowed regions of m_h and λ_{hhh} in various SUSY Higgs models . . .	86
4.4	SUSY Higgs sectors with quasi-nondecoupling effects	89
4.4.1	Model	89
4.4.2	Definition of the large mass limit	93
II	Models which can explain the phenomena beyond the SM at the TeV scale	103
5	Review of radiative seesaw models	105
6	Three-loop neutrino mass model	107
6.1	Model	108
6.2	Neutrino mass and mixing	110
6.3	Lepton flavor violation	111
6.4	Typical scenarios	112
6.5	Dark matter and electroweak phase transition	113
6.6	Bounds from triviality and vacuum stability	114
6.7	The conditions	116
6.8	Allowed regions in the parameter space	116

7	Supersymmetric extension of the Zee-Babu model	119
7.1	Model	119
7.2	Allowed parameter region under the current constraint	124
7.3	Phenomenology at the LHC	128
8	Models with the $Y = 3/2$ doublet scalar field	131
8.1	Model I	131
8.2	Model II	134
9	Conclusion	137
A	$W_L W_L \rightarrow W_L W_L$ scattering amplitude	139
B	Renormalization group equations	141
B.1	Beta functions in the SM	141
B.2	Beta functions in the THDM	142
B.3	Beta functions in the three-loop neutrino mass model	142
B.4	Beta functions in SUSY models	144
B.4.1	MSSM.	144
B.4.2	NMSSM	144
B.4.3	TMSSM	145
B.4.4	4D Ω	145
C	Decay rates	147
C.1	Decay rates of the Higgs boson in the SM	147
C.2	Decay rates of the Higgs bosons in the THDM	149
C.3	Decay rates of the Higgs bosons in the HTM.	152
C.3.1	Decay rates of $H^{\pm\pm}$	152
C.3.2	Decay rates of H^\pm	153
C.3.3	Decay rates of H	154
C.3.4	Decay rates of A	154
D	One-loop functions	155
E	Gauge boson self-energies and vertex corrections	159
E.1	Fermionic-loop contributions	160
E.2	Bosonic-loop contributions	160
E.3	Vertex correction	162

Chapter 1

Introduction

1.1 Overview

Although the Standard Model (SM) for particle physics has been successful for over three decades, the Higgs sector, which is introduced for the spontaneous breakdown of the electroweak gauge symmetry, remains unknown. In the SM, weak gauge bosons obtain their masses through the Higgs mechanism; i.e., the Nambu-Goldstone (NG) bosons are absorbed into the longitudinal components of W and Z bosons. At the same time, the masses for quarks and leptons are generated via the Yukawa interaction. Therefore, the Higgs boson is the origin of the mass for the elementary particles.

Exploration of the Higgs boson is the most important issue in current high energy physics. The upper bound for the Higgs boson mass can be obtained by taking into account the tree level unitarity for elastic scattering processes of the longitudinal component of the gauge bosons, e.g., $W_L^+ W_L^- \rightarrow W_L^+ W_L^-$ [1]. If we assume the validity of the perturbative calculation, then the Higgs boson mass should be lower than around 1 TeV in the SM. If there is no Higgs boson or if the Higgs boson is heavier than 1 TeV, the WW scattering amplitude should be grown as a function of the squared center of mass energy. As a result, the unitarity is broken at around the 1 TeV. Therefore, the Higgs boson does not exist, there must appear some new phenomena beyond the SM in the WW scattering process.

The CERN Large Hadron Collider (LHC) has built in order to survey the essence of electroweak symmetry breaking. At the LHC, the most important production process for the Higgs boson is the gluon fusion process ($gg \rightarrow H$) [2]. There are the other important production processes; the vector-boson fusion process ($qq' \rightarrow qq'H$) [3], the vector-boson associated production process ($q\bar{q} \rightarrow WH/ZH$) [4] and the top-quark pair associated production process ($q\bar{q}/gg \rightarrow t\bar{t}H$) [5]. From the recent Higgs boson searches at the LHC, the mass of the Higgs boson in the SM has already constrained to be between 115 GeV and 127 GeV or to be higher than 600 GeV at the 95% confidence level [6]. By the combination with the electroweak precise measurement at the LEP, we may expect that a light Higgs boson exists as long as the Higgs boson interactions are of SM-like and that it will be discovered in near future.

When the Higgs boson is discovered at the LHC, is physics of the elementary particle completed? The answer is “No”. There are several problems which cannot be explained within the SM.

- 1.) As a purely theoretical issue, the SM has the gauge hierarchy problem [7]. The quantum corrections to the Higgs boson mass depend on the quadratic power of the cutoff scale Λ ,

so that if Λ is assumed to be at an ultra-high energy such as the grand unification scale, it is required a huge fine tuning in renormalization of the Higgs boson mass.

- 2.) There are phenomena which cannot be explained within the SM such as the neutrino oscillation [8], existence of the dark matter [9] and baryon asymmetry of the Universe [10].

Many new physics models have been proposed which are motivated to solve these problems. Regarding the hierarchy problem, it comes from the Higgs sector in the SM, where the elementary Higgs scalar boson is just introduced to break the electroweak symmetry. The mass terms for the gauge bosons and the fermions in the SM are forbidden by the gauge symmetry and the chiral symmetry, respectively, so that the radiative corrections to these particles are proportional to the logarithmic divergence at most. On the other hand, since the mass terms for the scalar bosons cannot be forbidden by the symmetry in the SM, the quadratic divergence appears in the radiative corrections to the Higgs boson mass.

Therefore, new physics models which are motivated by solving the hierarchy problem have been proposed by considering what is the essence of the electroweak symmetry breaking. For example, in supersymmetric (SUSY) models, although the existence of the elementary Higgs scalar boson is admitted, the quadratic divergence due to a particle in the loop is cancelled by that due to a superpartner particles. Dynamical symmetry breaking [11] is the other idea to solve the hierarchy problem. In such models, the elementary Higgs scalar boson is not introduced, but the composite states of fermions play a role of the Higgs scalar boson, so that the quadratic divergence does not appear because of the chiral symmetry. The ideas of the little Higgs mechanism [12] and the gauge Higgs unification [13, 14] have also been proposed to solve the hierarchy problem. These new physics models often predict extended Higgs sectors as the low energy effective theory.

Apart from the hierarchy problem, there are scenarios which can explain the phenomena beyond the SM listed as 2.) by the extension of the Higgs sector. The type II seesaw model [15], where a Higgs triplet field with $Y = 1$ is added to the SM, can generate tiny neutrino masses at the tree level. Radiative seesaw models [16–21] can also explain tiny neutrino masses at the loop level, where additional scalar bosons, e.g., charged scalar bosons are running in the loop. Imposing an unbroken discrete symmetry such as Z_2 symmetry to a part of the Higgs sector, dark matter candidates can be obtained. The inert doublet model [22] is one of the examples. Furthermore, baryon asymmetry can be generated at the electroweak phase transition by the nondecoupling property [23] and additional CP violating phases in the extended Higgs sector [24, 25].

In both model explaining the problem 1) and that explaining the problems 2), the Higgs sector is often extended. The structure of a Higgs sector strongly depends on the property of the corresponding new physics model at the high energy scale, so that experimental reconstruction of the Higgs sector is extremely important to determine new paradigm for physics beyond the SM. In this thesis, we discuss the phenomenology of extended Higgs sectors from this view point.

The Higgs sector in the SM takes a minimal form, which is composed of only one isospin doublet Higgs field. However, there is no strong reason for taking into account the minimal Higgs sector. Since the Higgs sector has not been confirmed yet, there are various possibilities for extended Higgs sectors. For example, we can consider extended Higgs sectors with extra $SU(2)$ singlet, doublet and triplet fields adding to the minimal Higgs sector. The important point is

how we can constrain these possibilities. There are two important experimental observables to constrain the structure of the Higgs sector: the electroweak rho parameter and the flavor changing neutral current (FCNC).

The experimental value of the rho parameter ρ_{exp} is quite close to unity; $\rho_{\text{exp}} = 1.0008^{+0.0017}_{-0.0007}$ [26]. This fact suggests that a global $SU(2)$ symmetry (custodial symmetry) plays an important role in the Higgs sector. The theoretical prediction of the rho parameter is determined by the number of scalar fields as well as their representations under the isospin $SU(2)_L$ and the hypercharge $U(1)_Y$. In the Higgs model which contains complex scalar fields with the isospin T_i and the hypercharge Y_i as well as real ($Y = 0$) scalar fields with the isospin T'_i , the rho parameter is given at the tree level by

$$\rho_{\text{tree}} = \frac{\sum_i [|v_i|^2 (T_i(T_i + 1) - Y_i^2) + u_i^2 T'_i(T'_i + 1)]}{2 \sum_i |v_i|^2 Y_i^2}, \quad (1.1)$$

where v_i (u_i) represents the vacuum expectation value (VEV) of the complex (real) scalar field [27]. In models with only scalar doublet fields (and singlets), $\rho_{\text{tree}} = 1$ is predicted because of the custodial symmetry in the kinetic term of the Higgs sector. On the other hand, addition of Higgs fields with the isospin larger than one half can shift the rho parameter from unity at the tree level, whose deviation is proportional to VEVs of these exotic scalar fields such as triplet fields. The rho parameter, therefore, has been used to constrain a class of Higgs models.

In the SM, FCNC phenomena are suppressed due to the electromagnetic gauge symmetry and the Glashow-Iliopoulos-Maiani mechanism [28], so that the experimental bounds on the FCNC processes, which are mediated by the neutral gauge bosons, are satisfied. At the same time, neutral Higgs boson mediating FCNC processes are absent at the tree level in the SM. Since the matrix for the Yukawa interaction and that for the fermion masses are given by the same Yukawa matrix, those two matrices can be diagonalized simultaneously. In models with more than one Higgs doublet, this is not true in general, because two or more Yukawa matrices for each fermion cannot be simultaneously diagonalized. It is well known that, to avoid such Higgs-boson-associated FCNC interactions, each fermion should couple to only one of the Higgs doublets. This can be realized in a natural way by imposing a discrete Z_2 symmetry [29].

In addition to these two basic experimental constraints, by focusing on the physics of charged Higgs bosons H^\pm , which are contained in most of the extended Higgs models, we can obtain the other constraint to the Higgs sector. In particular, the $H^\pm W^\mp Z$ vertex can be a useful probe of the extended Higgs sector [30–33]. The magnitude of the vertex depends on the violation of the custodial symmetry such as the rho parameter. In general, this can be independent of the rho parameter. If a charged Higgs boson is from a doublet field, the $H^\pm W^\mp Z$ vertex vanishes at the tree level. The vertex is then one-loop induced and its magnitude is proportional to the violation of the global symmetry in the sector of particles in the loop. On the other hand, in models with exotic representations such as triplet scalar fields this vertex appears at the tree level. Therefore, the determination of the $H^\pm W^\mp Z$ vertex can be a complementary tool to the rho parameter in testing the *exoticness* of the Higgs sector.

We should discuss extended Higgs sectors based on physics motivations which can satisfy these experimental data. In Part I, as concrete examples, we discuss the phenomenology of extended Higgs sectors such as the two Higgs doublet model (THDM), the Higgs triplet model (HTM) and Higgs sectors in the supersymmetry. In Part II, we discuss applications of extended

Higgs sectors to models which can explain tiny neutrino masses, dark matter and/or baryon asymmetry of the Universe at the TeV scale.

1.2 The Two Higgs Doublet Model

The THDM is an important example as an extended Higgs model, since that appears in the Higgs sector of the minimal supersymmetric standard model (MSSM) [34]. Radiative seesaw models, e.g., the Zee model [16] contain two Higgs doublets. In addition, additional CP-violating phases appear in the THDM, which is required by the scenario of electroweak baryogenesis. Recently, in Ref. [35], theoretical and phenomenological aspects in the THDM have been reviewed, where extensive references to the original literature are included. In the THDM, neutral scalar boson mediating FCNC processes appear at the tree level. To avoid such a dangerous FCNC process, a softly-broken discrete Z_2 symmetry is often introduced [29]. Under the Z_2 symmetry, there are four types of the Yukawa interaction depending on its charge assignment for quarks and leptons [36, 37]. We call these types of Yukawa interaction as type-I, type-II, type-X, and type-Y [38]. We discuss the phenomenological difference among these types of Yukawa interaction.

The type in the Yukawa interaction can be related to each new physics scenarios. For example, the Higgs sector of the MSSM is the THDM with a SUSY relation among the parameters of the Higgs sector, whose Yukawa interaction is of type-II, in which only a Higgs doublet couples to up-type quarks and the other couples to down-type quarks and charged leptons. On the other hand, a model has been proposed in Ref. [21], where neutrino masses, dark matter and baryogenesis would be explained simultaneously at the TeV scale. In this model the Higgs sector contains the two Higgs doublets, and its Yukawa interaction corresponds to the type-X THDM, in which only a Higgs doublet couples to quarks and the other couples to leptons [38, 39]. Therefore, in order to select the true model from various new physics candidates that predict THDMs, it is important to experimentally determine the type of Yukawa interaction.

We first study the total widths and the decay branching ratios of the extra Higgs bosons such as the CP-odd (CP-even) Higgs boson A (H) and the charged Higgs bosons H^\pm in the four types of Yukawa interaction. We then summarize constraints on the mass of the charged Higgs bosons from current experimental bounds, especially from the B -meson decay data such as $B \rightarrow X_s \gamma$ [40] and $B \rightarrow \tau \nu$ [41–43] depending on the type of Yukawa interaction. The $B \rightarrow X_s \gamma$ results give a severe lower bound, $m_{H^\pm} > 295$ GeV, at the next-to-next-to leading order in the (non-SUSY) type-II THDM and the type-Y THDM [44, 45], while in the type-I and the type-X THDM, the mass of $\mathcal{O}(100)$ GeV is allowed in the wide regions of the parameter space. We finally discuss the possibility of discriminating the types of Yukawa interaction at the LHC and also at the international Linear Collider (ILC). We discuss the signal of extra neutral and charged Higgs bosons at the LHC, which may be useful to distinguish the type of Yukawa interaction. Recently, a detailed simulation study for the type-X THDM has been performed for multi- τ signatures at the LHC [46]. In that paper, assuming the integrated luminosity of 100 fb^{-1} , the excess can be seen in various three- and four-lepton channels via the processes $q\bar{q} \rightarrow Z^* \rightarrow HA$ and $q\bar{q}' \rightarrow W^{\pm*} \rightarrow HH^\pm$ (AH^\pm).

1.3 The Higgs Triplet Model

The HTM is also a well-motivated extended Higgs model, where the $Y = 1$ Higgs triplet field is added to the SM, since tiny masses of neutrinos can be generated at the tree level. Assuming that the triplet scalar field carries two units of lepton number, the lepton number conservation is violated in a trilinear interaction terms among the Higgs doublet field and the Higgs triplet field. Majorana masses for neutrinos are then generated through the Yukawa interaction of the lepton doublet and the triplet scalar field. When we take the lepton number violating coupling to be eV scale, the masses of the component fields of the triplet can be taken to be of the TeV scale or less. In such a case, the model can be tested by directly detecting the triplet-like scalar bosons, such as the doubly-charged ($H^{\pm\pm}$), the singly-charged (H^\pm), the neutral CP-even (H) and the neutral CP-odd (A) scalar bosons. In Ref. [47], a simple suppression mechanism for μ has been proposed, where lepton number violating coupling is induced at the one-loop level.

In addition to the appearance of these scalar bosons, a striking prediction of the HTM is the relationships among the masses of the triplet-like scalar bosons, i.e., $m_{H^{++}}^2 - m_{H^+}^2 \simeq m_{H^+}^2 - m_A^2$ and $m_A^2 \simeq m_H^2$, where $m_{H^{++}}$, m_{H^+} , m_A and m_H are the masses of $H^{\pm\pm}$, H^\pm , A and H , respectively. The squared mass difference is determined by the VEV of the doublet scalar field ($\simeq 246$ GeV), and a scalar self-coupling constant. As such a mass difference is not forbidden by the symmetry of the model, we may be able to distinguish the model from the others which contain charged Higgs bosons by testing these mass relations.

It is important that how the mass differences among the triplet-like scalar bosons are constrained by experiments. We study radiative corrections to the electroweak observables in the HTM to constrain the mass difference [48]. In the model with $\rho \neq 1$ at the tree level like the HTM, apart from the models with $\rho = 1$ at the tree level, a new input parameter has to be introduced in addition to the usual three input parameters such as: α_{em} , G_F and m_Z . In Ref. [49], the on-shell renormalization scheme is constructed in the Higgs model with the $Y = 0$ triplet field, in which four input electroweak parameters: α_{em} , G_F , m_Z and $\sin^2 \theta_W$ are chosen to describe all the other electroweak observables. The radiative corrections to the electroweak observables have been calculated in the $Y = 0$ triplet model [49–51] and in the left-right symmetric model [51].

In our analysis, we first define the on-shell renormalization scheme for the electroweak sector of the HTM by using the method in Ref. [49]. We then calculate radiative corrections to the electroweak observables such as m_W and ρ as a function of the four input parameters: α_{em} , G_F , m_Z and $\sin^2 \theta_W$. We examine the preferable values of the mass spectrum of the triplet-like scalar bosons and the VEV of the triplet field under the constraint from the electroweak precision data. We find that the hierarchical mass spectrum with large mass splitting is favored especially for the case of $m_A (\simeq m_H) > m_{H^+} > m_{H^{++}}$. On the contrary, the inverted hierarchical case with $m_{H^{++}} > m_{H^+} > m_A (\simeq m_H)$ is relatively disfavored.

We then discuss the phenomenology of the HTM at the LHC, especially focusing on the case with the mass difference. Phenomenology with the mass difference among the triplet-like scalar bosons [52–57] is drastically different from that in the case without the mass difference [52–62].

In the case without the mass difference, H^{++} decays into the same sign dilepton $\ell^+ \ell^+$ or the diboson $W^+ W^+$, depending on the size of v_Δ , $m_{H^{++}}$ and also the detail of neutrino masses, where v_Δ is the VEV of the triplet field. On the other hand, in the case with the mass difference, there are two cases, where H^{++} is the heaviest or the lightest of all the triplet-like

scalar bosons. In the case where H^{++} is the lightest, while H^+ can decay into $H^{++}W^{-(*)}$ [54] the decay pattern of H^{++} is the same as in the case without the mass difference. On the contrary, in the case where H^{++} is the heaviest, the cascade decay of H^{++} dominates; i.e., $H^{++} \rightarrow H^+W^{(*)} \rightarrow HW^{(*)}W^{(*)}$ ($AW^{(*)}W^{(*)}$) as long as v_Δ is neither too small nor too large¹.

In this thesis, we focus on the phenomenology of the HTM in the case with $m_{H^{++}} > m_{H^+} > m_H$ (m_A) [57]². In this case, the limit of the mass of H^{++} from the recent results at the LHC cannot be applied, so that the triplet-like scalar bosons with the mass of $\mathcal{O}(100)$ GeV are still allowed. We outline that all the masses of the triplet-like scalar bosons may be able to be reconstructed by measuring the Jacobian peak [63] in the transverse mass distribution as well as the invariant mass distributions of the systems which are generated via the decays of the triplet-like scalar bosons.

1.4 Supersymmetric Higgs sectors

We also study extended Higgs sectors in the supersymmetry. In general, SUSY Higgs sectors are written by a simple formula; i.e., those are constructed from F-term, D-term and soft-breaking terms. In the MSSM, the interaction terms in the Higgs potential are given only by D-term contributions. This fact predicts the mass m_h of the lightest CP-even Higgs boson h less than that of the Z boson at the tree level. At the one-loop level the trilinear top-Yukawa term in the superpotential gives a significant F-term contribution to m_h [64–66], by which m_h can be above the lower bound from the direct search results at the LEP experiment. Predictions to m_h can be different drastically in the extended SUSY standard models, where additional chiral superfields are added to the MSSM. These SUSY models can be classified into two models; i.e., those with interaction terms from the tree level F-term contributions and those without such F-term contributions. In the former models, we discuss effects of F-term contributions to m_h and the triple h coupling hhh at the one-loop level when h looks the SM Higgs boson [67]. We find that in the model with an extra neutral singlet superfield or extra triplet superfields, possible allowed regions of m_h can be much larger than that in the MSSM if we allow the appearance of a strong coupling constant at the TeV scale. The deviation of hhh from the SM prediction can be significant in some models; e.g., a model with four doublets and charged singlet superfields. In extended SUSY standard models without interaction terms from F-term contributions in the Higgs potential at the tree level, there are no such significant effects to m_h and hhh coupling. However, even without such F-term contributions, large deviations can be seen in the MSSM observables due to the mixing among the MSSM-like Higgs bosons and the extra Higgs bosons. As a simplest example, we discuss the model, where two extra doublet superfields are added to the MSSM [68].

¹Recently the importance of this cascade decay has been mentioned in Refs. [54, 55].

²As mentioned above, although this scenario is disfavored by the electroweak precision data, we can still consider the scenario by the extension of the minimal HTM.

1.5 Extended Higgs sectors and the phenomena beyond the SM

In Part II, we discuss TeV scale models including extended Higgs sectors which can explain the phenomena beyond the SM; i.e., neutrino masses, dark matter and/or baryon asymmetry of the Universe.

First, we study a model proposed in Ref. [21], in which neutrino oscillation, dark matter, and the baryon asymmetry of the Universe can be simultaneously explained by the TeV-scale physics without fine tuning. We investigate theoretical constraints from the vacuum stability and the triviality in the model [69]. We calculate the scale dependence of the coupling constants from the renormalization group equations at the one-loop level in the model. As the result, we find that the model can be consistent up to above 10 TeV, where the model would be expected to be replaced by a more fundamental model. We also confirm that the model can explain the constraints from the current experimental data, for example $\mu \rightarrow e\gamma$, $\mu \rightarrow eee$, the WMAP data and the neutrino oscillation data.

Next, we consider the SUSY extension of the Zee-Babu model [17, 18] which can generate neutrino masses at the two-loop level by adding charged singlet fields [70]. In the original (non-SUSY) Zee-Babu model, there remain the hierarchy problem as well as the dark matter problem. By introducing supersymmetry, the quadratic divergence in the one-loop correction to the Higgs boson mass can be cancelled. In addition, due to the R-parity, the stability of the lightest super partner particle such as the neutralino are guaranteed, which may be identified as a candidate of dark matter. In this model, doubly-charged iso-singlet scalar bosons and those SUSY partner fermions appear. We discuss the collider signature of these particles, and we show that the distinctive signature may be measured in the invariant mass distribution of the system which is produced via the decay of the doubly-charged scalar bosons and fermions.

Finally, we consider the isospin doublet field $\Phi_{3/2}$ with $Y = 3/2$ [71], in which doubly-charged scalar states as well as singly-charged ones are contained. Although it has been well studied the phenomenology of doubly-charged scalar bosons from the isospin singlet ($Y = 2$) and the triplet ($Y = 1$), the phenomenology of doubly-charged scalar bosons from $\Phi_{3/2}$ has hardly been studied. First, we discuss the phenomenology of the simple model with $\Phi_{3/2}$ at the LHC. We find that the transverse mass distribution may be useful to measure the masses of scalar bosons including the doubly-charged scalar bosons in the model. We then show that $\Phi_{3/2}$ can be applied to the model, where neutrino masses can explain at the one-loop level and there are the dark matter candidates.

1.6 Organization of this thesis

Part I is composed of three sections: chapter 2, chapter 3 and chapter 4. In chapter 2, we give a brief review of the SM Higgs sector. Phenomenology of extended Higgs sectors are discussed in chapter 3, where we consider the THDM and the HTM. In chapter 4, we discuss the SUSY Higgs sectors and their decoupling properties. Succeeding five sections from chapter 5 to chapter 8 are included in Part II. In chapter 5, we outline the radiative seesaw models. In chapter 6, after we introduce the model proposed in Ref. [21], we then discuss the theoretical constraints from the vacuum stability and the triviality, and also study the constraints from the current experimental data. In chapter 7, we discuss the SUSY extension of the Zee-Babu model and

its phenomenology at the LHC. In chapter 8, we discuss the model with isospin doublet with $Y = 3/2$ field and its phenomenology at the LHC. We also discuss that such a $Y = 3/2$ doublet field can apply to the radiative seesaw model. The conclusion of this thesis is given in chapter 9.

Part I

Phenomenology of Higgs sectors

Chapter 2

The Standard Model Higgs sector

In this chapter, we review the Higgs sector in the SM. In the SM, the Higgs sector takes the minimal form, where there is only one $SU(2)_L$ doublet Higgs scalar field Φ . After the spontaneous breakdown of the $SU(2)_L \times U(1)_Y$ gauge symmetry, weak gauge bosons, fermions and the Higgs boson obtain their masses in the kinetic term of the Higgs doublet field, the Yukawa Lagrangian and the Higgs potential, respectively. In Table 2.1, the charge assignments for the SM particles under the $SU(3)_c \times SU(2)_L \times U(1)_Y$ gauge symmetry are listed. Throughout this thesis, the relationship among the hypercharge Y , the isospin I_3 and the electromagnetic charge Q is defined by $Q = I_3 + Y$. In Table 2.1, Q_L^i (L_L^i) is the i th generation left-handed quark (lepton) doublet, and e_R^i and u_R^i (d_R^i) are the right-handed charged lepton and the up-quark (down-quark) singlet, respectively. We first discuss how all the masses of the SM particles are generated. Second, the bounds of the Higgs boson mass are discussed. Third, we calculate the decay rates of the Higgs boson.

2.1 The masses of particles

2.1.1 The masses for the Higgs boson and the gauge bosons

The Higgs Lagrangian is composed of the kinetic term and the Higgs potential as

$$\mathcal{L}_{\text{Higgs}} = |D^\mu \Phi|^2 - V_{\text{SM}}, \quad V_{\text{SM}} = -\mu^2(\Phi^\dagger \Phi) + \lambda(\Phi^\dagger \Phi)^2, \quad (2.1)$$

where the Higgs doublet field Φ can be parameterized as

$$\Phi = \begin{bmatrix} w^+ \\ \frac{1}{\sqrt{2}}(h + v + iz) \end{bmatrix}, \quad (2.2)$$

with w^\pm and z are the NG bosons which are absorbed by the longitudinal components of W^\pm boson and Z boson, respectively, and $v \simeq 246$ GeV is the VEV of Φ . The covariant derivative for Φ is given as

$$D_\mu \Phi = \left(\partial_\mu - i\frac{g}{2}\tau^a W_\mu^a - i\frac{g'}{2}B_\mu \right) \Phi, \quad (2.3)$$

where W_μ^a ($a = 1, 2, 3$) is the $SU(2)_L$ gauge boson, and B_μ is the $U(1)_Y$ gauge boson. By imposing the vacuum condition:

$$\left. \frac{\partial V_{\text{SM}}}{\partial h} \right|_0 = 0, \quad (2.4)$$

	$SU(3)_c$	$SU(2)_L$	$U(1)_Y$
Q_L^i	3	2	$+\frac{1}{6}$
u_R^i	3	1	$+\frac{2}{3}$
d_R^i	3	1	$-\frac{1}{3}$
L_L^i	1	2	$-\frac{1}{2}$
e_R^i	1	1	-1
Φ	1	2	$+\frac{1}{2}$

Table 2.1: Particle content and its charge assignment under the $SU(3)_c \times SU(2)_L \times U(1)_Y$ gauge symmetry in the SM.

we obtain

$$\mu^2 = v^2 \lambda. \quad (2.5)$$

Plugging Eq. (2.5) into the Higgs potential in Eq. (2.1), the mass m_h of the physical neutral Higgs boson h is obtained as

$$m_h^2 = 2\lambda v^2. \quad (2.6)$$

The mass terms of the weak gauge bosons are derived in the kinetic term $|D_\mu \Phi|^2$ as

$$|D_\mu \Phi|^2 = \frac{g^2 v^2}{8} [(W_\mu^1)^2 + (W_\mu^2)^2] + \frac{v^2}{8} (W_\mu^3, B_\mu) \begin{pmatrix} g^2 & -gg' \\ -gg' & g'^2 \end{pmatrix} \begin{pmatrix} W_\mu^3 \\ B_\mu \end{pmatrix} + \dots \quad (2.7)$$

The charged gauge bosons W^\pm and the neutral gauge bosons are obtained by

$$W_\mu^\pm = \frac{1}{\sqrt{2}}(W_\mu^1 \mp iW_\mu^2), \quad \begin{pmatrix} Z_\mu \\ A_\mu \end{pmatrix} = \begin{pmatrix} \cos \theta_W & -\sin \theta_W \\ \sin \theta_W & \cos \theta_W \end{pmatrix} \begin{pmatrix} W_\mu^3 \\ B_\mu \end{pmatrix}, \quad (2.8)$$

where θ_W is the weak mixing angle with

$$\cos \theta_W = \frac{g}{\sqrt{g^2 + g'^2}}, \quad \sin \theta_W = \frac{g'}{\sqrt{g^2 + g'^2}}. \quad (2.9)$$

The masses of W^\pm and Z are then

$$m_W^2 = \frac{g^2 v^2}{4}, \quad m_Z^2 = \frac{g^2 + g'^2}{4} v^2, \quad (2.10)$$

and the mass of the photon A_μ remains zero.

2.1.2 The fermion masses

The Yukawa Lagrangian is given by

$$\mathcal{L}_{\text{SM}}^Y = - \left[\bar{Q}_L^i Y_d^{ij} \Phi d_R^j + \bar{Q}_L^i Y_u^{ij} \tilde{\Phi} u_R^j + \bar{L}_L^i Y_e^{ij} \Phi e_R^j + \text{h.c.} \right], \quad (2.11)$$

where, $\tilde{\Phi} = i\tau_2\Phi^*$ and $Y_{u,d,e}$ are the 3×3 complex matrices. By taking the following base transformations:

$$\begin{aligned} u_R^i &\rightarrow V_u^{ij} u_R^j, & d_R^i &\rightarrow V_d^{ij} d_R^j, & e_R^i &\rightarrow V_e^{ij} e_R^j, \\ Q_L^i &= \begin{pmatrix} u_L^i \\ d_L^i \end{pmatrix} \rightarrow \begin{pmatrix} U_u^{ij} u_L^j \\ U_d^{ij} d_L^j \end{pmatrix} = U_u^{ij} \begin{pmatrix} u_L^j \\ V_{\text{CKM}} d_L^j \end{pmatrix}, \\ L_L^i &= \begin{pmatrix} \nu_L^i \\ e_L^i \end{pmatrix} \rightarrow U_\ell^{ij} \begin{pmatrix} \nu_L^j \\ e_L^j \end{pmatrix}, \end{aligned} \quad (2.12)$$

where $V_{\text{CKM}} = U_u^\dagger U_d$ is the Cabibbo-Kobayashi-Maskawa matrix [72], the matrices $Y_{u,d,e}$ can be diagonalized as

$$\begin{aligned} \mathcal{L}_{\text{SM}}^Y &\rightarrow - \left[\bar{Q}_L (U_d^\dagger Y_d V_d) \Phi d_R + \bar{Q}_L (U_u^\dagger Y_u V_u) \tilde{\Phi} u_R + \bar{L}_L (U_\ell^\dagger Y_e V_e) \Phi e_R + \text{h.c.} \right] \\ &= - \left[\bar{Q}_L Y_d^{\text{diag}} \Phi d_R + \bar{Q}_L Y_u^{\text{diag}} \tilde{\Phi} u_R + \bar{L}_L Y_e^{\text{diag}} \Phi e_R + \text{h.c.} \right]. \end{aligned} \quad (2.13)$$

The diagonalized matrices $Y_{u,d,e}^{\text{diag}}$ can be expressed as

$$Y_d^{\text{diag}} = \begin{pmatrix} y_d & 0 & 0 \\ 0 & y_s & 0 \\ 0 & 0 & y_b \end{pmatrix}, \quad Y_u^{\text{diag}} = \begin{pmatrix} y_u & 0 & 0 \\ 0 & y_c & 0 \\ 0 & 0 & y_t \end{pmatrix}, \quad Y_e^{\text{diag}} = \begin{pmatrix} y_e & 0 & 0 \\ 0 & y_\mu & 0 \\ 0 & 0 & y_\tau \end{pmatrix}. \quad (2.14)$$

Replacing Φ in Eq. (2.13) by the VEV of the Higgs doublet field $\langle \Phi \rangle = (0, v/\sqrt{2})^T$, the masses of the fermions are

$$\begin{aligned} \mathcal{L}_{\text{SM}}^Y &\rightarrow - \left[\bar{Q}_L Y_d^{\text{diag}} \langle \Phi \rangle d_R + \bar{Q}_L Y_u^{\text{diag}} \langle \tilde{\Phi} \rangle u_R + \bar{L}_L Y_e^{\text{diag}} \langle \Phi \rangle e_R + \text{h.c.} \right] \\ &= - \frac{v}{\sqrt{2}} \bar{d}_L Y_d^{\text{diag}} d_R - \frac{v}{\sqrt{2}} \bar{u}_L Y_u^{\text{diag}} u_R - \frac{v}{\sqrt{2}} \bar{e}_L Y_e^{\text{diag}} e_R + \text{h.c.} \end{aligned} \quad (2.15)$$

Therefore, the fermion masses are written as

$$m_f = \frac{y_f v}{\sqrt{2}}. \quad (2.16)$$

We note that the coupling constants between the Higgs boson and the fermions $h\bar{f}f$ are given by Y_f^{diag} , so that there is no interaction which causes scalar mediating FCNC processes at the tree level in the SM. In addition, the tree level neutral gauge boson mediating FCNC processes are also forbidden by the GIM mechanism [28].

2.2 Bounds for the Higgs boson mass

In the SM, the only unknown parameter is the Higgs boson mass m_h or the Higgs self-coupling constant λ . Here, we discuss the constraints for the Higgs boson mass in the theoretical point of view.

2.2.1 Perturbative unitarity bound

The upper bound for the Higgs boson mass can be obtained by assuming the unitarity of the S-matrix. This approach has been first proposed by Lee, Quigg and Thacker [1]. From the optical theorem, the total cross section σ_{tot} can be written by the imaginary part of the scattering amplitude with the scattering angle $\theta = 0$ as

$$\sigma_{\text{tot}} = \frac{1}{s} \text{Im}[\mathcal{M}(\theta = 0)], \quad (2.17)$$

where s is the squared center of mass energy. Since the main contribution of σ_{tot} comes from 2 body \rightarrow 2 body process, we can write

$$\sigma_{\text{tot}} \gtrsim \frac{1}{s} \int d\cos\theta \frac{|\mathcal{M}|^2}{32\pi}. \quad (2.18)$$

On the other hand, the amplitude \mathcal{M} can be expanded in terms of the J th partial wave amplitude a_J as

$$\mathcal{M} = 16\pi \sum_{J=0}^{\infty} (2J+1) P_J(\cos\theta) a_J. \quad (2.19)$$

By the combination of Eqs. (2.17), (2.18) and Eq. (2.19), we obtain

$$\begin{aligned} \text{Im}(a_J) &\gtrsim |a_J|^2 \\ \Leftrightarrow \text{Re}(a_J)^2 + \left[\text{Im}(a_J) - \frac{1}{2} \right]^2 &\gtrsim \left(\frac{1}{2} \right)^2. \end{aligned} \quad (2.20)$$

This inequality suggests that a_J has to be on the circle with the radius 1/2 and the center of coordinate (0,1/2) in the complex plane. Therefore, we can require that $\text{Re}(a_J)$ is satisfied

$$|\text{Re}(a_J)| < 1/2, \quad (2.21)$$

at the tree level. We apply this constraint to the $W_L^+ W_L^- \rightarrow W_L^+ W_L^-$ process, where W_L is the longitudinal component of the W boson. In Appendix A, detailed calculations for this process are given. In the high energy limit, 0th partial wave amplitude can be calculated as

$$a_0 \sim -\frac{G_F m_h^2}{4\sqrt{2}\pi}. \quad (2.22)$$

From Eq. (2.21), we can obtain the upper bound of the mass of the Higgs boson:

$$m_h^2 < \frac{2\pi\sqrt{2}}{G_F} \sim (871\text{GeV})^2. \quad (2.23)$$

The stronger constraint can be obtained by including the other scattering processes;

$$\frac{1}{\sqrt{2}} Z_L Z_L, \quad \frac{1}{\sqrt{2}} h h, \quad h Z_L. \quad (2.24)$$

In the high energy limit, the scattering process for the longitudinal component of the massive gauge bosons can be replaced by that for corresponding NG boson modes which is known as the equivalence theorem [73]. The 0th partial wave amplitude can be written as the 4×4 matrix in the basis of $(w^+w^-, \frac{1}{\sqrt{2}}zz, \frac{1}{\sqrt{2}}hh, hz)$:

$$a_0 = \frac{-G_F m_h^2}{4\pi\sqrt{2}} \begin{pmatrix} 1 & \frac{1}{\sqrt{8}} & \frac{1}{\sqrt{8}} & 0 \\ \frac{1}{\sqrt{8}} & \frac{3}{4} & \frac{1}{4} & 0 \\ \frac{1}{\sqrt{8}} & \frac{1}{4} & \frac{3}{4} & 0 \\ 0 & 0 & 0 & \frac{1}{2} \end{pmatrix}. \quad (2.25)$$

By diagonalizing this matrix, we obtain the eigenvalues of $(3/2, 1/2, 1/2, 1/2)$ in the unit of $\frac{-G_F m_h^2}{4\pi\sqrt{2}}$. By imposing the condition Eq. (2.21) to each eigenvalue, we obtain

$$m_h^2 < (710 \text{ GeV})^2. \quad (2.26)$$

2.2.2 Triviality and vacuum stability bounds

In the perturbative unitarity bound which is discussed just above, the upper bound for the Higgs boson mass can be obtained by only assuming the unitarity of the S-matrix. As the other approach to constrain the Higgs boson mass, there are the triviality and the vacuum stability bounds which are assumed the cutoff scale Λ of the theory [74–78]. First, recall the renormalization group equation (RGE) of the Higgs self-coupling λ at the one-loop level:

$$\frac{d\lambda}{d\log Q} \simeq \frac{1}{16\pi^2} [24\lambda^2 + 12y_t^2\lambda - 6y_t^4], \quad (2.27)$$

where Q is an arbitrary scale. Full set of the RGEs in the SM is listed in Appendix B. From this equation, large initial values of λ compared with that of the top-Yukawa coupling y_t suggest that λ is getting large value as Q is increasing. Thus, the value of λ becomes too large to rely on the perturbative calculation or close to the infinity which is known as the Landau pole [79]. On the other hand, when initial values of λ is small compared with that of y_t , due to the contribution from $-6y_t^4$ term in Eq. (2.27), λ is getting small value as Q is increasing. This suggests that the value of λ becomes negative in some scale Q , so that the vacuum stability is broken. Consequently, if we require that the model appears neither the Landau pole nor the vacuum instability up to the cutoff scale Λ , then we can obtain the constraint for the initial value of λ as a function of Λ . Since the Higgs boson mass is determined by $2\lambda v^2$, the constraint for λ can be translated into that for the Higgs boson mass. In Ref. [80], the upper bound for the Higgs boson mass has been obtained by using the two-loop level RGE with one-loop matching conditions. For $\Lambda = 10^{19}$ GeV, the upper bound is $m_h < 180 \pm 4 \pm 5$ GeV, the first error including the theoretical uncertainty and the second error reflecting the top-quark mass uncertainty due to $m_t = 175 \pm 6$ GeV.

2.3 Decay of the Higgs boson

The decay rates of the Higgs boson only depends on the mass of the Higgs boson in the SM. There are various decay modes of the Higgs boson; (1) fermion pair decays ($h \rightarrow f\bar{f}$), (2) gauge boson pair decays ($h \rightarrow W^+W^-$ and $h \rightarrow ZZ$), (3) loop-induced decays ($h \rightarrow \gamma\gamma$, $h \rightarrow \gamma Z$

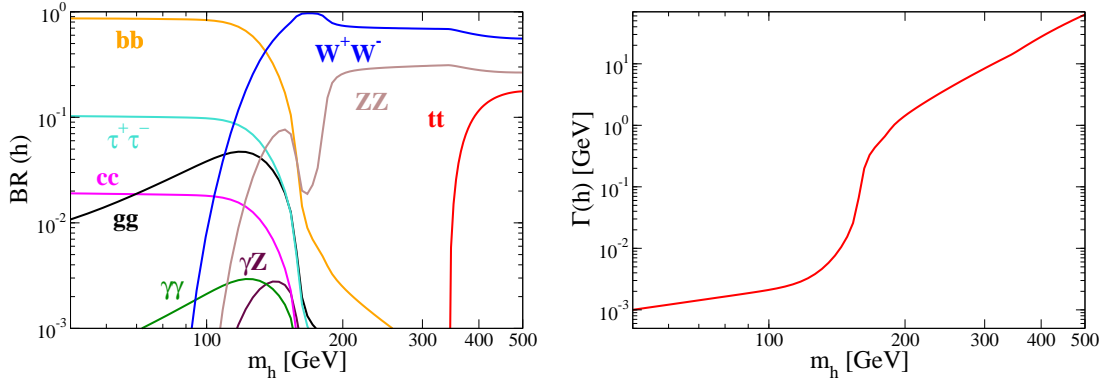


Figure 2.1: (Left) The decay branching ratio of the SM Higgs boson. (Right) The decay width of the SM Higgs boson.

and $h \rightarrow gg$) and (4) three body decays ($h \rightarrow WW^* \rightarrow Wff'$ and $h \rightarrow ZZ^* \rightarrow Zff$). The formulae for these decay rates are listed in Appendix C. The decay branching ratio and the decay width of the Higgs boson are shown in Fig. 2.1.

In this figure, the masses of the top quark, bottom quark and charm quark are taken to be 171.2 GeV, 3.0 GeV and 0.44 GeV. The decay branching ratio is drastically different in the region of $m_h \lesssim 135$ GeV from that in the region of $m_h > 135$ GeV. In the region of $m_h \lesssim 135$ GeV, the Higgs boson mainly decays into $b\bar{b}$, while in the region of $m_h > 135$ GeV, the gauge boson pair decay modes can be dominant. The decay width is grown rapidly when m_h is greater than 130-140 GeV, because of the partial decay width of $h \rightarrow f\bar{f}$ modes is proportional to m_h , while that of the $h \rightarrow VV$ ($V = W, Z$) modes is proportional to m_h^3 .

Chapter 3

Extended Higgs sectors

3.1 The Two Higgs Doublet Model

3.1.1 Model

The THDM contains two isospin doublet scalar fields Φ_1 and Φ_2 with $Y = 1/2$. The most general Higgs potential is given by

$$\begin{aligned} V = & m_1^2 |\Phi_1|^2 + m_2^2 |\Phi_2|^2 - (m_3^2 \Phi_1^\dagger \Phi_2 + \text{h.c.}) \\ & + \frac{1}{2} \lambda_1 |\Phi_1|^4 + \frac{1}{2} \lambda_2 |\Phi_2|^4 + \lambda_3 |\Phi_1|^2 |\Phi_2|^2 + \lambda_4 |\Phi_1^\dagger \Phi_2|^2 \\ & + \frac{1}{2} [\lambda_5 (\Phi_1^\dagger \Phi_2)^2 + \lambda_6 |\Phi_1|^2 \Phi_1^\dagger \Phi_2 + \lambda_7 |\Phi_2|^2 \Phi_1^\dagger \Phi_2 + \text{h.c.}], \end{aligned} \quad (3.1)$$

where m_1, m_2 and λ_1 - λ_4 are real while m_3 and λ_5 - λ_7 are complex in general. The Higgs doublets can be parameterized as

$$\Phi_i = \begin{bmatrix} w_i^+ \\ \frac{1}{\sqrt{2}}(v_i + h_i + iz_i) \end{bmatrix}, \quad (i = 1, 2). \quad (3.2)$$

The most general Yukawa Lagrangian is given by

$$\begin{aligned} \mathcal{L}_{\text{THDM}}^Y = & - \left[\bar{Q}_L (Y_{d1} \Phi_1 + Y_{d2} \Phi_2) d_R + \bar{Q}_L (Y_{u1} \tilde{\Phi}_1 + Y_{u2} \tilde{\Phi}_2) u_R + \bar{L}_L (Y_{e1} \Phi_1 + Y_{e2} \Phi_2) e_R + \text{h.c.} \right], \end{aligned} \quad (3.3)$$

where Y_{f1} and Y_{f2} , ($f = u, d, e$) are the 3×3 complex matrices and $\tilde{\Phi}_i = i\tau_2 \Phi_i^*$, ($i = 1, 2$). In the THDM, neutral scalar bosons mediated FCNC processes appear at the tree level in general. To understand the FCNC problem, we introduce so-called the Georgi basis or the Higgs basis [81] as

$$\begin{pmatrix} \Phi_1 \\ \Phi_2 \end{pmatrix} = R(\beta) \begin{pmatrix} \Phi \\ \Psi \end{pmatrix}, \quad R(\theta) \equiv \begin{pmatrix} \cos \beta & -\sin \beta \\ \sin \beta & \cos \beta \end{pmatrix}, \quad (3.4)$$

where

$$\Phi = \begin{bmatrix} w^+ \\ \frac{1}{\sqrt{2}}(v + h'_1 + iz) \end{bmatrix}, \quad \Psi = \begin{bmatrix} H^+ \\ \frac{1}{\sqrt{2}}(h'_2 + iA) \end{bmatrix}, \quad (3.5)$$

with $v \simeq 246$ GeV and $\tan \beta = v_2/v_1$. In Eq. (3.5), w^\pm and z are the NG bosons which are absorbed into the longitudinal component of W^\pm and Z , respectively. The scalar boson states in the Georgi basis are related to the original ones through the following relations:

$$\begin{pmatrix} w_1^\pm \\ w_2^\pm \end{pmatrix} = R(\beta) \begin{pmatrix} w^\pm \\ H^\pm \end{pmatrix}, \quad \begin{pmatrix} z_1 \\ z_2 \end{pmatrix} = R(\beta) \begin{pmatrix} z \\ A \end{pmatrix}, \quad \begin{pmatrix} h_1 \\ h_2 \end{pmatrix} = R(\beta) \begin{pmatrix} h'_1 \\ h'_2 \end{pmatrix}. \quad (3.6)$$

In the CP-conserving case, H^\pm are the charged scalar bosons, A is the CP-odd scalar boson and h'_1 and h'_2 are the CP-even scalar states whose mass matrix is non-diagonal at this stage. In this basis, the Yukawa Lagrangian can be rewritten as

$$\mathcal{L}_{\text{THDM}}^Y = - \left[\bar{Q}_L \left(\frac{\sqrt{2}}{v} M_d \Phi + Y_d \Psi \right) d_R + \bar{Q}_L \left(\frac{\sqrt{2}}{v} M_u \tilde{\Phi} + Y_u \tilde{\Psi} \right) u_R + \bar{L}_L \left(\frac{\sqrt{2}}{v} M_e \Phi + Y_e \Psi \right) e_R + \text{h.c.} \right], \quad (3.7)$$

where M_f is the non-diagonal 3×3 fermion mass matrix, while Y_f is the complex 3×3 matrix which is non-diagonal in general. These matrices can be written in terms of the original Yukawa matrices Y_{f1} and Y_{f2} as

$$\frac{\sqrt{2}}{v} M_f = Y_{f1} \cos \beta + Y_{f2} \sin \beta, \quad (3.8a)$$

$$Y_f = -Y_{f1} \sin \beta + Y_{f2} \cos \beta. \quad (3.8b)$$

In the mass eigenstates of fermions, the matrix Y_f is rotated by the unitary matrices which diagonalize the mass matrix M_f . However, the rotated matrix Y'_f is also non-diagonal in general, since there is no reason for Y_f to be proportional to M_f . Therefore, through the non-diagonal elements of Y_f , neutral scalar boson mediating FCNC processes can appear at the tree level.

There are several ways to avoid such a FCNC problem;

- (1) Introducing a texture to the Yukawa matrices [82].
- (2) Assuming that the masses of the neutral scalar bosons which are mediated the FCNC processes are sufficiently large.
- (3) Assuming that the two Yukawa matrices Y_{f1} and Y_{f2} are proportional to each other [83].
- (4) Imposing an additional symmetry such as the Z_2 symmetry [29] to forbid the one of the Yukawa matrices Y_{f1} and Y_{f2} .

A model with the prescription of (1) listed in the above is one of a realization for a phenomenologically viable model which deduces so-called the type-III THDM [84], where tree-level FCNC processes appear. In Ref. [82], by the assumption that non-diagonal Yukawa couplings are proportional to the geometric mean of the two fermion masses, $g_{ij} \propto m_i m_j$, the FCNC interactions can be suppressed.

The way of (2) is the obvious possibility and not so phenomenologically interesting. In this case, the THDM is just reduced to the SM.

The THDM with the assumption of (3), which is so-called the Yukawa alignment, has been discussed in Ref. [83]. Following [83], we assume that the one of the two Yukawa matrices is proportional to the other one:

$$Y_{f2} = \zeta_f Y_{f1}, \quad (3.9)$$

where ζ_f is the complex constant. In this case, Eq. (3.8) can be rewritten as

$$\frac{\sqrt{2}}{v} M_f = Y_{f1} (\cos \beta + \zeta_f \sin \beta), \quad (3.10a)$$

$$Y_f = Y_{f1} (-\sin \beta + \zeta_f \cos \beta), \quad (3.10b)$$

so that the matrix Y_f is given by the same matrix for the fermion masses as

$$Y_f = \frac{\zeta_f - \tan \beta}{1 + \zeta_f \tan \beta} \times \frac{\sqrt{2}}{v} M_f. \quad (3.11)$$

Therefore, the matrices Y_f and M_f can be diagonalized simultaneously.

In this section, we study the THDM with a softly-broken discrete Z_2 symmetry which is corresponding to the prescription of (4) as the simplest but the natural way¹. Hereafter, we discuss the Z_2 invariant THDM. Under the Z_2 symmetry, we suppose that the Higgs doublets are translated into $\Phi_1 \rightarrow +\Phi_1$ and $\Phi_2 \rightarrow -\Phi_2$. The Z_2 invariant Higgs potential can be written as

$$\begin{aligned} V = & m_1^2 |\Phi_1|^2 + m_2^2 |\Phi_2|^2 - m_3^2 (\Phi_1^\dagger \Phi_2 + \text{h.c.}) \\ & + \frac{1}{2} \lambda_1 |\Phi_1|^4 + \frac{1}{2} \lambda_2 |\Phi_2|^4 + \lambda_3 |\Phi_1|^2 |\Phi_2|^2 + \lambda_4 |\Phi_1^\dagger \Phi_2|^2 + \frac{1}{2} \lambda_5 [(\Phi_1^\dagger \Phi_2)^2 + \text{h.c.}], \end{aligned} \quad (3.12)$$

where the terms of λ_6 and λ_7 in Eq. (3.1) are forbidden by the Z_2 symmetry. In the Z_2 invariant Higgs potential, there are six real parameters and two complex parameters. In Eq. (3.12), we assume the CP-conserving Higgs potential; i.e., the imaginary parts of m_3 and λ_5 are neglected. From the vacuum condition:

$$m_1^2 = m_3^2 \tan \beta - \frac{v^2}{2} (\lambda_1 \cos^2 \beta + \bar{\lambda} \sin^2 \beta), \quad (3.13)$$

$$m_2^2 = m_3^2 \cot \beta - \frac{v^2}{2} (\lambda_1 \sin^2 \beta + \bar{\lambda} \cos^2 \beta), \quad (3.14)$$

we can eliminate m_1^2 and m_2^2 in the Higgs potential, where $\bar{\lambda} = \lambda_3 + \lambda_4 + \lambda_5$. The masses of H^\pm and A can be calculated as

$$m_{H^\pm}^2 = M^2 - \frac{v^2}{2} (\lambda_4 + \lambda_5), \quad m_A^2 = M^2 - v^2 \lambda_5, \quad (3.15)$$

where M is the soft breaking Z_2 symmetry parameter:

$$M^2 = \frac{m_3^2}{\sin \beta \cos \beta}. \quad (3.16)$$

¹ In Ref. [85], the THDM with an additional local $U(1)$ symmetry instead of the Z_2 symmetry has been discussed.

The mass matrix for the neutral CP-even scalar states is

$$V_{\text{THDM}}^{\text{CP-even}} = \frac{1}{2}(h'_1, h'_2) \begin{pmatrix} M_{11}^2 & M_{12}^2 \\ M_{12}^2 & M_{22}^2 \end{pmatrix} \begin{pmatrix} h'_1 \\ h'_2 \end{pmatrix}, \quad (3.17)$$

where matrix elements are

$$M_1^2 = v^2(\lambda_1 \cos^4 \beta + \lambda_2 \sin^4 \beta) + \frac{v^2}{2} \bar{\lambda} \sin^2 2\beta, \quad (3.18a)$$

$$M_2^2 = M^2 + v^2 \sin^2 \beta \cos^2 \beta (\lambda_1 + \lambda_2 - 2\bar{\lambda}), \quad (3.18b)$$

$$M_{12}^2 = \frac{v^2}{2} \sin 2\beta (-\lambda_1 \cos^2 \beta + \lambda_2 \sin^2 \beta) + \frac{v^2}{2} \sin 2\beta \cos 2\beta \bar{\lambda}. \quad (3.18c)$$

We here introduce the mixing angle α to diagonalize the mass matrix for the CP-even scalar states as:

$$\begin{pmatrix} h'_1 \\ h'_2 \end{pmatrix} = R(\alpha - \beta) \begin{pmatrix} H \\ h \end{pmatrix}. \quad (3.19)$$

The mass eigenvalues are

$$m_{H,h}^2 = \frac{1}{2} \left[M_1^2 + M_2^2 \pm \sqrt{(M_1^2 - M_2^2)^2 + 4M_{12}^2} \right]. \quad (3.20)$$

The mixing angle $\alpha - \beta$ is expressed in terms of the mass matrix elements in Eq. (3.18)

$$\tan 2(\alpha - \beta) = \frac{2M_{12}^2}{M_1^2 - M_2^2}. \quad (3.21)$$

The original eight parameters in the Higgs potential: $\lambda_1 - \lambda_5$ and $m_1^2 - m_3^2$ are described by the four physical scalar boson masses: m_{H^\pm} , m_A , m_H , m_h , two mixing angles α and β , the VEV v and the soft-breaking scale of the Z_2 symmetry M . It is useful to rewrite the quartic couplings $\lambda_1 - \lambda_5$ to the physical parameters as

$$\lambda_1 = \frac{1}{v^2 \cos^2 \beta} [-\sin^2 \beta M^2 + \cos^2 \alpha m_H^2 + \sin^2 \alpha m_h^2], \quad (3.22a)$$

$$\lambda_2 = \frac{1}{v^2 \sin^2 \beta} [-\cos^2 \beta M^2 + \sin^2 \alpha m_H^2 + \cos^2 \alpha m_h^2], \quad (3.22b)$$

$$\lambda_3 = -\frac{M^2}{v^2} + \frac{2m_{H^\pm}^2}{v^2} + \frac{1}{v^2} \frac{\sin 2\alpha}{\sin 2\beta} (m_H^2 - m_h^2), \quad (3.22c)$$

$$\lambda_4 = \frac{1}{v^2} (M^2 + m_A^2 - 2m_{H^\pm}^2), \quad (3.22d)$$

$$\lambda_5 = \frac{1}{v^2} (M^2 - m_A^2). \quad (3.22e)$$

The most general Yukawa interaction under the Z_2 symmetry can be written as

$$\mathcal{L}_{\text{THDM}}^Y = -y_u \bar{Q}_L \tilde{\Phi}_u u_R - y_d \bar{Q}_L \Phi_d d_R - y_e \bar{L}_L \Phi_e e_R + \text{h.c.}, \quad (3.23)$$

	Φ_1	Φ_2	u_R	d_R	ℓ_R	Q_L, L_L
Type-I	+	−	−	−	−	+
Type-II	+	−	−	+	+	+
Type-X	+	−	−	−	+	+
Type-Y	+	−	−	+	−	+

Table 3.1: Variation in charge assignments of the Z_2 symmetry [38].

	ξ_h^u	ξ_h^d	ξ_h^ℓ	ξ_H^u	ξ_H^d	ξ_H^ℓ	ξ_A^u	ξ_A^d	ξ_A^ℓ
Type-I	$\frac{\cos \alpha}{\sin \beta}$	$\frac{\cos \alpha}{\sin \beta}$	$\frac{\cos \alpha}{\sin \beta}$	$\frac{\sin \alpha}{\sin \beta}$	$\frac{\sin \alpha}{\sin \beta}$	$\frac{\sin \alpha}{\sin \beta}$	$-\cot \beta$	$\cot \beta$	$\cot \beta$
Type-II	$\frac{\cos \alpha}{\sin \beta}$	$-\frac{\sin \alpha}{\cos \beta}$	$-\frac{\sin \alpha}{\cos \beta}$	$\frac{\sin \alpha}{\sin \beta}$	$\frac{\cos \alpha}{\cos \beta}$	$\frac{\cos \alpha}{\cos \beta}$	$-\cot \beta$	$-\tan \beta$	$-\tan \beta$
Type-X	$\frac{\cos \alpha}{\sin \beta}$	$\frac{\cos \alpha}{\sin \beta}$	$-\frac{\sin \alpha}{\cos \beta}$	$\frac{\sin \alpha}{\sin \beta}$	$\frac{\sin \alpha}{\sin \beta}$	$\frac{\cos \alpha}{\cos \beta}$	$-\cot \beta$	$\cot \beta$	$-\tan \beta$
Type-Y	$\frac{\cos \alpha}{\sin \beta}$	$-\frac{\sin \alpha}{\cos \beta}$	$\frac{\cos \alpha}{\sin \beta}$	$\frac{\sin \alpha}{\sin \beta}$	$\frac{\cos \alpha}{\cos \beta}$	$\frac{\sin \alpha}{\sin \beta}$	$-\cot \beta$	$-\tan \beta$	$\cot \beta$

Table 3.2: The mixing factors in Yukawa interactions in Eq. (3.24) [38].

where Φ_f ($f = u, d$ or e) is either Φ_1 or Φ_2 . There are four independent Z_2 charge assignments on quarks and charged leptons, as summarized in TABLE 3.1 [36, 37]. In the type-I THDM, all quarks and charged leptons obtain their masses from the VEV of Φ_2 . In the type-II THDM, masses of up-type quarks are generated by the VEV of Φ_2 , while those of down-type quarks and charged leptons are acquired by that of Φ_1 . The Higgs sector of the MSSM is a special THDM whose Yukawa interaction is of type-II. The type-X Yukawa interaction (all quarks couple to Φ_2 while charged leptons couple to Φ_1) is used in the model in Ref. [21]. The remaining one is referred to as the type-Y THDM.

The Yukawa interactions are expressed in terms of mass eigenstates of the Higgs bosons as

$$\begin{aligned} \mathcal{L}_{\text{THDM}}^Y = & - \sum_{f=u,d,e} \left(\frac{m_f}{v} \xi_h^f \bar{f} f h + \frac{m_f}{v} \xi_H^f \bar{f} f H + i \frac{m_f}{v} \xi_A^f \bar{f} \gamma_5 f A \right) \\ & - \left[\frac{\sqrt{2} V_{ud}}{v} \bar{u} (m_u \xi_A^u P_L + m_d \xi_A^d P_R) d H^+ + \frac{\sqrt{2} m_\ell \xi_A^\ell}{v} \bar{\nu}_L e_R H^+ + \text{h.c.} \right], \end{aligned} \quad (3.24)$$

where $P_{L/R}$ are projection operators for left-/right-handed fermions, and the factors ξ_φ^f are listed in TABLE 3.2.

For the successful electroweak symmetry breaking, a combination of quartic coupling constants should satisfy the condition of vacuum stability [86–88]. We also take into account bounds from perturbative unitarity to restrict parameters in the Higgs potential [89, 90]. The top and bottom Yukawa coupling constants cannot be taken too large. The requirement $|Y_{t,b}|^2 < \pi$ at the tree level can provide a milder constraint $0.4 \lesssim \tan \beta \lesssim 91$, where $|Y_t| = (\sqrt{2}/v) m_t \cot \beta$ and $|Y_b| = (\sqrt{2}/v) m_b \tan \beta$.

3.1.2 Decay

Here, we discuss the difference in decays of the Higgs bosons for the types of Yukawa interactions in the THDM. We calculate the decay rates of the Higgs bosons and evaluate the total widths and the branching ratios. In particular, we show the result with $\sin(\beta - \alpha) = 1$ [91, 92], where h is the SM-like Higgs boson while the VEV of H is zero. The decay pattern of h is almost the same as that of the SM Higgs boson with the same mass at the leading order except for the loop-induced channels when $\sin(\beta - \alpha) = 1$. In this case, H does not decay into the gauge boson pair at tree level, so it mainly decays into fermion pairs². We note that A and H^\pm do not decay into the gauge boson pair at the tree level for all values of $\sin(\beta - \alpha)$.

The decay patterns are therefore completely different among the different types of Yukawa interactions [36, 37]. For the decays of H and A , we take into account the decay channels of $q\bar{q}$, $\ell^+\ell^-$, $(WW^{(*)}, ZZ^{(*)})$ at the tree level, and gg , $\gamma\gamma$, $Z\gamma$ at the leading order, where q represents s , c , b (and t), and ℓ represents μ and τ . Running masses for b , c , and s quarks are fixed as $\overline{m}_b = 3.0$ GeV, $\overline{m}_c = 0.81$ GeV and $\overline{m}_s = 0.077$ GeV, respectively. For the decay of the charged Higgs boson, the modes into tb , cb , cs , $\tau\nu$, and $\mu\nu$ are taken into account as long as they are kinematically allowed.

In FIG. 3.1, the total widths of H , A and H^\pm are shown as a function of the mass of decaying Higgs bosons for several values of $\tan\beta$ in the four different types of Yukawa interactions. We assume $\sin(\beta - \alpha) = 1$ and $m_\Phi = m_H = m_A = m_{H^\pm}$. The widths strongly depend on the types of Yukawa interactions for each $\tan\beta$ value before and after the threshold of the $t\bar{t}$ (tb) decay mode opens.

In FIG. 3.2, the decay branching ratios of H , A and H^\pm are shown for $m_\Phi = 150$ GeV and $\sin(\beta - \alpha) = 1$ as a function of $\tan\beta$. In the type-I THDM, the decay of H into a gauge boson pair $\gamma\gamma$ or $Z\gamma$ can increase for large $\tan\beta$ values, because all the other fermionic decays (including the gg mode) are suppressed but the charged scalar loop contribution to $\gamma\gamma$ and $Z\gamma$ decay modes is not always suppressed for large $\tan\beta$. Such an enhancement of the bosonic decay modes cannot be seen in the decay of A since there is no AH^+H^- coupling. In the type-X THDM, the main decay mode of H and A is $\tau^+\tau^-$ for $\tan\beta \gtrsim 2$, and the leptonic decays $\tau^+\tau^-$ and $\mu^+\mu^-$ become almost 99% and 0.35% for $\tan\beta \gtrsim 10$, while the $b\bar{b}$ (or gg) mode is always the main decay mode in all other cases. In the type-Y THDM, the leptonic decay modes of H and A are rapidly suppressed for large $\tan\beta$ values, and only the branching ratios of $b\bar{b}$ and gg modes are sizable for $\tan\beta \gtrsim 10$. In charged Higgs boson decays with $m_{H^\pm} = 150$ GeV, the decay into $\tau\nu$ is dominant in the type-I THDM, the type-II THDM and the type-X THDMs for $\tan\beta \gtrsim 1$, while hadronic decay modes can also be dominant in the type-Y THDM.

3.1.3 Constraints from the current experimental data on THDMs

One of the direct signal of the THDM is the discovery of extra Higgs bosons, which have been searched at the LEP and Tevatron [94, 95]. Indirect contributions of Higgs bosons to precisely measurable observables can also be used to constrain Higgs boson parameters. In this section, we summarize these experimental bounds.

A direct mass bound is given from the LEP direct search results as $m_{H^0} \gtrsim 92.8$ GeV for CP-even Higgs bosons and $m_A \gtrsim 93.4$ GeV for CP-odd Higgs bosons in supersymmetric models.

²In the case with a more complicated mass spectrum a heavy Higgs boson can decay into the states which contain lighter Higgs bosons [93].

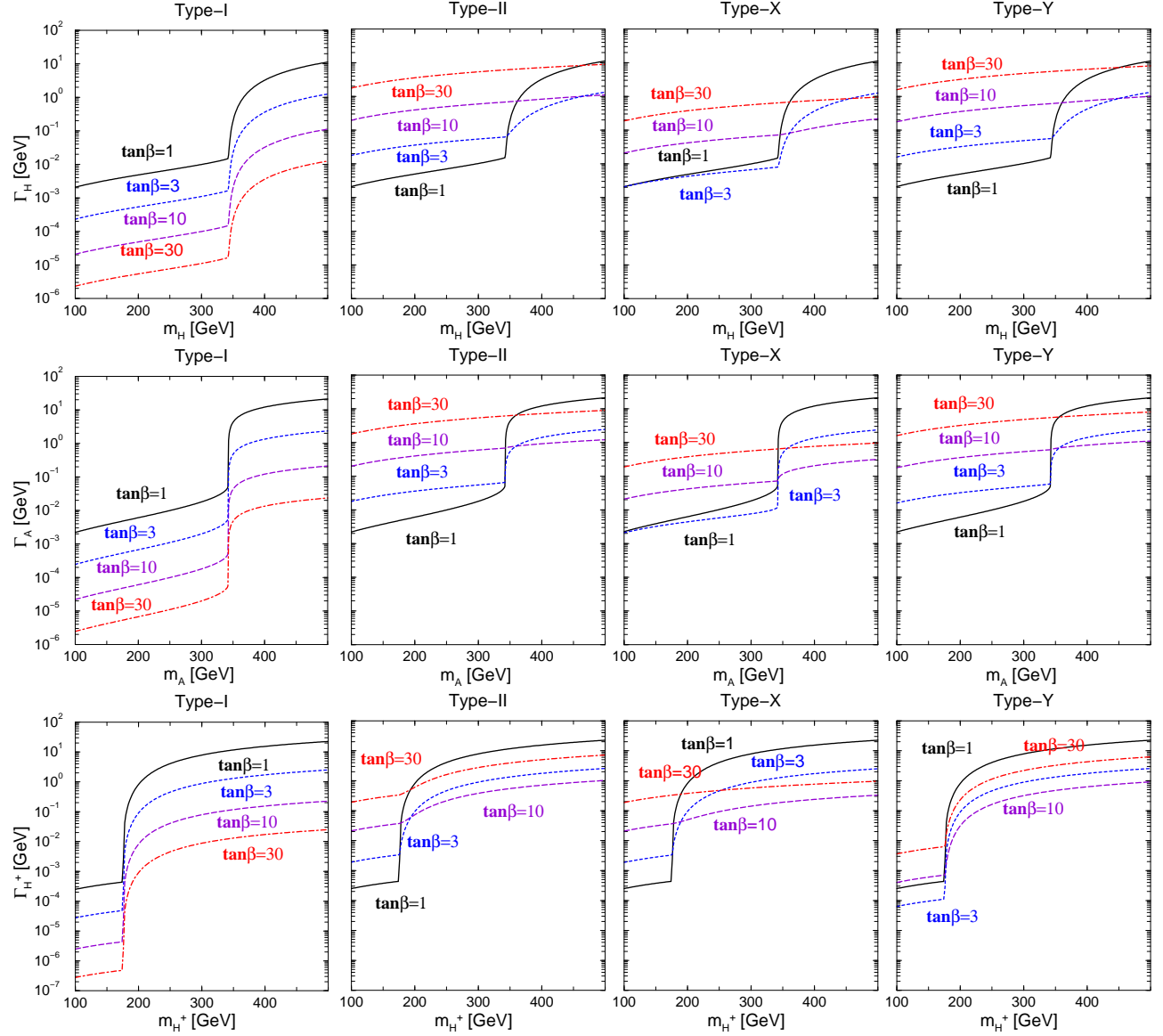


Figure 3.1: Total decay widths of H , A and H^\pm in the four different types of THDM as a function of the decaying scalar boson mass for several values of $\tan\beta$ under the assumption $m_\Phi = m_H = m_A = m_{H^\pm}$. The SM-like limit $\sin(\beta - \alpha) = 1$ is taken, where h is the SM-like Higgs boson [38].

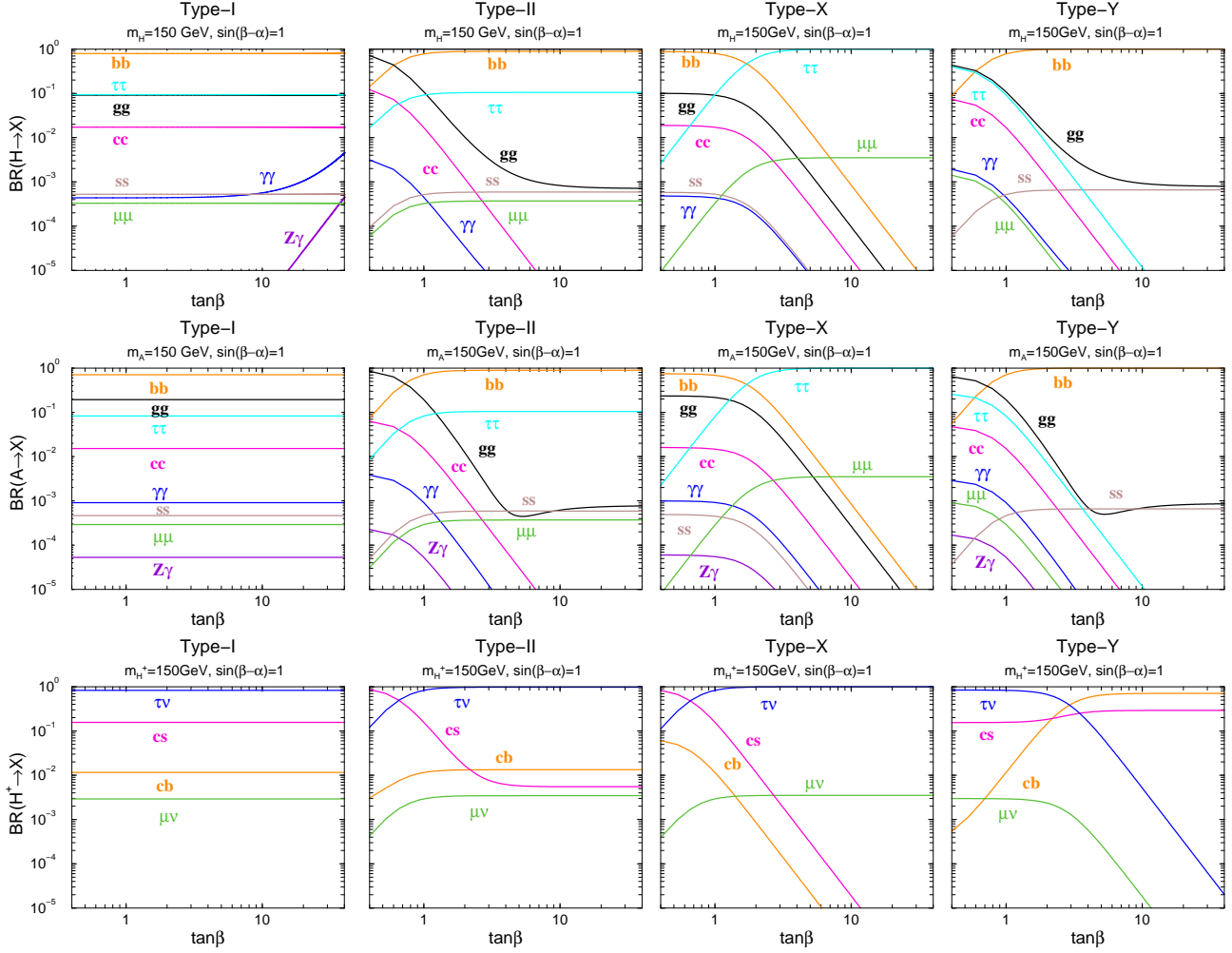


Figure 3.2: Decay branching ratios of H , A and H^\pm in the four different types of THDM as a function of $\tan\beta$ for $m_H = m_A = m_{H^\pm} = 150$ GeV. The SM-like limit $\sin(\beta - \alpha) = 1$ is taken, where h is the SM-like Higgs boson [38].

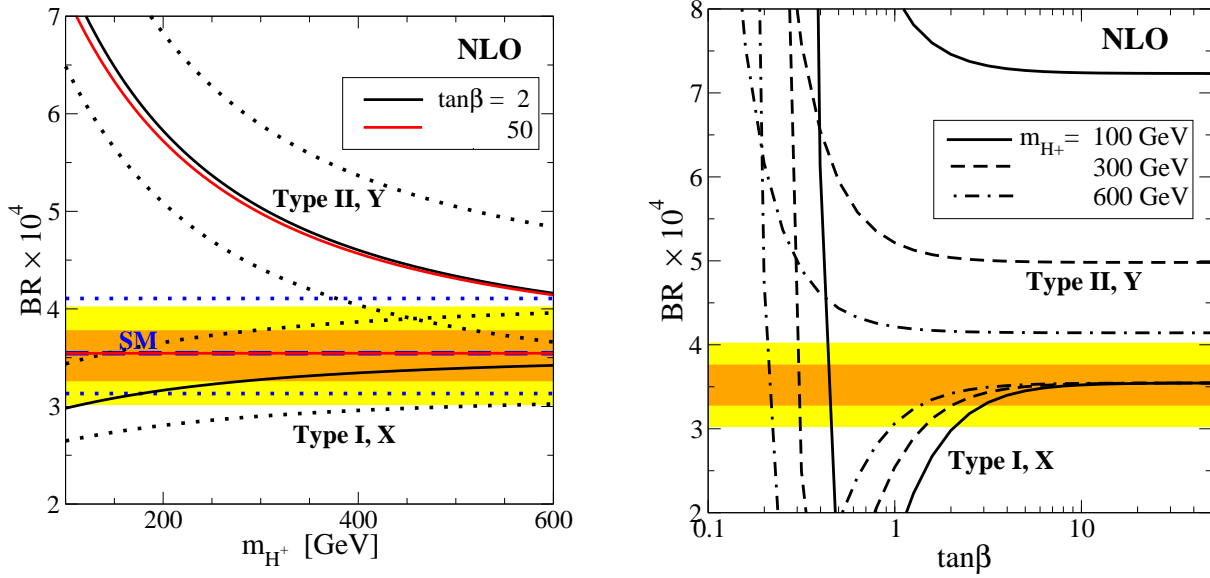


Figure 3.3: Predictions of the decay branching ratio for $b \rightarrow s\gamma$ are shown at the NLO approximation as a function of m_{H^\pm} and $\tan\beta$. The dark (light) shaded band represents 1σ (2σ) allowed region of current experimental data. In the left panel, solid (dashed) curves denote the prediction for $\tan\beta = 2$ (50) in various THDMs. In the right panel, solid, dashed and dot-dashed curves are those for $m_{H^\pm} = 100, 300$ and 600 GeV, respectively [38].

The bound for charged Higgs boson has also been set as $m_{H^\pm} \gtrsim 79.3$ GeV [94].

In the THDM, one-loop contributions of scalar loop diagrams to the rho parameter are expressed as [27]

$$\delta\rho_{\text{THDM}} = \frac{\sqrt{2}G_F}{16\pi^2} \left\{ F_5(m_A, m_{H^\pm}) - \cos^2(\alpha - \beta) [F_5(m_h^2, m_A^2) - F_5(m_h, m_{H^\pm})] \right. \\ \left. - \sin^2(\alpha - \beta) [F_5(m_H, m_A) - F_5(m_H, m_{H^\pm})] \right\}, \quad (3.25)$$

where $F_5(x, y) = \frac{1}{2}(m_1^2 + m_2^2) - \frac{m_1^2 m_2^2}{m_1^2 - m_2^2} \ln \frac{m_1^2}{m_2^2}$ with $F_5(m, m) = 0^3$. These quadratic mass contributions can cancel out when Higgs boson masses satisfy the following relation: (i) $m_A \simeq m_{H^\pm}$, (ii) $m_H \simeq m_{H^\pm}$ with $\sin(\beta - \alpha) \simeq 1$, and (iii) $m_h \simeq m_{H^\pm}$ with $\sin(\beta - \alpha) \simeq 0$. These relations correspond to the custodial symmetry invariance [96, 97]. This constraint is independent of the type of Yukawa interaction.

It has been known that the charged Higgs boson mass in the type-II THDM is stringently constrained by the precision measurements of the radiative decay of $b \rightarrow s\gamma$ at Belle [98] and BABAR [99] as well as CLEO [100]. The process $b \rightarrow s\gamma$ receives contributions from the W boson loop and the charged Higgs boson loop in the THDM. A notable point is that these two contributions always work constructively in the type-II (type-Y) THDM, while this is not the case in the type-I (type-X) THDM [36]. In FIG. 3.3, we show the branching ratio of $B \rightarrow X_s \gamma$

³ There are other (relatively smaller in most of the parameter space) contributions to the rho parameter in the THDM, i.e., those from the diagrams where the gauge boson (as well as HG boson) and the Higgs boson are running together in the loop [27]. We have included these effect in our numerical analysis.

for each type of THDM as a function of m_{H^\pm} (left-panel) and $\tan\beta$ (right-panel), which are evaluated at the next-to-leading order (NLO) following the formulas in Ref. [40]. The SM prediction at the NLO is also shown for comparison. The theoretical uncertainty is about 15%⁴ in the branching ratio (as indicated by dotted curves in FIG. 3.3), which mainly comes from the pole mass of charm quark $m_c^{\text{pole}} = 1.65 \pm 0.18$ GeV [26]. The experimental bounds of the branching ratio are also indicated, where the current world average value is given by $\mathcal{B}(B \rightarrow X_s \gamma) = (3.52 \pm 0.23 \pm 0.09) \times 10^{-4}$ [101]. It is seen in FIG. 3.3 that the branching ratio in the type-I (type-X) THDM lies within the 2σ experimental error in all the regions of m_{H^\pm} indicated for $\tan\beta \gtrsim 2$, while that in the type-II (type-Y) THDM is far from the value indicated by the data for a light charged Higgs boson region ($m_{H^\pm} \lesssim 200$ GeV). In the right figure, a cancellation occurs in the type-I (type-X) THDM since there are destructive interferences between the W boson and the H^\pm contributions. It is emphasized that the charged Higgs boson could be light in the type-I (type-X) THDM under the constraint from $B \rightarrow X_s \gamma$ results. We note that in the MSSM the chargino contribution can compensate the charged Higgs boson contribution [102]. This cancellation weakens the limit on m_{H^\pm} from $b \rightarrow s \gamma$ in the type-II THDM, and allows a light charged Higgs boson as in the type-I (type-X) THDM.

We give some comments on the NNLO analysis, although it is basically out of the scope of this paper. At the NNLO, the branching ratio for $b \rightarrow s \gamma$ has been evaluated in the SM in Ref. [44, 45]. The predicted value at the NNLO is less than that at the NLO approximation in a wide range of renormalization scale. In Ref. [44], the SM branching ratio is $(3.15 \pm 0.23) \times 10^{-4}$, and the lower bound of the m_{H^\pm} , after adding the NLO charged Higgs contribution, is estimated as $m_{H^\pm} \gtrsim 295$ GeV (95% CL) in the type-II (type-Y) THDM [44]⁵. On the other hand, in the type-I (type-X) THDM, although the branching ratio becomes smaller as compared to the NLO evaluation, no serious bound on m_{H^\pm} can be found for $\tan\beta \gtrsim 2$. Therefore, charged Higgs boson mass is not expected to be strongly constrained in the type-I (type-X) THDM even at the NNLO, and our main conclusion that the type-I (type-X) THDM is favored for $m_{H^\pm} \lesssim 200$ GeV based on the NLO analysis should not be changed.

The decay $B \rightarrow \tau \nu$ has been discussed in the type-II THDM [42, 43]. The data for $\mathcal{B}(B^+ \rightarrow \tau^+ \nu_\tau) = (1.4 \pm 0.4) \times 10^{-4}$ are obtained at the B factories [26, 103]. The decay branching ratio can be written as [42, 104]

$$\frac{\mathcal{B}(B^+ \rightarrow \tau^+ \nu_\tau)_{\text{THDM}}}{\mathcal{B}(B^+ \rightarrow \tau^+ \nu_\tau)_{\text{SM}}} \simeq \left(1 - \frac{m_B^2}{m_{H^\pm}^2} \xi_A^d \xi_A^\ell \right)^2. \quad (3.26)$$

In FIG. 3.4, the allowed region from the $B \rightarrow \tau \nu$ results is shown in the type-II THDM. The dark (light) shaded region denotes the 2σ (1σ) exclusion from the $B \rightarrow \tau \nu$ measurements. The process is important only in the type-II THDM with large $\tan\beta$ values. The other types of Yukawa interactions do not receive constraints from this process.

The rate for the leptonic decay of the tau lepton $\tau \rightarrow \mu \bar{\nu} \nu$ can be deviated from the SM value by the presence of a light charged Higgs boson [105]. The partial decay rate is approximately

⁴In Ref. [40], the theoretical uncertainty is smaller because the value for the error in $m_c^{\text{pole}}/m_b^{\text{pole}}$ is taken to be 7%, which gives main uncertainty in the branching ratio.

⁵In Ref. [45] the NNLO branching ratio in the SM is calculated as $(2.98 \pm 0.26) \times 10^{-4}$, and the mass bound is a little bit relaxed.

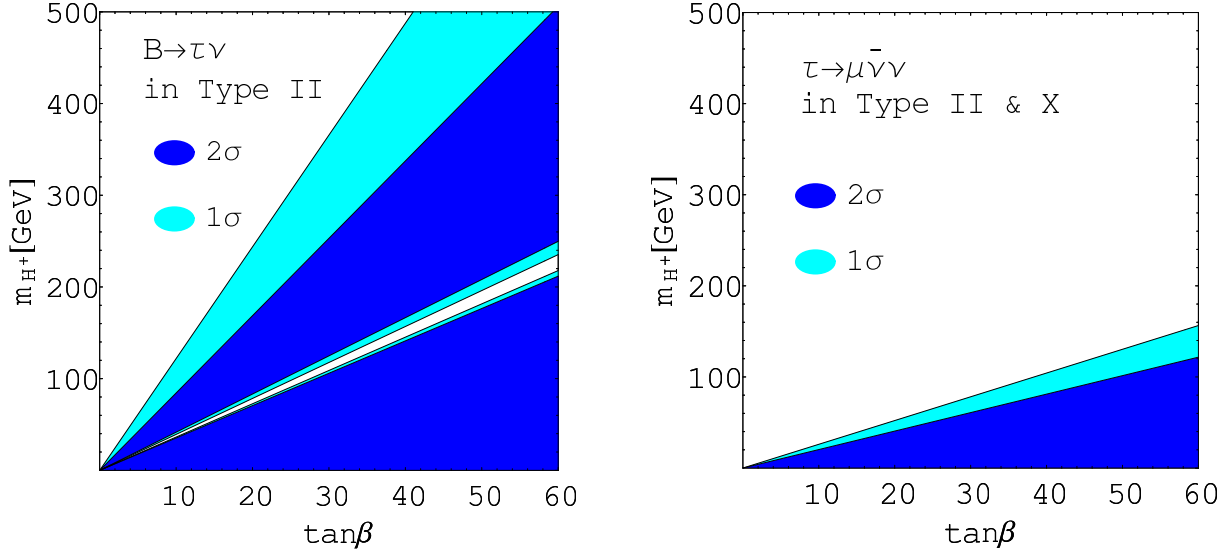


Figure 3.4: Bounds from $B \rightarrow \tau \nu$ (left panel) and tau leptonic decay (right panel) on m_{H^\pm} as a function of $\tan \beta$ are shown. The dark (light) shaded region corresponds to the 2σ (1σ) exclusion of these experimental results. In the type-II THDM the wide parameter space is constrained by $B \rightarrow \tau \nu$, while only the tau leptonic decays are important for the type-X THDM [38].

expressed as [41, 42]

$$\frac{\Gamma_{\tau \rightarrow \mu \bar{\nu} \nu}^{\text{THDM}}}{\Gamma_{\tau \rightarrow \mu \bar{\nu} \nu}^{\text{SM}}} \simeq 1 - \frac{2m_\mu^2}{m_{H^\pm}^2} \xi_A^{\ell^2} \kappa \left(\frac{m_\mu^2}{m_\tau^2} \right) + \frac{m_\mu^2 m_\tau^2}{4m_{H^\pm}^4} \xi_A^{\ell^4}, \quad (3.27)$$

where $\kappa(x) = g(x)/f(x)$ is defined by $f(x) = 1 - 8x - 12x^2 \ln x + 8x^3 - x^4$, and $g(x) = 1 + 9x - 9x^2 - x^3 + 6x(1+x) \ln x$. In the type-II (type-X) THDM, the leptonic Yukawa interaction can be enhanced in the large $\tan \beta$ region. Hence, both the models are weakly constrained by tau decay data, as in FIG. 3.4.

The precision measurement for the muon anomalous magnetic moment can give mass bound on the Higgs boson in the SM [106]. This constraint can be applied for more general interaction, including THDMs [107]. At the one-loop level, the contribution is given by

$$\delta a_\mu^{1\text{-loop}} \simeq \frac{G_F m_\mu^4}{4\pi^2 \sqrt{2}} \left[\sum_{\phi^0=h,H} \frac{\xi_{\phi^0}^{\ell^2}}{m_{\phi^0}^2} \left(\ln \frac{m_{\phi^0}^2}{m_\mu^2} - \frac{7}{6} \right) + \frac{\xi_A^{\ell^2}}{m_A^2} \left(-\ln \frac{m_A^2}{m_\mu^2} + \frac{11}{6} \right) - \frac{\xi_A^{\ell^2}}{6m_{H^\pm}^2} \right]. \quad (3.28)$$

This process is also purely leptonic and only gives milder bounds on the Higgs boson masses for very large $\tan \beta$ values in the type-II (type-X) THDM. It gives no effective bound on the type-I (type-Y) THDM. It is also known that the two-loop (Barr-Zee type) diagram can significantly affect a_μ [108, 109]. The contribution can be large because of the enhancement factors of m_f^2/m_μ^2 and also of the mixing factors ξ_ϕ^f as [109]

$$\delta a_\mu^{\text{BZ}} \simeq \frac{N_c^f Q_f^2 G_F \alpha m_\mu^2}{4\pi^3 v^2} \left[- \sum_{\phi^0=h,H} \xi_{\phi^0}^{\ell} \xi_{\phi^0}^f f \left(\frac{m_f^2}{m_{\phi^0}^2} \right) + \xi_A^{\ell} \xi_A^f g \left(\frac{m_f^2}{m_A^2} \right) \right], \quad (3.29)$$

where

$$f(z) = \frac{z}{2} \int_0^1 dx \frac{1 - 2x(1-x)}{x(1-x) - z} \ln \frac{x(1-x)}{z}, \quad (3.30)$$

$$g(z) = \frac{z}{2} \int_0^1 dx \frac{1}{x(1-x) - z} \ln \frac{x(1-x)}{z}. \quad (3.31)$$

The contribution from this kind of diagram is only important for large $\tan \beta$ values with smaller Higgs boson masses in the type-II THDM. For the other types of THDM, it would give a much less effective bound on the parameter space.

3.1.4 Collider signals in the Type-X THDM at the LHC and the ILC

We discuss the collider phenomenology of the models at the LHC and the ILC. There have already been many studies on the production and decays of the Higgs bosons in the type-II THDM, especially in the context of the MSSM, while the phenomenology of the other types of THDMs has not yet been studied sufficiently. Recently, the type-X THDM has been introduced in the model to explain phenomena such as neutrino masses, dark matter, and baryogenesis at the TeV scale [21]. We therefore concentrate on the collider signals in the type-X THDM, and discuss how we can distinguish the model from the type-II THDM (the MSSM), mainly in scenarios with a light charged Higgs boson ($100 \text{ GeV} \lesssim m_{H^\pm} \lesssim 300 \text{ GeV}$). (Such a light charged Higgs boson is severely constrained by the $b \rightarrow s\gamma$ result in the non-supersymmetric type-II THDM and the type-Y THDM, while it can be allowed in the MSSM and the type-X (type-I) THDM.) As we are interested in the differences in the types of the Yukawa interactions, we focus here on the case of $m_{H^\pm} \simeq m_A \simeq m_H$ with $\sin(\beta - \alpha) \simeq 1$ for definiteness.

Charged Higgs boson searches at the LHC

A light charged Higgs boson with $m_{H^\pm} \lesssim m_t - m_b$ can be produced in the decay of top quarks at the LHC. The discovery potential for the charged Higgs boson via the $t\bar{t}$ production has been studied in the MSSM [110]. Assuming an integrated luminosity of 30 fb^{-1} , the expected signal significance of the event $t\bar{t} \rightarrow H^\pm W^\mp b\bar{b} \rightarrow \ell\nu\tau\nu_\tau b\bar{b}$ is greater than 5σ for $m_{H^\pm} \lesssim 130 \text{ GeV}$ for $\tan \beta \lesssim 2$ and $\tan \beta \gtrsim 20$ [110]. The same analysis can also be applied for the type-X THDM as well as the type-I THDM, in which a similar number of H^\pm can be produced when $\tan \beta \sim \mathcal{O}(1)$. The main decay mode ($\tau\nu$) is common in the type-II THDM, the type-X THDM and the type-I THDM, except for very low $\tan \beta$ values. In Fig. 3.1.4, we present the region of the parameter space that can be excluded at 95% CL in the type-X THDM (left panel) and the type-I THDM (right panel) at the LHC [112] after collecting 10 and 30 fb^{-1} of integrated luminosity using the results from the ATLAS collaboration [113].

For $m_{H^\pm} \gtrsim m_t$, charged Higgs bosons can be produced in $q\bar{q}/gg \rightarrow t\bar{t}H^\pm$, $gb \rightarrow tH^\pm$ [111, 114], $gg(q\bar{q}) \rightarrow H^+H^-$ [115, 116] and $gg(b\bar{b}) \rightarrow H^\pm W^\mp$ [117]. These processes, except for the H^+H^- production, are via the Yukawa coupling of $t\bar{t}H^\pm$, so that the cross sections are significant for $\tan \beta \sim \mathcal{O}(1)$ or $\tan \beta \gtrsim 10$ – 20 in the type-II THDM and only for $\tan \beta \sim \mathcal{O}(1)$ in the type-X THDM. The type of Yukawa interaction in the THDM can then be discriminated by measuring the difference in decay branching ratios of H^\pm . In the type-II THDM H^\pm mainly

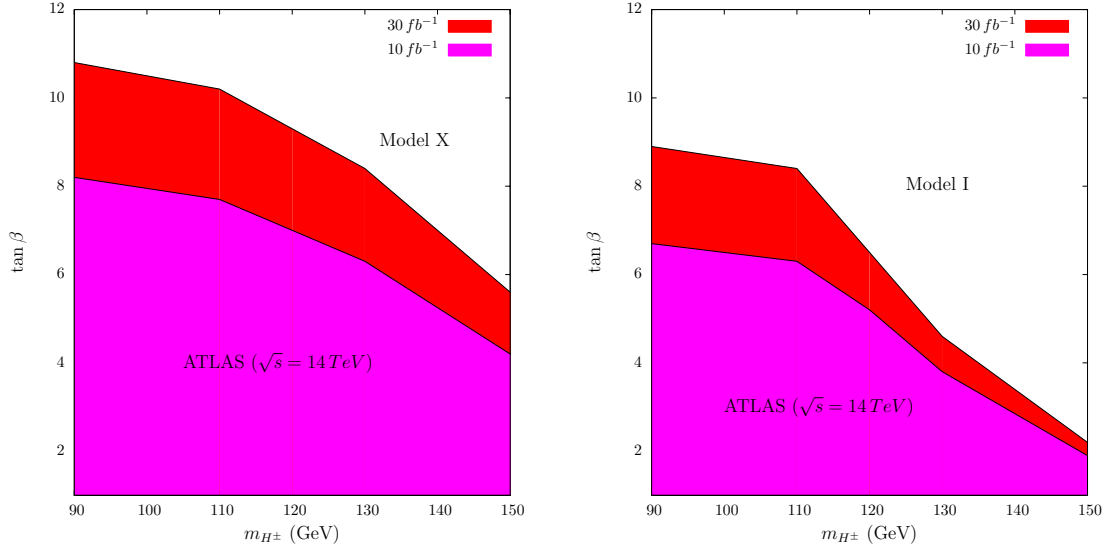


Figure 3.5: Region of the parameter space excluded by the ATLAS collaboration for $\sqrt{s} = 14$ TeV in the type-X THDM (left) and the type-I THDM (right) using the channel $pp \rightarrow t\bar{t} \rightarrow H^\pm b W^\pm \bar{b} \rightarrow \tau \nu b \bar{b} q \bar{q}$ [112]. The plot was done using the data in [113].

decay into tb , while $\tau\nu$ is dominant for $\tan\beta \gtrsim 10$ in the type-X THDM.

Neutral Higgs boson (A and H) production at the LHC

At the LHC, the type of the Yukawa interaction may be determined in the search for neutral Higgs bosons through the direct production via gluon fusion $gg \rightarrow A/H$ [116, 118], vector boson fusion $V^*V^* \rightarrow H$, $V = W, Z$ [119, 120], and also via associated production $pp \rightarrow b\bar{b}A$ ($b\bar{b}H$) [121, 122]. The production process $pp \rightarrow t\bar{t}A$ ($t\bar{t}H$) [114, 122, 123] can also be useful for $\tan\beta \sim 1$. We discuss the possibility of discriminating the type of the Yukawa interaction by using the production and decay processes of A and H for $\sin(\beta - \alpha) = 1$. Additional neutral Higgs bosons A and H are directly produced by the gluon fusion mechanism at the one-loop level. When $\sin(\beta - \alpha) \simeq 1$, the production rate can be significant due to the top quark loop contribution for $\tan\beta \sim 1$ and, in the MSSM (the type-II THDM), also for large $\tan\beta$ via the bottom quark loop contributions [116]. Notice that there is no rate of $V^*V^* \rightarrow A$ because there is no VVA coupling, and that the production of H from the vector boson fusion $V^*V^* \rightarrow H$ is relatively unimportant when $\sin(\beta - \alpha) \simeq 1$. The associate production process $pp \rightarrow b\bar{b}A$ ($b\bar{b}H$) can be significant for large $\tan\beta$ values in the MSSM (the type-II THDM) [121].

In the MSSM (the type-II THDM), the produced A and H in these processes decay mainly into $b\bar{b}$ when $\sin(\beta - \alpha) \simeq 1$, which would be challenging to detect because of huge QCD backgrounds. Instead, the decays into a lepton pair $\tau^+\tau^-$ ($\mu^+\mu^-$) would be useful for searches of A (and H). However, the decay branching ratios of $A \rightarrow \tau^+\tau^-$ ($\mu^+\mu^-$) are less than 0.1 (0.0004). A simulation study [124] shows that the Higgs boson search via the associate production $b\bar{b}A$ ($b\bar{b}H$) is better than that via the direct production from gluon fusion to see both $\tau^+\tau^-$ and $\mu^+\mu^-$ modes, especially in the large $\tan\beta$ area. The largest background is the

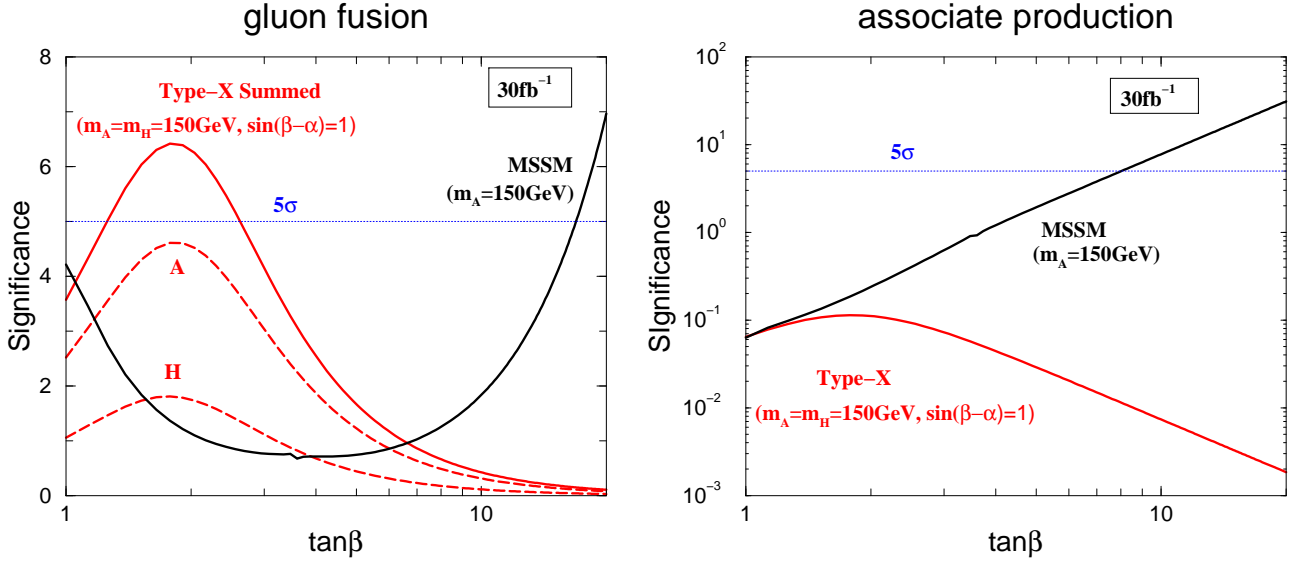


Figure 3.6: Signal significance (S/\sqrt{B}) for gluon fusion $gg \rightarrow A/H$ (left panel) and the associated production $pp \rightarrow b\bar{b}A$ ($b\bar{b}H$) (right panel) with the $\tau^+\tau^-$ final state in the type-X THDM and the MSSM. In both figures, the dashed and the solid curves represent the expected values of signal significance for A/H and summed over A and H . The red (thin) curves denote the significance in the type-X THDM, while the black (thick) solid curves denote that in the MSSM [38].

Drell-Yan process from $\gamma^*/Z^* \rightarrow \tau^+\tau^-$ (and $\mu^+\mu^-$). The other ones, such as $t\bar{t}$, $b\bar{b}$ and $W + jet$, also contribute to the backgrounds. The rate of the $\tau^+\tau^-$ process from the signal is much larger than that of the $\mu^+\mu^-$ one. However, the resolution for tau leptons is much broader than that for muons, so that for relatively small m_A (m_H) the $\mu^+\mu^-$ mode can be more useful than the $\tau^+\tau^-$ mode [125].

In the type-X THDM, signals from the associate production $pp \rightarrow b\bar{b}A$ are very difficult to detect. The production cross section is at most 150 fb for $m_A = 150$ GeV at $\tan\beta = 1$ [124], where the branching ratio $A \rightarrow \tau^+\tau^-$ and $A \rightarrow \mu^+\mu^-$ are small, and the produced signals are less for larger values of $\tan\beta$. On the other hand, the direct production from $gg \rightarrow A/H$ can be used to see the signal. The cross sections are significant for $\tan\beta \sim 1$, and they decrease for larger values of $\tan\beta$ by a factor of $1/\tan^2\beta$. However, the branching ratios of $A/H \rightarrow \tau^+\tau^-$ dominate over those of $A/H \rightarrow b\bar{b}$ for $\tan\beta \gtrsim 2$ and become almost 100% for $\tan\beta \gtrsim 4$ (see FIG. 3.2). Therefore, large significances can be expected around $\tan\beta \sim 2$ in the type-X THDM.

In FIG. 3.6, we show the expected signal significance of the direct production $pp(gg) \rightarrow A/H \rightarrow \tau^+\tau^-$ in the type-X THDM and the MSSM at the LHC, assuming an integrated luminosity of 30fb^{-1} . The mass of the CP-odd Higgs boson m_A is taken to be 150 GeV in both models, while m_H is 150 GeV for the results of the type-X THDM and that in the MSSM is deduced using the MSSM mass relation. For the detailed analysis of background simulation, we employed the one shown in the ATLAS TDR [124]. The basic cuts, such as the high p_T cut and the standard $A/H \rightarrow \tau^+\tau^-$ reconstruction, are assumed [124]. We can see that, for the search of the direct production, the signal significance in the type-X THDM can be larger than that in

m_ϕ [GeV]	SM (H_{SM})	MSSM(A)	Type-X (H)	Type-X (A)	Type-X(Sum) ($m_A \simeq m_H$)
115	2.41	1.31	4.31	12.0	16.3
120	2.51	1.49	4.89	13.4	18.3
130	2.25	1.81	5.78	15.6	21.4
140	1.61	2.11	6.60	17.5	24.1

Table 3.3: Expected signal significances for $gg \rightarrow \phi \rightarrow \mu^+\mu^-$ ($\phi = H_{\text{SM}}, H, A$) in the SM, the MSSM, and the type-X THDM. For the results in the MSSM $\tan\beta = 2$ is taken, and for that in the type-X THDM $\tan\beta = 2$ and $\sin(\beta - \alpha) = 1$ are taken. The integrated luminosity is assumed to be 300 fb^{-1} [38].

the MSSM for $\tan\beta \lesssim 5$. In particular, the signal in the type-X THDM can be expected to be detectable ($S/\sqrt{B} > 5$) when $\tan\beta \sim 2$ for the luminosity of 30 fb^{-1} . For smaller values of m_A (m_H), the production cross section becomes large so that the signal rate is more significant, but the separation from the Drell-Yan background becomes more difficult because the resolution of the tau lepton is broad. Therefore, the significance becomes worse for $m_A(m_H) \lesssim 130 \text{ GeV}$.

When A and H are lighter than 130 GeV , the $\mu^+\mu^-$ mode can be more useful than the $\tau^+\tau^-$ mode. The resolution of muons is much better than that of tau leptons, so that the invariant mass cut is very effective in reducing the background from $\gamma^*/Z^* \rightarrow \mu^+\mu^-$. The feasibility of the process $gg \rightarrow A/H \rightarrow \mu^+\mu^-$ has been studied in the SM and the MSSM in Refs. [124, 125]. We evaluate the signal significances of $gg \rightarrow A/H \rightarrow \mu^+\mu^-$ in the type-X THDM by using the result in Ref. [125]. In TABLE 3.3, we list the results of the significance in the SM and the type-X THDM. According to Tao Han's paper, the basic kinematic cuts of $p_T > 20 \text{ GeV}$, $|\eta| < 2.5$ and the invariant mass cuts as $m_{A/H} - 2.24 \text{ GeV} < M_{\mu\mu} < m_{A/H} + 2.24 \text{ GeV}$ are used ⁶. The integrated luminosity is assumed to be 300 fb^{-1} . For the results in the type-X THDM, $\tan\beta = 2$ and $\sin(\beta - \alpha) = 1$ are taken. The results show that the significance can be substantial for $m_A \gtrsim 115 \text{ GeV}$ when $\tan\beta = 2$. For smaller masses of the extra Higgs bosons, the cross section for the signal processes can be larger, but the invariant mass cut becomes less effective in the reduction of the Drell-Yan background because of the smaller mass difference between m_Z and m_A ; hence, the signal significance becomes worse. The $\tan\beta$ dependence in the signal significance for the muon final states is also shown in FIG. 3.7. The shape of the curves is similar to that for the tau lepton final state in FIG 3.6.

In summary, we would be able to distinguish the type-X THDM from the MSSM by measuring the leptonic decays of the additional Higgs bosons produced via the direct search processes $gg \rightarrow A/H \rightarrow \tau^+\tau^-$ ($\mu^+\mu^-$) and the associated processes $pp \rightarrow b\bar{b}A$ ($b\bar{b}H$). First, if a light scalar boson is found via $gg \rightarrow h \rightarrow \gamma\gamma$ or $W^+W^- \rightarrow h \rightarrow \gamma\gamma$ ($\tau^+\tau^-$) and if the event number is consistent with the prediction in the SM, then we know that the scalar boson is of the SM or at least SM-like: in the THDM framework this means $\sin(\beta - \alpha) \simeq 1$, assuming that it is the lightest one. Second, under the situation above, when the associated production $pp \rightarrow b\bar{b}A$ ($b\bar{b}H$) is detected at a different invariant mass than the mass of the SM-like one and no $gg \rightarrow A/H \rightarrow \tau^+\tau^-$ ($\mu^+\mu^-$) is found at that point, we would be able to identify the MSSM

⁶This choice for the invariant mass cut is rather severe; i.e., it requires the precise determination of m_A and m_H . If the range of the invariant mass cut is taken to be double, roughly speaking, background events also become double. This would suppress the signal significance in TABLE 3.3 by a factor of $\sim 1/\sqrt{2}$.

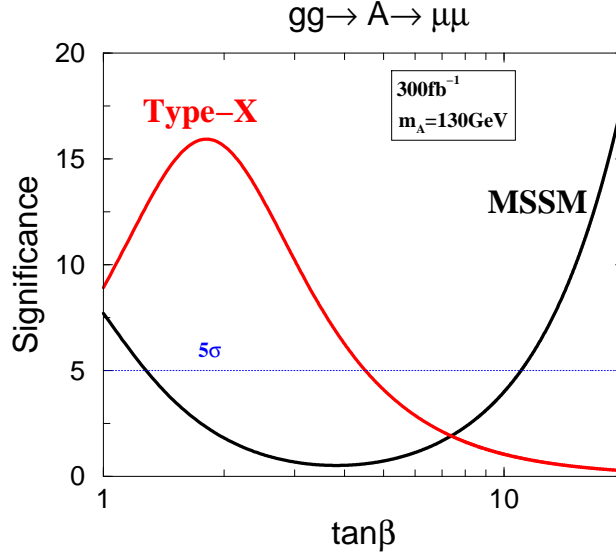


Figure 3.7: Signal significance (S/\sqrt{B}) for the $\mu^+\mu^-$ final state from gluon fusion $gg \rightarrow A$ in the type-X THDM and the MSSM. The red (thin) curves denote significance in the type-X THDM, while the black (thick) solid curves denote that in the MSSM [38].

Higgs sector (or the type-II THDM) with high $\tan\beta$ values. On the other hand, the type-X THDM with low $\tan\beta$ would be identified by finding the signal from the gluon fusion process without that from the $b\bar{b}\tau^+\tau^-$. If signals from the direct production processes are found but the number is not sufficient, then the value of $\tan\beta$ would be around 6–10 ($m_t \cot\beta \sim m_b \tan\beta$), where the rates in the MSSM and the type-X THDM are similar. In this case, it would be difficult to distinguish these models from the above processes. As we discussed in the next subsection, Higgs pair production processes $pp \rightarrow AH^\pm, HH^\pm$, and AH can be useful to measure the Yukawa interaction through branching fractions, because these production mechanism do not depend on $\tan\beta$ in such a situation.

We have concentrated on $\sin(\beta - \alpha) \simeq 1$ in this analysis because the parameter is motivated in Ref. [21]. Here we comment on the situation without the condition $\sin(\beta - \alpha) = 1$. If $\sin(\beta - \alpha)$ is not close to unity, our conclusion can be modified. The production cross sections of $gg \rightarrow A/H$ and $pp \rightarrow b\bar{b}A(b\bar{b}H)$ can be enhanced in the type-X THDM for $\tan\beta \gtrsim 1$ since the factor $(\sin\alpha/\sin\beta)$ of quark-Higgs couplings can be large in a specific region of the parameter space. The signal of the CP odd Higgs boson A can then be significant. On the other hand, the CP even Higgs boson H can decay into WW^* when $\sin(\beta - \alpha)$ is not unity. This would reduce leptonic branching fractions. The signal can be enhanced only for large $\tan\beta$ regions because leptonic decays are significant only for such a parameter space. We also note that H can be produced significantly by the vector boson fusion mechanism in a mixing case.

Pair production of extra Higgs bosons at the LHC

The types of the Yukawa interactions can be studied using the process of $q\bar{q}' \rightarrow W^{\pm*} \rightarrow AH^\pm (HH^\pm)$ [116, 126–129] and $q\bar{q} \rightarrow Z^* \rightarrow AH$ [116], unless the extra Higgs bosons H , A

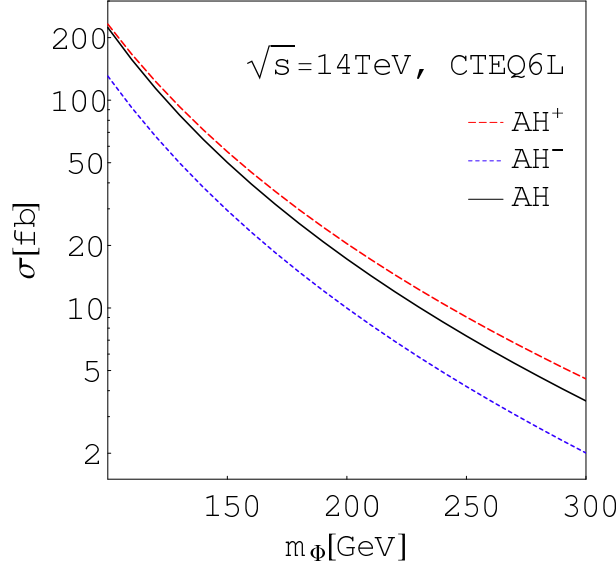


Figure 3.8: Production cross sections of $pp \rightarrow AH^\pm$ and AH are shown at the leading order as a function of scalar boson masses in the THDM where $m_\Phi = m_H = m_A = m_{H^\pm}$ are chosen. The long-dashed, dashed and solid curves denote the pair production of AH^+ , AH^- and AH , respectively. The cross section of $pp \rightarrow HH^\pm$ is the same as those of $pp \rightarrow AH^\pm$ when $\sin(\beta - \alpha) = 1$ [38].

and/or H^\pm are too heavy ⁷. Hadronic cross sections for these processes are shown at the leading order in FIG. 3.8 as a function of the mass of the produced scalar boson Φ , where $m_\Phi = m_H = m_A = m_{H^\pm}$. Expected rates of AH^\pm (sum) and AH are about 143 fb and 85 fb for $m_{H^\pm} = 130$ GeV and about 85 fb and 50 fb for $m_{H^\pm} = 150$ GeV, respectively. The NLO QCD corrections are expected to enhance these rates typically by about 20% [126, 128]. The production rates are common in all the types of THDMs, because the cross sections are determined only by the masses of the produced scalar bosons. Therefore, they are very sensitive to the difference in the decay branching ratios of the produced Higgs bosons. In the MSSM, the $b\bar{b}\tau^\pm\nu$ ($b\bar{b}\tau^+\tau^-$) events can be the main signal of the AH^\pm and HH^\pm (AH) processes, while in the type-X THDM ($\tan\beta \gtrsim 2$), $\tau^+\tau^-\tau^\pm\nu$ ($\tau^+\tau^-\tau^+\tau^-$) would be the main signal events.

In the MSSM, the parton level background analysis for the AH^\pm (HH^\pm) production process has been performed in Ref. [128, 129] by using the $b\bar{b}\tau\nu$ final state. The largest background comes from $q\bar{q}' \rightarrow Wg^* \rightarrow Wb\bar{b}$, which can be reduced by basic kinematic cuts and the invariant mass cut of $b\bar{b}$, as well as by the kinematic cut to select hard hadrons from the parent τ^\pm from H^\pm . It has been shown that a sufficient signal significance can be obtained for smaller masses of Higgs bosons [128].

In the type-X THDM, the produced AH^\pm (HH^\pm) and AH pairs can be studied via the leptonic decays. Hence these channels can be useful to discriminate the type-X THDM from the MSSM. Assuming an integrated luminosity of 300 fb^{-1} , 8.6×10^4 and 5.1×10^4 of the signal events are produced from both AH^\pm and HH^\pm production for $m_\Phi = 130$ GeV and 150 GeV, respectively, where $m_\Phi = m_H = m_A = m_{H^\pm}$. A and H (H^\pm) decay into $\tau^+\tau^-$ ($\tau\nu$) by more

⁷When the mixing between h and H is large, the hH^\pm production can also be important [129].

	$AH^\pm, HH^\pm(m_\Phi = 130 \text{ GeV})$	$AH^\pm, HH^\pm(m_\Phi = 150 \text{ GeV})$	ZW^\pm
$\tau^+\tau^-\tau\nu$	8.4×10^4	5.0×10^4	3.2×10^4
$\mu^+\mu^-\tau\nu$	3.0×10^2	1.8×10^2	3.1×10^4

Table 3.4: Events for the $\tau^+\tau^-\tau\nu$ and $\mu^+\mu^-\tau\nu$ final states from the Higgs boson pair production and ZW^\pm background [38]. The signal events are summed over AH^\pm and HH^\pm . The integrated luminosity is taken to be 300 fb^{-1} . Values for the decay branching ratios are taken to be $\mathcal{B}(A/H \rightarrow \tau^+\tau^-) = 0.99$, $\mathcal{B}(A/H \rightarrow \mu^+\mu^-) = 0.0035$, and $\mathcal{B}(H^\pm \rightarrow \tau\nu) = 0.99$, which correspond to the values for $\tan\beta \gtrsim 7$. The cross section of $pp \rightarrow ZW^\pm$ is evaluated as $\sigma_{ZW} = 27.7 \text{ pb}$ by CalcHEP [130].

than 95% and 95% (99%) for $\tan\beta \gtrsim 4$, respectively. The purely leptonic signal would have an advantage in the signal to background ratio because the background from the intermediate state $q\bar{q} \rightarrow Wg^*$ would be negligible. For $\tan\beta = 7$, the produced AH^\pm and HH^\pm pairs almost all (more than 99%) go to $\tau^+\tau^-\tau\nu$ final states. The numbers of signal and background are summarized in TABLE 3.4. The signal to background ratio for $\tau^+\tau^-\tau\nu$ final state is not so small $\mathcal{O}(0.1-1)$, before cuts⁸. The backgrounds are expected to be reduced by using high- p_T cuts, hard hadrons from the parent tau leptons from H^\pm , and invariant mass cuts for $\tau^+\tau^-$ from A and H , in addition to the basic cuts. However, the signal significance strongly depend on the rate of miss identification of hadrons as tau leptons, so that a realistic simulation is necessary.

We also would be able to use the $\mu^+\mu^-\tau^+\nu$ events to identify the AH^+ and HH^+ production in the type-X THDM, by using the much better resolution of $\mu^+\mu^-$ in performing the invariant mass cuts. For 300 fb^{-1} , the AH^+ and HH^+ process can produce about $\mathcal{O}(100)$ of $\mu^+\mu^-\tau^+\nu$ events for $m_A = m_H = 130 \text{ GeV}$. The number of background events is about 3.1×10^5 of $\mu^+\mu^-\tau^+\nu$ from ZW^\pm production. Signals and background for $\mu^+\mu^-\tau^+\nu$ events are also summarized in TABLE 3.4. The background can be expected to be reduced by imposing a selection of the events around the invariant mass of $m_A \sim M_{\mu\mu}$ and the high p_T cuts. Hard hadrons from the decay of τ 's from H^+ can also be used to reduce the background. In the MSSM, much smaller signals are expected, so that this process can be a useful probe of the type-X THDM.

In a similar way, we may use AH production [116] to identify the type-X THDM. For the $\tau^+\tau^-\tau^+\tau^-$ decay mode, the signal is evaluated approximately as 2.5×10^4 events, assuming 300 fb^{-1} for $m_A = m_H = 130 \text{ GeV}$ and $\tan\beta = 7$. The main background may come from the $q\bar{q} \rightarrow ZZ$ process. We also consider the $\mu^+\mu^-\tau^+\tau^-$ decay mode. The number of signal event is $\mathcal{O}(100)$ for an integrated luminosity 300 fb^{-1} . The numbers of signal and background event are listed in TABLE 3.5. It would be valuable to use the detailed background simulation.

Pair production of extra Higgs bosons at the ILC

At the ILC, we would be able to test the types of the Yukawa interactions via the pair production of the additional Higgs bosons $e^+e^- \rightarrow AH$ [116, 131]. In Fig. 3.9, the production cross

⁸The γW^\pm production may give a much larger cross section for background events. It may also be reduced considerably by kinematic cuts.

	$AH(m_\Phi = 130 \text{ GeV})$	$AH(m_\Phi = 150 \text{ GeV})$	ZZ
$\tau^+\tau^-\tau^+\tau^-$	2.5×10^5	1.5×10^5	3.6×10^3
$\tau^+\tau^-\mu^+\mu^-$	1.8×10^2	1.0×10^2	7.1×10^3

Table 3.5: Events for the $\tau^+\tau^-\tau^+\tau^-$ and $\tau^+\tau^-\mu^+\mu^-$ final states from the Higgs boson pair production and ZZ background [38]. The integrated luminosity is taken to be 300 fb^{-1} . The cross section of $pp \rightarrow ZZ$ is evaluated as $\sigma_{ZZ} = 10.5 \text{ pb}$ by CalcHEP [130].

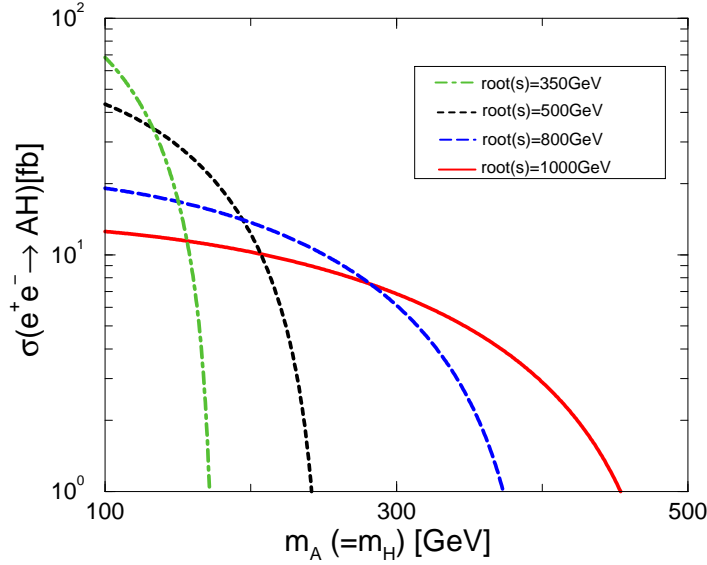


Figure 3.9: The production cross section of $e^+e^- \rightarrow AH$ is shown as a function of the Higgs boson mass. The dot-dashed, dashed, long-dashed, and solid curves correspond to $\sqrt{s} = 350, 500, 800$, and 1000 GeV , respectively [38].

section is shown for $\sqrt{s} = 350, 500, 800$, and 1000 GeV as a function of m_A assuming $m_A = m_H$ in the THDM. The production rate is determined only by m_A , and m_H at the leading order, and is independent of $\tan\beta$. (In the MSSM, it depends indirectly on $\tan\beta$ via the mass spectrum.) The signal of the type-X THDM can be identified by searching for the events of $\tau^+\tau^-\tau^+\tau^-$ and $\mu^+\mu^-\tau^+\tau^-$. When $\sqrt{s} = 500 \text{ GeV}$, assuming an integrated luminosity of 500 fb^{-1} , the event number is estimated as 1.6×10^4 (1.8×10^2) in the type-X (type-II) THDM for $\tau^+\tau^-\tau^+\tau^-$, and 1.1×10^2 (0.6) for $\mu^+\mu^-\tau^+\tau^-$ assuming $m_H = m_A = m_{H^\pm} = 130 \text{ GeV}$, $\sin(\beta - \alpha) = 1$ and $\tan\beta = 10$. This number does not change much for $\tan\beta \gtrsim 3$. The main background comes from the Z pair production, whose rate is about $4 \times 10^2 \text{ fb}$. The event numbers from the background are then 2.3×10^2 for $\tau^+\tau^-\tau^+\tau^-$ and 4.6×10^2 for $\mu^+\mu^-\tau^+\tau^-$. Therefore, the signal should be easily detected in the type-X THDM, by which we would be able to distinguish the type-X from the type-II (the MSSM).

The detailed measurement of the masses of additional Higgs bosons and Yukawa coupling constants will make it possible to determine the scenario of physics beyond the SM through the Higgs physics.

3.2 The Higgs Triplet Model

In this section, we discuss the extended Higgs sector which contains the Higgs triplet fields. The Higgs triplet fields are introduced in various new physics models such as the left-right symmetric model [132], the type II seesaw model [164] and so on. Here, we focus on the Higgs Triplet Model (HTM) which is motivated by the type II seesaw model, where neutrino masses can be generated at the tree-level. In the HTM, the Higgs triplet field Δ with $Y = 1$ is added to the SM.

First, we define the Lagrangian of the HTM, and we discuss tree level formulae such as masses for physical scalar bosons, gauge bosons and neutrinos as well as the rho parameter. Second, the on-shell renormalization scheme is introduced for the electroweak precision observables. We then calculate the predictions for m_W and ρ at the one-loop level. Third, we discuss the phenomenology of the HTM; i.e., we calculate the decay branching ratios of scalar bosons which are originated from the triplet Higgs field, and we show how masses of these scalar bosons can be reconstructed at the LHC. Finally, we evaluate the deviation from the SM prediction of the decay rate of $h \rightarrow \gamma\gamma$.

3.2.1 Tree level formulae

The scalar sector of the HTM is composed of the isospin doublet field Φ with hypercharge $Y = 1/2$ and the triplet field Δ with $Y = 1$. The relevant terms in the Lagrangian are given by

$$\mathcal{L}_{\text{HTM}} = \mathcal{L}_{\text{kin}} + \mathcal{L}_Y - V(\Phi, \Delta), \quad (3.32)$$

where \mathcal{L}_{kin} , \mathcal{L}_Y and $V(\Phi, \Delta)$ are the kinetic term, the Yukawa interaction and the scalar potential, respectively. The kinetic term of the Higgs fields is given by

$$\mathcal{L}_{\text{kin}} = (D_\mu \Phi)^\dagger (D^\mu \Phi) + \text{Tr}[(D_\mu \Delta)^\dagger (D^\mu \Delta)], \quad (3.33)$$

where the covariant derivatives are defined as

$$D_\mu \Phi = \left(\partial_\mu + i\frac{g}{2}\tau^a W_\mu^a + i\frac{g'}{2}B_\mu \right) \Phi, \quad D_\mu \Delta = \partial_\mu \Delta + i\frac{g}{2}[\tau^a W_\mu^a, \Delta] + ig'B_\mu \Delta. \quad (3.34)$$

The Yukawa interaction for neutrinos is given by

$$\mathcal{L}_Y = h_{ij} \overline{L_L^{ic}} i\tau_2 \Delta L_L^j + \text{h.c.}, \quad (3.35)$$

where h_{ij} is the 3×3 complex symmetric Yukawa matrix. Notice that the triplet field Δ carries the lepton number of 2. The most general form of the Higgs potential under the gauge symmetry is given by

$$\begin{aligned} V(\Phi, \Delta) = & m^2 \Phi^\dagger \Phi + M^2 \text{Tr}(\Delta^\dagger \Delta) + [\mu \Phi^T i\tau_2 \Delta^\dagger \Phi + \text{h.c.}] \\ & + \lambda_1 (\Phi^\dagger \Phi)^2 + \lambda_2 [\text{Tr}(\Delta^\dagger \Delta)]^2 + \lambda_3 \text{Tr}[(\Delta^\dagger \Delta)^2] + \lambda_4 (\Phi^\dagger \Phi) \text{Tr}(\Delta^\dagger \Delta) + \lambda_5 \Phi^\dagger \Delta \Delta^\dagger \Phi, \end{aligned} \quad (3.36)$$

where m and M are the dimension full real parameters, μ is the dimension full complex parameter which violates the lepton number, and λ_1 - λ_5 are the coupling constants which are real.

We here take μ to be real. The scalar fields Φ and Δ can be parameterized as

$$\Phi = \begin{bmatrix} \varphi^+ \\ \frac{1}{\sqrt{2}}(\varphi + v_\Phi + i\chi) \end{bmatrix}, \quad \Delta = \begin{bmatrix} \frac{\Delta^+}{\sqrt{2}} & \Delta^{++} \\ \Delta^0 & -\frac{\Delta^+}{\sqrt{2}} \end{bmatrix} \text{ with } \Delta^0 = \frac{1}{\sqrt{2}}(\delta + v_\Delta + i\eta), \quad (3.37)$$

where v_Φ and v_Δ are the VEVs of the doublet Higgs field and the triplet Higgs field, respectively which satisfy $v^2 \equiv v_\Phi^2 + 2v_\Delta^2 \simeq (246 \text{ GeV})^2$.

From the stationary condition at the vacuum (v_Φ, v_Δ) , we obtain

$$m^2 = \frac{1}{2} \left[-2v_\Phi^2 \lambda_1 - v_\Delta^2 (\lambda_4 + \lambda_5) + 2\sqrt{2}\mu v_\Delta \right], \quad (3.38)$$

$$M^2 = M_\Delta^2 - \frac{1}{2} \left[2v_\Delta^2 (\lambda_2 + \lambda_3) + v_\Phi^2 (\lambda_4 + \lambda_5) \right], \text{ with } M_\Delta^2 \equiv \frac{v_\Phi^2 \mu}{\sqrt{2}v_\Delta}, \quad (3.39)$$

and we can eliminate m^2 and M^2 . The mass matrices for the scalar bosons can be diagonalized by rotating the scalar fields as

$$\begin{pmatrix} \varphi^\pm \\ \Delta^\pm \end{pmatrix} = \begin{pmatrix} \cos \beta_\pm & -\sin \beta_\pm \\ \sin \beta_\pm & \cos \beta_\pm \end{pmatrix} \begin{pmatrix} w^\pm \\ H^\pm \end{pmatrix}, \quad \begin{pmatrix} \chi \\ \eta \end{pmatrix} = \begin{pmatrix} \cos \beta_0 & -\sin \beta_0 \\ \sin \beta_0 & \cos \beta_0 \end{pmatrix} \begin{pmatrix} z \\ A \end{pmatrix},$$

$$\begin{pmatrix} \varphi \\ \delta \end{pmatrix} = \begin{pmatrix} \cos \alpha & -\sin \alpha \\ \sin \alpha & \cos \alpha \end{pmatrix} \begin{pmatrix} h \\ H \end{pmatrix}, \quad (3.40)$$

with the mixing angles

$$\tan \beta_\pm = \frac{\sqrt{2}v_\Delta}{v_\Phi}, \quad \tan \beta_0 = \frac{2v_\Delta}{v_\Phi}, \quad \tan 2\alpha = \frac{v_\Delta}{v_\Phi} \frac{2v_\Phi^2 (\lambda_4 + \lambda_5) - 4M_\Delta^2}{2v_\Phi^2 \lambda_1 - M_\Delta^2 - v_\Delta^2 (\lambda_2 + \lambda_3)}, \quad (3.41)$$

In addition to the three NG bosons w^\pm and z which are absorbed by the longitudinal components of the W boson and the Z boson, there are seven physical mass eigenstates $H^{\pm\pm}$, H^\pm , A , H and h . The masses of these physical states are expressed as

$$m_{H^{++}}^2 = M_\Delta^2 - v_\Delta^2 \lambda_3 - \frac{\lambda_5}{2} v_\Phi^2, \quad (3.42)$$

$$m_{H^+}^2 = \left(M_\Delta^2 - \frac{\lambda_5}{4} v_\Phi^2 \right) \left(1 + \frac{2v_\Delta^2}{v_\Phi^2} \right), \quad (3.43)$$

$$m_A^2 = M_\Delta^2 \left(1 + \frac{4v_\Delta^2}{v_\Phi^2} \right), \quad (3.44)$$

$$m_H^2 = \mathcal{M}_{11}^2 \sin^2 \alpha + \mathcal{M}_{22}^2 \cos^2 \alpha + \mathcal{M}_{12}^2 \sin 2\alpha, \quad (3.45)$$

$$m_h^2 = \mathcal{M}_{11}^2 \cos^2 \alpha + \mathcal{M}_{22}^2 \sin^2 \alpha - \mathcal{M}_{12}^2 \sin 2\alpha, \quad (3.46)$$

where \mathcal{M}_{11}^2 , \mathcal{M}_{22}^2 and \mathcal{M}_{12}^2 are the elements of the mass matrix \mathcal{M}_{ij}^2 for the CP-even scalar states in the (φ, δ) basis which are given by

$$\mathcal{M}_{11}^2 = 2v_\Phi^2 \lambda_1, \quad (3.47)$$

$$\mathcal{M}_{22}^2 = M_\Delta^2 + 2v_\Delta^2 (\lambda_2 + \lambda_3), \quad (3.48)$$

$$\mathcal{M}_{12}^2 = -\frac{2v_\Delta}{v_\Phi} M_\Delta^2 + v_\Phi v_\Delta (\lambda_4 + \lambda_5). \quad (3.49)$$

The six parameters μ and λ_1 - λ_5 in the Higgs potential in Eq. (3.36) can be written in terms of the physical scalar masses, the mixing angle α and VEVs v_Φ and v_Δ as

$$\mu = \frac{\sqrt{2}v_\Delta^2}{v_\Phi^2} M_\Delta^2 = \frac{\sqrt{2}v_\Delta}{v_\Phi^2 + 4v_\Delta^2} m_A^2, \quad (3.50)$$

$$\lambda_1 = \frac{1}{2v_\Phi^2} (m_h^2 \cos^2 \alpha + m_H^2 \sin^2 \alpha), \quad (3.51)$$

$$\lambda_2 = \frac{1}{2v_\Delta^2} \left[2m_{H^{++}}^2 + v_\Phi^2 \left(\frac{m_A^2}{v_\Phi^2 + 4v_\Delta^2} - \frac{4m_{H^+}^2}{v_\Phi^2 + 2v_\Delta^2} \right) + m_H^2 \cos^2 \alpha + m_h^2 \sin^2 \alpha \right], \quad (3.52)$$

$$\lambda_3 = \frac{v_\Phi^2}{v_\Delta^2} \left(\frac{2m_{H^+}^2}{v_\Phi^2 + 2v_\Delta^2} - \frac{m_{H^{++}}^2}{v_\Phi^2} - \frac{m_A^2}{v_\Phi^2 + 4v_\Delta^2} \right), \quad (3.53)$$

$$\lambda_4 = \frac{4m_{H^+}^2}{v_\Phi^2 + 2v_\Delta^2} - \frac{2m_A^2}{v_\Phi^2 + 4v_\Delta^2} + \frac{m_h^2 - m_H^2}{2v_\Phi v_\Delta} \sin 2\alpha, \quad (3.54)$$

$$\lambda_5 = 4 \left(\frac{m_A^2}{v_\Phi^2 + 4v_\Delta^2} - \frac{m_{H^+}^2}{v_\Phi^2 + 2v_\Delta^2} \right). \quad (3.55)$$

Bounds from the tree-level unitarity and the vacuum stability have been studied in Ref. [133]. The masses of the W boson and the Z boson are obtained at the tree level as

$$m_W^2 = \frac{g^2}{4} (v_\Phi^2 + 2v_\Delta^2), \quad m_Z^2 = \frac{g^2}{4 \cos^2 \theta_W} (v_\Phi^2 + 4v_\Delta^2). \quad (3.56)$$

The electroweak rho parameter can deviate from unity at the tree level;

$$\rho \equiv \frac{m_W^2}{m_Z^2 \cos^2 \theta_W} = \frac{1 + \frac{2v_\Delta^2}{v_\Phi^2}}{1 + \frac{4v_\Delta^2}{v_\Phi^2}}. \quad (3.57)$$

As the experimental value of the rho parameter is near unity, v_Δ^2/v_Φ^2 is required to be much smaller than unity at the tree level. In this case, the state h behaves mostly as the SM Higgs boson, while the other states are almost originated from the components of the triplet field. Then, from Eqs. (3.42), (3.43), (6.7) and (3.45), there are interesting relations among the masses;

$$m_{H^{++}}^2 - m_{H^+}^2 \simeq m_{H^+}^2 - m_A^2 \left(\simeq -\frac{\lambda_5}{4} v_\Phi^2 \equiv \xi \right), \quad (3.58)$$

$$m_H^2 \simeq m_A^2 \left(\simeq M_\Delta^2 \right). \quad (3.59)$$

These characteristic mass relations would be used as a probe of the Higgs potential in the HTM [57]. If the masses of the triplet-like Higgs bosons are hierarchical, there are two patterns of the mass hierarchy among the triplet-like scalar bosons; i.e., when λ_5 is positive (negative), the mass hierarchy is $m_{\phi^0} > m_{H^+} > m_{H^{++}}$ ($m_{H^{++}} > m_{H^+} > m_{\phi^0}$), where $m_{\phi^0} = m_A$ or m_H . We here define the mass difference between $H^{\pm\pm}$ and H^\pm as

$$\Delta m \equiv m_{H^{++}} - m_{H^+}. \quad (3.60)$$

In the HTM, tiny Majorana masses of neutrinos are generated by the Yukawa interaction with the VEV of the triplet field, which is proportional to the lepton number violating coupling constant μ as

$$(m_\nu)_{ij} = \sqrt{2}h_{ij}v_\Delta = h_{ij}\frac{\mu v_\Phi^2}{M_\Delta^2}. \quad (3.61)$$

If $\mu \ll M_\Delta$ the smallness of the neutrino masses are explained by the so-called type II seesaw mechanism [15]. In this section, we assume that the lepton number violating parameter μ is sufficiently smaller than the electroweak scale so that the mass scale of the triplet-like field is $\mathcal{O}(100\text{-}1000)$ GeV.

We here give some comments on radiative corrections to the relation $m_{H^{++}}^2 - m_{H^+}^2 \simeq m_{H^+}^2 - m_{\phi^0}^2$. This relation can be changed when we take into account radiative corrections to the Higgs potential. At the one-loop level, the relation in mass differences can be rewritten as

$$\frac{m_{H^{++}}^2 - m_{H^+}^2}{m_{H^+}^2 - m_{\phi^0}^2} \simeq 1 + \delta_{\phi^0}, \quad (\phi^0 = H \text{ or } A), \quad (3.62)$$

where δ_{ϕ^0} is the deviation from the tree level prediction due to radiative corrections, which is given as a function of the masses and mixing angles. In principle, we may test the HTM with this kind of the corrected mass relation instead of the tree level formula by measuring the masses of the bosons. A detailed study of radiative corrections to the Higgs potential in the HTM is an important and interesting issue which will be performed in elsewhere [134].

3.2.2 One-loop corrections to electroweak parameters

Here, we calculate one-loop corrected electroweak observables in the on-shell scheme which was at first proposed by Blank and Hollik [49] in the model with a triplet Higgs field with $Y = 0$. In the SM, and in all the models with $\rho = 1$ at the tree level, the kinetic term of the Higgs field contains three parameters g , g' and v . All the electroweak parameters are determined by giving a set of three input parameters which are well known; i.e., for example, α_{em} , G_F and m_Z [135, 136]. On the other hand, in models with $\rho \neq 1$ at the tree level like the HTM, an additional input parameter is necessary to describe electroweak parameters. Therefore, in addition to the three input parameters α_{em} , G_F and m_Z , we take the weak angle $\sin^2 \theta_W$ as the fourth input parameter in our calculation as in Ref. [49]. The experimental values of these input parameters are given by [26]

$$\begin{aligned} \alpha_{\text{em}}^{-1}(m_Z) &= 128.903(15), & G_F &= 1.16637(1) \times 10^{-5} \text{ GeV}^{-2}, \\ m_Z &= 91.1876(21) \text{ GeV}, & \hat{s}_W^2(m_Z) &= 0.23146(12), \end{aligned} \quad (3.63)$$

where $\hat{s}_W^2(m_Z)$ is defined as the ratio of the coefficients of the vector part and the axial vector part in the $Z\bar{e}e$ vertex;

$$1 - 4\hat{s}_W^2(m_Z) = \frac{\text{Re}(v_e)}{\text{Re}(a_e)}, \quad (3.64)$$

here v_e and a_e are defined in Eq. (3.79). Tree level formulae for the other electroweak parameters are given in terms of the four input parameters:

$$g^2 = \frac{4\pi\alpha_{\text{em}}}{\hat{s}_W^2}, \quad (3.65)$$

$$m_W^2 = \frac{\pi\alpha_{\text{em}}}{\sqrt{2}G_F\hat{s}_W^2}, \quad (3.66)$$

$$v^2 = \frac{1}{\sqrt{2}G_F}, \quad (3.67)$$

$$v_\Delta^2 = \frac{\hat{s}_W^2\hat{c}_W^2}{2\pi\alpha_{\text{em}}}m_Z^2 - \frac{\sqrt{2}}{4G_F}, \quad (3.68)$$

where $\hat{s}_W^2 = \hat{s}_W^2(m_Z)$ and $\hat{c}_W^2 = 1 - \hat{s}_W^2$ ⁹.

The deviation from the relation in Eq. (3.66) due to radiative corrections can be parameterized as

$$G_F = \frac{\pi\alpha_{\text{em}}}{\sqrt{2}m_W^2\hat{s}_W^2}(1 + \Delta r), \quad (3.70)$$

where Δr is

$$\Delta r = -\frac{\delta G_F}{G_F} + \frac{\delta\alpha_{\text{em}}}{\alpha_{\text{em}}} - \frac{\delta\hat{s}_W^2}{\hat{s}_W^2} - \frac{\delta m_W^2}{m_W^2}. \quad (3.71)$$

The counter terms are obtained by imposing the renormalization conditions given in Ref. [136] as

$$\frac{\delta G_F}{G_F} = -\frac{\Pi_T^{WW}(0)}{m_W^2} - \delta_{VB}, \quad (3.72)$$

$$\frac{\delta\alpha_{\text{em}}}{\alpha_{\text{em}}} = \frac{d}{dp^2}\Pi_T^{\gamma\gamma}(p^2)\Big|_{p^2=0} + \frac{2\hat{s}_W}{\hat{c}_W}\frac{\Pi_T^{\gamma Z}(0)}{m_Z^2}, \quad (3.73)$$

$$\frac{\delta m_W^2}{m_W^2} = \frac{\Pi_T^{WW}(m_W^2)}{m_W^2}, \quad (3.74)$$

and in Ref. [49] as

$$\frac{\delta\hat{s}_W^2}{\hat{s}_W^2} = \frac{\hat{c}_W}{\hat{s}_W}\frac{\Pi_T^{\gamma Z}(m_Z^2)}{m_Z^2} - \delta'_V, \quad (3.75)$$

⁹In the limit of $v_\Delta \rightarrow 0$, we obtain the following relation

$$\frac{\hat{s}_W^2\hat{c}_W^2}{\pi\alpha_{\text{em}}}m_Z^2 = \frac{1}{\sqrt{2}G_F}. \quad (3.69)$$

By using this relation, m_W can be expressed by $m_W^2 = m_Z^2\hat{c}_W^2$. This relation can be found in models with $\rho = 1$ at the tree level such as the SM.

where δ_{VB} and δ'_V are the vertex and the box diagram corrections to G_F and the radiative corrections to the $Z\bar{e}e$ vertex, respectively. These are calculated as [49, 137]

$$\delta_{VB} = \frac{\alpha_{\text{em}}}{4\pi\hat{s}_W^2} \left[6 + \frac{10 - 10\hat{s}_W^2 - 3(R/\hat{c}_W^2)(1 - 2\hat{s}_W^2)}{2(1 - R)} \ln R \right], \quad R \equiv \frac{m_W^2}{m_Z^2}, \quad (3.76)$$

$$\delta'_V = \frac{v_e}{2\hat{s}_W^2} \left[\frac{\Gamma_V^{Z\bar{e}e}(m_Z^2)}{v_e} - \frac{\Gamma_A^{Z\bar{e}e}(m_Z^2)}{a_e} \right], \quad (3.77)$$

where $\Gamma_{V,A}^{Z\bar{e}e}$ are defined through the renormalized $Z\bar{e}e$ vertex as [49]

$$\hat{\Gamma}_\mu^{Z\bar{e}e}(m_Z^2) = i \frac{g}{2\hat{c}_W} \left[(v_e + a_e \gamma_5) \gamma_\mu + \gamma_\mu \Gamma_V^{Z\bar{e}e}(m_Z^2) + \gamma_\mu \gamma_5 \Gamma_A^{Z\bar{e}e}(m_Z^2) \right], \quad (3.78)$$

$$v_e = -\frac{1}{2} + 2\hat{s}_W^2, \quad a_e = -\frac{1}{2}. \quad (3.79)$$

In Eqs. (3.72)-(3.74), $\Pi_T^{XY}(p^2)$ ($X, Y = W, Z, \gamma$) are the 1PI diagrams for the gauge boson self-energies. We show the list of all the analytic expressions for the gauge boson self-energies in the HTM with the $Y = 1$ triplet field in Appendix E. The radiative correction Δr can be obtained by

$$\begin{aligned} \Delta r = & \frac{\Pi_T^{WW}(0) - \Pi_T^{WW}(m_W^2)}{m_W^2} + \frac{d}{dp^2} \Pi_T^{\gamma\gamma}(p^2) \Big|_{p^2=0} + \frac{2\hat{s}_W}{\hat{c}_W} \frac{\Pi_T^{\gamma Z}(0)}{m_Z^2} - \frac{\hat{c}_W}{\hat{s}_W} \frac{\Pi_T^{\gamma Z}(m_Z^2)}{m_Z^2} \\ & + \delta_{VB} + \delta'_V. \end{aligned} \quad (3.80)$$

From Eqs. (3.57) and (3.70), the renormalized W boson mass as well as the renormalized rho parameter are given by

$$m_W^2 = \frac{\pi\alpha_{\text{em}}}{\sqrt{2}G_F\hat{s}_W^2} (1 + \Delta r), \quad (3.81)$$

$$\rho = \frac{\pi\alpha_{\text{em}}}{\sqrt{2}G_F m_Z^2 \hat{s}_W^2 \hat{c}_W^2} (1 + \Delta r). \quad (3.82)$$

Therefore, with four input parameters (α_{em} , G_F , m_Z and \hat{s}_W^2), Δr determines both the one-loop corrected mass of the W boson and the rho parameter in the HTM.

In the following, we show numerical results for the radiative corrections to m_W^2 as well as ρ in the HTM. The radiative correction depends on the mass spectrum and the mixing angle in the Higgs potential; i.e., $m_{H^{++}}$, m_{H^+} , m_A , m_H , m_h and $\tan\alpha$. Although these six parameters are all free parameters, under the requirement of $v_\Delta^2 \ll v^2$ the approximated formulae given in Eqs. (3.58) and (3.59) tell us to pick up the following three parameters such as the mass of the SM-like Higgs boson m_h , the mass of the lightest triplet-like scalar boson m_A (or $m_{H^{++}}$) and the mass difference Δm between $H^{\pm\pm}$ and H^\pm . In the following analysis, we consider the scenarios with mass splitting for the triplet-like Higgs bosons; namely, for Case I ($m_{\phi^0} > m_{H^+} > m_{H^{++}}$) and Case II ($m_{H^{++}} > m_{H^+} > m_{\phi^0}$). We take pole masses of the top quark $m_t = 173$ GeV and the bottom quark $m_b = 4.7$ GeV and $\alpha_s(m_Z) = 0.118$ [26]. We take into account the leading order QCD correction in the calculation of the one-loop corrected m_W as well as the rho parameter.

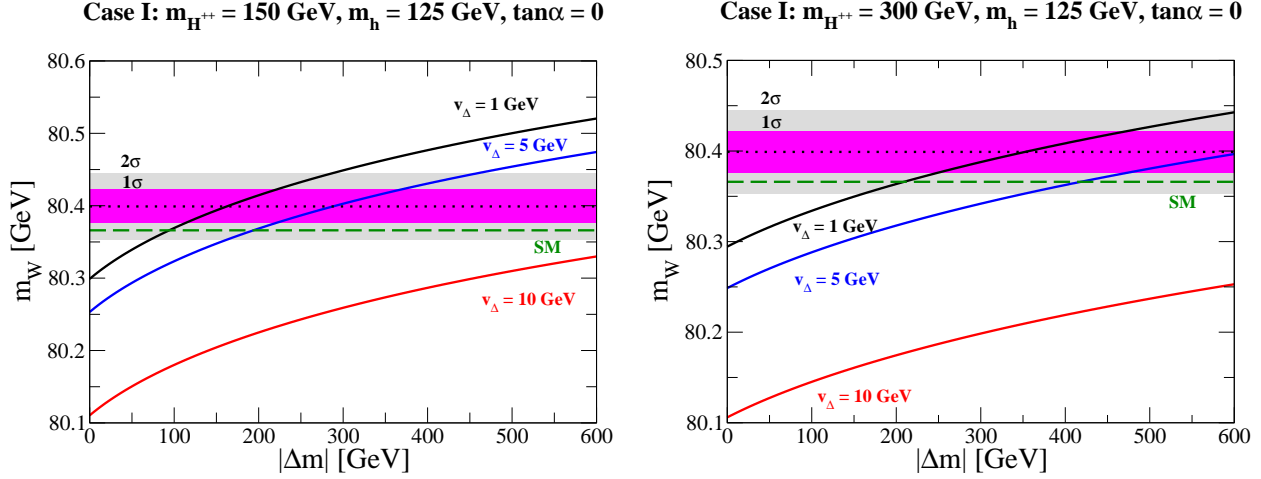


Figure 3.10: The one-loop corrected values of m_W as a function of the absolute value of Δm for each fixed value of v_Δ in Case I ($m_{\phi^0} > m_{H^+} > m_{H^{++}}$). We take $m_h = 125$ GeV, $m_t = 173$ GeV and $\tan\alpha = 0$ in the both figures. The pink (gray) shaded region represents the 1σ (2σ) error for the experimental data of m_W^{exp} ($=80.399 \pm 0.23$ GeV [26]). In the left (right) figure, we take $m_{H^{++}} = 150$ GeV (300 GeV). The dashed line shows the SM prediction of m_W at the one-loop level with the SM Higgs boson mass to be 125 GeV [48].

In Fig. 3.10, the renormalized value of m_W is shown as a function of $|\Delta m|$ for several values of v_Δ in Case I with the data $m_W^{\text{exp}} = 80.399 \pm 0.023$ GeV [26]. The mass of the SM-like Higgs boson h is taken as $m_h = 125$ GeV, and the mixing angle $\tan\alpha$ is set on zero. The mass of the lightest triplet-like Higgs boson $m_{H^{++}}$ is taken to be 150 GeV (left figure) and 300 GeV (right figure). It is seen that the predicted value of m_W for the degenerate mass case ($|\Delta m| = 0$) is outside the region within the 2σ error. The prediction satisfies the data when $|\Delta m|$ has a non-zero value. When $m_{H^{++}} = 150$ GeV, the favored value of $|\Delta m|$ by the data within the 2σ error is $80 \text{ GeV} \lesssim |\Delta m| \lesssim 280 \text{ GeV}$ ($190 \text{ GeV} \lesssim |\Delta m| \lesssim 430 \text{ GeV}$) for $v_\Delta = 1$ GeV (5 GeV). The preferred value of $|\Delta m|$ for smaller values of v_Δ than 1 GeV is similar to that for $v_\Delta = 1$ GeV. When $m_{H^{++}} = 300$ GeV, the allowed values of $|\Delta m|$ are larger than the case of $m_{H^{++}} = 150$ GeV for the same value of v_Δ . Smaller mass splitting which satisfies the data corresponds to the smaller value of v_Δ while largest value of $|\Delta m|$ (~ 500 -600 GeV), which comes from perturbative unitarity, corresponds to $v_\Delta \sim \mathcal{O}(10)$ GeV. We note that the result is almost unchanged even if we vary $\tan\alpha$ in the region of $0 < \tan\alpha < 1$ as long as $H^{\pm\pm}$ is not too heavy.

In Fig. 3.11, the renormalized value of m_W is shown as a function of Δm for several values of v_Δ in Case II with the data $m_W^{\text{exp}} = 80.399 \pm 0.023$ GeV [26]. The mass of the SM-like Higgs boson h is taken as $m_h = 125$ GeV, and the mixing angle $\tan\alpha$ is set on zero. The mass of the lightest triplet-like Higgs boson m_A is taken to be 150 GeV (left figure) and 300 GeV (right figure). It is found that Case II is strongly constrained by the electroweak precision data for entire range of Δm . The situation is worse for larger values of Δm and also for larger values of v_Δ . Therefore, Case I can be more consistent with the electroweak precision data than the degenerate mass case and also Case II. We note that the result is almost unchanged even if we

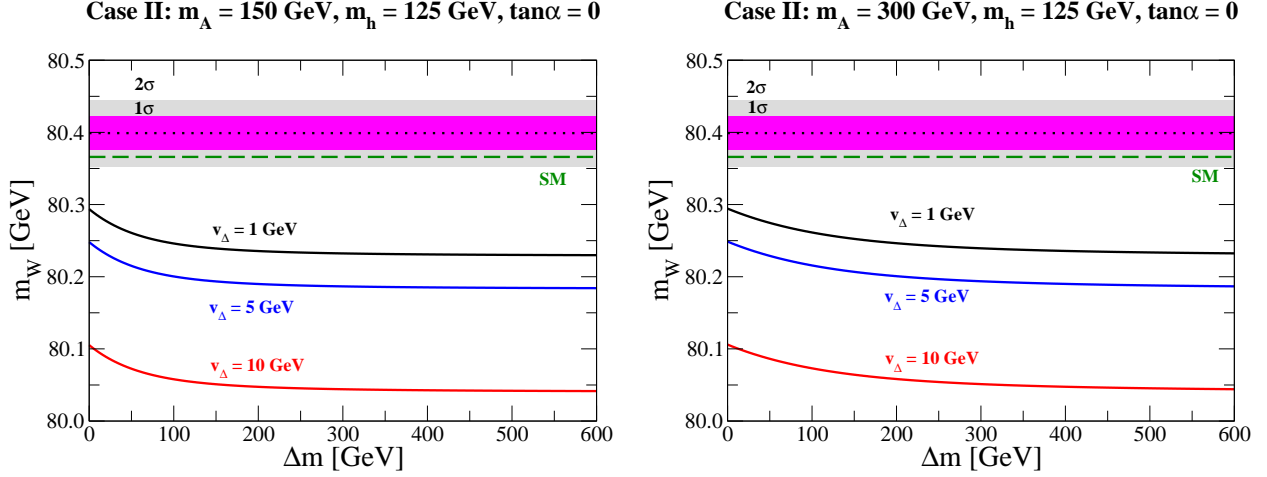


Figure 3.11: The one-loop corrected values of m_W as a function of Δm for each fixed value of v_Δ in Case II ($m_{H^{++}} > m_{H^+} > m_{\phi^0}$). We take $m_h = 125$ GeV, $m_t = 173$ GeV and $\tan \alpha = 0$ in the both figures. The pink (gray) shaded region represents the 1σ (2σ) error for the experimental data of m_W^{exp} ($=80.399 \pm 0.23$ GeV [26]). In the left (right) figure, we take $m_A = 150$ GeV (300 GeV). The dashed line shows the SM prediction of m_W at the one-loop level with the SM Higgs boson mass to be 125 GeV [48].

vary $\tan \alpha$ in the region of $0 < \tan \alpha < 1$ as long as A is not too heavy.

In Fig. 3.12, we show the renormalized values for m_W for each value of Δm as a function of the input parameter \hat{s}_W^2 in Case I. The values of $(m_{H^{++}}, m_h)$ are taken to be (150 GeV, 125 GeV), (300 GeV, 125 GeV), (150 GeV, 700 GeV) and (300 GeV, 700 GeV) in the figures located at the upper left, the upper right, the lower left and the lower right panels, respectively. In all figures, the mixing angle $\tan \alpha$ is set to be zero. Regions indicated by the data of m_W and \hat{s}_W^2 within the 1σ error and the 2σ error are also shown in each figure for the fixed value of m_t ($=173$ GeV). When $m_h = 125$ GeV (upper figures), the predicted values of m_W for $\Delta m = 0$ are far from the allowed region by the data. For $m_{H^{++}} = 150$ GeV and $m_h = 125$ GeV (upper left), the prediction is consistent with the data within the 2σ error when about $160 \text{ GeV} \lesssim |\Delta m| \lesssim 600$ GeV is taken. On the other hand, for $m_{H^{++}} = 300$ GeV and $m_h = 125$ GeV (upper right), smaller values are predicted for m_W as compared to the case with $m_{H^{++}} = 150$ GeV for non-zero value of $|\Delta m|$. They approach to the predicted values of m_W with $|\Delta m| = 0$ in the large mass limit for $H^{\pm\pm}$. It is consistent with the data when we take $\Delta m \gtrsim 400$ GeV in this case. When $m_h = 700$ GeV (lower figures), the predicted values of m_W for $\Delta m = 0$ are far from the allowed region by the data but closer than the case of $m_h = 125$ GeV. For $m_{H^{++}} = 150$ GeV and $m_h = 700$ GeV (lower left), the prediction is consistent with the data within the 2σ error when about $100 \text{ GeV} \lesssim |\Delta m| \lesssim 400$ GeV is taken. On the other hand, for $m_{H^{++}} = 300$ GeV and $m_h = 700$ GeV (lower right), it is consistent with the data when we take $\Delta m \gtrsim 200$ GeV in this case. The edge of each curve at $\hat{s}_W^2 \simeq 0.2311$ corresponds to $v_\Delta = 0$. We note that the result is almost unchanged even if we vary $\tan \alpha$ in the region of $0 < \tan \alpha < 1$ as long as $H^{\pm\pm}$ is not too heavy.

In Fig. 3.13, we show the renormalized values for m_W for each value of Δm as a function

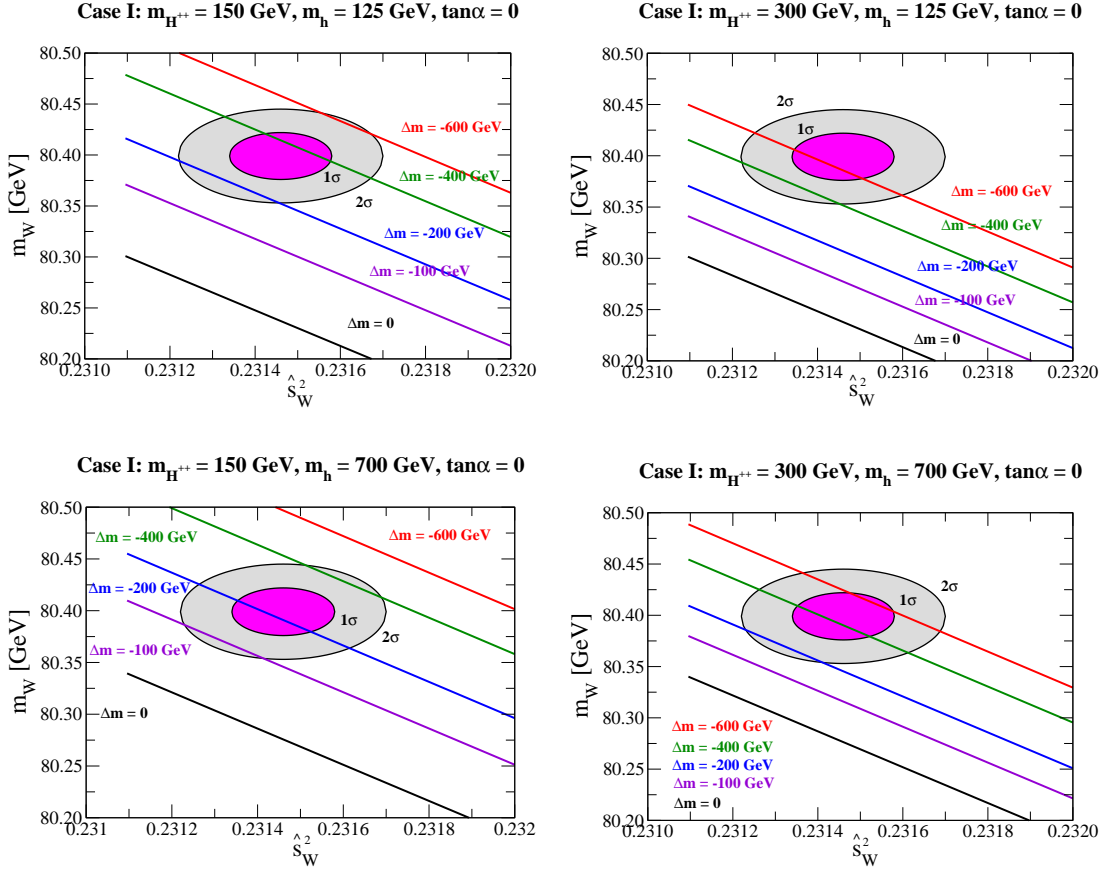


Figure 3.12: The one-loop corrected values of m_W as a function of \hat{s}_W^2 in Case I ($m_{\phi^0} > m_{H^+} > m_{H^{++}}$). We take $m_t = 173$ GeV and $\tan \alpha = 0$ in all the figures. The pink (gray) shaded region represents the 1σ (2σ) error for the experimental data of m_W^{exp} ($=80.399 \pm 0.23$ GeV [26]) and \hat{s}_W^{exp} ($=0.23146 \pm 0.00012$ GeV [26]). In the left (right) two figures, we take $m_h = 125$ GeV (700 GeV). The mass of the lightest triplet-like Higgs boson is taken to be 150 GeV and 300 GeV [48].

of the input parameter \hat{s}_W^2 in Case II. The values of (m_A, m_h) are taken to be (150 GeV, 125 GeV), (300 GeV, 125 GeV), (150 GeV, 700 GeV) and (300 GeV, 700 GeV) for the figures located at the upper left, the upper right, the lower left and the lower right, respectively. In all figures, the mixing angle α is set to be zero. Regions indicated by the data within the 1σ error and the 2σ error are also shown in each figure for the fixed value of m_t ($=173$ GeV). For $m_A = 150$ GeV and $m_h = 125$ GeV (upper left), the predicted values for m_W with non-zero Δm (> 0) are smaller than that with $\Delta m = 0$. The situation is unchanged for the other choices of $(m_A, m_h) = (300 \text{ GeV}, 125 \text{ GeV})$, (150 GeV, 700 GeV) and (300 GeV, 700 GeV). Therefore, the hierarchical scenario with non-zero Δm is highly constrained by the combined data of m_W and \hat{s}_W^2 . The edge of each curve at $\hat{s}_W^2 \simeq 0.2311$ corresponds to $v_\Delta = 0$. We note that the result is almost unchanged even if we vary $\tan \alpha$ in the region of $0 < \tan \alpha < 1$ as long as A is not too heavy.

In Fig. 3.14, the deviation in the one-loop corrected rho parameter in the HTM from that

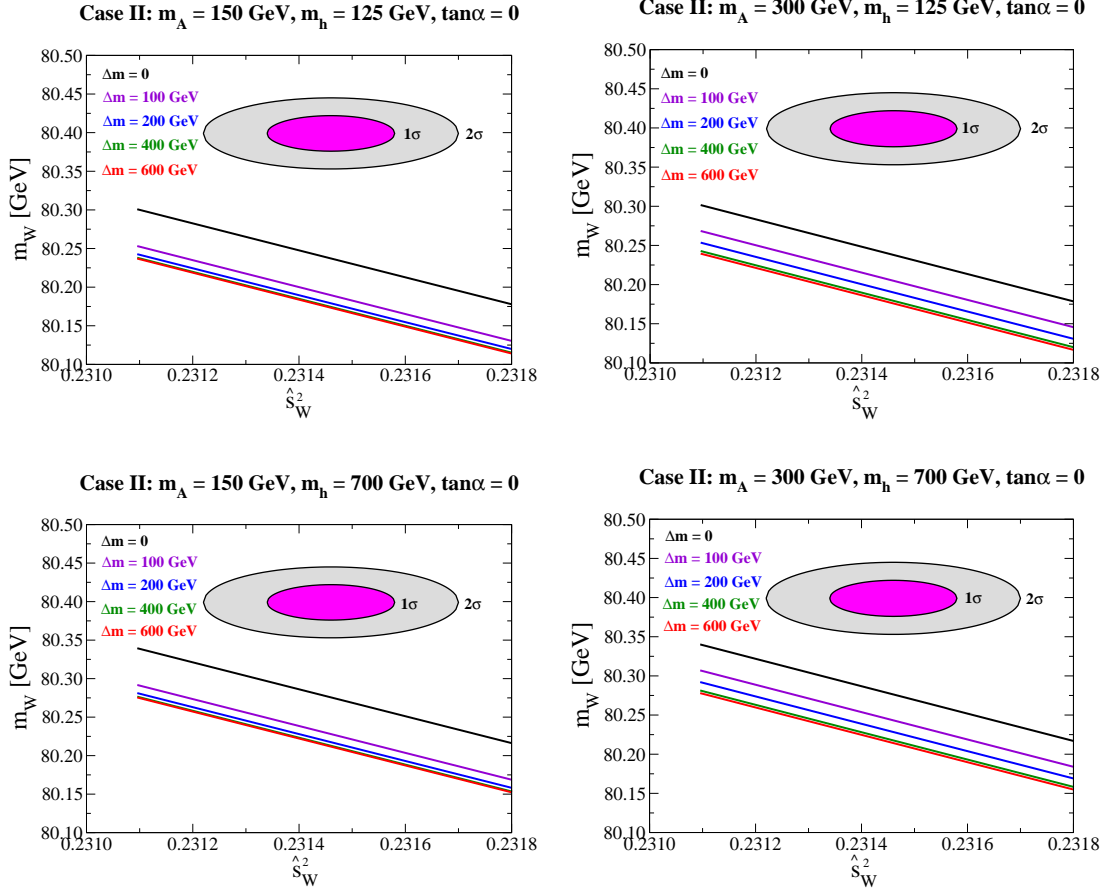


Figure 3.13: The one-loop corrected values of m_W as a function of \hat{s}_W^2 in Case II ($m_{H^{++}} > m_{H^+} > m_{\phi^0}$). We take $m_t = 173$ GeV and $\tan \alpha = 0$ in all the figures. The pink (gray) shaded region represents the 1σ (2σ) error for the experimental data of m_W^{exp} ($=80.399 \pm 0.23$ GeV [26]) and \hat{s}_W^{exp} ($=0.23146 \pm 0.00012$ GeV [26]). In the left (right) two figures, we take $m_h = 125$ GeV (700 GeV). The mass of the lightest triplet-like Higgs boson is taken to be 150 GeV and 300 GeV [48].

of the SM one-loop prediction ($\Delta\rho \equiv \rho - \rho_{\text{SM}}(m_h^{\text{ref}})$) is shown as a function of v_Δ , where v_Δ is defined in Eq. (3.63). In order to describe the allowed region of $\Delta\rho$, we employ the data for the electroweak T parameter [138] of $T = 0.07 \pm 0.08$ [26], in which $T = 0$ is chosen for the reference value of the SM Higgs boson mass m_h^{ref} to be 117 GeV and $m_t = 173$ GeV. We then obtain $\Delta\rho^{\text{exp}} = 0.000632 \pm 0.000621$, where $m_h^{\text{ref}} = 125$ GeV is chosen by taking into account the recent direct search results at the LHC [6]. In the left figure, the results in Case I are shown, while in the right figure those in Case II are shown for several values of Δm . The mass of the SM-like Higgs boson is taken to be $m_h = 125$ GeV, and the mixing angle $\tan \alpha$ is set to be zero. In Case I (left figure), the predicted values of $\Delta\rho$ for $\Delta m = 0$ are outside the region within the 2σ error under the data $\Delta\rho^{\text{exp}}$ and \hat{s}_W^{exp} given in Eq. (3.63) with $m_t = 173$ GeV. But the effect of non-zero $|\Delta m|$ makes $\Delta\rho$ larger. The allowed value for v_Δ within the 2σ error is about $3.5 \text{ GeV} \lesssim v_\Delta \lesssim 8 \text{ GeV}$ for about $100 \text{ GeV} \lesssim |\Delta m| \lesssim 440 \text{ GeV}$. Notice that, as shown in Fig. 3.12, the

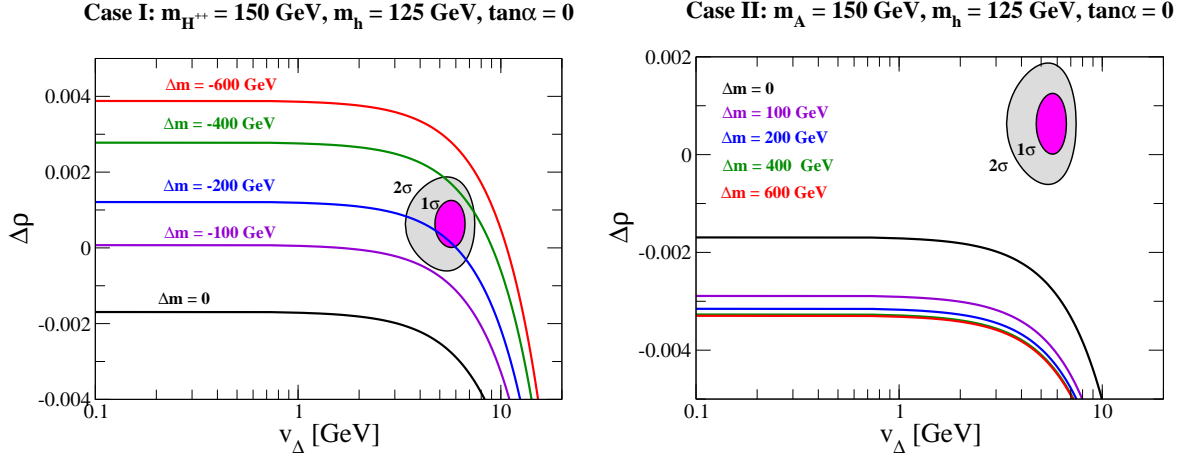


Figure 3.14: The deviation of the one-loop corrected values of the rho parameter from those of the SM one-loop prediction as a function of v_Δ . We take $m_h = 125$ GeV, $m_t = 173$ GeV and $\tan\alpha = 0$ in the both figures. The pink (gray) shaded region represents the 1σ (2σ) error for the experimental data of $\Delta\rho^{\text{exp}} (=0.000632 \pm 0.000621)$ which is derived from the data of the T parameter ($=0.07 \pm 0.08$ [26]). In the left figure, the mass hierarchy of the triplet-like Higgs bosons is taken to be Case I ($m_{\phi^0} > m_{H^+} > m_{H^{++}}$), and m_{ϕ^0} is fixed to be 150 GeV. In the right figure, the mass hierarchy of the triplet-like Higgs bosons is taken to be Case II ($m_{H^{++}} > m_{H^+} > m_{\phi^0}$), and $m_{H^{++}}$ is fixed to be 150 GeV [48].

avored value of $|\Delta m|$ from the data of m_W and \hat{s}_W^2 is about $200 \text{ GeV} \lesssim |\Delta m| \lesssim 600 \text{ GeV}$ in Case I. Therefore, we may conclude that the combined data indicate the favored value of v_Δ to be 3.5-8 GeV in Case I with $m_{H^{++}} = 150$ GeV. Next, the result in Case II is shown in the right figure, where the effect of Δm (> 0) gives the negative contribution to $\Delta\rho$. However, it can be seen that Case II is already highly constrained by the data of m_W and \hat{s}_W^2 with $m_A = 150$ GeV.

We here give a comment on the decoupling property of the heavy triplet-like Higgs bosons in the electroweak observables. In Fig. 3.15, we show $\Delta\rho$ as a function of the lightest of all the triplet-like Higgs bosons for each value ξ ($\equiv m_{H^{++}}^2 - m_{H^+}^2$). We again take $m_h = 125$ GeV and $m_t = 173$ GeV. In the left figure, v_Δ is fixed to be 0 while in the right figure, v_Δ is fixed to be the central value indicated by the data ($v_\Delta = 5.78$ GeV). In this figure, $\tan\alpha$ is chosen to be $2v_\Delta/v$, which is the asymptotic value in the limit of $m_{\text{lightest}} \rightarrow \infty$. It can be seen that the one-loop contribution of these particles decouples in the large mass limit even in the case with $v_\Delta = 0$. The asymptotic value in this limit is determined in the renormalization scheme with the four input parameters α_{em} , G_F , m_Z and \hat{s}_W^2 without the tree level relation of $m_W^2 = \hat{c}_W^2 m_Z^2$. Therefore, it is not surprising that the asymptotic value in the HTM does not coincide with the SM value ($\Delta\rho = 0$ in this figure) with the three input parameters with $m_W^2 = \hat{c}_W^2 m_Z^2$. In

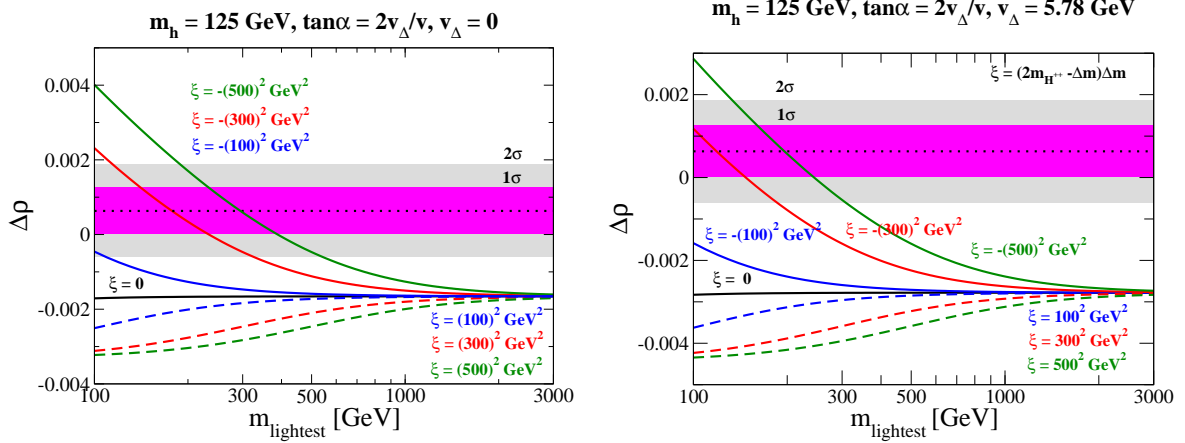


Figure 3.15: The deviation of the one-loop corrected values of the rho parameter from those of the SM one-loop prediction as a function of the mass of the lightest triplet-like Higgs boson m_{lightest} for each fixed value of ξ ($\equiv m_{H^{++}}^2 - m_{H^+}^2$). We take $m_t = 173 \text{ GeV}$, $m_h = 125 \text{ GeV}$ and $\tan\alpha = 2v_\Delta/v$ in the both figures. In the left (right) figure, v_Δ is taken to be 0 (5.78 GeV). The pink (gray) shaded region represents the 1σ (2σ) error for the experimental data of $\Delta\rho^{\text{exp}}$ ($=0.000632 \pm 0.000621$) which is derived from the data of the T parameter ($=0.07 \pm 0.08$ [26]) [48].

the large mass limit and $v_\Delta \rightarrow 0$, the one-loop corrected rho parameter can be expressed as

$$\begin{aligned} \rho_{\text{HTM}}^{\text{as}} \xrightarrow{m_{\text{lightest}} \rightarrow \infty} & 1 + \frac{g^2 N_c}{16\pi^2} \left[\frac{2}{3} \ln m_t - \frac{1}{9} + \frac{4}{9} \hat{s}_W^2 Q_t^2 - 4I_t Q_t \left(\frac{1}{3} \ln m_t + \frac{1}{18} \right) \right. \\ & \left. + \frac{8}{3} \hat{s}_W^2 Q_b^2 \ln m_b - \frac{1}{9} (-4\hat{s}_W^2 Q_b^2 + 2I_b Q_b) (-5 + 6 \ln m_Z) \right] \\ & + 0.0027 + \delta_{VB} + \delta'_V \\ & \simeq 1.00834, \end{aligned} \quad (3.83)$$

where 0.0027 is the contribution from the SM bosonic loop. On the other hand, the one-loop corrected rho parameter in the SM can be expressed as

$$\rho_{\text{SM}} \simeq 1 + \frac{s_W^2}{c_W^2 - s_W^2} \left[\frac{c_W^2}{s_W^2} \frac{N_c \sqrt{2}}{16\pi^2} G_F m_t^2 - \delta_{VB} \right] \simeq 1.0102. \quad (3.84)$$

From Eqs. (3.83) and (3.84), it can be seen that the rho parameter in the HTM can deviate from that in the SM even in the large triplet-like scalar mass and $v_\Delta \rightarrow 0$ limit, and the value of $\rho_{\text{SM}} - \rho_{\text{HTM}}^{\text{as}}$ is approximately 0.00186. In the SM and all the models with $\rho = 1$ at the tree level, $\delta\rho$ ($\equiv \rho - 1$) measures the violation of the custodial $SU(2)$ symmetry [96, 97]. Such effects appear as the quadratic power-like contributions of the mass difference between particles in the $SU(2)$ multiplet; i.e., $\delta\rho \simeq (m_u - m_d)^2/v^2$ for $m_u \simeq m_d$ via the chiral fermion loop diagram [139], and $\delta\rho \simeq (m_{H^+} - m_A)^2/v^2$ for $m_{H^+} \simeq m_A$ via the additional scalar boson loop diagram [140–144] in the general two Higgs doublet model. On the other hand, in the models with $\rho \neq 1$ at the tree level like the HTM, such quadratic power-like mass contributions are absorbed by renormalization of the new independent input parameter $\delta\hat{s}_W^2$. Consequently,

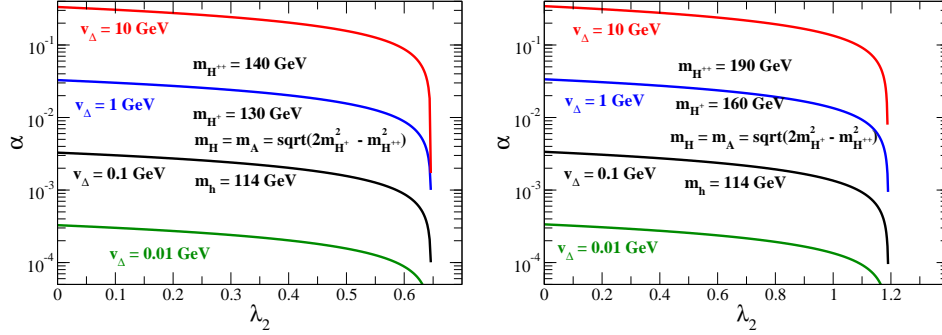


Figure 3.16: The mixing angle α as a function of λ_2 for each fixed value of v_Δ in the case of $m_h = 114$ GeV. In the left (right) figure, we take $m_{H^{++}} = 140$ GeV and $\Delta m = 10$ GeV ($m_{H^{++}} = 190$ GeV and $\Delta m = 30$ GeV).

only a logarithmic dependence on the masses of the particles in the loop diagram remain. In other words, in these models the rho parameter is no more the parameter which measures the violation of the $SU(2)$ custodial symmetry in the sector of particles in the loop. This has already been known in the calculation of the model with the $Y = 0$ triplet field [49, 51].

3.2.3 Decay of the triplet-like scalar bosons

In the previous section, we have discussed the constraint from the electroweak precision data such as m_W and the rho parameter. We have concluded that the hierarchical mass scenario for Case II as well as the degenerated mass scenario are highly constrained by the data. On the other hand, the hierarchical mass scenario for Case I is allowed by the data in the case where the mass of $H^{\pm\pm}$ is of $\mathcal{O}(100-200)$ GeV with Δm to be several hundred GeV and v_Δ of several GeV. Although the degenerated mass scenario and Case II are highly constrained by the electroweak precision data¹⁰, we discuss the decay branching ratios of the triplet-like scalar bosons in Case I, Case II and also the degenerate mass scenario.

The decay modes of the triplet-like scalar bosons can be classified into three modes: (i) decay via the Yukawa coupling defined in Eq. (3.35), (ii) that via v_Δ and (iii) that via the gauge coupling. The magnitude of the Yukawa coupling constant and v_Δ are related from the neutrino mass as in Eq. (3.61). The main decay modes of H^{++} and H^+ depend on the size of v_Δ and ξ . The decay mode (iii) particularly is important in the case of $\xi \neq 0$. Typically, in this case, the heaviest triplet-like scalar boson decays into the second heaviest one associated with the W boson. The formulae of the decay rates of $H^{\pm\pm}$, H^\pm , H and A are listed in Appendix A. Here, the leptonic decay modes through the Yukawa coupling h_{ij} are summed over all flavors and each element of h_{ij} is taken to be $0.1 \text{ eV}/(\sqrt{2}v_\Delta)$. In the calculation of the decay rates for the triplet-like scalar bosons, we use the relations in Eqs. (3.58) and (3.59), so that five mass parameters: $m_{H^{++}}$, m_{H^+} , m_A , m_H and m_h can be described by three parameters: $m_{H^{++}}$, m_h and Δm or m_A , m_h and Δm . Furthermore, we here take α to not be an independent

¹⁰ In the minimal Higgs triplet model in which a doublet Higgs field with $Y = 1/2$ and a triplet Higgs field with $Y = 1$ are contained, these two cases are highly constrained. However, this constraint would be relaxed when we consider extended Higgs models such as the HTM with inert doublet scalar fields or inert triplet scalar fields.

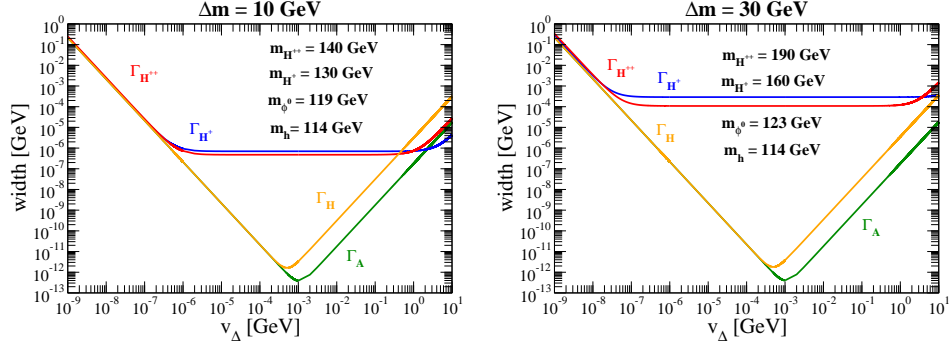


Figure 3.17: Decay width of H^{++} , H^+ , H and A as a function of v_Δ . We take $m_{H^{++}} = 140$ GeV (190 GeV), $\Delta m = 10$ GeV (30 GeV) in the left (right) figure. In both the figures, m_h is fixed to be 114 GeV [57].

parameter but dependent parameter which is determined by v_Δ , $m_{H^{++}}$ (m_A), m_h , Δm and λ_2 . In Fig. (3.2.3), the mixing angle α is shown as a function of λ_2 for each fixed value of v_Δ in the case of $m_h = 114$ GeV. In the left figure, we take $m_{H^{++}} = 140$ GeV and $\Delta m = 10$ GeV, while in the right figure, we take $m_{H^{++}} = 190$ GeV and $\Delta m = 30$ GeV. In the both figure, we can see that the mixing angle α is not so sensitive to λ_2 . In the following analysis, we take λ_2 to be zero.

In FIG. 3.17, the decay width for the triplet-like scalar bosons is shown in the case of $\Delta m = 10$ GeV and $\Delta m = 30$ GeV. Since there is a decay mode through the gauge coupling the minimum value of the decay widths of H^{++} and H^+ are $\mathcal{O}(10^{-6})$ GeV for $\Delta m = 10$ GeV and $\mathcal{O}(10^{-4})$ GeV for $\Delta m = 30$ GeV. On the other hand, the decay widths of H and A become minimum at $v_\Delta \simeq 10^{-4} - 10^{-3}$ GeV with the magnitude of $\mathcal{O}(10^{-13} - 10^{-12})$ GeV. This result is consistent with Ref. [53].

We consider the decay branching ratio of H^{++} . In the case with $\Delta m = 0$ and $m_{H^{++}} = 140$ GeV, H^{++} decays into $\ell^+\ell^+$ with $v_\Delta \lesssim 10^{-3}$ GeV or W^+W^+ with $v_\Delta \gtrsim 10^{-3}$ GeV. The value of v_Δ where the main decay mode changes from $H^{++} \rightarrow \ell^+\ell^+$ to $H^{++} \rightarrow W^+W^+$ is shifted at $v_\Delta \simeq 10^{-4}$ GeV when $m_{H^{++}} = 300$ GeV. In the case of $\Delta m = 10$ GeV, H^{++} decays into H^+W^{+*} in the region of 10^{-6} GeV $\lesssim v_\Delta \lesssim 1$ GeV (10^{-6} GeV $\lesssim v_\Delta \lesssim 0.1$ GeV) for $m_{H^{++}} = 140$ GeV (320 GeV). Similarly, in the case of $\Delta m = 30$ GeV, H^{++} decays into H^+W^{+*} in the region of 10^{-7} GeV $\lesssim v_\Delta \lesssim 1$ GeV for $m_{H^{++}} = 190$ GeV and 360 GeV. In FIG. 3.18, the decay branching ratio of H^{++} is shown as a function of v_Δ .

The decay branching ratio of H^+ is shown in FIG. 3.19. In the case of $\Delta m = 0$, H^+ decays into $\ell^+\nu$ with $v_\Delta < 10^{-4} - 10^{-3}$ GeV. When $v_\Delta > 10^{-4} - 10^{-3}$ GeV, H^+ decays into $\tau^+\nu$, W^+Z and $c\bar{s}$ for $m_{H^+} = 120$ GeV, while H^+ decays into $t\bar{b}$, W^+Z and hW^+ for $m_{H^+} = 300$ GeV. In the case of $\Delta m = 10$ GeV, similarly to the decay of H^{++} , H^+ decays into ϕ^0W^{+*} in the region of 10^{-6} GeV $\lesssim v_\Delta \lesssim 1$ GeV (10^{-6} GeV $\lesssim v_\Delta \lesssim 10^{-2}$ GeV) for $m_{H^+} = 130$ GeV (310 GeV). In the case of $\Delta m = 30$ GeV, H^+ decays into ϕ^0W^{+*} in the region of 10^{-7} GeV $\lesssim v_\Delta \lesssim 10$ GeV (10^{-7} GeV $\lesssim v_\Delta \lesssim 10^{-1}$ GeV) for $m_{H^+} = 160$ GeV (330 GeV).

The decay branching ratios of H and A are shown in FIG. 3.20. Both H and A decay into neutrinos in the region of $v_\Delta < 10^{-4} - 10^{-3}$ GeV. When $v_\Delta > 10^{-4} - 10^{-3}$ GeV, both H and A decay into $b\bar{b}$ with $m_{\phi^0} = 119$ GeV while H (A) decay into hh and ZZ (hZ) with $m_{\phi^0} = 300$

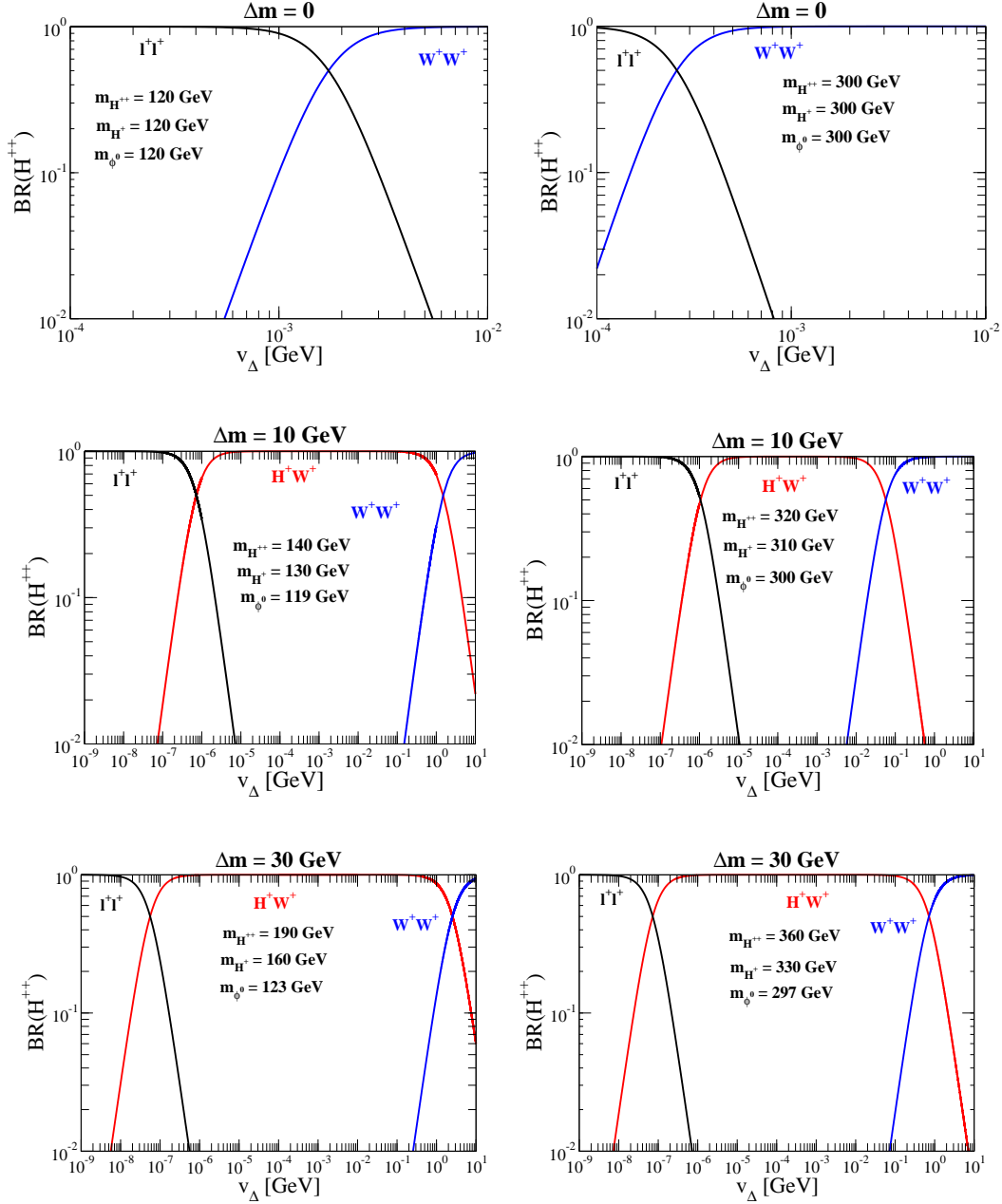


Figure 3.18: Decay branching ratio of H^{++} as a function of v_{Δ} . In the upper left (right) figure, $m_{H^{++}}$ is fixed to be 120 GeV (300 GeV), and Δm is taken to be zero. In the middle left (right) figure, $m_{H^{++}}$ is fixed to be 140 GeV (320 GeV), and Δm is taken to be 10 GeV. In the bottom left (right) figure, $m_{H^{++}}$ is fixed to be 190 GeV (360 GeV), and Δm is taken to be 30 GeV [57].

GeV.

Finally, we comment on the case of $\xi < 0$. In this case, H and A can decay into $H^{\pm}W^{\mp(*)}$ depending on the magnitude of ξ and v_{Δ} . At the same time, H^+ can decay into $H^{++}W^{-(*)}$. The decay of H^{++} is the same as in the case without the mass difference.

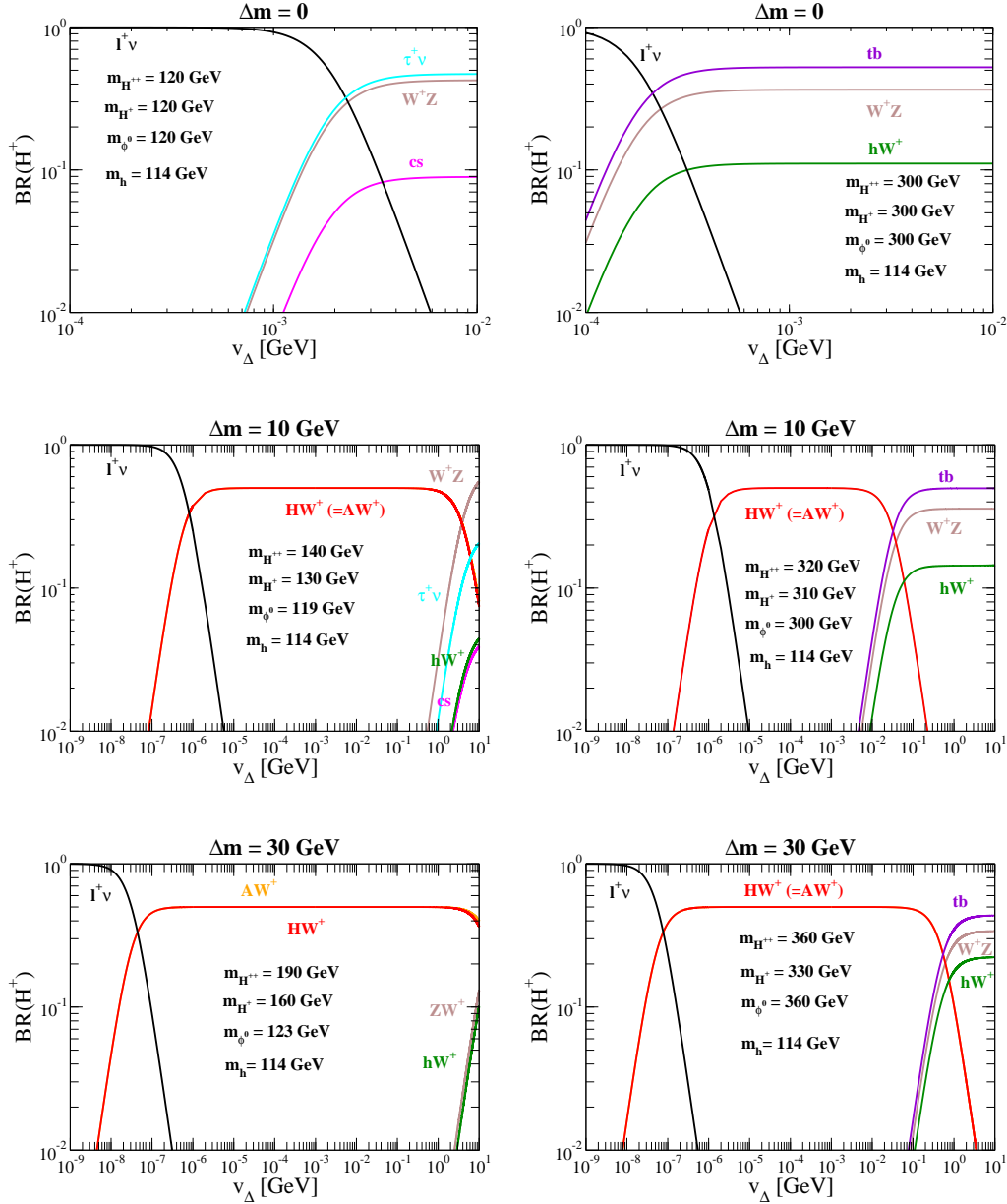


Figure 3.19: Decay branching ratio of H^+ as a function of v_Δ . In all the figures, m_h is taken to be 114 GeV. In the upper left (right) figure, m_{H^+} is fixed to be 120 GeV (300 GeV), and Δm is taken to be zero. In the middle left (right) figure, m_{H^+} is fixed to be 130 GeV (310 GeV), and Δm is taken to be 10 GeV. In the bottom left (right) figure, m_{H^+} is fixed to be 160 GeV (330 GeV), and Δm is taken to be 30 GeV [57].

3.2.4 Mass determination of the triplet-like scalar bosons at the LHC

We discuss how the HTM with $\xi > 0$ can be tested at the LHC. At the LHC, the triplet-like scalar bosons $H^{\pm\pm}$, H^\pm , H and A are mainly produced through the Drell-Yan processes, for

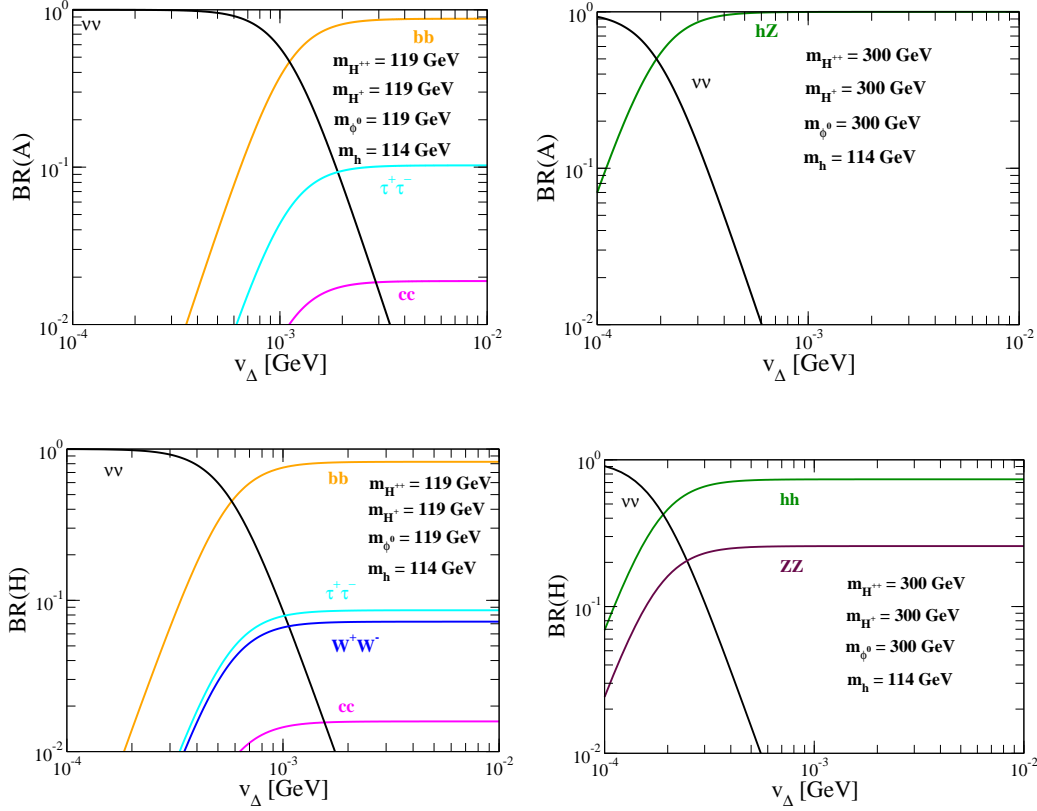


Figure 3.20: Decay branching ratios of A and H as a function of v_Δ . In all the figures, m_h is taken to be 114 GeV. In the upper left (right) figure, the branching ratio of A is shown in the case of $m_A = 119$ GeV (300 GeV). In the lower left (right) figure, the branching ratio of H is shown in the case of $m_H = 119$ GeV (300 GeV) [57].

instance, $pp \rightarrow H^{++}H^{--}$, $pp \rightarrow H^+H^-$, $pp \rightarrow H^{\pm\pm}H^\mp$ and $pp \rightarrow H^\pm\phi^0$ and $pp \rightarrow HA$. In particular, latter three processes are important when we consider the case of $\xi > 0$. The cross sections for the latter three production processes are shown in FIG. 8.1.

We comment on vector boson fusion production processes. There are two types of the vector boson fusion processes. First one is the process via $VV\Delta$ vertices, where $V = Z$ or W^\pm . The cross section of this process is small, since the $VV\Delta$ vertex is proportional to v_Δ ¹¹. The other one is the process via the gauge coupling constant. In particular, $qq \rightarrow q'q'H^{++}\phi^0$ is the unique process whose difference of the electric charge between produced scalar bosons is two. This production cross section is 0.51 fb (0.13 fb) at $\sqrt{s} = 14$ TeV ($\sqrt{s} = 7$ TeV) assuming mass parameters Set 1 which is given just below.

We consider the following two sets for mass parameters:

- (Set 1) $m_{H^{++}} = 140$ GeV, $m_{H^+} = 130$ GeV, $m_H = m_A = 119$ GeV, $m_h = 114$ GeV,
 (Set 2) $m_{H^{++}} = 190$ GeV, $m_{H^+} = 160$ GeV, $m_H = m_A = 123$ GeV, $m_h = 114$ GeV,

¹¹The magnitude of v_Δ may be determined indirectly via B_{ee}/B_{WW} or Γ_{ee} and $0\nu\beta\beta$ where $H^{++} \rightarrow \ell^+\ell^+$, W^+W^+ are dominant [62]. On the other hand, it could be directly measured via $qq \rightarrow q'q'W^{\pm*}Z^* \rightarrow q'qH^\pm$ at the LHC [145] and via $e^+e^- \rightarrow Z^* \rightarrow H^\pm W^\mp$ at the ILC [146, 147].

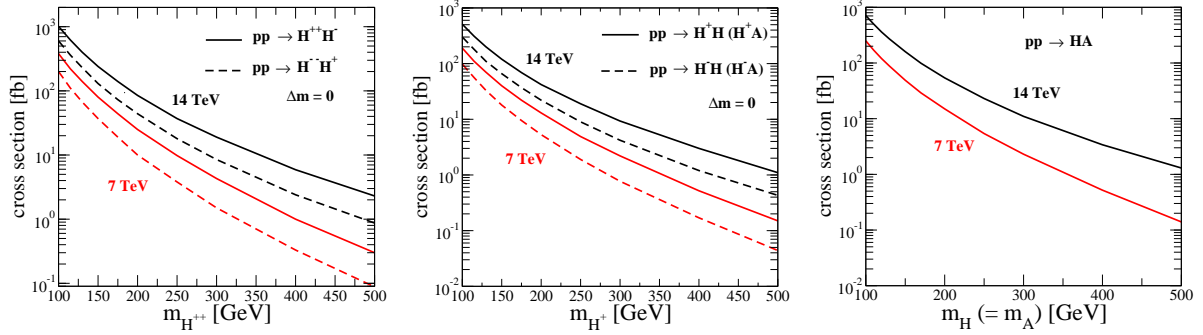


Figure 3.21: Production cross sections for the triplet-like scalar bosons in the Drell-Yan process [57].

which correspond to the cases with $\xi=(52 \text{ GeV})^2$ and $\xi=(102 \text{ GeV})^2$, respectively. In the following numerical analysis, $\lambda_2 = 0$ is taken. In these parameter sets, the production cross sections for the triplet-like scalar bosons are listed in TABLE 3.6. We can classify scenarios by the following four regions of v_Δ for Set 1:

Scenario (1a)	$v_\Delta \gtrsim 1 \text{ GeV}$,
Scenario (1b)	$10^{-3} \text{ GeV} \lesssim v_\Delta \lesssim 1 \text{ GeV}$,
Scenario (1c)	$10^{-6} \text{ GeV} \lesssim v_\Delta \lesssim 10^{-3} \text{ GeV}$,
Scenario (1d)	$v_\Delta \lesssim 10^{-6} \text{ GeV}$.

We can also classify scenarios by the following four regions of v_Δ for Set 2:

Scenario (2a)	$v_\Delta \gtrsim 1 \text{ GeV}$,
Scenario (2b)	$10^{-4} \text{ GeV} \lesssim v_\Delta \lesssim 1 \text{ GeV}$,
Scenario (2c)	$10^{-7} \text{ GeV} \lesssim v_\Delta \lesssim 10^{-4} \text{ GeV}$,
Scenario (2d)	$v_\Delta \lesssim 10^{-7} \text{ GeV}$.

In each scenario, main decay modes of the triplet-like scalar bosons are listed in TABLE 3.7 and TABLE 3.8. We here analyse the signal for Set 1 which may be used to reconstruct the masses of the triplet-like scalar bosons. The signal distributions discussed below are calculated by using CalcHEP [130].

Scenario (1a) ;

We can measure $m_{H^{++}}$ by observing the endpoint in the transverse mass distribution of the $\ell^+\ell^+\cancel{E}_T$ system in the process $pp \rightarrow H^{++}H^- \rightarrow (W^{++}W^+)(W^{-*}Z) \rightarrow (\ell^+\ell^+\cancel{E}_T)(jjjj)$, (FIG. 3.22 upper left). At the same time, we can also determine m_{H^+} by measuring the endpoint in the transverse mass distribution of the $\ell^+jj\cancel{E}_T$ system or the $\ell^+\cancel{E}_T$ system in the process $pp \rightarrow H^+\phi^0 \rightarrow (W^{+*}Z)(b\bar{b}) \rightarrow (\ell^+jj\cancel{E}_T)(j_bj_b)$ or $pp \rightarrow H^+\phi^0 \rightarrow (\tau^+\nu)(b\bar{b}) \rightarrow (\ell^+\cancel{E}_T)(j_bj_b)$, (FIG. 3.22 upper right and lower left). In addition, m_{ϕ^0} can be determined by using the invariant mass distribution or by observing the endpoint in the transverse mass distribution of the $b\bar{b}$ system in the process $pp \rightarrow HA \rightarrow (b\bar{b})(b\bar{b}) \rightarrow (j_bj_b)(j_bj_b)$, (FIG. 3.22 lower right).

Process	$\Delta m = 0$	$\Delta m = 10$ GeV	$\Delta m = 30$ GeV
$pp \rightarrow H^{++}H^-$	310 fb (110 fb)	350 fb (120 fb)	140 fb (43 fb)
$pp \rightarrow H^+H$	150 fb (53 fb)	230 fb (81 fb)	150 fb (50 fb)
$pp \rightarrow HA$	200 fb (65 fb)	370 fb (130 fb)	330 fb (110 fb)

Table 3.6: Production cross sections for the triplet-like scalar bosons in the case of $\Delta m = 0$ with $m_{H^{++}} = 140$ GeV, those of the case for Set 1 and Set 2. The numbers without (with) the bracket are the production cross sections at $\sqrt{s} = 14$ TeV ($\sqrt{s} = 7$ TeV) [57].

Scenario	Decay of H^{++}	Decay of H^+	Decay of H	Decay of A
(1a) ($v_\Delta = 5$ GeV)	W^+W^{+*} [0.93]	$W^{+*}Z$ [0.37], $\tau^+\nu$ [0.14]	$b\bar{b}$ [0.82]	$b\bar{b}$ [0.89]
(1b) ($v_\Delta = 10^{-2}$ GeV)	H^+W^{+*} [1.0]	AW^{+*} [0.5], HW^{+*} [0.5]	$b\bar{b}$ [0.82]	$b\bar{b}$ [0.89]
(1c) ($v_\Delta = 10^{-5}$ GeV)	H^+W^{+*} [1.0]	AW^{+*} [0.5], HW^{+*} [0.5]	$\nu\nu$ [1.0]	$\nu\nu$ [1.0]
(1d) ($v_\Delta = 10^{-8}$ GeV)	$\ell^+\ell^+$ [1.0]	$\ell^+\nu$ [1.0]	$\nu\nu$ [1.0]	$\nu\nu$ [1.0]

Table 3.7: The main decay mode of the triplet-like scalar bosons in Scenario (1a) to Scenario (1d). The masses of the triplet-like scalar bosons are taken to be as for Set 1. The number in () represents the sample value of v_Δ corresponding to the scenario. The number in [] represents the value of the decay branching ratio corresponding to the value of v_Δ displayed in () in the same row. Here, $\ell\ell$ mode and $\ell\nu$ mode are summed over all flavors [57].

Scenario	Decay of H^{++}	Decay of H^+	Decay of H	Decay of A
(2a) [$v_\Delta = 5$ GeV]	W^+W^{+*} [0.76]	AW^{+*} [0.47] HW^{+*} [0.46]	$b\bar{b}$ [0.78]	$b\bar{b}$ [0.89]
(2b) [$v_\Delta = 10^{-2}$ GeV]	H^+W^{+*} [1.0]	AW^{+*} [0.5] HW^{+*} [0.5]	$b\bar{b}$ [0.78]	$b\bar{b}$ [0.89]
(2c) [$v_\Delta = 10^{-5}$ GeV]	H^+W^{+*} [1.0]	AW^{+*} [0.5] HW^{+*} [0.5]	$\nu\nu$ [1.0]	$\nu\nu$ [1.0]
(2d) [$v_\Delta = 10^{-8}$ GeV]	$\ell^+\ell^+$ [0.97]	$\ell^+\nu$ [0.91]	$\nu\nu$ [1.0]	$\nu\nu$ [1.0]

Table 3.8: The main decay mode of the triplet-like scalar bosons in Scenario (2a) to Scenario (2d). The masses of the triplet-like scalar bosons are taken to be as for Set 2. The number in () represents the sample value of v_Δ corresponding to the scenario. The number in [] represents the value of the decay branching ratio corresponding to the value of v_Δ displayed in () in the same row. Here, $\ell\ell$ mode and $\ell\nu$ mode are summed over all flavors [57].

Scenario (1b) ;

We can determine $m_{H^{++}}$ by measuring the endpoint in the transverse mass distribution of the $\ell^+\ell^+j_bj_b\cancel{E}_T$ system in the process $pp \rightarrow H^{++}H^- \rightarrow (W^{+*}W^{+*}b\bar{b})(W^{-*}b\bar{b}) \rightarrow (\ell^+\ell^+j_bj_b\cancel{E}_T)(jjj_bj_b)$, (FIG. 3.23 left). Analysing the transverse mass distribution for the $\ell^+\ell^+j_bj_b\cancel{E}_T$ system, we treat that a lepton pair $\ell^+\nu$ from W^{+*} as one massless fermion as represented X^+ in FIG. 3.23. This procedure is justified since the angle between ℓ^+ and ν is distributed almost around 0° . We can also determine m_{H^+} by measuring the endpoint in the transverse mass distribution of the $\ell^+j_bj_b\cancel{E}_T$ system in the process $pp \rightarrow H^+\phi^0 \rightarrow (W^{+*}b\bar{b})(b\bar{b}) \rightarrow (\ell^+j_bj_b\cancel{E}_T)(j_bj_b)$, (FIG. 3.23 center). In addition, m_{ϕ^0} can be reconstructed by measuring the invariant mass distribution of the $b\bar{b}$ system and by

	$m_{H^{++}}$	m_{H^+}	m_H/m_A
(1a)	$pp \rightarrow H^{++}H^- \rightarrow$ $(\ell^+\ell^+\cancel{E}_T)(jjjj)$ [2.8 fb] (0.95 fb)	$pp \rightarrow H^+H \rightarrow (\ell^+jj\cancel{E}_T)(j_bj_b)$ [11 fb] (3.8 fb) $pp \rightarrow H^+H \rightarrow (\ell^+\cancel{E}_T)(j_bj_b)$ [9.3 fb] (3.3 fb)	$pp \rightarrow HA \rightarrow (j_bj_b)(j_bj_b)$ [270 fb] (95 fb) $pp \rightarrow H^+H \rightarrow (\ell^+\cancel{E}_T)(j_bj_b)$ [9.3 fb] (3.3 fb)
(1b)	$pp \rightarrow H^{++}H^- \rightarrow$ $(\ell^+\ell^+j_bj_b\cancel{E}_T)(jjj_bj_b)$ [8.4 fb] (2.9 fb)	$pp \rightarrow H^+H \rightarrow (\ell^+j_bj_b\cancel{E}_T)(j_bj_b)$ [36 fb] (13 fb)	$pp \rightarrow HA \rightarrow (j_bj_b)(j_bj_b)$ [270 fb] (95 fb) $pp \rightarrow H^+H \rightarrow (\ell^+j_bj_b\cancel{E}_T)(j_bj_b)$ [36 fb] (13 fb)
(1c)	Challenging		
(1d)	Excluded		

Table 3.9: The processes which can be used to reconstruct the masses of the triplet-like scalar bosons are summarized. The numbers in [] and () represent the cross section for the final state of the process at $\sqrt{s} = 14$ TeV and $\sqrt{s} = 7$ TeV, respectively, for Set 1. The values of the decay branching ratios of the triplet-like scalar bosons are listed in TABLE 3.7. In this table, the b -tagging efficiency is assumed to be 100 % [57].

	$m_{H^{++}}$	m_{H^+}	m_H/m_A
(2a)	$pp \rightarrow H^{++}H^- \rightarrow$ $(\ell^+\ell^+\cancel{E}_T)(jjj_bj_b)$ [2.7 fb] (0.84 fb)	$pp \rightarrow H^+H \rightarrow (\ell^+j_bj_b\cancel{E}_T)(j_bj_b)$ [21 fb] (6.9 fb)	$pp \rightarrow HA \rightarrow (j_bj_b)(j_bj_b)$ [230 fb] (76 fb)
(2b)	$pp \rightarrow H^{++}H^- \rightarrow$ $(\ell^+\ell^+j_bj_b\cancel{E}_T)(jjj_bj_b)$ [3.2 fb] (0.99 fb)	$pp \rightarrow H^+H \rightarrow (\ell^+j_bj_b\cancel{E}_T)(j_bj_b)$ [22 fb] (7.2 fb)	$pp \rightarrow HA \rightarrow (j_bj_b)(j_bj_b)$ [230 fb] (76 fb)
(2c)	Challenging		
(2d)	Excluded		

Table 3.10: The processes which can be used to reconstruct the masses of the triplet-like scalar bosons are summarized. The numbers in [] and () represent the cross section for the final state of the process at $\sqrt{s} = 14$ TeV and $\sqrt{s} = 7$ TeV, respectively, for Set 2. The values of the decay branching ratios of the triplet-like scalar bosons are listed in TABLE 3.8. In this table, the b -tagging efficiency is assumed to be 100 % [57].

observing the endpoint of the transverse mass distribution of the $b\bar{b}$ system in the process $pp \rightarrow HA \rightarrow (b\bar{b})(b\bar{b}) \rightarrow (j_bj_b)(j_bj_b)$ (FIG. 3.23 right).

Scenario (1c) ;

The final state of the decay of the triplet-like scalar bosons always include neutrinos, so

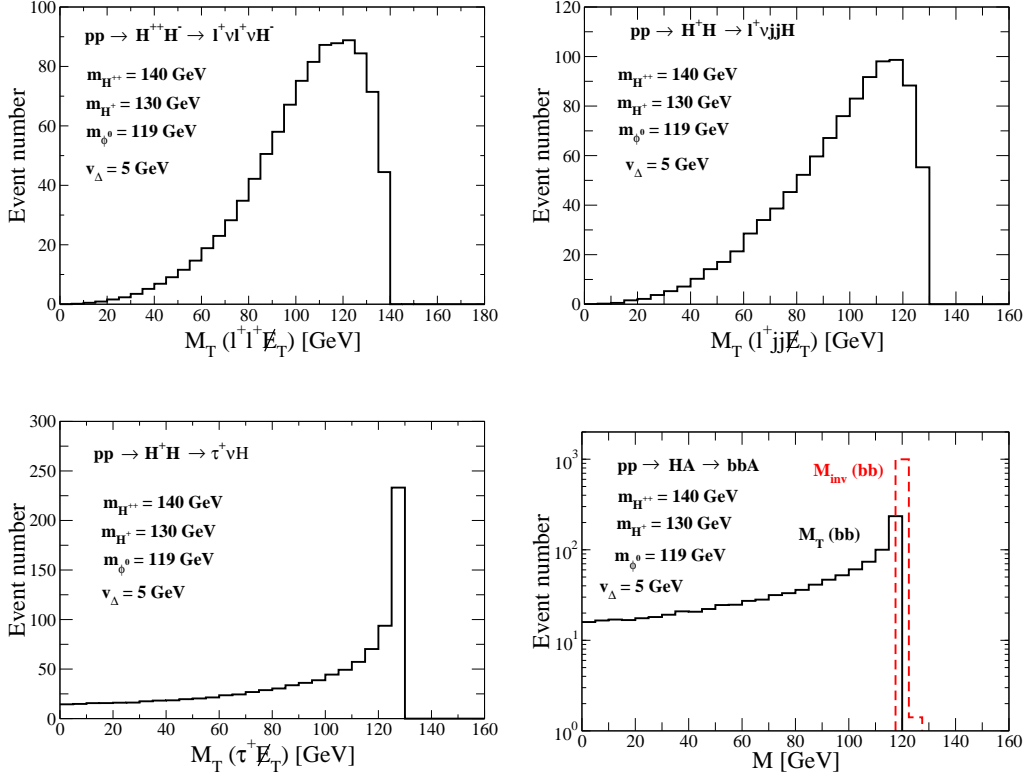


Figure 3.22: The transvers mass distributions for each system in Scenario (1a). The total event number is assumed to be 1000. In the bottom-right figure, the horizontal axis M represents the transvers mass distribution for the $b\bar{b}$ system $M_T(b\bar{b})$ (solid) or the invariant mass distribution for the $b\bar{b}$ system $M_{inv}(b\bar{b})$ (dashed) [57].

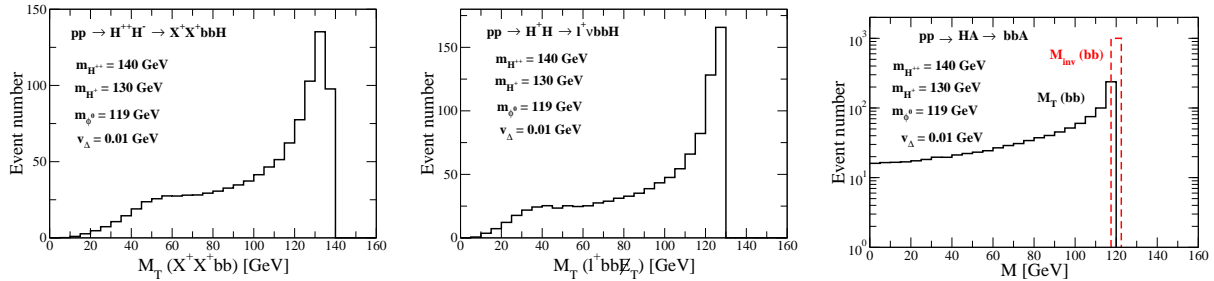


Figure 3.23: The transvers mass distributions for each system in Scenario (1b). The total event number is assumed to be 1000. In the right figure, the horizontal axis M represents the transvers mass distribution for the $b\bar{b}$ system $M_T(b\bar{b})$ (solid) or the invariant mass distribution for the $b\bar{b}$ system $M_{inv}(b\bar{b})$ (dashed) [57].

that the reconstruction of the masses of the triplet-like scalar bosons would be challenging.

Scenario (1d) ;

This scenario is already excluded from the direct search results at the LHC for the processes of $pp \rightarrow H^{++}H^{--}(H^{\pm\pm}H^\mp) \rightarrow \ell^+\ell^+\ell^-\ell^-(\ell^\pm\ell^\pm\ell^\mp\nu)$.

In TABLE 3.9, processes which can use the reconstruction of the masses of the triplet-like scalar bosons are summarized in each scenario. The cross sections for the final states of each process are also listed. In the case of Set 2, the masses of the triplet like scalar bosons may be able to reconstruct in the similar way to the case of Set 1. Thus, we show only the signal cross sections for the final states for Set 2 in TABLE 3.10.

3.2.5 The two photon decay of the SM-like Higgs boson

We discuss the radiative effect of triplet-like Higgs bosons on the decay rate of $h \rightarrow \gamma\gamma$ in the HTM under the constraint from the electroweak precision data. The $h\gamma\gamma$ vertex is generated at the one-loop level, so that the significant one-loop contributions of additional charged particles can appear. In the HTM, there are doubly- and singly-charged Higgs bosons which would give substantial one-loop contributions to the decay rate of $h \rightarrow \gamma\gamma$. In Ref. [148], this decay process have been discussed in the HTM under the constraint from perturbative unitarity and vacuum stability. We here analyze the decay rate taking into account our new results of the radiative corrections to the electroweak parameters.

The decay rate of $\phi \rightarrow \gamma\gamma$ is calculated at the one-loop level by [149]

$$\Gamma(\phi \rightarrow \gamma\gamma) = \frac{G_F \alpha_{\text{em}}^2 m_\phi^3}{128 \sqrt{2} \pi^3} \left| -2 \sum_f N_f^c Q_f^2 \tau_f [1 + (1 - \tau_f) f(\tau_f)] + 2 + 3\tau_W + 3\tau_W(2 - \tau_W) f(\tau_W) \right. \\ \left. + Q_{H^{++}}^2 \frac{2vc_{hH^{++}H^{--}}}{m_\phi^2} [1 - \tau_{H^{++}} f(\tau_{H^{++}})] + Q_{H^+}^2 \frac{2vc_{hH^+H^-}}{m_\phi^2} [1 - \tau_{H^+} f(\tau_{H^+})] \right|^2, \quad (3.85)$$

where the function $f(x)$ is given by

$$f(x) = \begin{cases} [\arcsin(1/\sqrt{x})]^2, & \text{if } x \geq 1, \\ -\frac{1}{4} [\ln \frac{1+\sqrt{1-x}}{1-\sqrt{1-x}} - i\pi]^2, & \text{if } x < 1 \end{cases}. \quad (3.86)$$

In Eq. (3.85), Q_φ is the electric charge of the field φ , N_f^c is the color factor and $\tau_\varphi = 4m_\varphi^2/m_\phi^2$. In the HTM, the coupling constants $c_{hH^+H^-}$ and $c_{hH^{++}H^{--}}$ are given by

$$c_{hH^+H^-} = \frac{1}{v_\Delta} \left[m_{H^+}^2 \left(\sqrt{2} s_{\beta_\pm} c_{\beta_\pm} c_\alpha + 2s_{\beta_\pm}^2 s_\alpha \right) - m_A^2 s_\alpha \left(c_{\beta_0}^2 + \frac{s_{\beta_0}^2}{2} \right) + m_h^2 \left(\frac{s_{\beta_\pm}^3 c_\alpha}{\sqrt{2} c_{\beta_\pm}} + c_{\beta_\pm}^2 s_\alpha \right) \right], \quad (3.87)$$

$$c_{hH^{++}H^{--}} = \frac{1}{v_\Delta} \left[2m_{H^{++}}^2 s_\alpha + m_h^2 s_\alpha - 2m_{H^+}^2 \left(2c_{\beta_\pm}^2 s_\alpha - \sqrt{2} s_{\beta_\pm} c_{\beta_\pm} c_\alpha \right) - m_A^2 (s_{\beta_0} c_{\beta_0} c_\alpha - c_{\beta_0}^2 s_\alpha) \right]. \quad (3.88)$$

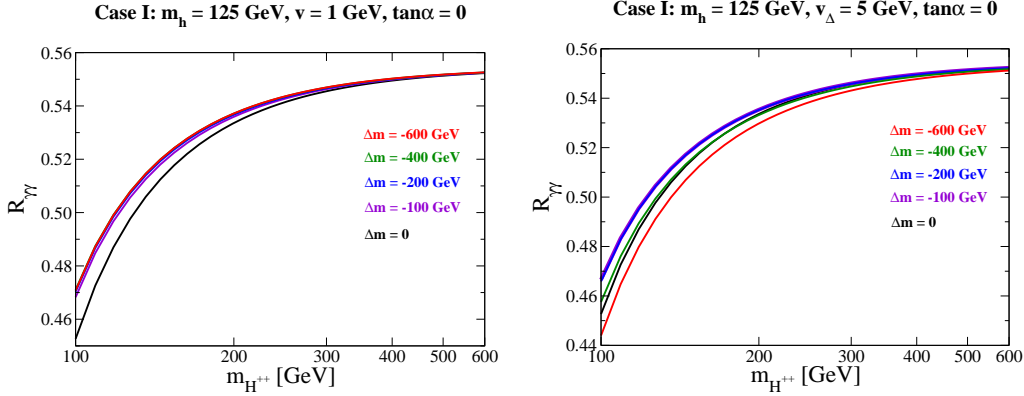


Figure 3.24: The ratio of the decay rate for $h \rightarrow \gamma\gamma$ in the HTM to that in the SM as a function of $m_{H^{++}}$ for each fixed value of Δm (< 0) in Case I ($m_{\phi^0} > m_{H^+} > m_{H^{++}}$). In the both figures, we take $m_t = 173$ GeV, $m_h = 125$ GeV and $\tan \alpha = 0$. In the left (right) figure, we take $v_\Delta = 1$ GeV (5 GeV) [48].

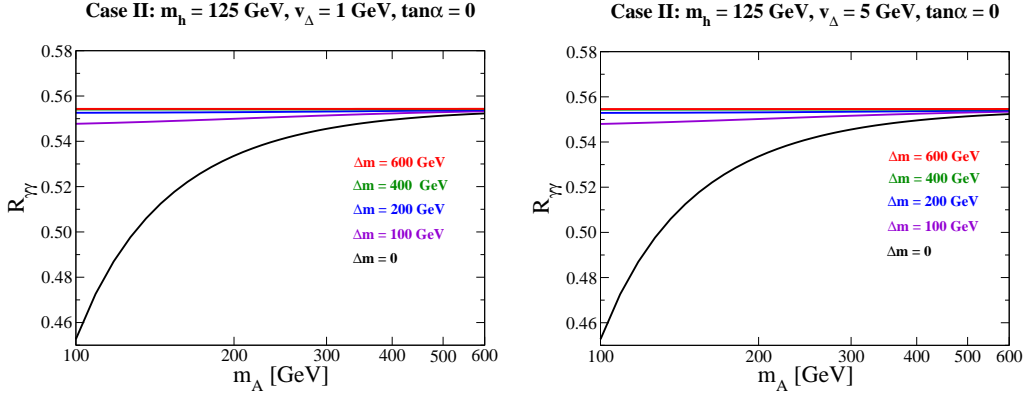


Figure 3.25: The ratio of the decay rate for $h \rightarrow \gamma\gamma$ in the HTM to that in the SM as a function of m_A for each fixed value of Δm (> 0) in Case II ($m_{H^{++}} > m_{H^+} > m_{\phi^0}$). In the both figures, we take $m_t = 173$ GeV, $m_h = 125$ GeV and $\tan \alpha = 0$. In the left (right) figure, we take $v_\Delta = 1$ GeV (5 GeV) [48].

In the case with $\alpha \simeq 0$ and $v_\Delta \simeq 0$, coupling constants in Eqs. (3.87) and (3.88) can be written as the simple form:

$$c_{hH^+H^-} \simeq \frac{2m_{H^+}^2}{v}, \quad (3.89)$$

$$c_{hH^{++}H^{--}} \simeq \frac{2m_{H^{++}}^2}{v}. \quad (3.90)$$

In Fig. 3.24, the ratio of the decay rates $R_\gamma \equiv \Gamma(h \rightarrow \gamma\gamma)_{\text{HTM}}/\Gamma(\phi_{\text{SM}} \rightarrow \gamma\gamma)_{\text{SM}}$ is shown as a function of $m_{H^{++}}$ for each value of Δm at $m_h (= m_{\phi_{\text{SM}}}) = 125$ GeV and $\tan \alpha = 0$ in Case I ($m_{\phi^0} > m_{H^+} > m_{H^{++}}$). For the left figure, v_Δ is taken to be 1 GeV, while it is taken to be 5 GeV for the right figure. In the both figures, $R_\gamma < 1$ because the one-loop contributions of

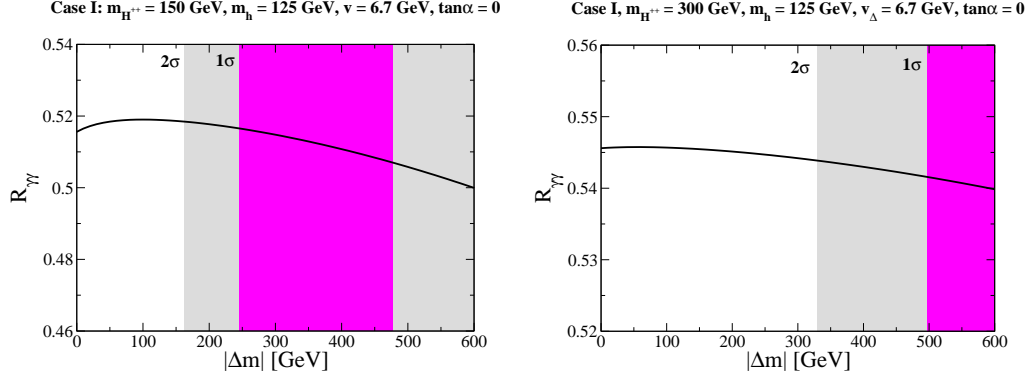


Figure 3.26: The ratio of the decay rate for $h \rightarrow \gamma\gamma$ in the HTM to that in the SM as a function of the absolute value of Δm in Case I ($m_{\phi^0} > m_{H^+} > m_{H^{++}}$). We take $m_t = 173$ GeV, $m_h = 125$ GeV, $v_\Delta = 6.7$ GeV and $\tan\alpha = 0$ in all the figures. In the left (right) figure, we take $m_{H^{++}} = 150$ GeV (300 GeV). The pink (gray) shaded region represents the 1σ (2σ) allowed region of Δm under the constraint from the data for m_W^{exp} and $\hat{s}_W^{2\text{exp}}$ [48].

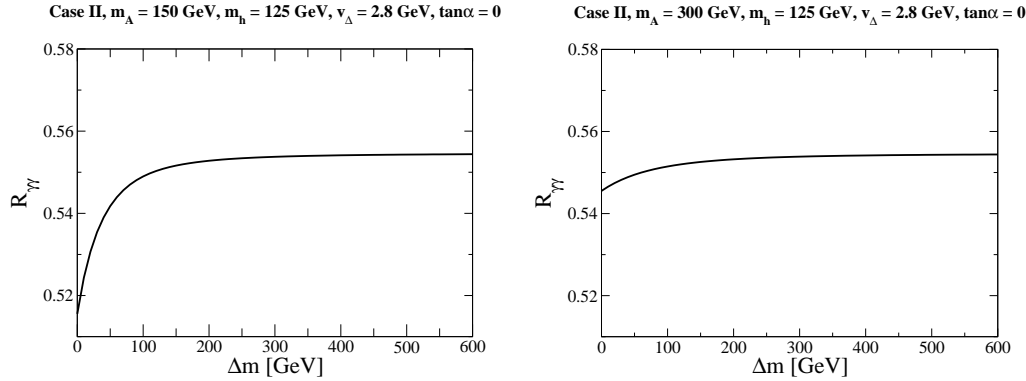


Figure 3.27: The ratio of the decay rate for $h \rightarrow \gamma\gamma$ in the HTM to that in the SM as a function of Δm in Case II ($m_{H^{++}} > m_{H^+} > m_{\phi^0}$). We take $m_t = 173$ GeV, $m_h = 125$ GeV, $v_\Delta = 2.8$ GeV and $\tan\alpha = 0$ in all the figures. In the left (right) figure, we take $m_A = 150$ GeV (300 GeV). There is no consistent region with the data for m_W^{exp} and $\hat{s}_W^{2\text{exp}}$ [48].

the singly-charged Higgs boson and the doubly-charged Higgs boson to $\Gamma(\phi \rightarrow \gamma\gamma)$ have the same sign which is destructive to the contribution of the SM loop diagrams. The magnitude of the deviation from the SM can be significant, which amounts to larger than 40%. For $v_\Delta = 1$ GeV the deviation is smaller when larger Δm is taken. The deviation becomes smaller and insensitive to Δm in the large mass region for $H^{\pm\pm}$.

One might think that the deviation would approach to zero in the large mass limit for $H^{\pm\pm}$. This can be true in a generic case. However, such decoupling is not applied to the present case. Since the coupling constants $c_{hH^+H^-}$ and $c_{hH^{++}H^{--}}$ are both proportional to the mass squared of triplet-like Higgs bosons, the large mass limit with a fixed value of Δm with $\alpha = 0$ can only be realized by taking these coupling constants to be infinity. It is known that in such a case, Appelquist's decoupling theorem [150] does not hold, and the one-loop contributions of H^\pm

and $H^{\pm\pm}$ remain in the large mass limit as non-decoupling effects. We note that, in this case with $\alpha = 0$, we have the relation $m_A^2 \simeq M_\Delta^2 = (\lambda_4 + \lambda_5)v_\Phi^2/2$ from Eq. (3.41), so that all the masses of triplet-like Higgs bosons cannot be taken to be larger than TeV scales because of the perturbative unitarity constraint. On the contrary, if $\alpha = 0$ is relaxed, m_A is a free parameter, which satisfies $m_A^2 \simeq M_\Delta^2 = (\mu/v_\Delta)v_\Phi^2/\sqrt{2}$ from Eq. (3.39), and it can be taken to be much larger than the electroweak scale when $\mu/v_\Delta \gg 1$ is assumed. Then, the correction due to the triplet field is suppressed by a factor of v^2/m_A^2 . Namely, the decoupling theorem holds in this case.

In Fig. 3.25, $R_{\gamma\gamma}$ is shown as a function of m_A for each value of Δm at $m_h (= m_{\phi_{\text{SM}}}) = 125$ GeV and $\alpha = 0$ in Case II ($m_{H^{++}} > m_{H^+} > m_{\phi^0}$). It is seen that as compared to Case I $R_{\gamma\gamma}$ is sensitive to the choice of Δm . Similarly to Case I, the deviation from the SM value is negative. However, smaller deviation is obtained for larger Δm for the both cases with $v_\Delta = 1$ GeV and $v_\Delta = 5$ GeV in the region of relatively lower values of m_A .

In Fig. 3.26, we show the results of $R_{\gamma\gamma}$ as a function of $|\Delta m|$ in Case I with indicating the allowed regions of each confidence level under the electroweak precision data. The mass of $H^{\pm\pm}$ is taken to be 150 GeV (left) and 300 GeV (right). In all the figures, we take $m_h = 125$ GeV, $\tan \alpha = 0$ and $v_\Delta = 6.7$ GeV. The magnitude of the ratio $R_{\gamma\gamma}$ strongly depends on $m_{H^{++}}$. Therefore, we may be able to obtain the indirect information of the mass spectrum of the triplet-like Higgs bosons by measuring the decay rate of $h \rightarrow \gamma\gamma$.

Finally, in Fig. 3.27, $R_{\gamma\gamma}$ is shown as a function of Δm in Case II with indicating the allowed regions of each confidence level under the electroweak precision data. The mass of A is taken to be 150 GeV (left) and 300 GeV (right). In all the figures, we take $m_h = 125$ GeV, $\tan \alpha = 0$ and $v_\Delta = 2.8$ GeV. As compared to the case shown in Fig. 3.26, the mass dependence on m_A is small among the three values of m_A . As we already discussed, Case II is not preferred by the electroweak precision data, and only the region with larger deviation than 2σ appears in each figure.

3.3 Testing Higgs models via the $H^\pm W^\mp Z$ vertex

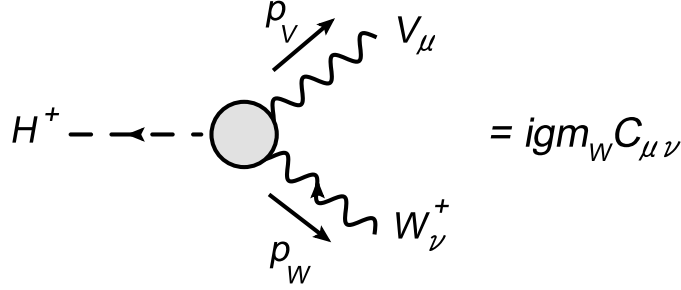
A common feature in the extended Higgs models is the appearance of physical charged scalar components. Most of the extended Higgs models contain singly charged Higgs bosons H^\pm such as the THDM, the HTM, etc., which are discussed in the previous sections. Hence, we may be able to discriminate each Higgs model through the physics of charged Higgs bosons. In particular, the $H^\pm W^\mp Z$ vertex can be a useful probe of the extended Higgs sector [30–33]. Assuming that there are several physical charged scalar states H_α^\pm ($\alpha \geq 2$) and the NG modes H_1^\pm , The vertex parameter ξ_α in $\mathcal{L} = igm_W \xi_\alpha H_\alpha^+ W^- Z + \text{h.c.}$ is calculated at the tree level as [30]

$$\sum_{\alpha \geq 2} |\xi_\alpha|^2 = \frac{1}{\cos^2 \theta_W} \left[\frac{2g^2}{m_W^2} \left\{ \sum_i [T_i(T_i + 1) - Y_i^2] |v_i|^2 Y_i^2 \right\} - \frac{1}{\rho_{\text{tree}}^2} \right], \quad (3.91)$$

where ρ_{tree} is given in Eq. (1.1). A non-zero value of ξ_α appears at the tree level only when H_α^\pm comes from an exotic representation such as triplets. Similarly to the case of the rho parameter, the vertex is related to the custodial symmetry. In general, this can be independent of the rho parameter. If a charged Higgs boson H_α^\pm is from a doublet field, ξ_α vanishes at the tree level. The vertex is then one-loop induced and its magnitude is proportional to the violation of the global symmetry in the sector of particles in the loop. Therefore, the determination of the $H^\pm W^\mp Z$ vertex can be a complementary tool to the rho parameter in testing the *exoticness* of the Higgs sector.

In this section, we discuss how accurately the $H^\pm W^\mp Z$ vertex can be determined at the collider experiments. At the LHC, the vertex would be determined by using the single H^\pm production from the WZ fusion [145]. The results are strongly model dependent, and the vertex may not be measured unless the H^\pm is light enough and $|\xi_\alpha|^2$ is greater than 10^{-2} . If kinematically allowed, the $H^\pm W^\mp Z$ vertex may also be measured via the decay process of $H^\pm \rightarrow W^\pm Z$ [31, 32].

We here focus on the process $e^+e^- \rightarrow W^\pm H^\mp$ at the ILC [146, 151–154]. At the ILC, the neutral Higgs boson is produced via the Higgs strahlung process $e^+e^- \rightarrow ZH$ [155]. The mass of the Higgs boson can be determined in a model independent way by using the so-called recoil method [156], where the information of the Higgs boson can be extracted by measuring the leptonic decay products of the recoiled Z boson. In this section, we employ this method to test the $H^\pm W^\mp Z$ vertex via $e^+e^- \rightarrow W^\pm H^\mp$. We analyze the signal and backgrounds at the parton level by using CalcHEP [130]. We take into account the beam polarization and the expected resolution for the two-jet system. We find that assuming that H^\pm decays into lepton pairs, the $H^\pm W^\mp Z$ vertex can be explored accurately by measuring the signal of the two-jet with one charged lepton with missing momentum. For relatively light charged Higgs bosons, the signal significance with the value of $|\xi_\alpha|^2 \sim O(10^{-3})$ can be as large as two after appropriate kinematic cuts for the collision energy $\sqrt{s} = 300$ GeV and the integrated luminosity 1 ab^{-1} , even when the initial state radiation (ISR) is taken into account.

Figure 3.28: The $H^\pm W^\mp V$ vertex ($V = Z$ or γ) [147].

3.3.1 The $H^\pm W^\mp Z$ vertex

The $H^\pm W^\mp V$ vertex ($V = Z$ or γ) is defined in FIG. 3.28, where $C^{\mu\nu}$ is expressed in terms of the form factors F_{HWV} , G_{HWV} and H_{HWV} as

$$C^{\mu\nu} = F_{HWV} g^{\mu\nu} + G_{HWV} \frac{p_W^\mu p_V^\nu}{m_W^2} + i H_{HWV} \frac{p_W^\rho p_V^\sigma}{m_W^2} \epsilon^{\mu\nu\rho\sigma}, \quad (3.92)$$

with $\epsilon_{\mu\nu\rho\sigma}$ being the anti-symmetric tensor with $\epsilon_{0123} = +1$, and p_V^μ and p_W^μ being the outgoing momenta of V and W bosons, respectively. Among the form factors, $F_{HW\gamma} = 0$ is derived at the tree level due to the $U(1)_{\text{em}}$ gauge invariance in any extended Higgs models. These form factors F_{HWV} , G_{HWV} and H_{HWV} are respectively related to the coefficients f_{HWV} , g_{HWV} and h_{HWV} in the effective Lagrangian [31, 32];

$$\mathcal{L}_{\text{eff}} = gm_W f_{HWV} H^\pm W^\mp V^\mu + g_{HWV} H^\pm F_V^{\mu\nu} F_{W\mu\nu} + (ih_{HWV} \epsilon_{\mu\nu\rho\sigma} H^\pm F_V^{\mu\nu} F_W^{\rho\sigma} + \text{H.c.}), \quad (3.93)$$

where $F_V^{\mu\nu}$, and $F_W^{\mu\nu}$ are the field strengths. We note that f_{HWZ} is the coefficient of the dimension three operator, while the g_{HWV} and h_{HWV} are those of the dimension five operator, so that only f_{HWZ} may appear at the tree level. Therefore, the dominant contribution to the $H^\pm W^\mp V$ vertex is expected to be from F_{HWZ} .

In the Higgs model with only doublet scalar fields (plus singlets) all the form factors including F_{HWZ} vanish at the tree level [30], because of the custodial invariance in the kinetic term. The form factors F_{HWV} , G_{HWV} and H_{HWV} ($V = \gamma$ and Z) are generally induced at the loop level. In particular, the leading one-loop contribution to F_{HWZ} are proportional to the violation of the custodial symmetry in the sector of the particle in the loop. For example, in THDM, the custodial symmetry is largely broken via the t - b loop contribution as well as via the Higgs sector with the mass difference between the CP-odd Higgs boson (A^0) and the charged Higgs boson H^\pm [32]. The one-loop induced form factors are theoretically constrained from above by perturbative unitarity [89, 90]. In such a case, the effect of the custodial symmetry violation also can deviate the rho parameter from unity at the one loop level. However, when the lightest of CP-even neutral Higgs bosons is approximately regarded as the SM-like Higgs boson, the rho parameter can be unity even with a large mass splitting between A^0 and H^\pm when the masses of the heavier CP-even neutral Higgs boson H^0 and H^\pm are common [96]. This means that the appearance of the $H^\pm W^\mp Z$ vertex and the deviation from unity in the rho parameter

Model	SM with η ($Y = 0$)	SM with Δ ($Y = 1$)	the GM model
$ F_{HWZ} ^2 =$	$\frac{4v^2 v_\eta^2}{\cos^2 \theta_W (v^2 + 4v_\eta^2)^2}$	$\frac{2v^2 v_\Delta^2}{\cos^2 \theta_W (v^2 + 2v_\Delta^2)^2}$	$\frac{4v_\Delta^2}{\cos^2 \theta_W (v^2 + 4v_\Delta^2)}$
$\rho_{\text{tree}} =$	$1 + \frac{4v_\eta^2}{v^2}$	$\frac{1 + 2\frac{v_\Delta^2}{v^2}}{1 + 4\frac{v_\Delta^2}{v^2}}$	1

Table 3.11: The tree-level expression for F_{HWZ} and rho parameter at the tree level [147] in the model with a real triplet field, that with a complex triplet field and the Georgi-Machacek (GM) model [157].

are not necessarily correlated at the one-loop level, and they can be independent quantities, in principle.

The simplest models in which the $H^\pm W^\mp Z$ vertex appears at the tree level are those with triplet scalar fields. In the model with an isospin doublet field ($Y = 1/2$) and either an real triplet field η ($Y = 0$) or an additional complex triplet field Δ ($Y = 1$), concrete expressions for the tree-level formulae for $|F_{HWZ}|^2$ and that of ρ_{tree} are shown in TABLE 3.11, where v , v_η and v_Δ are respectively VEVs of the doublet scalar field and the additional triplet scalar field η and Δ . These triplet scalar fields also contribute to the rho parameter at the tree level, so that their VEVs are constrained by the current rho parameter data, $\rho_{\text{exp}} = 1.0008^{+0.0017}_{-0.0007}$; i.e., $v_\eta \lesssim 6$ GeV for the real triplet field η , and $v_\Delta \lesssim 8$ GeV for the complex triplet Δ (95 % CL). We note that in order to obtain the similar accuracy to the rho parameter data by measuring the $H^\pm W^\mp Z$ vertex, the vertex has to be measured with the detectability to $|F_{HWZ}|^2 \sim \mathcal{O}(10^{-3})$.

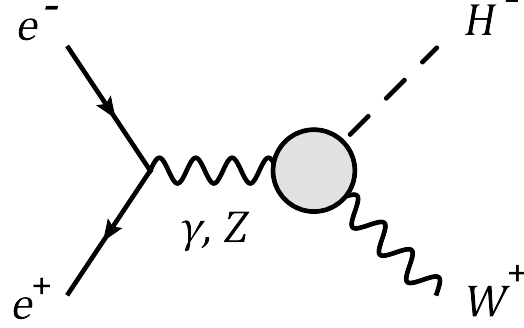
Finally, we mention about the model with a real triplet field η and a complex triplet field Δ in addition to the SM, which is proposed by Georgi-Machacek and Chanowiz-Golden [151, 157–159]. In this model, an alignment of the VEVs for η and Δ are introduced ($v_\eta = v_\Delta/\sqrt{2}$), by which the Higgs potential is invariant under the custodial $SU(2)$ symmetry at the tree level. Physical scalar states in this model can be classified using the transformation property against the custodial symmetry; i.e., the five-plet, the three-plet and the singlet. Only the charged Higgs boson from the five-plet state has the non-zero value of F_{HWZ} at the tree level. Its value is proportional to the VEV v_Δ for the triplet scalar fields. However, the value of v_Δ is not strongly constrained by the rho parameter data, because the tree level contribution to the rho parameter is zero due to the custodial symmetry: see TABLE 3.11. Consequently, the magnitude of $|F_{HWZ}|^2$ can be of order one.

3.3.2 The $e^+e^- \rightarrow H^\pm W^\mp$ process

The process $e^+e^- \rightarrow H^-W^+$ [152–154] is depicted in FIG. 3.29. This process is directly related to the $H^\pm W^\mp Z$ vertex. The helicity amplitudes are calculated by

$$\mathcal{M}(\tau, \lambda) = \sum_{V=Z, \gamma} igm_W C_V \frac{1}{s - m_V^2} j_\mu(\tau) C^{\mu\nu} \epsilon_\nu(\lambda), \quad (3.94)$$

where \sqrt{s} is the center-of-mass energy, $j_\mu(\tau)$ is the electron current, and $\epsilon_\nu(\lambda)$ is the polarization vector of the W^+ boson [152]. The helicities of the electron and the W^+ boson can be $\tau = \pm 1$

Figure 3.29: The $e^+e^- \rightarrow H^-W^+$ process [147].

and $\lambda = 0, \pm 1$, respectively. The coefficient C_V is given by

$$C_V = \begin{cases} eQ_e, & \text{for } V = \gamma, \\ \frac{g}{\cos \theta_W}(T_e^3 - \sin^2 \theta_W Q_e), & \text{for } V = Z, \end{cases} \quad (3.95)$$

with $Q_e = -1$, $T_e^3 = -1/2$ (0) for $\tau = -1$ (+1). The squared amplitude is evaluated as

$$\begin{aligned} |\mathcal{M}(\tau)|^2 &\equiv \sum_{\lambda=0,\pm} |\mathcal{M}(\tau, \lambda)|^2 \\ &= g^2 \left| C_\gamma \frac{F_{HW\gamma}}{s} + C_Z \frac{F_{HWZ}}{s - m_Z^2} \right|^2 \left[\frac{\sin^2 \theta}{4} (s + m_W^2 - m_{H^\pm}^2)^2 + sm_W^2 (\cos^2 \theta + 1) \right], \end{aligned} \quad (3.96)$$

where θ is the angle between the momentum of H^\pm and the beam axis, m_{H^\pm} is the mass of H^\pm and the form factors G_{HWV} and H_{HWV} are taken to be zero. The helicity specified cross sections are written in terms of the squared amplitude in Eq. (3.96),

$$\sigma(s; \tau) = \frac{1}{32\pi s} \beta \left(\frac{m_{H^\pm}^2}{s}, \frac{m_W^2}{s} \right) \int_{-1}^1 d\cos \theta |\mathcal{M}(\tau)|^2, \quad (3.97)$$

where $\sigma(s; +1) = \sigma(e_L^+ e_R^- \rightarrow H^- W^+)$ and $\sigma(s; -1) = \sigma(e_R^+ e_L^- \rightarrow H^- W^+)$, and

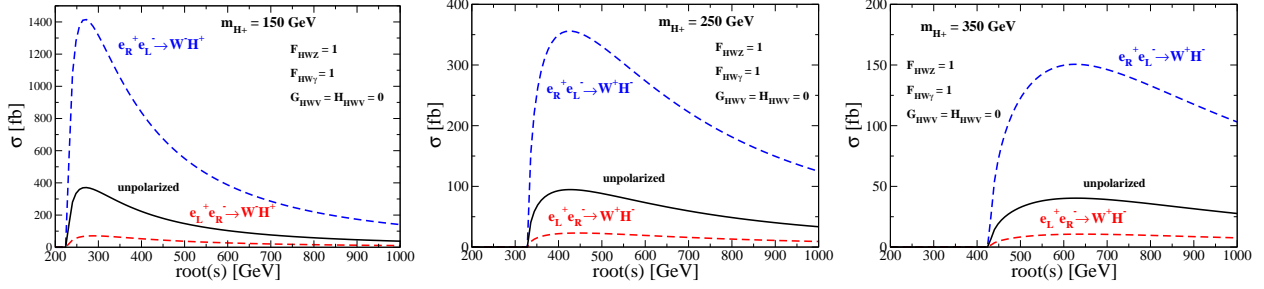
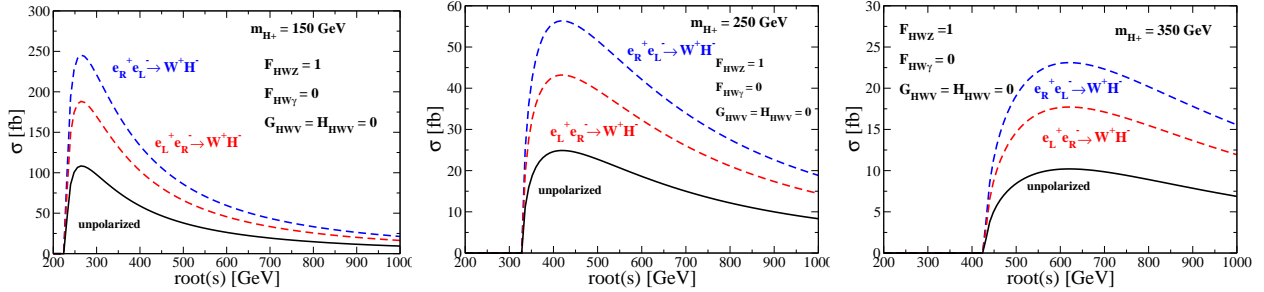
$$\beta(x, y) = \sqrt{1 + x^2 + y^2 - 2xy - 2x - 2y}. \quad (3.98)$$

The helicity averaged cross section is given by $\sigma(e^+e^- \rightarrow H^-W^+) = (\sigma(s, +1) + \sigma(s, -1))/4$.

In FIGs. 3.30 and 3.31, we show that the \sqrt{s} dependence of the helicity dependent and the helicity averaged cross sections. Notice that the behavior of these cross sections drastically changes depending on the initial electron helicity in the case of $F_{HWZ} \simeq F_{HW\gamma}$. On the contrary, there is no such a difference in the case of $F_{HWZ} \gg F_{HW\gamma}$. As mentioned before, $F_{HW\gamma}$ is zero at the tree level in any models because of the $U(1)_{\text{em}}$ gauge invariance. The relation of $F_{HWZ} \gg F_{HW\gamma}$ or $F_{HWZ} \simeq F_{HW\gamma}$ can be tested by using the initial electron helicities.

3.3.3 Recoil method and the assumption for the ILC performance

We investigate the possibility of measuring the $H^\pm W^\mp Z$ vertex by using a recoil method at the ILC. It has been known that this method is a useful tool for measuring the mass of the SM-like

Figure 3.30: The total cross section as a function of \sqrt{s} in the case of $F_{HWZ} = F_{HW\gamma} = 1$ [147].Figure 3.31: The total cross section as a function of \sqrt{s} in the case of $F_{HWZ} = 1, F_{HW\gamma} = 0$ [147].

Higgs boson H_{SM} without assuming the decay branching fraction of the Higgs boson [156]. In the Higgs-strahlung process $e^+e^- \rightarrow ZH_{\text{SM}}$ [155], the Higgs boson mass can be obtained as the recoil mass m_{recoil} from two leptons produced from the Z boson, whose energy is $E_{\ell\ell}$, and the invariant mass is $M_{\ell\ell}$. They satisfy the relation,

$$m_{\text{recoil}}^2(\ell\ell) = s - 2\sqrt{s}E_{\ell\ell} + M_{\ell\ell}^2. \quad (3.99)$$

The information of the Higgs boson mass can be extracted by measuring $E_{\ell\ell}$ and $m_{\ell\ell}$ in a model independent way.

In this section, we apply this method to $e^+e^- \rightarrow W^\pm H^\mp$ in order to measure the $H^\pm W^\mp Z$ vertex. In order to identify the process, we consider the hadronic decays $W \rightarrow jj$ instead of the leptonic decay of the produced W boson, and obtain information of the $H^\pm W^\mp Z$ vertex by using the recoil of the two-jet system. The recoiled mass of H^\pm is given in terms of the two-jet energy E_{jj} and the two-jet invariant mass M_{jj} as

$$m_{\text{recoil}}^2(jj) = s - 2\sqrt{s}E_{jj} + M_{jj}^2. \quad (3.100)$$

This process is shown in FIG. 3.32. It is clear that the detector performance for the resolution of two jets is crucial in such an analysis. In particular, the jets from the W boson in the signal process has to be precisely measured in order to be separated with those from the Z boson in the background process. At the ILC, the resolution for the two jet system with the energy E in the unit of GeV is expected to be $\sigma_E = 0.3\sqrt{E}$ GeV, by which the background from $Z \rightarrow jj$ can be considerably reduced. We here adopt the similar value for σ_E (~ 3 GeV) in our later analysis.

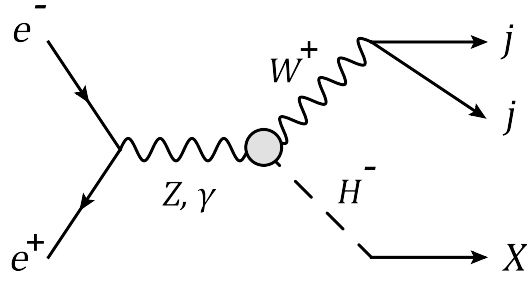


Figure 3.32: The signal process [147].

At the ILC, the polarized electron and positron beams can be used, by which the background from the W boson pair production process can be reduced. We here use the following beams polarized as

$$\frac{N_{e_R^-} - N_{e_L^-}}{N_{e_L^-} + N_{e_R^-}} = 0.8, \quad \frac{N_{e_L^+} - N_{e_R^+}}{N_{e_L^+} + N_{e_R^+}} = 0.5, \quad (3.101)$$

which are expected to be attained at the ILC [160], where $N_{e_{R,L}^-}$ and $N_{e_{R,L}^+}$ are numbers of right- (left-) handed electron and positron in the beam flux per unit time. The total cross sections for the signal and the backgrounds can be evaluated from the helicity specified cross sections as

$$\begin{aligned} \sigma_{\text{tot}}(e^+e^- \rightarrow X) = & x_-x_+\sigma(e_L^+e_R^- \rightarrow X) + (1-x_-)(1-x_+)\sigma(e_R^+e_L^- \rightarrow X) \\ & + x_-(1-x_+)\sigma(e_R^+e_R^- \rightarrow X) + x_+(1-x_-)\sigma(e_L^+e_L^- \rightarrow X), \end{aligned} \quad (3.102)$$

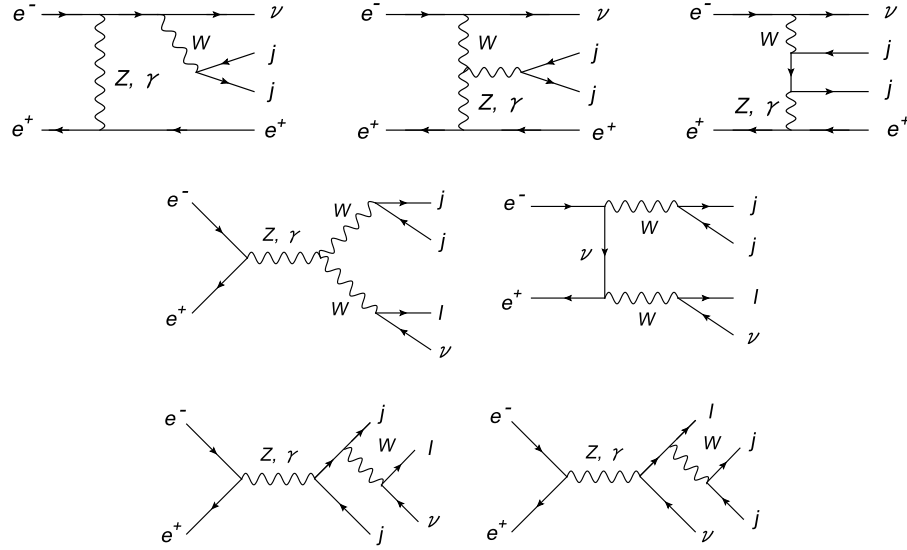
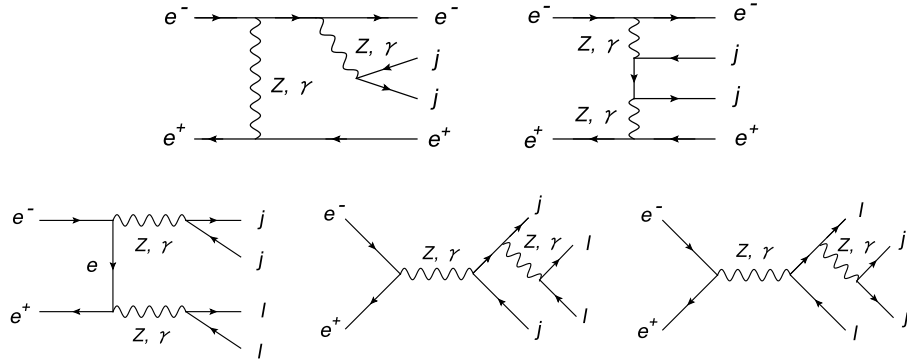
where $x_- = N_{e_R^-}/(N_{e_L^-} + N_{e_R^-})$ and $x_+ = N_{e_L^+}/(N_{e_L^+} + N_{e_R^+})$.

The high-energy electron and positron beams lose their incident energies by the ISR. In our analysis, we also take into account such effect, and see how the results without the ISR are changed by including the effect of the ISR.

3.3.4 Signal and Backgrounds

The size of the signal cross section is determined by the center of mass energy \sqrt{s} , the mass m_{H^\pm} and the form factors F_{HWZ} and $F_{HW\gamma}$. In the following analysis, we consider the case of $(F_{HWZ}, F_{HW\gamma}) \equiv (\xi, 0)$. This approximately corresponds to most of the cases we are interested, such as the triplet models. In order to examine the possibility of constraining $|\xi|^2$, we here assume that the mass of the charged Higgs boson is already known with some accuracy by measuring the other processes at the LHC or at the ILC. Then $|\xi|^2$ is the only free parameter in the production cross section.

In order to perform the signal and background analysis, we here assume that the decay of the produced charged Higgs boson is lepton specific; i.e., $H^\pm \rightarrow \ell\nu$ where ℓ is either e , μ or τ . The final state of the signal is then $e^+e^- \rightarrow H^\pm W^\mp \rightarrow \ell\nu jj$. We first consider $m_{H^\pm} < m_W + m_Z$ to avoid the complexness with the possible decay mode of $H^\pm \rightarrow W^\pm Z$, whose branching ratio strongly depends on the model. The main backgrounds come from the W boson pair production process $e^+e^- \rightarrow W^+W^-$ and the single W production processes in FIG. 3.33. For the $e^\pm\nu jj$

Figure 3.33: The $e^+e^- \rightarrow \ell \nu jj$ backgrounds [147].Figure 3.34: The $e^+e^- \rightarrow \ell \ell jj$ backgrounds [147].

final state, additional processes shown in FIG. 3.33 (upper figures) can also be a significant background. In addition, we take into account the processes with the final state of $\ell \ell jj$ shown in FIG. 3.34. They can be backgrounds if one of the outgoing leptons escapes from the detection at the detector. We here assume that the efficiency for lepton identification is 90 %.

We impose the basic cuts for all events such as

$$10^\circ < A_j < 170^\circ, \quad 5^\circ < A_{jj} < 175^\circ, \quad 10 \text{ GeV} < E_{jj}, \quad (3.103)$$

where A_j is the angle between a jet and the beam axis, A_{jj} is the angle between the two jets and E_{jj} is the energy of the two jets. In the numerical evaluation, we use CalcHEP [130].

After the basic cuts, the event numbers of both the signal and the backgrounds are listed in TABLE 6.5 for the case without ISR, and in TABLE 6.6 for that with ISR, where the center of mass energy is set $\sqrt{s} = 300 \text{ GeV}$, the mass of the charged Higgs boson m_{H^\pm} is 150 GeV, and the parameter $|\xi|^2$ for the $H^\pm W^\mp Z$ vertex is set to be 10^{-3} . For both the cases signal over

background ratios are less than 10^{-4} before imposing the other kinematic cuts than the basic cuts in Eq. (3.103). In the following we first discuss the case without the ISR, then present the results for that with the ISR.

In order to improve the signal over background ratio, we impose additional kinematic cuts. The two jets come from the W boson for the signal, so that the invariant mass cut is useful to reduce the backgrounds where a parent of the two jets is not the W boson. We here impose the condition;

$$m_W - n\sigma_E < M_{jj} < m_W + n\sigma_E, \quad (3.104)$$

where σ_E represents the resolution of the detector which we assume 3 GeV, and n is taken to be 2 here.

In FIG. 3.35, the differential cross sections of the signal and the backgrounds are shown for the events after the M_{jj} cut in Eq. (3.104) as a function of the transverse momentum p_T^{jj} , the energy of the jj system, the angle θ_{lep} of a charged lepton with the beam axis, and the invariant mass $M_{\ell\nu}$ of the charged lepton and the missing momentum in the final state. For the signal, the results are shown for $|\xi|^2 = 1$ with the mass of the charged Higgs boson to be 110, 130, 150 and 170 GeV. The E_{jj} distribution shown in FIG. 3.35 (upper-right) can be translated into the distribution as a function of m_{recoil} by using the relation in Eq. (3.100), which is shown in FIG. 3.36. The signal events form the peak at $m_{\text{recoil}} \sim m_{H^\pm}$.

In the following, we discuss the case with $m_{H^\pm} = 150$ GeV¹². According to FIG. 3.35, we impose the following four kinematic cuts sequentially:

$$75 \text{ GeV} < p_T^{jj} < 100 \text{ GeV}, \quad (3.105)$$

and

$$115 \text{ GeV} < E_{jj} < 125 \text{ GeV} \quad (3.106)$$

for the jj system in the final state. In TABLE 6.5, the resulting values for the cross sections for the signal and backgrounds are shown in each step of the cuts. The backgrounds can be reduced in a considerable extent. For $|\xi|^2 = 10^{-3}$, the signal significance reaches to $\mathcal{O}(1)$ assuming the integrated luminosity of 1 ab^{-1} .

Until now, we have imposed the cuts on the jj system, and no information from the $\ell\nu$ system has been used. Here, in order to further improve the signal significance, we impose new cuts related to the $\ell\nu$ system in order, which are determined from FIG. 3.35;

$$|\cos \theta_{\text{lep}}| < 0.75, \quad (3.107)$$

and

$$144 \text{ GeV} < M_{\ell\nu} < 156 \text{ GeV}. \quad (3.108)$$

As shown in TABLE 6.5, for $|\xi|^2 = 10^{-3}$ the signal significance after these cuts can reach to $S/\sqrt{B} \simeq 2.5$ and the signal over background ratio can be $S/B \sim 10 \%$, assuming the integrated luminosity of 1 ab^{-1} .

¹² Notice that the additional cuts given in Eqs. (3.105)-(3.108) are optimized for the case with $m_{H^\pm} = 150$ GeV. From FIG. 3.35, we can find and impose such additional cuts optimized for each value of m_{H^\pm} .

Next let us see how this results can be changed by including the ISR. The beam parameters at $\sqrt{s} = 500$ GeV are given in Ref. [160], such as the bunch $x + y$ size, the bunch length and the number of particles per a bunch. We here use the default values defined in CalcHEP [130]; i.e., the bunch $x + y$ size = 560 nm, bunch length = 400 μm , and the number of particles/bunch = 2×10^{10} at $\sqrt{s} = 300$ GeV¹³.

In FIG. 3.37, the similar distributions to those in FIG. 3.35 but with the ISR are given for the signal and the backgrounds after the invariant mass M_{jj} cut in Eq. (3.104). The biggest change can be seen in the E_{jj} distribution. The background events originally located at the point just below 150 GeV in the case without the ISR, which corresponds to the W boson mass, tend to move in the lower E_{jj} regions, so that the signal over background ratio becomes worse. The recoil mass distribution is shown in FIG. 3.38.

Consequently, the signal significance after all the cuts is smeared from 2.5 to 2.0, while the signal over background ratio is changed from 8.7×10^{-2} to 7.5×10^{-2} . Cross sections of the signal and the backgrounds with the ISR are listed in TABLE 6.6 with the values of S/\sqrt{B} and S/B for each stage of kinematic cuts. We stress that even taking the ISR into account, the $H^\pm W^\mp Z$ vertex with $|\xi|^2 > 10^{-3}$ can be excluded with 95% CL.

¹³ We have confirmed that the results are almost unchanged even when we use the values given in Ref. [160].

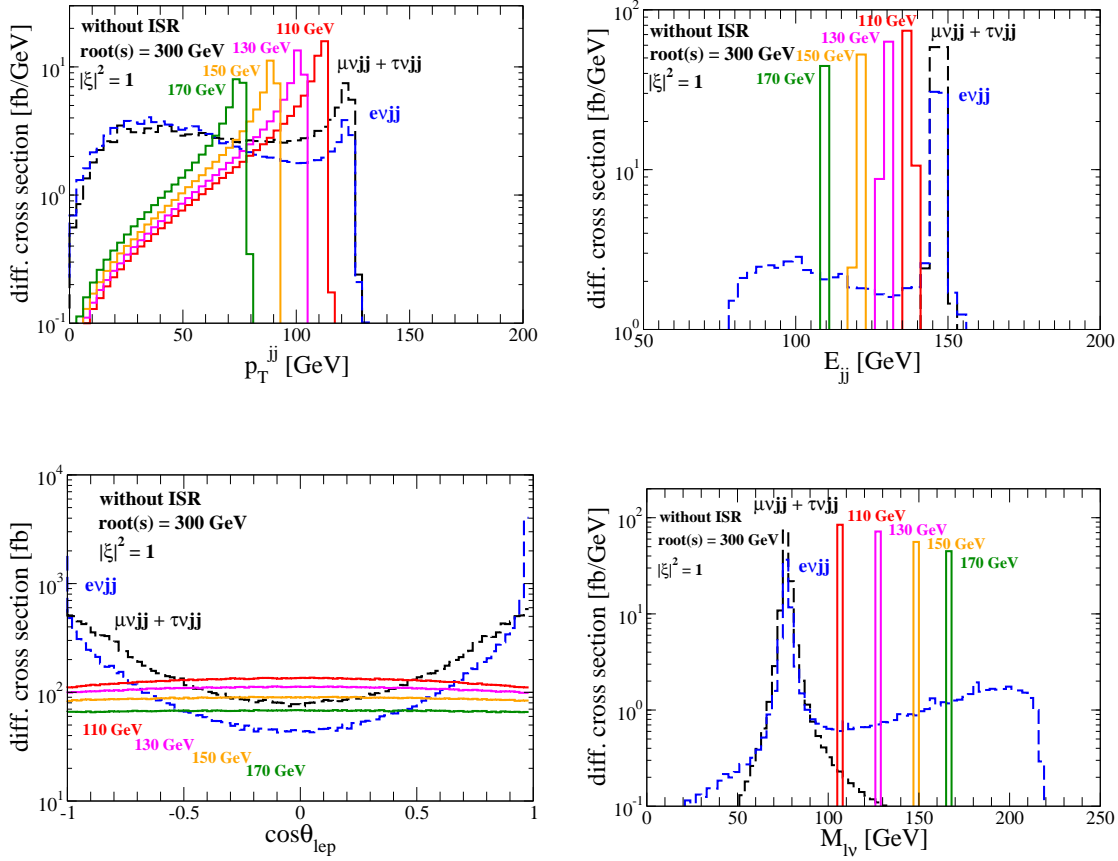


Figure 3.35: Distributions of the signal for $m_{H^\pm} = 110, 130, 150$ and 170 GeV as well as the backgrounds after the invariant mass M_{jj} cut in Eq. (3.104) without the ISR as a function of the transverse momentum p_T^{jj} (upper left), the energy of the jj system (upper right), the angle θ_{lep} of a charged lepton with the beam axis (lower left), and the invariant mass $M_{\ell\nu}$ of the charged lepton and the missing momentum in the final state (lower right). $|\xi|^2$ is taken to be 1 [147].

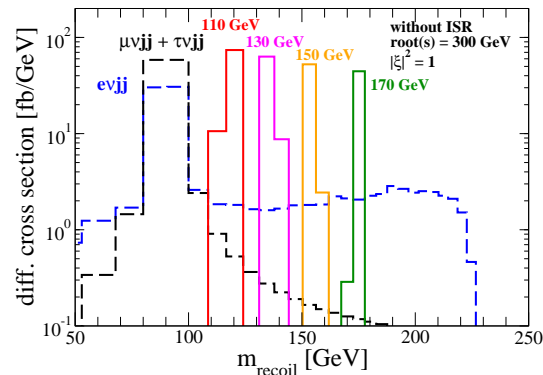


Figure 3.36: Distributions of the signal for $m_{H^\pm} = 110, 130, 150$ and 170 GeV as well as the backgrounds after the cut in Eq. (3.104) without the ISR as a function of the recoil mass m_{recoil} [147].

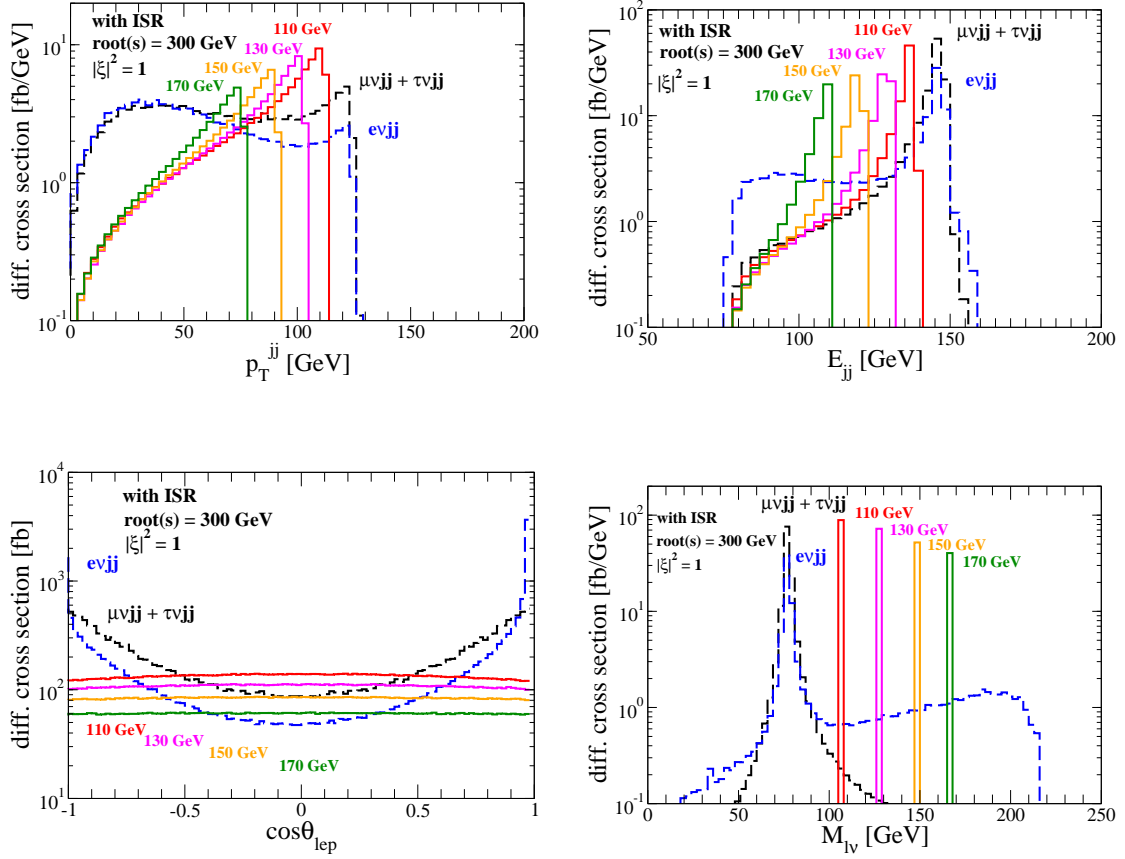


Figure 3.37: Distributions of the signal for $m_{H^\pm} = 110, 130, 150$ and 170 GeV as well as the backgrounds after the invariant mass M_{jj} cut in Eq. (3.104) with the ISR as a function of the transverse momentum p_T^{jj} (upper left), the energy of the jj system (upper right), the angle θ_{lep} of a charged lepton with the beam axis (lower left), and the invariant mass $M_{\ell\nu}$ of the charged lepton and the missing momentum in the final state (lower right). $|\xi|^2$ is taken to be 1 [147].

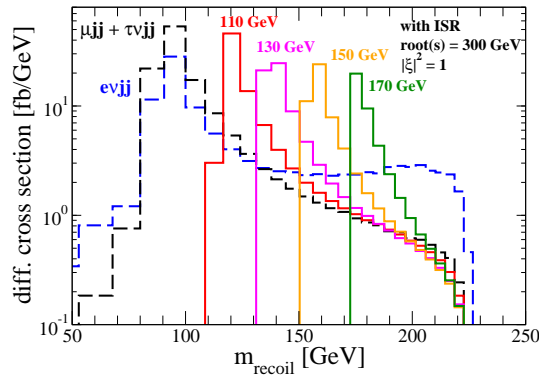


Figure 3.38: Distributions of the signal for $m_{H^\pm} = 110, 130, 150$ and 170 GeV as well as the backgrounds after the cut in Eq. (3.104) with the ISR as a function of the recoil mass m_{recoil} [147].

	Basic	M_{jj}	p_T^{jj}	E_{jj}	$\cos \theta_{\text{lep}}$	$M_{\ell\nu}$
$e_R^+ e_L^- \rightarrow \ell^\pm \nu jj$	7.2×10^{-3}	6.4×10^{-3}	4.4×10^{-3}	4.4×10^{-3}	3.3×10^{-3}	3.3×10^{-3}
$e_L^+ e_R^- \rightarrow \ell^\pm \nu jj$	1.4×10^{-1}	1.3×10^{-1}	8.5×10^{-2}	8.5×10^{-2}	6.7×10^{-2}	6.7×10^{-2}
Total signal	1.5×10^{-1}	1.4×10^{-1}	8.9×10^{-2}	8.9×10^{-2}	7.0×10^{-2}	7.0×10^{-2}
$e_R^+ e_L^- \rightarrow \mu^\pm \nu jj + \tau^\pm \nu jj$	340	300	53	2.9×10^{-1}	2.2×10^{-1}	1.3×10^{-1}
$e_L^+ e_R^- \rightarrow \mu^\pm \nu jj + \tau^\pm \nu jj$	80	71	13	2.8×10^{-1}	2.1×10^{-1}	1.1×10^{-1}
$e_R^+ e_L^- \rightarrow e^\pm \nu jj$	220	190	31	1.6	6.4×10^{-1}	3.4×10^{-1}
$e_L^+ e_R^- \rightarrow e^\pm \nu jj$	40	36	6.4	1.4×10^{-1}	1.1×10^{-1}	5.7×10^{-2}
$e_R^+ e_R^- \rightarrow e_R^- \bar{\nu} jj$	100	92	11	3.8	2.2×10^{-1}	1.2×10^{-1}
$e_L^+ e_L^- \rightarrow e_L^- \bar{\nu} jj$	40	31	4.3	1.3	7.2×10^{-2}	4.1×10^{-2}
Total $\ell \nu jj$ background	820	720	120	7.4	1.5	8.0×10^{-1}
$e_R^+ e_L^- \rightarrow \mu^+ \mu^- jj + \tau^+ \tau^- jj$	1.2	3.7×10^{-2}	5.5×10^{-3}	1.1×10^{-4}	9.4×10^{-5}	5.0×10^{-5}
$e_L^+ e_R^- \rightarrow \mu^+ \mu^- jj + \tau^+ \tau^- jj$	19	1.0	1.4×10^{-1}	3.0×10^{-3}	2.5×10^{-3}	1.4×10^{-3}
$e_R^+ e_L^- \rightarrow e^+ e^- jj$	8.4	9.0×10^{-2}	4.6×10^{-3}	5.8×10^{-4}	2.6×10^{-4}	1.3×10^{-4}
$e_L^+ e_R^- \rightarrow e^+ e^- jj$	220	2.4	1.2×10^{-1}	1.5×10^{-2}	6.7×10^{-3}	3.4×10^{-3}
$e_R^+ e_R^- \rightarrow e^+ e^- jj$	59	7.2×10^{-1}	2.4×10^{-2}	4.5×10^{-3}	2.0×10^{-3}	1.0×10^{-3}
$e_L^+ e_L^- \rightarrow e^+ e^- jj$	19	1.0	8.0×10^{-3}	1.4×10^{-3}	6.7×10^{-4}	3.7×10^{-4}
Total $\ell \ell jj$ background	330	5.2	3.0×10^{-1}	2.5×10^{-2}	1.2×10^{-2}	6.4×10^{-3}
S/\sqrt{B} (assuming 1 ab^{-1})	1.4×10^{-1}	1.6×10^{-1}	2.6×10^{-1}	1.0	1.8	2.5
S/B (assuming 1 ab^{-1})	1.3×10^{-4}	1.9×10^{-4}	7.4×10^{-4}	1.2×10^{-2}	4.6×10^{-2}	8.7×10^{-2}

Table 3.12: The results without ISR. The cross sections of both the signal and the backgrounds are shown for $\sqrt{s} = 300 \text{ GeV}$ in the unit of fb. For the signal, m_{H^\pm} is 150 GeV and $|\xi|^2$ is taken to be 10^{-3} . For the $\ell \ell jj$ processes, the misidentity rate of one of the leptons is assumed to be 0.1. The signal significance S/\sqrt{B} and the ratio S/B are evaluated for the integrated luminosity to be 1 ab^{-1} [147].

	Basic	M_{jj}	p_T^{jj}	E_{jj}	$\cos \theta_{\text{lep}}$	$M_{\ell\nu}$
$e_R^+ e_L^- \rightarrow \ell^\pm \nu jj$	6.8×10^{-3}	6.0×10^{-3}	3.3×10^{-3}	3.1×10^{-3}	2.4×10^{-3}	2.4×10^{-3}
$e_L^+ e_R^- \rightarrow \ell^\pm \nu jj$	1.3×10^{-1}	1.2×10^{-1}	6.6×10^{-2}	6.3×10^{-2}	5.0×10^{-2}	4.9×10^{-2}
Total signal	1.4×10^{-1}	1.3×10^{-1}	6.9×10^{-2}	6.6×10^{-2}	5.2×10^{-2}	5.1×10^{-2}
$e_R^+ e_L^- \rightarrow \mu^\pm \nu jj + \tau^\pm \nu jj$	350	310	55	2.9	2.2	1.1×10^{-1}
$e_L^+ e_R^- \rightarrow \mu^\pm \nu jj + \tau^\pm \nu jj$	84	76	17	1.8	1.4	9.7×10^{-2}
$e_R^+ e_L^- \rightarrow e^\pm \nu jj$	210	190	32	2.8	1.6	2.8×10^{-1}
$e_L^+ e_R^- \rightarrow e^\pm \nu jj$	42	38	8.5	9.0×10^{-1}	7.0×10^{-1}	4.9×10^{-2}
$e_R^+ e_R^- \rightarrow e_R^- \bar{\nu} jj$	92	81	10	3.2	2.2×10^{-1}	1.0×10^{-1}
$e_L^+ e_L^- \rightarrow e_L^+ \nu jj$	32	29	3.7	1.1	7.8×10^{-2}	3.4×10^{-2}
Total $\ell \nu jj$ background	810	720	130	13	6.2	6.7×10^{-1}
$e_R^+ e_L^- \rightarrow \mu^+ \mu^- jj + \tau^+ \tau^- jj$	1.2	4.2×10^{-2}	5.9×10^{-3}	3.7×10^{-4}	3.1×10^{-4}	4.6×10^{-5}
$e_L^+ e_R^- \rightarrow \mu^+ \mu^- jj + \tau^+ \tau^- jj$	22	1.2	1.5×10^{-1}	9.9×10^{-3}	8.3×10^{-3}	1.2×10^{-3}
$e_R^+ e_L^- \rightarrow e^+ e^- jj$	9.6	9.2×10^{-2}	4.1×10^{-3}	6.3×10^{-4}	3.2×10^{-4}	1.0×10^{-4}
$e_L^+ e_R^- \rightarrow e^+ e^- jj$	230	2.4	1.0×10^{-1}	1.7×10^{-2}	9.2×10^{-3}	2.9×10^{-3}
$e_R^+ e_R^- \rightarrow e^+ e^- jj$	70	6.4×10^{-1}	2.3×10^{-2}	4.2×10^{-3}	2.1×10^{-3}	9.1×10^{-4}
$e_L^+ e_L^- \rightarrow e^+ e^- jj$	24	2.2×10^{-1}	7.4×10^{-3}	1.4×10^{-3}	6.3×10^{-4}	3.1×10^{-4}
Total $\ell \ell jj$ background	360	4.6	2.9×10^{-1}	3.4×10^{-2}	2.1×10^{-2}	5.5×10^{-3}
S/\sqrt{B} (assuming 1 ab^{-1})	1.3×10^{-1}	1.5×10^{-1}	1.9×10^{-1}	5.8×10^{-1}	6.6×10^{-1}	2.0
S/B (assuming 1 ab^{-1})	1.2×10^{-4}	1.8×10^{-4}	5.3×10^{-4}	5.1×10^{-3}	8.4×10^{-3}	7.5×10^{-2}

Table 3.13: The results with the ISR. The cross sections of both the signal and the backgrounds are shown for $\sqrt{s} = 300 \text{ GeV}$ in the unit of fb. For the signal, m_{H^\pm} is 150 GeV and $|\xi|^2$ is taken to be 10^{-3} . For the $\ell \ell jj$ processes, the misidentity rate of one of the leptons is assumed to be 0.1. The signal significance S/\sqrt{B} and the ratio S/B are evaluated for the integrated luminosity to be 1 ab^{-1} [147].

Chapter 4

Decoupling property of SUSY Higgs sectors

In this chapter, we focus on SUSY Higgs sectors. Supersymmetry is expected to be a good candidate of new physics. It can solve the hierarchy problem by the consequence of the non-renormalization theorem [161]. The stabilized Higgs boson mass makes it possible to directly connect the electroweak scale with very high scales such as the Planck scale or that of grand unification. SUSY extensions of the SM with the R parity also provide dark matter candidates [162]. In addition, various mechanisms of generating tiny neutrino masses [15–21, 163, 164] as well as those of baryogenesis [24, 165, 166] may also be compatible to SUSY models.

The MSSM is a SUSY extension of the SM with the minimal number of particle content. In the MSSM, two Higgs doublets are introduced because of the anomaly cancellation. The most striking phenomenological prediction of the model is that on the mass (m_h) of the lightest CP-even Higgs boson h . It can be calculated to be less than the mass of the Z boson at the tree level. Such an upper bound on m_h comes from the fact that the interaction terms in the Higgs potential are given only by D-term contributions which are determined by the gauge coupling constants. At the one-loop level the trilinear top-Yukawa term in the superpotential gives a significant F-term contribution to m_h [64–66], by which m_h can be above the lower bound from the direct search results at the CERN LEP experiment [94]. The calculation has been improved with higher order corrections [167–169]. Apart from m_h , the masses of H , H^\pm and the mixing angle α are a function of only two input parameters at the tree level; i.e., m_A and $\tan\beta$, where m_A is the mass of CP-odd Higgs boson A , H is the heavier CP-even Higgs boson, H^\pm are the charged Higgs bosons, $\tan\beta$ is the ratio of VEVs of the two Higgs bosons and α is the angle which diagonalizes the CP-even scalar states. In particular, there is a simple tree-level relationship among the masses of H^\pm , A and the W boson W^\pm as $m_{H^\pm}^2 = m_A^2 + m_W^2$, where m_{H^\pm} and m_W are respectively the masses of H^\pm and W^\pm . These characteristic predictions can be used to confirm the MSSM.

However, these characteristic features which are seen in the MSSM Higgs sector can be changed when we consider extended SUSY standard models which are motivated to solve various physics problem. For example, the model with a neutral gauge singlet field to the MSSM, which is known as the next-to-MSSM (NMSSM) [170–172], solves the μ problem [173]. Models with additional charged singlet fields can be used for radiative neutrino mass generation [17, 18]. Those with additional doublet fields may be required for dark doublet models [22], and the model with triplets may be motivated for the SUSY left-right model [132] or those with so-

	Spin 0	Spin 1/2	$SU(3)_c$	$SU(2)_L$	$U(1)_Y$
\hat{Q}_i	\tilde{Q}_{Li}	Q_{Li}	3	2	$+\frac{1}{6}$
\hat{U}_i^c	\tilde{u}_{Ri}^*	u_{Ri}^c	$\bar{\mathbf{3}}$	1	$-\frac{2}{3}$
\hat{D}_i^c	\tilde{d}_{Ri}^*	d_{Ri}^c	$\bar{\mathbf{3}}$	1	$+\frac{1}{3}$
\hat{L}_i	\tilde{L}_{Li}	L_{Li}	1	2	$-\frac{1}{2}$
\hat{E}_i^c	\tilde{e}_{Ri}^*	e_{Ri}^c	1	1	$+1$
\hat{H}_d	H_d	\tilde{H}_d	1	2	$-\frac{1}{2}$
\hat{H}_u	H_u	\tilde{H}_u	1	2	$+\frac{1}{2}$

Table 4.1: Charge assignment for the chiral superfield in the MSSM under the $SU(3)_c \times SU(2)_L \times U(1)$ gauge symmetry.

	Spin 1/2	Spin 1	$SU(3)_c$	$SU(2)_L$	$U(1)_Y$
\hat{G}	\tilde{G}	G_μ	8	1	0
\hat{W}	\tilde{W}	W_μ	1	3	0
\hat{B}	\tilde{B}	B_μ	1	1	0

Table 4.2: Charge assignment for the vector superfield in the MSSM under the $SU(3)_c \times SU(2)_L \times U(1)$ gauge symmetry.

called the type-II seesaw mechanism [15, 174].

These extended SUSY Higgs sectors with additional chiral superfields can be classified to the two groups: i.e., 1.) models with additional F-term contributions to the interaction terms in the Higgs potential such as the NMSSM, a model with triplet superfields added to the MSSM and so on, 2.) those without such F-term contributions, e.g., the model with four Higgs doublet superfields (4HDM). In the models classified to 1.), additional F-term contributions to the mass of the lightest CP-even Higgs boson m_h and the triple h coupling hhh can be significant even when h looks the SM Higgs boson. In the models classified to 2.), even without F-term contributions in the Higgs potential, large deviations can be seen in the MSSM observables due to the mixing among the MSSM-like Higgs bosons and the extra Higgs bosons at the tree level.

In this chapter, we first discuss the MSSM Higgs sector. Next, we discuss models with additional F-term contributions to interaction terms in the Higgs potential. Finally, we discuss the 4HDM as a simplest example for a model without such F-term contributions.

4.1 The Higgs sector of the Minimal Supersymmetric Standard Model

The charge assignment for the chiral superfields which are denoted as the symbol with the hat in the MSSM are listed in Table 4.1. In the MSSM, two Higgs doublets are introduced because of the anomaly cancellation. In addition, there is another reason to introduce the two Higgs doublets. We cannot use the hermitian conjugate of chiral superfields in the superpotential, so

that the Higgs doublet with $Y = 1/2$ and that with $Y = -1/2$ are necessary to give masses for the up-type quarks (and also the charged leptons) and the up-type quarks, respectively.

The superpotential of the MSSM is given as

$$W_{\text{MSSM}} = -(Y_u)^{ij} \hat{U}_i^c (\hat{H}_u \cdot \hat{Q}_j) + (Y_d)^{ij} \hat{D}_i^c (\hat{H}_d \cdot \hat{Q}_j) + (Y_e)^{ij} \hat{E}_i^c (\hat{H}_d \cdot \hat{L}_j) + \mu (\hat{H}_u \cdot \hat{H}_d). \quad (4.1)$$

The soft-SUSY breaking terms are

$$\begin{aligned} \mathcal{L}_{\text{MSSM}}^{\text{soft}} = & -\frac{1}{2}(M_1 \tilde{B}\tilde{B} + M_2 \tilde{W}\tilde{W} + M_3 \tilde{G}\tilde{G}) \\ & - \left[(M_{\tilde{Q}}^2)_{ij} \tilde{Q}_{Li}^\dagger \tilde{Q}_{Lj} + (M_{\tilde{u}}^2)_{ij} \tilde{u}_{Ri}^* \tilde{u}_{Rj} + (M_{\tilde{d}}^2)_{ij} \tilde{d}_{Ri}^* \tilde{d}_{Rj} + (M_{\tilde{L}}^2)_{ij} \tilde{L}_{Li}^\dagger \tilde{L}_{Lj} + (M_{\tilde{e}}^2)_{ij} \tilde{e}_{Ri}^* \tilde{e}_{Rj} \right. \\ & \quad \left. + (M_-^2) H_d^\dagger H_d + (M_+^2) H_u^\dagger H_u \right] - (B\mu H_d \cdot H_u + \text{h.c.}) \\ & - \left[(Y_u)_{ij} (A_u)_{ij} \tilde{u}_{Ri}^* H_u \cdot \tilde{Q}_{Lj} + (Y_d)_{ij} (A_d)_{ij} \tilde{d}_{Ri}^* H_d \cdot \tilde{Q}_{Lj} + (Y_e)_{ij} (A_e)_{ij} \tilde{e}_{Ri}^* H_d \cdot \tilde{L}_{Lj} + \text{h.c.} \right], \end{aligned} \quad (4.2)$$

In SUSY models, the Higgs potential can be calculated as

$$V_H = |D|^2 + |F|^2 - \mathcal{L}_{\text{soft}}, \quad (4.3)$$

where $\mathcal{L}_{\text{soft}}$ is the soft SUSY breaking Lagrangian, $|D|^2$ is the D-term, and $|F|^2$ is the F-term. The D-term and the F-term are expressed by the given superpotential W as

$$|D|^2 = \frac{1}{2}(g_a)^2 (\varphi_i^* T_{ij}^a \varphi_j)^2, \quad |F|^2 = \left| \frac{\partial W}{\partial \varphi_i} \right|^2, \quad (4.4)$$

where φ_j represent scalar component fields of chiral superfields in the model. In the MSSM, the Higgs potential can be written as

$$\begin{aligned} V_{\text{MSSM}} = & m_1^2 H_d^\dagger H_d + m_2^2 H_u^\dagger H_u + (B\mu H_d \cdot H_u + \text{h.c.}) \\ & + \frac{g^2}{8} (H_d^\dagger \tau^a H_d + H_u^\dagger \tau^a H_u)^2 + \frac{g'^2}{8} (H_d^\dagger H_d - H_u^\dagger H_u)^2 \\ = & m_1^2 H_d^\dagger H_d + m_2^2 H_u^\dagger H_u + (B\mu H_d \cdot H_u + \text{h.c.}) \\ & + \frac{g^2 + g'^2}{8} (H_d^\dagger H_d - H_u^\dagger H_u)^2 - \frac{g^2}{2} (H_d^\dagger H_u) (H_u^\dagger H_d), \end{aligned} \quad (4.5)$$

where m_1^2 and m_2^2 are $|\mu|^2 + (M_-^2)$ and $|\mu|^2 + (M_+^2)$, respectively. The Higgs doublets H_d and H_u can be parameterized as

$$H_d = \begin{bmatrix} \frac{1}{\sqrt{2}}(h_d + v_d - iz_d) \\ -w_d^- \end{bmatrix}, \quad H_u = \begin{bmatrix} w_u^+ \\ \frac{1}{\sqrt{2}}(h_u + v_u + iz_u) \end{bmatrix}, \quad (4.6)$$

where $v_d = v \cos \beta$ and $v_u = v \sin \beta$ are the VEV of the Higgs doublet with $v_d^2 + v_u^2 = v^2 \simeq (246 \text{ GeV})^2$. By the vacuum condition m_1 and m_2 can be eliminated as:

$$\left. \frac{\partial V_{\text{MSSM}}}{\partial h_d} \right|_0 = m_1^2 \cos \beta + \frac{1}{2} m_2^2 \cos \beta \cos 2\beta + B\mu \sin \beta = 0, \quad (4.7a)$$

$$\left. \frac{\partial V_{\text{MSSM}}}{\partial h_u} \right|_0 = m_2^2 \sin \beta - \frac{1}{2} m_2^2 \sin \beta \cos 2\beta + B\mu \cos \beta = 0. \quad (4.7b)$$

The two-point terms in the Higgs potential can be calculated as

$$\begin{aligned}
V_{\text{MSSM}}^{\text{mass}} = & (w_d^+, w_u^+) \begin{pmatrix} m_W^2 \sin^2 \beta - B\mu \tan \beta & B\mu - \frac{m_W^2}{2} \sin 2\beta \\ B\mu - \frac{m_W^2}{2} \sin 2\beta & m_W^2 \cos^2 \beta - B\mu \cot \beta \end{pmatrix} \begin{pmatrix} w_d^- \\ w_u^- \end{pmatrix} \\
& + \frac{1}{2} (z_1, z_2) \begin{pmatrix} -B\mu \tan \beta & B\mu \\ B\mu & -B\mu \cot \beta \end{pmatrix} \begin{pmatrix} z_d \\ z_u \end{pmatrix} \\
& + \frac{1}{2} (h_d, h_u) \begin{pmatrix} m_Z^2 \cos^2 \beta - B\mu \tan \beta & B\mu - \frac{m_Z^2}{2} \sin 2\beta \\ B\mu - \frac{m_Z^2}{2} \sin 2\beta & m_Z^2 \sin^2 \beta - B\mu \cot \beta \end{pmatrix} \begin{pmatrix} h_d \\ h_u \end{pmatrix}. \quad (4.8)
\end{aligned}$$

The mass eigenstates are obtained by the mixing angles β and α :

$$\begin{aligned}
\begin{pmatrix} z_d \\ z_u \end{pmatrix} &= \begin{pmatrix} \cos \beta & -\sin \beta \\ \sin \beta & \cos \beta \end{pmatrix} \begin{pmatrix} z \\ A \end{pmatrix}, \quad \begin{pmatrix} w_d^\pm \\ w_u^\pm \end{pmatrix} = \begin{pmatrix} \cos \beta & -\sin \beta \\ \sin \beta & \cos \beta \end{pmatrix} \begin{pmatrix} w^\pm \\ H^\pm \end{pmatrix}, \\
\begin{pmatrix} h_d \\ h_u \end{pmatrix} &= \begin{pmatrix} \cos \alpha & -\sin \alpha \\ \sin \alpha & \cos \alpha \end{pmatrix} \begin{pmatrix} H \\ h \end{pmatrix}, \quad (4.9)
\end{aligned}$$

where w^\pm and z are the NG bosons which are absorbed by the longitudinal components of W^\pm and Z . All the other mass eigenstates are the physical scalar bosons, those are the pair of the singly-charged scalar bosons H^\pm , neutral CP-even scalar bosons H and h and a neutral CP-odd scalar boson A . Originally, the number of the parameter is five in the Higgs potential (v_u, v_d, m_1, m_2 and $B\mu$) at the tree level. Three of the five parameters are determined by v and the vacuum conditions Eq. (4.7). Thus, remaining parameters are $\tan \beta$ and $B\mu$. The $B\mu$ parameter can be rewritten as the mass of A :

$$m_A^2 = -\frac{B\mu}{\sin \beta \cos \beta}. \quad (4.10)$$

The masses of the other physical scalar bosons are expressed in terms of β and m_A :

$$m_{H^\pm}^2 = m_W^2 + m_A^2, \quad (4.11)$$

$$m_{h,H}^2 = \frac{1}{2} \left[m_A^2 + m_Z^2 \mp \sqrt{(m_A^2 + m_Z^2)^2 - 4m_Z^2 m_A^2 \cos^2 2\beta} \right], \quad (4.12)$$

and the mixing angle α is

$$\tan 2\alpha = \tan 2\beta \frac{m_A^2 + m_Z^2}{m_A^2 - m_Z^2}. \quad (4.13)$$

From Eq. (4.12), the mass of the lightest Higgs boson h can be expressed in the large m_A limit:

$$m_h \xrightarrow{m_A \gg m_Z} m_Z \cos 2\beta \leq m_Z. \quad (4.14)$$

Thus, at the tree level, m_h cannot exceed the LEP bound. This upper limit for m_h can be changed by considering the one-loop correction. In this section, we take into account the effects of the one-loop level correction by the effective potential method. The effective potential is given as

$$V^{\text{eff}} = -\frac{\mu_0^2}{2} \varphi^2 + \frac{\lambda_0}{4} \varphi^4 + \sum_f \frac{(-1)^{s_f} N_c^f N_s^f}{64\pi^2} m_f^4(\varphi) \left[\ln \frac{m_f^2(\varphi)}{Q^2} - \frac{3}{2} \right], \quad (4.15)$$

where μ_0^2 and λ_0 are the bare squared mass and the coupling constant, $\varphi = v + \langle h \rangle$, N_c^f is the color number, s_f (N_s^f) is the spin (degree of freedom) of the field f in the loop, $m_f(\varphi)$ is the field dependent mass of f , and Q is an arbitrary scale. When the extra Higgs scalars are heavy enough, only the lightest Higgs boson h stays at the EW scale, and behaves as the SM-like one. The effective potential in Eq. (4.15) can then be applied with a good approximation. The vacuum, the mass m_h and the hhh coupling constant λ_{hhh} are determined at the one-loop order by the conditions;

$$\left. \frac{\partial V^{\text{eff}}}{\partial \varphi} \right|_{\varphi=v} = 0, \quad \left. \frac{\partial^2 V^{\text{eff}}}{\partial \varphi^2} \right|_{\varphi=v} = m_h^2, \quad \left. \frac{\partial^3 V^{\text{eff}}}{\partial \varphi^3} \right|_{\varphi=v} = \lambda_{hhh}. \quad (4.16)$$

Here we consider the top quark and its scalar partner (stop) effects at the one-loop level in the MSSM. The effective potential is

$$V_{\text{MSSM}}^{\text{eff}(1)} = \frac{3}{32\pi^2} \left[m_{\tilde{t}_1}^4 \left(\log \frac{m_{\tilde{t}_1}^2}{Q^2} - \frac{3}{2} \right) + m_{\tilde{t}_2}^4 \left(\log \frac{m_{\tilde{t}_2}^2}{Q^2} - \frac{3}{2} \right) - 2m_t^4 \left(\log \frac{m_t^2}{Q^2} - \frac{3}{2} \right) \right], \quad (4.17)$$

where $m_t = \frac{y_t}{\sqrt{2}}\varphi \sin \beta$ and $m_{\tilde{t}_{1,2}}$ are the masses of the top quark and the stops \tilde{t}_1 and \tilde{t}_2 , respectively. The stop masses are obtained by diagonalizing the mass matrix:

$$\mathcal{M}_{\text{stop}}^2 = \begin{bmatrix} m_t^2 + M_{\tilde{t}_L}^2 + m_Z^2 \left(\frac{1}{2} - \frac{1}{6} \sin^2 \theta_W \right) \cos 2\beta & m_t X_t \\ m_t X_t & m_{\tilde{t}_R}^2 + M_{\tilde{t}_R}^2 + \frac{2}{3} m_Z^2 \cos 2\beta \end{bmatrix}, \quad (4.18)$$

where $(M_{\tilde{t}_L}^2) = (M_{\tilde{Q}}^2)_{33}$, $M_{\tilde{t}_R}^2 = (M_{\tilde{u}}^2)_{33}$, and $X_t = A_t - \mu \cot \beta$ with $A_t = (A_u)_{33}/y_t$ and

$$m_{\tilde{t}_{1,2}}^2 = \frac{1}{2} \left[\text{tr} \mathcal{M}_{\text{stop}}^2 \mp \sqrt{(\text{tr} \mathcal{M}_{\text{stop}}^2)^2 - 4 \det \mathcal{M}_{\text{stop}}^2} \right]. \quad (4.19)$$

The mass of the lightest Higgs boson h can be calculated at the one-loop level:

$$m_h^2(\text{MSSM}) \simeq m_Z^2 \cos^2 2\beta + \frac{3m_t^4}{4\pi^2 v^2} \ln \frac{m_{\tilde{t}_1}^2 m_{\tilde{t}_2}^2}{m_t^4} + \frac{3m_t^2 X_t^2 \sin^2 \beta}{4\pi^2 (m_{\tilde{t}_2}^2 - m_{\tilde{t}_1}^2)} \ln \frac{m_{\tilde{t}_2}^2}{m_{\tilde{t}_1}^2}. \quad (4.20)$$

The one-loop renormalized triple h coupling λ_{hhh} is also calculated according to Eq. (4.16) as

$$\lambda_{hhh}^{\text{MSSM}} \simeq \left[\frac{3m_h^2(\text{MSSM})}{v} \right] \left[1 - \frac{m_t^4}{\pi^2 v^2 m_h^2(\text{MSSM})} + \frac{m_t^6 (m_{\tilde{t}_1}^2 + m_{\tilde{t}_2}^2)}{2\pi^2 v^2 m_{\tilde{t}_1}^2 m_{\tilde{t}_2}^2 m_h^2(\text{MSSM})} \right]. \quad (4.21)$$

For later convenience, we here define $\bar{\lambda}_{hhh}^{\text{Model}}$ as

$$\bar{\lambda}_{hhh}^{\text{Model}} \equiv \left[\frac{3m_h^2(\text{Model})}{v} \right] \left[1 - \frac{m_t^4}{\pi^2 v^2 m_h^2(\text{Model})} + \frac{m_t^6 (m_{\tilde{t}_1}^2 + m_{\tilde{t}_2}^2)}{2\pi^2 v^2 m_{\tilde{t}_1}^2 m_{\tilde{t}_2}^2 m_h^2(\text{Model})} \right]. \quad (4.22)$$

4.2 Nondecoupling effects in supersymmetric Higgs sectors

In general, new physics can be tested not only by direct searches but also by indirect searches. The indirect searches are performed by precise experiments to find effects of a heavy new physics particle on the observables which are well predicted in the low energy theory such as the SM. Such new particle effects on the low energy observables usually decouple in the large mass limit after the renormalization calculation is completed. This is known as the decoupling theorem proposed by Appelquist and Carazzone [150]. It is also known that the decoupling theorem does not hold when the new particles receive their masses from the VEV of the Higgs boson. In fact, there is a class of the new physics models where nondecoupling effects of heavy particles can appear on the low energy observables. For example, chiral fermions such as quarks and charged leptons cannot have the mass term because of the chiral symmetry, so that their masses are generated after the chiral symmetry is spontaneously broken by the VEV. Therefore, the effect of a heavy chiral fermion does not decouple, and it appears as powerlike or logarithmic contributions of the mass in the predictions for the low energy observables. Another example is the additional scalar fields in extended Higgs sectors. To see this type of nondecoupling effects, we here discuss the quantum effect on the $hhhh$ coupling in the non-SUSY THDM, where h is regarded as the SM-like Higgs boson. The $hhhh$ coupling can receive large nondecoupling effects from the loop contribution of extra Higgs bosons, when their masses are generated mainly by EWSB [23, 92]. When h is the SM like Higgs boson, physical masses of the extra scalar bosons are expressed by

$$m_{\Phi_i}^2 = M^2 + \frac{\lambda_i v^2}{2}, \quad (4.23)$$

where Φ_i represents H , H^\pm or A , and M is the invariant mass scale which is defined in Eq. (3.16), and λ_i is a coupling for $\Phi_i^\dagger \Phi_i hh$. The one-loop contribution to the renormalized $hhhh$ coupling is calculated as [23, 92]

$$\frac{\lambda_{hhhh}^{\text{THDM}}}{\lambda_{hhhh}^{\text{SM}}} \simeq 1 + \frac{1}{12\pi^2 m_h^2 v^2} \left\{ m_{H^0}^4 \left(1 - \frac{M^2}{m_{H^0}^2}\right)^3 + m_{A^0}^4 \left(1 - \frac{M^2}{m_{A^0}^2}\right)^3 + 2m_{H^\pm}^4 \left(1 - \frac{M^2}{m_{H^\pm}^2}\right)^3 \right\}. \quad (4.24)$$

One finds that for $M^2 \gg \lambda_i v^2$ it becomes

$$\frac{\lambda_{hhhh}^{\text{THDM}}}{\lambda_{hhhh}^{\text{SM}}} \simeq 1 + \frac{v^2}{96\pi^2 m_h^2} (\lambda_{H^0}^3 + \lambda_{A^0}^3 + 2\lambda_{H^\pm}^3) \left(\frac{v^2}{M^2}\right), \quad (4.25)$$

which vanishes in the large M limit according to the decoupling theorem [150]. On the contrary, when the physical scalar masses are mainly determined by the $\lambda_i v^2$ term, the loop contribution to the $hhhh$ coupling does not decouple, and the quartic powerlike contributions of m_{Φ_i} remain;

$$\frac{\lambda_{hhhh}^{\text{THDM}}}{\lambda_{hhhh}^{\text{SM}}} \simeq 1 + \frac{1}{12\pi^2 m_h^2 v^2} (m_{H^0}^4 + m_{A^0}^4 + 2m_{H^\pm}^4). \quad (4.26)$$

Consequently, a significant quantum effect can be realized for the $hhhh$ coupling when $m_{\Phi_i}^2 > m_h^2$. The size of the correction from the SM value can be of 100% for $m_h = 120$ GeV, $M \simeq 0$, and

$m_{H^0} \simeq m_{A^0} \simeq m_{H^\pm} \simeq 400$ GeV under the constraint from perturbative unitarity [89, 90]. Such a large non-decoupling effect on the hhh coupling is known to be related to the strongly first order electroweak phase transition [25] which is required for the electroweak baryogenesis [24].

In addition to hhh coupling, indirect effects of nondecoupling particles such as additional scalar bosons and chiral fermions appear in the low energy observables at the tree level, or at loop levels such as the electroweak S , T and U parameters [138] and $\gamma\gamma h$ vertex [149].

Let us consider the effect of the heavy particles in SUSY standard models. In general, a SUSY Higgs potential is composed of the D-term, the F-term and the soft-breaking term given in Eqs. (4.3) and (4.4). Quartic coupling constants in the potential can come from both the D-term and the F-term. As we have discussed in the previous section, in the MSSM, because of the multi-doublet structure only D-terms contribute to them, which are given by gauge coupling constants. Consequently, the mass of the lightest CP-even Higgs boson is determined by the gauge coupling constants and the VEVs at the tree level, which is less than m_Z . A substantial F-term contribution through the top Yukawa interaction enters into the Higgs potential at the one-loop level via the superpotential. This contribution is proportional to m_t^4 as expressed in Eq. (4.20). This one-loop correction shows a nondecoupling property in the large mass limit of stops. Consequently m_h can be above the LEP bound at least when one of the stops is heavy enough. There are also contributions from the μ parameter and the soft-breaking A_t (A_b) parameter when there is the left-right mixing in the stop (sbottom) sector (see the last term in Eq. (4.20)). Their one-loop effects can also be nondecoupling and then can be significant to some extent when they are taken to be as large as the scale of the soft-SUSY-breaking mass m_{SUSY} . In the NMSSM and the MSSM with triplets, m_h can be significantly enhanced by the F-term contribution. Notice that these F-term contributions should vanish in the SUSY limit due to the nonrenormalization theorem. These F-term contributions also affect the prediction on the other SM observables such as the triple Higgs boson coupling constants λ_{hhh} similarly to the case of non-SUSY extended Higgs models. We discuss this class of SUSY models in section 4.3.

On the other hand, a typical example for extended SUSY Higgs sectors without interactions from the tree-level F-term is that with only multi-doublet structures, such as the 4HDM. In this class of models, if there is no mixing between the light two doublet fields and the additional ones, the effects of the extra fields on the MSSM observables become suppressed due to the decoupling theorem when the extra doublet fields are heavy, and the model behaves like the MSSM. However, nonvanishing effects can appear through the mixing between the light two doublet fields and the additional ones via the soft breaking B-term. These effects appear at the tree level, so that they would give substantial modifications in the predictions in the MSSM for the low energy observables. We stress that these nonvanishing effects due to the B-term mixing are not the nondecoupling effects which appear in the large mass limit for the new particles when $\lambda v^2 \gtrsim M^2$ as a consequence of violation of the decoupling theorem. In this sense, we call the nonvanishing B-term mixing effect as the *quasi-nondecoupling effect*. Notice that the quasi-nondecoupling effect only appears in the predicted values in the MSSM. It gives modifications in the MSSM predictions such as the masses of h , H and H^\pm and the mixing angle α as well as coupling constants for the MSSM-like Higgs bosons. Such an effect, however, does disappear in the predictable SM coupling constants of $h\gamma\gamma$, hWW , hZZ and hhh in the SM-like limit ($m_A \rightarrow \infty$) according to the decoupling theorem.

Therefore, we would like to address the question of how the extra doublet fields in the

	\hat{S}	$\hat{\Omega}_R^c$	$\hat{\Omega}_L$	\hat{K}_R^c	\hat{K}_L	\hat{H}'_u	\hat{H}'_d	$\hat{\xi}$	$\hat{\Delta}_R^c$	$\hat{\Delta}_L$
$SU(2)_L$	1	1	1	1	1	2	2	3	3	3
$U(1)_Y$	0	+1	-1	+2	-2	+1/2	-1/2	0	+1	-1

Table 4.3: Properties of the additional chiral superfields

extended SUSY model can affect the observables which appear in the MSSM, such as the mass m_ϕ (ϕ represent h , H and H^\pm), the mixing angle α and the vertex $F_{\phi'VV}$ ($V = W^\pm$ and Z ; $\phi' = h$ and H). Deviations from the renormalized MSSM observable parameters may be expressed as

$$m_\phi \simeq m_\phi^{\text{MSSM}} (1 + \delta_\phi) , \quad (4.27)$$

$$\sin^2(\beta - \alpha_{\text{eff}}) \simeq [\sin^2(\beta - \alpha)]^{\text{MSSM}} (1 + \delta_s) , \quad (4.28)$$

$$F_{\phi'VV} \simeq F_{\phi'VV}^{\text{MSSM}} (1 + \delta_{\phi'VV}) , \quad (4.29)$$

where δ_ϕ , δ_s or $\delta_{\phi'VV}$ represent the effect of the extra heavy scalar fields on each observable in the extended SUSY models.

In section 4.4, we study δ_h , δ_H , δ_{H^\pm} and δ_s in the 4HDM. The MSSM predictions are evaluated at the one-loop level using the on-shell renormalization scheme in Ref. [66].

4.3 SUSY Higgs sectors with nondecoupling effects

In this section, we consider various extension of SUSY Higgs sectors. One way of the extension of the MSSM may be adding new chiral superfields such as isospin singlets (neutral \hat{S} , singly charged $\hat{\Omega}_{L,R}$ or doubly charged $\hat{K}_{L,R}$), doublets (\hat{H}'_u and \hat{H}'_d), or triplets ($\hat{\xi}$ with the hypercharge $Y = 0$ or $\hat{\Delta}_{L,R}$ with $Y = \pm 1$), whose properties are defined in Table 4.3. For anomaly cancellation, charged superfields are introduced in pair in each model. As we are interested in the variation in the Higgs sector, these new fields are supposed to be colour singlet. Although there can be further possibilities such as introduction of new vector superfields which contain gauge fields for extra gauge symmetries, models with extra dimensions, those with the R-parity violation, etc., we here do not discuss them.

Although models in Table 4.3 can be imposed additional exact or softly-broken discrete symmetries for various reasons, we here do not specify them as they do not affect our discussions. In this section, we discuss the three SUSY models in addition to the MSSM: the MSSM with extra \hat{S} which is so-called the next-to MSSM (NMSSM), that with pair of extra triplets $\hat{\Delta}_{L,R}$ (TMSSM) and that with pair of extra doublet fields \hat{H}'_u and \hat{H}'_d and pair of charged singlet fields $\hat{\Omega}_{L,R}$ (4D Ω).

4.3.1 The next-to-MSSM

The superpotential in the NMSSM is

$$W_{\text{NMSSM}} = W_{\text{MSSM}} + \lambda_{HHS} \hat{S} \hat{H}_u \cdot \hat{H}_d + \frac{\kappa}{3} \hat{S}^3 + \frac{\mu_S}{2} \hat{S}^2. \quad (4.30)$$

The soft-breaking terms are

$$\mathcal{L}_{\text{NMSSM}}^{\text{soft}} = \mathcal{L}_{\text{MSSM}}^{\text{soft}} - M_S^2 |S|^2 - \left(A_\lambda H_u \cdot H_d S + \frac{A_\kappa}{3} S^3 + B_S \mu_S S^2 + \text{h.c.} \right). \quad (4.31)$$

The Higgs potential is

$$\begin{aligned} V_{\text{NMSSM}} = & m_1^2 H_d^\dagger H_d + m_2^2 H_u^\dagger H_u + m_S^2 |S|^2 + (B\mu H_d \cdot H_u + B_S \mu_S S^2 + \text{h.c.}) \\ & + \frac{g^2 + g'^2}{8} (H_d^\dagger H_d - H_u^\dagger H_u)^2 - \frac{g^2}{2} (H_d^\dagger H_u)(H_u^\dagger H_d) \\ & + |\lambda_{HHS}|^2 [|H_u \cdot H_d|^2 + |S|^2 (|H_u|^2 + |H_d|^2)] + |\kappa|^2 S^2 |S|^2 \\ & + (\lambda_{HHS} \mu_S^* S^* H_u \cdot H_d + \kappa \mu_S^* S^2 S^* + \lambda_{HHS}^* \kappa S^2 H_u \cdot H_d + A_\lambda H_u \cdot H_d S + \frac{A_\kappa}{3} S^3 + \text{h.c.}). \end{aligned} \quad (4.32)$$

The singlet scalar boson S can be parameterized as

$$S = \frac{1}{\sqrt{2}} (S_\varphi + i S_\chi). \quad (4.33)$$

Here, we consider the case where the singlet scalar boson does not obtain the VEV. In this case, the mixing among the scalar bosons from the doublet Higgs field and those from singlet field can be neglected. The one-loop level m_h^2 and the triple h coupling in the NMSSM can be calculated as

$$m_h^2(\text{NMSSM}) \simeq m_h^2(\text{MSSM}) + \frac{v^2}{2} |\lambda_{HHS}|^2 \sin^2 2\beta + \frac{|\lambda_{HHS}|^4 v^2}{32\pi^2} \ln \frac{m_{S_\varphi}^2 m_{S_\chi}^2}{m_{\tilde{S}}^4}, \quad (4.34)$$

$$\lambda_{hhh}^{\text{NMSSM}} \simeq \bar{\lambda}_{hhh}^{\text{NMSSM}} + \left[\frac{3m_h^2(\text{NMSSM})}{v} \right] \frac{|\lambda_{HHS}|^6 v^4}{96\pi^2 m_h^2(\text{NMSSM})} \left(\frac{1}{m_{S_\varphi}^2} + \frac{1}{m_{S_\chi}^2} \right), \quad (4.35)$$

where $m_{S_\varphi}^2$, $m_{S_\chi}^2$ and $m_{\tilde{S}}$ are the masses of S_φ , S_χ and \tilde{S} , respectively. The masses of $m_{S_\varphi}^2$ and $m_{S_\chi}^2$ can be expressed as

$$m_{S_{\varphi,\chi}}^2 = \mathcal{M}_{S_{\varphi,\chi}}^2 + \frac{|\lambda_{HHS}|^2}{2} v^2, \quad (4.36)$$

where $\mathcal{M}_{S_{\varphi,\chi}}^2$ is the invariant mass parameters.

4.3.2 Model with extra triplet superfields

The superpotential in the TMSSM is

$$W_{\text{TMSSM}} = W_{\text{MSSM}} + \frac{h_\Delta^{ij}}{2} \hat{L}_i \cdot \hat{\Delta}_R^c \hat{L}_j + \frac{\lambda_{HH\Delta_L}}{2} \hat{H}_d \cdot \hat{\Delta}_R^c \hat{H}_d + \frac{\lambda_{HH\Delta_R}}{2} \hat{H}_u \cdot \hat{\Delta}_L \hat{H}_u + \mu_\Delta \text{tr}(\hat{\Delta}_R^c \hat{\Delta}_L). \quad (4.37)$$

The soft-breaking terms are

$$\begin{aligned} \mathcal{L}_{\text{TMSSM}}^{\text{soft}} = & \mathcal{L}_{\text{MSSM}}^{\text{soft}} - M_{\Delta_R}^2 \text{tr}(\Delta_R^\dagger \Delta_R) - M_{\Delta_L}^2 \text{tr}(\Delta_L^\dagger \Delta_L) \\ & - \left[\frac{(A_\Delta)_{ij}}{2} \tilde{L}_i \cdot \Delta_R^* \tilde{L}_j + \frac{A_1}{2} H_d \cdot \Delta_R^* H_d + \frac{A_2}{2} H_u \cdot \Delta_L H_u + B_\Delta \mu_\Delta \text{tr}(\Delta_R^* \Delta_L) + \text{h.c.} \right]. \end{aligned} \quad (4.38)$$

The Higgs potential is

$$\begin{aligned}
V_{\text{TMSSM}} = & m_1^2 H_d^\dagger H_d + m_2^2 H_u^\dagger H_u + m_{\Delta_R}^2 \text{tr}(\Delta_R^\dagger \Delta_R) + m_{\Delta_L}^2 \text{tr}(\Delta_L^\dagger \Delta_L) \\
& + (B\mu H_d \cdot H_u + B_{\Delta}\mu_{\Delta} \text{tr}(\Delta_R^* \Delta_L) + \text{h.c.}) \\
& + \frac{g^2}{8} \left[H_d^\dagger \tau^a H_d + H_u^\dagger \tau^a H_u + \text{tr}(\Delta_R^T \tau^a \Delta_R^*) + \text{tr}(\Delta_L^\dagger \tau^a \Delta_L) \right]^2 \\
& + \frac{g'^2}{8} \left[-H_d^\dagger H_d + H_u^\dagger H_u + 2\text{tr}(\Delta_R^T \Delta_R^*) - 2\text{tr}(\Delta_L^\dagger \Delta_L) \right]^2 \\
& + \left(\lambda_{HH\Delta_L} \mu H_u^\dagger \Delta_R^* H_d + \lambda_{HH\Delta_R} \mu H_d^\dagger \Delta_L H_u + \lambda_{HH\Delta_L} \mu_{\Delta} H_d \cdot \Delta_L^\dagger H_d + \lambda_{HH\Delta_R} \mu_{\Delta} H_u \cdot \Delta_R^T H_u + \text{h.c.} \right) \\
& + |\lambda_{HH\Delta_L}|^2 (H_d \cdot \Delta_R^*)(H_d \cdot \Delta_R^*)^\dagger + |\lambda_{HH\Delta_R}|^2 (H_u \cdot \Delta_L)(H_u \cdot \Delta_L)^\dagger \\
& + \frac{|\lambda_{HH\Delta_L}|^2}{4} (H_d^\dagger H_d)^2 + \frac{|\lambda_{HH\Delta_R}|^2}{4} (H_u^\dagger H_u)^2.
\end{aligned} \tag{4.39}$$

The scalar bosons from the triplet fields Δ_R^* and Δ_L can be parametrized as

$$\Delta_R^* = \begin{pmatrix} \frac{1}{\sqrt{2}} \Delta_R^+ & \Delta_R^{++} \\ \frac{1}{\sqrt{2}}(v_L + \Delta_{L\varphi} + i\Delta_{L\chi}) & -\frac{1}{\sqrt{2}} \Delta_R^+ \end{pmatrix}, \quad \Delta_L = \begin{pmatrix} \frac{1}{\sqrt{2}} \Delta_L^- & \frac{1}{\sqrt{2}}(v_L + \Delta_{L\varphi} + i\Delta_{L\chi}) \\ \Delta_L^{--} & -\frac{1}{\sqrt{2}} \Delta_L^+ \end{pmatrix}. \tag{4.40}$$

The one-loop level m_h^2 and the triple h coupling in the NMSSM can be calculated as

$$\begin{aligned}
m_h^2(\text{TMSSM}) \simeq & m_h^2(\text{MSSM}) + \frac{v^2}{2} (|\lambda_{HH\Delta_L}|^2 \cos^4 \beta + |\lambda_{HH\Delta_R}|^2 \sin^4 \beta) \\
& + \frac{|\lambda_{HH\Delta_L}|^4 v^2 \cos^4 \beta}{32\pi^2} \left(\ln \frac{m_{\Delta_{R\varphi}}^2 m_{\Delta_{R\chi}}^2}{m_{\tilde{\Delta}_R^0}^4} + 2 \ln \frac{m_{\Delta_R^+}^2}{m_{\tilde{\Delta}_R^+}^2} \right) \\
& + \frac{|\lambda_{HH\Delta_R}|^4 v^2 \sin^4 \beta}{32\pi^2} \left(\ln \frac{m_{\Delta_{L\varphi}}^2 m_{\Delta_{L\chi}}^2}{m_{\tilde{\Delta}_L^0}^4} + 2 \ln \frac{m_{\Delta_L^+}^2}{m_{\tilde{\Delta}_L^+}^2} \right),
\end{aligned} \tag{4.41}$$

$$\begin{aligned}
\lambda_{hhh}^{\text{TMSSM}} \simeq & \bar{\lambda}_{hhh}^{\text{TMSSM}} + \left[\frac{3m_h^2(\text{TMSSM})}{v} \right] \frac{|\lambda_{HH\Delta_L}|^6 v^4 \cos^6 \beta}{96\pi^2 m_h^2(\text{TMSSM})} \left(\frac{1}{m_{\Delta_{R\varphi}}^2} + \frac{1}{m_{\Delta_{R\chi}}^2} + \frac{2}{m_{\Delta_R^+}^2} \right) \\
& + \left[\frac{3m_h^2(\text{TMSSM})}{v} \right] \frac{|\lambda_{HH\Delta_R}|^6 v^4 \sin^6 \beta}{96\pi^2 m_h^2(\text{TMSSM})} \left(\frac{1}{m_{\Delta_{L\varphi}}^2} + \frac{1}{m_{\Delta_{L\chi}}^2} + \frac{2}{m_{\Delta_L^+}^2} \right),
\end{aligned} \tag{4.42}$$

where $m_{\Delta_{R\varphi}}^2$, $m_{\Delta_{R\chi}}^2$, $m_{\Delta_R^+}^2$, $m_{\tilde{\Delta}_R^0}^2$ and $m_{\tilde{\Delta}_R^+}^2$ are the masses of $\Delta_{R\varphi}$, $\Delta_{R\chi}$, Δ_R^+ , $\tilde{\Delta}_R^0$ and $\tilde{\Delta}_R^+$, respectively. In the above definition, the parameters which are denoted as L instead of R are masses of the corresponding fields which are denoted as L instead of R . The scalar bosons

masses can be expressed as

$$m_{\Delta_{R\varphi,R\chi}}^2 = \mathcal{M}_{\Delta_{R\varphi,R\chi}}^2 + \frac{|\lambda_{HH\Delta_L}|^2}{2} v^2 \cos^2 \beta, \quad (4.43)$$

$$m_{\Delta_{L\varphi,L\chi}}^2 = \mathcal{M}_{\Delta_{L\varphi,L\chi}}^2 + \frac{|\lambda_{HH\Delta_R}|^2}{2} v^2 \sin^2 \beta, \quad (4.44)$$

$$m_{\Delta_R^\pm}^2 = \mathcal{M}_{\Delta_R^\pm}^2 + \frac{|\lambda_{HH\Delta_L}|^2}{2} v^2 \cos^2 \beta, \quad (4.45)$$

$$m_{\Delta_L^\pm}^2 = \mathcal{M}_{\Delta_L^\pm}^2 + \frac{|\lambda_{HH\Delta_R}|^2}{2} v^2 \sin^2 \beta, \quad (4.46)$$

where $\mathcal{M}_{\Delta_{R\varphi,R\chi}}^2$, $\mathcal{M}_{\Delta_{L\varphi,L\chi}}^2$, $\mathcal{M}_{\Delta_R^\pm}^2$ and $\mathcal{M}_{\Delta_L^\pm}^2$ are the invariant mass parameters.

4.3.3 Model with four Higgs doublets and charged singlet superfields

The 4D Ω contains the four Higgs doublets, so that in general, FCNC processes can appear at the tree level. We here impose the softly-broken Z_2 symmetry to avoid such processes. We assign that \hat{H}'_u , \hat{H}'_d , $\hat{\Omega}_R^c$ and $\hat{\Omega}_L$ are odd, while the other fields are even under this Z_2 symmetry [177]. The superpotential in the 4D Ω is

$$W_{4D\Omega} = W_{\text{MSSM}} + \lambda_{HH\Omega_R} \hat{H}_d \cdot \hat{H}'_d \hat{\Omega}_R^c + \lambda_{HH\Omega_L} \hat{H}_u \cdot \hat{H}'_u \hat{\Omega}_L + \mu' \hat{H}'_u \cdot \hat{H}'_d + \mu_\Omega \hat{\Omega}_R^c \hat{\Omega}_L. \quad (4.47)$$

The soft-breaking terms are

$$\begin{aligned} \mathcal{L}_{4D\Omega}^{\text{soft}} = & \mathcal{L}_{\text{MSSM}}^{\text{soft}} - M_{H'_d}^2 H_d^\dagger H'_d + M_{H'_u}^2 H_u^\dagger H'_u - M_{\Omega_R}^2 (\omega_R^* \omega_R) - M_{\Omega_L}^2 (\omega_L^* \omega_L) \\ & - \left[(A_f)_{ij} \omega_R^* \tilde{L}_i \cdot \tilde{L}_j + A_1 \omega_R^* H_d \cdot H'_d + A_2 \omega_L H_u \cdot H'_u + B' \mu' H'_u \cdot H'_d + B_\Omega \mu_\Omega \omega_R^* \omega_L + \text{h.c.} \right]. \end{aligned} \quad (4.48)$$

The Higgs potential is

$$\begin{aligned} V_{4D\Omega} = & m_1^2 H_d^\dagger H_d + m_2^2 H_u^\dagger H_u + m_3^2 H_d'^\dagger H'_d + m_4^2 H_u'^\dagger H'_u + m_{\omega_R}^2 \omega_R^* \omega_R + m_{\omega_L}^2 \omega_L^* \omega_L \\ & + (B \mu H_u \cdot H_d + B' \mu' H'_u \cdot H'_d + B_\Omega \mu_\Omega \omega_R^* \omega_L + \text{h.c.}) \\ & + \frac{g^2 + g'^2}{8} (H_u^\dagger H_u + H_d^\dagger H_d - H_u'^\dagger H'_u - H_d'^\dagger H'_d)^2 \\ & + \frac{g^2}{2} \left[(H_d^\dagger H_u)(H_u^\dagger H_d) + (H_d^\dagger H'_u)(H_u'^\dagger H'_d) + (H_d'^\dagger H_u)(H_u^\dagger H'_d) + (H_d'^\dagger H'_u)(H_u^\dagger H_d) \right. \\ & + (H_d^\dagger H'_d)(H_d'^\dagger H_d) - (H_d^\dagger H_d)(H_d'^\dagger H'_d) + (H_u^\dagger H'_u)(H_u'^\dagger H_u) - (H_u^\dagger H_u)(H_u'^\dagger H'_u) \left. \right] \\ & + \frac{g'^2}{2} (\omega_R^* \omega_R - \omega_L^* \omega_L)^2 + \frac{g'^2}{2} (H_u^\dagger H_u + H_u'^\dagger H'_u - H_d^\dagger H_d - H_d'^\dagger H'_d) (\omega_R^* \omega_R - \omega_L^* \omega_L) \\ & + |\lambda_{HH\Omega_R}|^2 \left[(H_d^\dagger H_d + H_d'^\dagger H'_d) \omega_R^* \omega_R + (H_d \cdot H'_d)^* (H_d \cdot H'_d) \right] \\ & + |\lambda_{HH\Omega_L}|^2 \left[(H_u^\dagger H_u + H_u'^\dagger H'_u) \omega_L^* \omega_L + (H_u \cdot H'_u)^* (H_u \cdot H'_u) \right] \\ & + [A_1 \omega_R^* H_d \cdot H'_d + A_2 \omega_L H_u \cdot H'_u + \mu^* \lambda_{HH\Omega_R} H_u^\dagger H'_d \omega_R^* + \mu \lambda_{HH\Omega_L} H_u'^\dagger H_d \omega_L^* + \mu'^* \lambda_{HH\Omega_R} H_u'^\dagger H_d \omega_R^* \\ & + \mu' \lambda_{HH\Omega_L} H_u^\dagger H'_d \omega_L^* + \mu_\Omega^* \lambda_{HH\Omega_R} H_d \cdot H'_d \omega_L^* + \mu_\Omega \lambda_{HH\Omega_L} H_u^\dagger \cdot H_u'^\dagger \omega_R^* + \text{h.c.}]. \end{aligned} \quad (4.49)$$

The one-loop level m_h^2 and the triple h coupling in the NMSSM can be calculated as

$$m_h^2(4\text{D}\Omega) \simeq m_h^2(\text{MSSM}) + \frac{|\lambda_{HH\Omega_R}|^4 v^2 \cos^4 \beta}{16\pi^2} \ln \frac{m_{\omega_R}^2}{m_{\tilde{\omega}}^2} + \frac{|\lambda_{HH\Omega_L}|^4 v^2 \sin^4 \beta}{16\pi^2} \ln \frac{m_{\omega_L}^2}{m_{\tilde{\omega}}^2}, \quad (4.50)$$

$$\lambda_{hhh}^{4\text{D}\Omega} \simeq \bar{\lambda}_{hhh}^{4\text{D}\Omega} + \left[\frac{3m_h^2(4\text{D}\Omega)}{v} \right] \frac{|\lambda_{HH\Omega_R}|^6 v^4 m_{\omega_R}^2 \cos^6 \beta}{48\pi^2 m_h^2(4\text{D}\Omega)} + \left[\frac{3m_h^2(4\text{D}\Omega)}{v} \right] \frac{|\lambda_{HH\Omega_L}|^6 v^4 m_{\omega_L}^2 \sin^6 \beta}{48\pi^2 m_h^2(4\text{D}\Omega)}, \quad (4.51)$$

where $m_{\omega_R}^2$, $m_{\omega_L}^2$, and $m_{\tilde{\omega}}$ are the masses of ω_R , ω_L and $\tilde{\omega}$, respectively. The scalar bosons masses can be expressed as

$$m_{\omega_R}^2 = \mathcal{M}_{\omega_R}^2 + \frac{|\lambda_{HH\Omega_R}|^2}{2} v^2 \cos^2 \beta, m_{\omega_L}^2 = \mathcal{M}_{\omega_L}^2 + \frac{|\lambda_{HH\Omega_L}|^2}{2} v^2 \sin^2 \beta, \quad (4.52)$$

where \mathcal{M}_{ω_R} and \mathcal{M}_{ω_L} are the invariant mass parameters.

4.3.4 Possible allowed regions of m_h and λ_{hhh} in various SUSY Higgs models

Here, we evaluate numerical calculation for m_h and the deviation of λ_{hhh} from the SM prediction in each SUSY Higgs model at the one-loop level.

In Fig. 4.1, the upper bounds on m_h in the NMSSM and TMSSM are shown as a function of $\tan \beta$, and the possible allowed region in the MSSM is also indicated by the red-filled region. The coupling constants $\lambda_{HH\phi}$ ($\phi = S, \Delta_L$ or Δ_R) are taken as $0 < \lambda_{HH\phi} < 2.5$. In the NMSSM with a fixed value of λ_{HHS} , m_h can be maximal for $\tan \beta = 1$, while in the TMSSM it becomes maximal for large values of $\tan \beta$ for a fixed value of $\lambda_{HH\Delta}$ ($= \lambda_{HH\Delta_L} = \lambda_{HH\Delta_R}$). The maximal value in the NMSSM becomes asymptotically the same as that in the MSSM in the large $\tan \beta$ limit up to the one-loop logarithmic contributions.

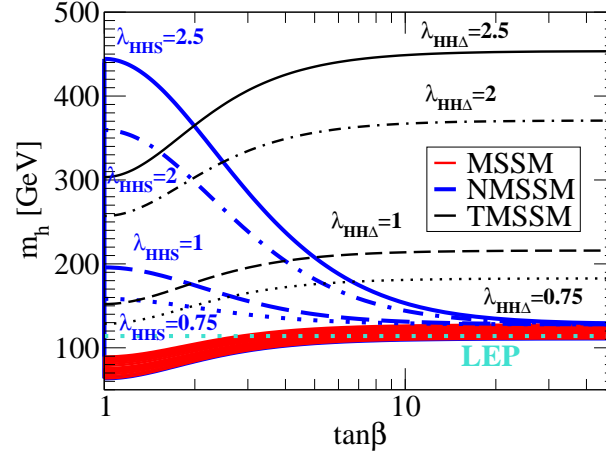


Figure 4.1: The upper bounds on m_h as a function of $\tan\beta$ for fixed values of λ_{HHS} and $\lambda_{HH\Delta_L} = \lambda_{HH\Delta_R} \equiv \lambda_{HH\Delta}$ in the NMSSM and the TMSSM, respectively. The red-filled region indicates the possible allowed region in the MSSM [67].

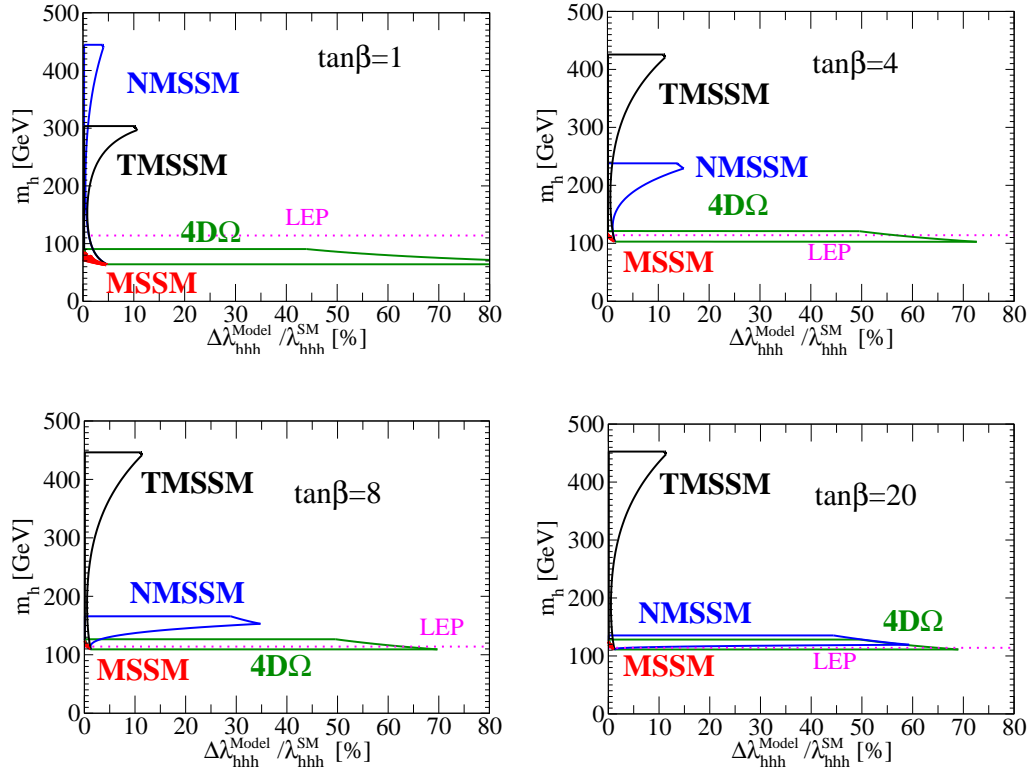


Figure 4.2: Possible allowed regions in the $m_h - (\Delta\lambda_{hhh}/\lambda_{hhh})$ plane in the MSSM, Model-1, Model-5 and Model-9 for each $\tan\beta$ value. We scan the parameter space as $0 < \lambda_{HH\phi} < 2.5$, $0.5 \text{ TeV} < m_{\tilde{\tau}_{1,2}} < 1.5 \text{ TeV}$, and $0.5 \text{ TeV} < m_\phi$ for each model [67], where m_ϕ is the physical mass of the extra scalar bosons.

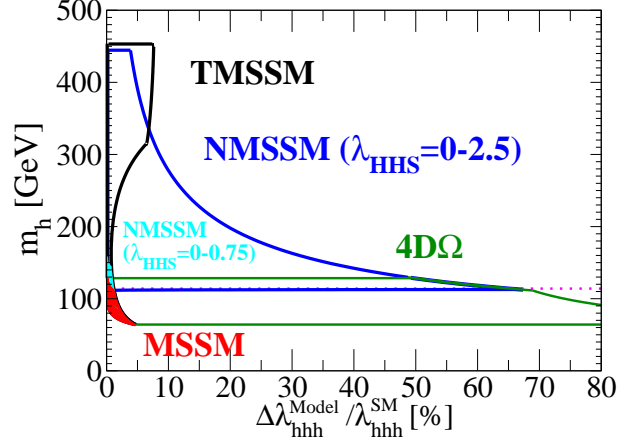


Figure 4.3: Possible allowed regions in the m_h -($\Delta\lambda_{hhh}/\lambda_{hhh}$) plane in the MSSM, the NMSSM, the TMSSM and the 4D Ω with scanned $\tan\beta$ [67].

We scan the parameter space in each model to find allowed regions in the m_h -($\Delta\lambda_{hhh}^{\text{Model}}/\lambda_{hhh}^{\text{SM}}$) plane under the assumption of $\lambda_{HH\phi} < 2.5$ at the EW scale, where $\Delta\lambda_{hhh}^{\text{Model}} = \lambda_{hhh}^{\text{Model}} - \lambda_{hhh}^{\text{SM}}$. In Fig. 4.2, we show the possible allowed region for several value of $\tan\beta = 1, 4, 8$ and 20 . The coupling constants $\lambda_{HH\phi}$ ($\phi = S, \chi_{\pm}$ and Ω_{\pm}) are taken to be less than 2.5 as in Fig. 4.1. The stop masses are scanned as $0.5 \text{ TeV} \leq m_{\tilde{t}_{1,2}} \leq 1.5 \text{ TeV}$. We also scan the physical masses of the extra scalar bosons as $0.5 \text{ TeV} \leq m_{\phi}$. The mass of fermion component is taken as same as the mass of the scalar component for each extra field. We note that the parameters are scanned such that the additional contributions to the rho parameter are negligible¹. The region in the MSSM is indicated as the red-filled one. The possible allowed region in the NMSSM depends largely on $\tan\beta$: for smaller (larger) $\tan\beta$, m_h can be higher (lower) and $\Delta\lambda_{hhh}^{\text{Model-1}}/\lambda_{hhh}^{\text{SM}}$ is smaller (larger). the TMSSM is relatively insensitive to the value of $\tan\beta$: m_h can always be larger than about 300 GeV while $\Delta\lambda_{hhh}^{\text{TMSSM}}/\lambda_{hhh}^{\text{SM}}$ remains less than about 10% . On the other hand, in the 4D Ω , although the possible value of m_h is similar to that in the MSSM, the deviation in the hhh coupling can be very large: i.e., $\Delta\lambda_{hhh}^{4D\Omega}/\lambda_{hhh}^{\text{SM}} \sim 30 - 60 \%$ ². When we consider the higher value of Λ , which corresponds to the smaller upper bound on $\lambda_{HH\phi}$, the possible allowed region becomes the smaller.

In Fig. 4.3, possible allowed regions with scanned $\tan\beta$ are shown in the m_h -($\Delta\lambda_{hhh}^{\text{Model}}/\lambda_{hhh}^{\text{SM}}$) plane in the NMSSM, the TMSSM and the 4D Ω as well as the MSSM. The maximal values of $\lambda_{HH\phi}$ in the NMSSM, the TMSSM and the 4D Ω are taken to be the same as those in Fig. 4.2. The region in the MSSM (the NMSSM with $0 \lesssim \lambda_{HHS} \lesssim 0.75$, which corresponds to $\Lambda \simeq 10^{16} \text{ GeV}$ [172]) is indicated as the red-filled (cyan-filled) one. The possible allowed regions are different among the models so that the information of m_h and $\Delta\lambda_{hhh}^{\text{Model}}$ can be used to classify the SUSY standard models.

¹For example, parameters in the stop-sbottom sector are taken to keep the rho parameter constraint satisfied.

² The definition of $\tan\beta$ in models with four Higgs doublets is that $\tan\beta = \sqrt{\langle H_u^0 \rangle^2 + \langle H_u'^0 \rangle^2} / \sqrt{\langle H_d^0 \rangle^2 + \langle H_d'^0 \rangle^2}$.

4.4 SUSY Higgs sectors with quasi-nondecoupling effects

In this section, we consider the 4HDM in order to examine the quasi-nondecoupling effect as discussed in the section 4.2. Studies for the 4HDM have been done by several papers. The Higgs potential and the mass matrices in the 4HDM have been analyzed by Gupta and Wells [178]. The collider phenomenology of the 4HDM has been analysed in Ref. [179]. The dark matter physics in the framework of the 4HDM has been investigated in Ref. [180]. In these papers, quasi-nondecoupling effects have not been studied.

4.4.1 Model

We here discuss the 4HDM, in which two extra isospin-doublet chiral superfields \hat{H}'_d ($Y = -1/2$) and \hat{H}'_u ($Y = 1/2$) are introduced to the MSSM in addition to the Higgs doublets \hat{H}_d and \hat{H}_u . The general expression for the superpotential with the R parity is given in terms of chiral superfields as

$$W = W_{\text{MSSM}} - (\hat{Y}'_u)_{ij} U_{Ri}^c \hat{H}'_u \cdot Q_{Lj} + (\hat{Y}'_d)_{ij} D_{Ri}^c \hat{H}'_d \cdot Q_{Lj} + (\hat{Y}'_e)_{ij} E_{Ri}^c \hat{H}'_d \cdot L_{Lj} - \mu_{14} \hat{H}_d \cdot \hat{H}'_u - \mu_{32} \hat{H}'_d \cdot \hat{H}_u - \mu_{34} \hat{H}'_d \cdot \hat{H}'_u, \quad (4.53)$$

The most general holomorphic soft-SUSY-breaking terms with the R parity is

$$\begin{aligned} \mathcal{L}^{\text{soft}} = & \mathcal{L}_{\text{MSSM}}^{\text{soft}} - (\bar{M}_-^2)_{33} H_d^\dagger H'_d - (\bar{M}_+^2)_{44} H_u^\dagger H'_u \\ & - \left[(\bar{M}_-^2)_{13} H_d^\dagger H'_d + (\bar{M}_+^2)_{24} H_u^\dagger H'_u + \text{h.c.} \right] \\ & - \left[-(A'_u)^{ij} \tilde{u}_{Ri}^* H'_u \cdot \tilde{Q}_{Lj} + (A'_d)^{ij} \tilde{d}_{Ri}^* H'_d \cdot \tilde{Q}_{Lj} + (A'_e)^{ij} \tilde{e}_{Ri}^* H'_d \cdot \tilde{L}_{Lj} + \text{h.c.} \right] \\ & - (B_{34} \mu_{34} H'_d \cdot H'_u + B_{14} \mu_{14} H_d \cdot H'_u + B_{32} \mu_{32} H'_d \cdot H_u + \text{h.c.}), \end{aligned} \quad (4.54)$$

where $\mathcal{L}_{\text{MSSM}}^{\text{soft}}$ is given in Eq. (4.2). The Higgs potential can be obtained by Eqs. (4.53) and (4.54) as

$$\begin{aligned} V_H = & (H_d^\dagger \ H_d'^\dagger) \begin{pmatrix} (M_-^2)_{11} & (M_-^2)_{12} \\ (M_-^2)_{12}^* & (M_-^2)_{22} \end{pmatrix} \begin{pmatrix} H_d \\ H'_d \end{pmatrix} + (H_u^\dagger \ H_u'^\dagger) \begin{pmatrix} (M_+^2)_{11} & (M_+^2)_{12} \\ (M_+^2)_{12}^* & (M_+^2)_{22} \end{pmatrix} \begin{pmatrix} H_u \\ H'_u \end{pmatrix} \\ & - \left((H_d \ H'_d) \begin{pmatrix} B\mu & B_{14}\mu_{14} \\ B_{32}\mu_{32} & B_{34}\mu_{34} \end{pmatrix} \cdot \begin{pmatrix} H_u \\ H'_u \end{pmatrix} + \text{h.c.} \right) \\ & + \frac{g'^2 + g^2}{8} \left(H_u^\dagger H_u + H_u'^\dagger H'_u - H_d^\dagger H_d - H_d'^\dagger H'_d \right)^2 \\ & + \frac{g^2}{2} \left[(H_d^\dagger H_u)(H_u^\dagger H_d) + (H_d^\dagger H'_u)(H_u'^\dagger H_d) + (H_d'^\dagger H_u)(H_u^\dagger H'_d) + (H_d'^\dagger H'_u)(H_u'^\dagger H'_d) \right. \\ & \left. + (H_d^\dagger H'_d)(H_d'^\dagger H_d) - (H_d^\dagger H_d)(H_d'^\dagger H'_d) + (H_u^\dagger H'_u)(H_u'^\dagger H_u) - (H_u^\dagger H_u)(H_u'^\dagger H'_u) \right], \end{aligned} \quad (4.55)$$

	\hat{H}_d	\hat{H}_u	\hat{H}'_d	\hat{H}'_u	\hat{U}_R^c	\hat{D}_R^c	\hat{E}_R^c	\hat{Q}_L	\hat{L}_L	\hat{N}_R^c
Type A	+	+	−	−	+	+	+	+	+	+
Type B	+	+	−	−	+	+	−	+	+	+
Type C	+	+	−	−	+	+	+	+	+	−
Type D	+	+	−	−	+	+	−	+	+	−

Table 4.4: Classification for the charge assignment for the Z_2 symmetry in the 4HDM. Type C and Type D are introduced only when N_{Ri}^c are added to the model [68].

where

$$\begin{aligned}
(M_-^2)_{11} &= (M_-^2) + |\mu|^2 + |\mu_{14}|^2, \\
(M_-^2)_{22} &= (\bar{M}_-^2)_{33} + |\mu_{32}|^2 + |\mu_{34}|^2, \\
(M_-^2)_{12} &= (\bar{M}_-^2)_{13} + \mu^* \mu_{32} + \mu_{14}^* \mu_{34}, \\
(M_+^2)_{11} &= (M_+^2) + |\mu|^2 + |\mu_{32}|^2, \\
(M_+^2)_{22} &= (\bar{M}_+^2)_{44} + |\mu_{14}|^2 + |\mu_{34}|^2, \\
(M_+^2)_{12} &= (\bar{M}_+^2)_{24} + \mu^* \mu_{14} + \mu_{32}^* \mu_{34}.
\end{aligned} \tag{4.56}$$

There are two Higgs doublets for each quantum number, so that they can mix with each other. The Yukawa sector then produces a dangerous FCNC via the scalar boson exchange at the tree level. There are several ways to eliminate such an excessive FCNC. In non-SUSY extended Higgs sectors with multi-doublets, a softly-broken discrete Z_2 symmetry is often imposed [29]. In the general two Higgs doublet model, there are four types of Yukawa interactions under such a Z_2 symmetry depending on the assignment of the Z_2 charge [36–38]. The other possibility of eliminating the FCNC may be to consider a certain of alignment in the Yukawa sector [83], but we do not consider this possibility in this paper. In the 4HDM, we also impose the Z_2 symmetry to eliminate the FCNC. There are two types of Yukawa interactions (Type A and Type B) as shown in Table 1, assuming that all the Higgs doublet fields receive VEVs. If we introduce additional chiral superfields N_{Ri}^c for right-handed neutrinos which are singlet under the SM gauge symmetries, possible number of the type of Yukawa interaction becomes doubled under the Z_2 symmetry, depending on the two possible assignment of the Z_2 charge for N_{Ri}^c . We define additional two types in Table 1 (Type C and Type D) which correspond to the Z_2 odd N_{Ri}^c . Under the Z_2 symmetry, some of the Yukawa coupling constants are forbidden for each type of Yukawa interaction. For example, in the MSSM-like Yukawa interaction (Type A) $\hat{Y}'_u = \hat{Y}'_d = \hat{Y}'_e = 0$ is required, while in the lepton specific one (Type B) we have $\hat{Y}'_u = \hat{Y}'_d = \hat{Y}'_e = 0$. Marshall and Sher discussed phenomenology of the Type B Yukawa interaction in the 4HDM [179]. Notice that the dimensionful parameters are not forbidden as long as the discrete symmetry is softly broken. In this paper, we assume that the FCNC is sufficiently suppressed by a softly-broken Z_2 symmetry. However, we do not specify the type of Yukawa interaction, because all the essential results in this paper do not depend on the types of Yukawa interaction.

From the Lagrangian in Eq. (4.3), we can extract the Higgs potential of the model, in which neutral scalar components of $H_{u,d}$ and $H'_{u,d}$ receive the VEV. However, because H_d and H'_d (H_u and H'_u) have the same quantum numbers under the $SU(2) \times U(1)$ gauge symmetries, there are $U(2)$ symmetries in the D-terms in the potential. By using the $U(2)$ symmetry, we may rotate

the fields H_d and H'_d as well as the fields H_u and H'_u and take the basis in which only one of the doublets receives the VEV while the other does not as

$$\begin{pmatrix} H_1 \\ H_3 \end{pmatrix} = U_- \begin{pmatrix} H_d \\ H'_d \end{pmatrix}, \quad \begin{pmatrix} H_2 \\ H_4 \end{pmatrix} = U_+ \begin{pmatrix} H_u \\ H'_u \end{pmatrix}, \quad (4.57)$$

where U_- and U_+ are the 2×2 unitary matrices. Consequently, without loss of generality we can rewrite the Higgs potential as

$$\begin{aligned} V_H = & (H_1^\dagger \ H_1'^\dagger) \begin{pmatrix} (M_1^2)_{11} & (M_1^2)_{12} \\ (M_1^2)_{12}^* & (M_1^2)_{22} \end{pmatrix} \begin{pmatrix} H_1 \\ H_1' \end{pmatrix} + (H_2^\dagger \ H_2'^\dagger) \begin{pmatrix} (M_2^2)_{11} & (M_2^2)_{12} \\ (M_2^2)_{12}^* & (M_2^2)_{22} \end{pmatrix} \begin{pmatrix} H_2 \\ H_2' \end{pmatrix} \\ & - \left((H_1 \ H_1') \begin{pmatrix} (M_3^2)_{11} & (M_3^2)_{12} \\ (M_3^2)_{21} & (M_3^2)_{22} \end{pmatrix} \cdot \begin{pmatrix} H_2 \\ H_2' \end{pmatrix} + \text{h.c.} \right) \\ & + \frac{g'^2 + g^2}{8} \left(H_2^\dagger H_2 + H_2'^\dagger H_2' - H_1^\dagger H_1 - H_1'^\dagger H_1' \right)^2 \\ & + \frac{g^2}{2} \left[(H_1^\dagger H_2)(H_2^\dagger H_1) + (H_1^\dagger H_2')(H_2'^\dagger H_1) + (H_1'^\dagger H_2)(H_2^\dagger H_1') + (H_1'^\dagger H_2')(H_2'^\dagger H_1') \right. \\ & \left. + (H_1^\dagger H_1')(H_1'^\dagger H_1) - (H_1^\dagger H_1)(H_1'^\dagger H_1') + (H_2^\dagger H_2')(H_2'^\dagger H_2) - (H_2^\dagger H_2)(H_2'^\dagger H_2') \right], \quad (4.58) \end{aligned}$$

where H_1 ($Y = -1/2$) and H_2 ($Y = 1/2$) have VEVs, while H_1' ($Y = -1/2$) and H_2' ($Y = 1/2$) do not. In Eq. (4.58), we use following the reparametrization:

$$\begin{aligned} \begin{pmatrix} (M_1^2)_{11} & (M_1^2)_{12} \\ (M_1^2)_{12}^* & (M_1^2)_{22} \end{pmatrix} &= U_- \begin{pmatrix} (M_-^2)_{11} & (M_-^2)_{12} \\ (M_-^2)_{12}^* & (M_-^2)_{22} \end{pmatrix} U_-^\dagger, \\ \begin{pmatrix} (M_2^2)_{11} & (M_2^2)_{12} \\ (M_2^2)_{12}^* & (M_2^2)_{22} \end{pmatrix} &= U_+ \begin{pmatrix} (M_+^2)_{11} & (M_+^2)_{12} \\ (M_+^2)_{12}^* & (M_+^2)_{22} \end{pmatrix} U_+^\dagger, \\ \begin{pmatrix} (M_3^2)_{11} & (M_3^2)_{12} \\ (M_3^2)_{21} & (M_3^2)_{22} \end{pmatrix} &= -U_-^* \begin{pmatrix} B\mu & B_{14}\mu_{14} \\ B_{32}\mu_{32} & B_{34}\mu_{34} \end{pmatrix} U_+^\dagger. \end{aligned} \quad (4.59)$$

Throughout this paper, we restrict ourselves in the CP invariant case. We thus hereafter neglect all CP violating phases in the dimensionful parameters.

The rotated Higgs doublet fields H_1 , H_1' , H_2 and H_2' are expressed as

$$H_1 = \begin{bmatrix} \varphi_1^{0*} \\ -\varphi_1^- \end{bmatrix}, \quad H_2 = \begin{bmatrix} \varphi_2^+ \\ \varphi_2^0 \end{bmatrix}, \quad H_1' = \begin{bmatrix} \varphi_1'^{0*} \\ -\varphi_1'^- \end{bmatrix}, \quad H_2' = \begin{bmatrix} \varphi_2'^+ \\ \varphi_2'^0 \end{bmatrix}, \quad (4.60)$$

where the neutral scalar fields can be parameterized as

$$\begin{aligned} \varphi_1^0 &= \frac{1}{\sqrt{2}} (v_1 + \phi_1 + i\chi_1), \quad \varphi_2^0 = \frac{1}{\sqrt{2}} (v_2 + \phi_2 + i\chi_2), \\ \varphi_1'^0 &= \frac{1}{\sqrt{2}} (\phi_1' + i\chi_1'), \quad \varphi_2'^0 = \frac{1}{\sqrt{2}} (\phi_2' + i\chi_2'), \end{aligned} \quad (4.61)$$

where the VEVs of these neutral components are given by $\langle \varphi_1^0 \rangle = v_1/\sqrt{2}$, $\langle \varphi_2^0 \rangle = v_2/\sqrt{2}$, $\langle \varphi_1'^0 \rangle = 0$ and $\langle \varphi_2'^0 \rangle = 0$. Introducing

$$v = (\sqrt{2}G_F)^{-1/2} \simeq 246 \text{ GeV}, \quad (4.62)$$

and the mixing angle β , we express v_1 and v_2 as $v_1 \equiv v \cos \beta$ and $v_2 \equiv v \sin \beta$. The vacuum conditions for the Higgs potential are given by

$$\begin{aligned}
\frac{1}{v} \frac{\partial V_H}{\partial \phi_1} \Big|_{\phi_i=0} &= c_\beta \left((M_1^2)_{11} + \frac{m_Z^2}{2} c_{2\beta} \right) - s_\beta (M_3^2)_{11} = 0, \\
\frac{1}{v} \frac{\partial V_H}{\partial \phi_2} \Big|_{\phi_i=0} &= s_\beta \left((M_2^2)_{11} - \frac{m_Z^2}{2} c_{2\beta} \right) - c_\beta (M_3^2)_{11} = 0, \\
\frac{1}{v} \frac{\partial V_H}{\partial \phi'_1} \Big|_{\phi_i=0} &= c_\beta (M_1^2)_{12} - s_\beta (M_3^2)_{21} = 0, \\
\frac{1}{v} \frac{\partial V_H}{\partial \phi'_2} \Big|_{\phi_i=0} &= s_\beta (M_2^2)_{12} - c_\beta (M_3^2)_{12} = 0.
\end{aligned} \tag{4.63}$$

Solving this set of conditions, one can eliminate $(M_1^2)_{11}$, $(M_2^2)_{11}$, $(M_1^2)_{12}$, and $(M_2^2)_{12}$.

After imposing the vacuum conditions, the mass matrices M_A^2 , $M_{H^\pm}^2$ and M_H^2 for the CP-odd, charged and CP-even scalar component states are respectively obtained in the basis of $(\Phi_1, \Phi_2, \Phi'_1, \Phi'_2)$. It is however more useful to work the mass matrices of the CP-odd scalar bosons and the charged Higgs bosons in the gauge eigenstate basis (the so-called Georgi basis) as [81]

$$\bar{M}_A^2 = O_0^T M_A^2 O_0 = \begin{pmatrix} 0 & 0 & 0 & 0 \\ 0 & \frac{2(M_3^2)_{11}}{s_{2\beta}} & \frac{(M_3^2)_{21}}{c_\beta} & \frac{(M_3^2)_{12}}{s_\beta} \\ 0 & \frac{(M_3^2)_{21}}{c_\beta} & (M_1^2)_{22} + \frac{m_Z^2}{2} c_{2\beta} & (M_3^2)_{22} \\ 0 & \frac{(M_3^2)_{12}}{s_\beta} & (M_3^2)_{22} & (M_2^2)_{22} - \frac{m_Z^2}{2} c_{2\beta} \end{pmatrix}, \tag{4.64}$$

$$\bar{M}_{H^\pm}^2 = O_0^T M_{H^\pm}^2 O_0 = \bar{M}_A^2 + m_W^2 \begin{pmatrix} 0 & 0 & 0 & 0 \\ 0 & 1 & 0 & 0 \\ 0 & 0 & -c_{2\beta} & 0 \\ 0 & 0 & 0 & c_{2\beta} \end{pmatrix}, \tag{4.65}$$

with the orthogonal matrix

$$O_0 = \begin{pmatrix} c_\beta & s_\beta & 0 & 0 \\ -s_\beta & c_\beta & 0 & 0 \\ 0 & 0 & 1 & 0 \\ 0 & 0 & 0 & 1 \end{pmatrix}, \tag{4.66}$$

where we used the abbreviation such as $\sin \theta = s_\theta$ and $\cos \theta = c_\theta$. In this basis the massless modes, which are NG bosons to be absorbed by the longitudinal modes of the weak gauge bosons, are separated in the mass matrices. The basis taken here is essentially the same as that discussed in Ref. [178]. It is also useful to rotate the mass matrix for the CP-even scalar bosons

as

$$\begin{aligned} \bar{M}_H^2 &= O_0 M_H^2 O_0^T \\ &= \begin{pmatrix} m_Z^2 c_{2\beta}^2 & -m_Z^2 s_{2\beta} c_{2\beta} & 0 & 0 \\ -m_Z^2 s_{2\beta} c_{2\beta} & m_Z^2 s_{2\beta}^2 + \frac{2(M_3^2)_{11}}{s_{2\beta}} & \frac{-(M_3^2)_{21}}{c_\beta} & \frac{(M_3^2)_{12}}{s_\beta} \\ 0 & \frac{-(M_3^2)_{21}}{c_\beta} & (M_1^2)_{22} + \frac{m_Z^2}{2} c_{2\beta} & -(M_3^2)_{22} \\ 0 & \frac{(M_3^2)_{12}}{s_\beta} & -(M_3^2)_{22} & (M_2^2)_{22} - \frac{m_Z^2}{2} c_{2\beta} \end{pmatrix}. \end{aligned} \quad (4.67)$$

4.4.2 Definition of the large mass limit

The soft-breaking mass parameters $(M_3^2)_{ij}$ come from the B-terms in Eq. (4.54). When we consider the case with $(M_3^2)_{12} = (M_3^2)_{21} = 0$, the mass matrices \bar{M}_A^2 , $\bar{M}_{H^\pm}^2$ and \bar{M}_H^2 are block diagonal. The upper 2×2 submatrix in each mass matrix corresponds to that in the MSSM; i.e., $2(M_3^2)_{11}/s_{2\beta} \rightarrow m_A^2$, and the other 2×2 submatrix corresponds to that for the extra two scalar bosons. They are separated completely in this case. The model effectively becomes the MSSM in the large mass limit of the extra scalar bosons. On the other hand, in the case with nonzero $(M_3^2)_{12}$ or $(M_3^2)_{21}$, the masses of the light scalars h , H and H^\pm are modified from the MSSM predictions by the mixing via the B-terms between Φ_1 and Φ_1' or between Φ_2 and Φ_2' . These effects are expected to be nonvanishing when $(M_3^2)_{12}$ or $(M_3^2)_{21}$ grows with taking a similar value to the 3-3 or 4-4 component in the mass matrices such as $(M_1^2)_{22}$ or $(M_2^2)_{22}$. We here discuss these effects in details in the following.

We start from discussing the CP-odd scalar mass matrix. In order to examine the decoupling property of the mass matrices, we further rotate \bar{M}_A^2 as

$$\hat{M}_A^2 = \begin{pmatrix} 1 & 0 & 0 & 0 \\ 0 & 1 & 0 & 0 \\ 0 & 0 & c_{\bar{\theta}} & s_{\bar{\theta}} \\ 0 & 0 & -s_{\bar{\theta}} & c_{\bar{\theta}} \end{pmatrix} \bar{M}_A^2 \begin{pmatrix} 1 & 0 & 0 & 0 \\ 0 & 1 & 0 & 0 \\ 0 & 0 & c_{\bar{\theta}} & -s_{\bar{\theta}} \\ 0 & 0 & s_{\bar{\theta}} & c_{\bar{\theta}} \end{pmatrix} = \begin{pmatrix} 0 & 0 & 0 & 0 \\ 0 & \frac{2(M_3^2)_{11}}{s_{2\beta}} & k' M^2 & k M^2 \\ 0 & k' M^2 & M^2 & 0 \\ 0 & k M^2 & 0 & r M^2 \end{pmatrix}, \quad (4.68)$$

where

$$\tan 2\bar{\theta} = \frac{2(M_3^2)_{22}}{(M_1^2)_{22} - (M_2^2)_{22} + m_Z^2 c_{2\beta}}, \quad (4.69)$$

and M^2 , k , k' and r are defined such that

$$\begin{aligned} (M_3^2)_{21} &= \kappa_{21} M^2, \quad (M_3^2)_{12} = \kappa_{12} M^2, \\ (M_1^2)_{22} c_{\bar{\theta}}^2 + (M_2^2)_{22} s_{\bar{\theta}}^2 + (M_3^2)_{22} s_{2\bar{\theta}} + \frac{m_Z^2}{2} c_{2\beta} c_{2\bar{\theta}} &= M^2, \\ (M_1^2)_{22} s_{\bar{\theta}}^2 + (M_2^2)_{22} c_{\bar{\theta}}^2 - (M_3^2)_{22} s_{2\bar{\theta}} - \frac{m_Z^2}{2} c_{2\beta} c_{2\bar{\theta}} &= r M^2, \end{aligned} \quad (4.70)$$

and

$$k' = \frac{c_{\bar{\theta}}}{c_\beta} \kappa_{21} + \frac{s_{\bar{\theta}}}{s_\beta} \kappa_{12}, \quad k = -\frac{s_{\bar{\theta}}}{c_\beta} \kappa_{21} + \frac{c_{\bar{\theta}}}{s_\beta} \kappa_{12}. \quad (4.71)$$

These parameters are relevant to the extra doublets, then the decoupling limit is taken as $M^2 \rightarrow \infty$. Here we assume that $m_A^2 \ll M^2$ and we treat m_A^2/M^2 as an expansion parameter.

One of the eigenvalues of \bar{M}_A^2 should be m_A^2 , the mass of the lightest CP-odd Higgs boson A , which should coincide with $2(M_3^2)_{11}/s_{2\beta}$ in the limit of $M \rightarrow \infty$ if $k = k' = 0$. In generic cases, after diagonalizing the mass matrix, $(M_3^2)_{11}$ is expressed in terms of m_A^2 as

$$\frac{2(M_3^2)_{11}}{s_{2\beta}} = m_A^2 \left\{ \frac{k^2 + (1 + k'^2)r^2}{r^2} + \mathcal{O}\left(\frac{m_A^2}{M^2}\right) \right\} + M^2 \frac{k^2 + rk'^2}{r}. \quad (4.72)$$

The mass eigenvalues for heavier states A_1 and A_2 are

$$m_{A_1}^2 \simeq a_1 M^2, \quad m_{A_2}^2 \simeq a_2 M^2, \quad (4.73)$$

where a_1 and a_2 are given by

$$a_1 = \frac{k^2 + rk'^2 + r(1 + r) - \sqrt{\{k^2 + rk'^2 - r(r - 1)\}^2 + 4k^2r(r - 1)}}{2r},$$

$$a_2 = \frac{k^2 + rk'^2 + r(1 + r) + \sqrt{\{k^2 + rk'^2 - r(r - 1)\}^2 + 4k^2r(r - 1)}}{2r}. \quad (4.74)$$

We note that $a_1 \rightarrow 1$ and $a_2 \rightarrow r$ for $k = k' \rightarrow 0$.

For the charged Higgs mass matrix, via the similar procedure to the case of the CP-odd Higgs bosons, we obtain the deviation in m_{H^\pm} , the mass eigenvalue for the lightest charged scalar H^\pm , from the MSSM prediction as

$$m_{H^\pm} = \sqrt{(m_{H^\pm}^2)^{\text{MSSM}}(1 + \delta_{H^\pm})}, \quad (4.75)$$

where

$$\delta_{H^\pm} = -\frac{1}{2} \frac{m_W^2}{m_A^2 + m_W^2} \frac{k^2 + k'^2 r^2 - c_{2\beta} \{(k^2 - k'^2 r^2) c_{2\bar{\theta}} + 2kk' r s_{2\bar{\theta}}\}}{\{k^2 + (1 + k'^2)r^2\}} + \mathcal{O}\left(\frac{m_A^2}{M^2}\right), \quad (4.76)$$

and $(m_{H^\pm}^2)^{\text{MSSM}}$ is the prediction in the MSSM renormalized in the on-shell scheme [66], which is simply given by [126, 128]

$$(m_{H^\pm}^2)^{\text{MSSM}} = m_A^2 + m_W^2 - \Pi_{H^+H^-}^{\text{1PI}}(m_A^2 + m_W^2) + \Pi_{AA}^{\text{1PI}}(m_A^2) + \Pi_{WW}^{\text{1PI}}(m_W^2), \quad (4.77)$$

where $\Pi_{\phi\phi}^{\text{1PI}}(p^2)$ represent the one particle irreducible diagram contributions to the two point function of the field ϕ at the squared momentum p^2 . Masses of the heavier charged scalar bosons H_1^\pm and H_2^\pm are obtained as

$$m_{H_1^\pm}^2 \simeq a_1 M^2, \quad m_{H_2^\pm}^2 \simeq a_2 M^2. \quad (4.78)$$

In Fig. 1, we show the numerical results for the deviation δ_{H^\pm} defined in Eq. (4.75) due to the quasi-nondecoupling effect of the B-term mixing parameterized by k and k' in our model. The solid curves in the figures represent the results from the full numerical calculation, while the dotted curves are those by using the approximated formula in Eq. (4.76). The deviation δ_{H^\pm} turns out to be negative, and amounts to -20% for a relatively small value of m_A . The magnitude of the deviation is smaller for a larger value of m_A , but still a few times -1% even

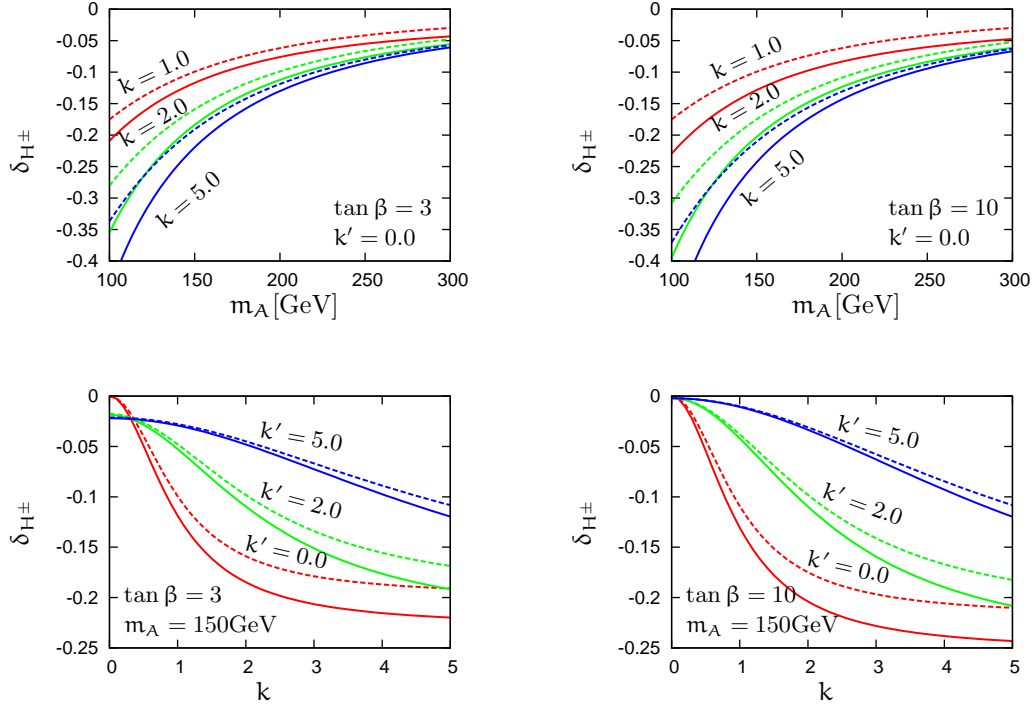


Figure 4.4: The deviation δ_{H^\pm} defined in Eq. (4.75) due to the quasi-nondecoupling effect of the B-term mixing parameterized by k and k' in the 4HDM. We here take $M = 500$ GeV, $r = 1$ and $\bar{\theta} = 0$. The SUSY breaking scale for the MSSM particles is taken to be 1 TeV, and the trilinear soft-breaking parameters A_t and A_b as well as the μ parameter are taken to be zero. The upper figures: δ_{H^\pm} as a function of m_A for $\tan\beta = 3$ (left) and $\tan\beta = 10$ (right) for $k = 1.0, 2.0$ and 5.0 with fixed $k' (= 0.0)$. The lower figures: δ_{H^\pm} as a function of k for $\tan\beta = 3$ (left) and $\tan\beta = 10$ (right) for $k' = 0.0, 2.0$ and 5.0 with the fixed m_A ($= 150$ GeV). In all figures, the solid curves are the results from the full numerical calculation, while the dotted curves are those by using the approximated formula in Eq. (4.76) [68].

for $m_A = 300$ GeV. On the other hand, the deviation is not very sensitive to $\tan\beta$. We note that the results are insensitive to the details of the MSSM parameters such as the soft-breaking mass parameters, the μ parameter and the trilinear $A_{t,b}$ parameters. In fact, when μ and $A_{t,b}$ are varied in the phenomenologically acceptable regions, the radiative corrections vary at most from -2% to $+2\%$. We have confirmed that our results on the one-loop correction in the MSSM agree with those given in Ref. [126, 128]. The mass of H^\pm can be determined with the accuracy of a few percent via the decays of $H^\pm \rightarrow \tau\nu$ and $H^\pm \rightarrow tb$ at the LHC [181], and with the statistical error of less than 1% via $e^+e^- \rightarrow H^+H^-$ at the ILC [182]. The mass of A can also be determined with the resolution about 2% via the decays $A \rightarrow \mu^+\mu^-$ at the LHC, while at the ILC it can be measured with the precision 0.2% via $e^+e^- \rightarrow HA$ [182]. Therefore, the quasi-nondecoupling effect on m_{H^\pm} can be extracted when both m_{H^\pm} and m_A are measured at future collider experiments. The prediction on m_{H^\pm} (not on δ_{H^\pm}) in the 4HDM is shown in Fig. 5 with the comparison of the result in the MSSM.

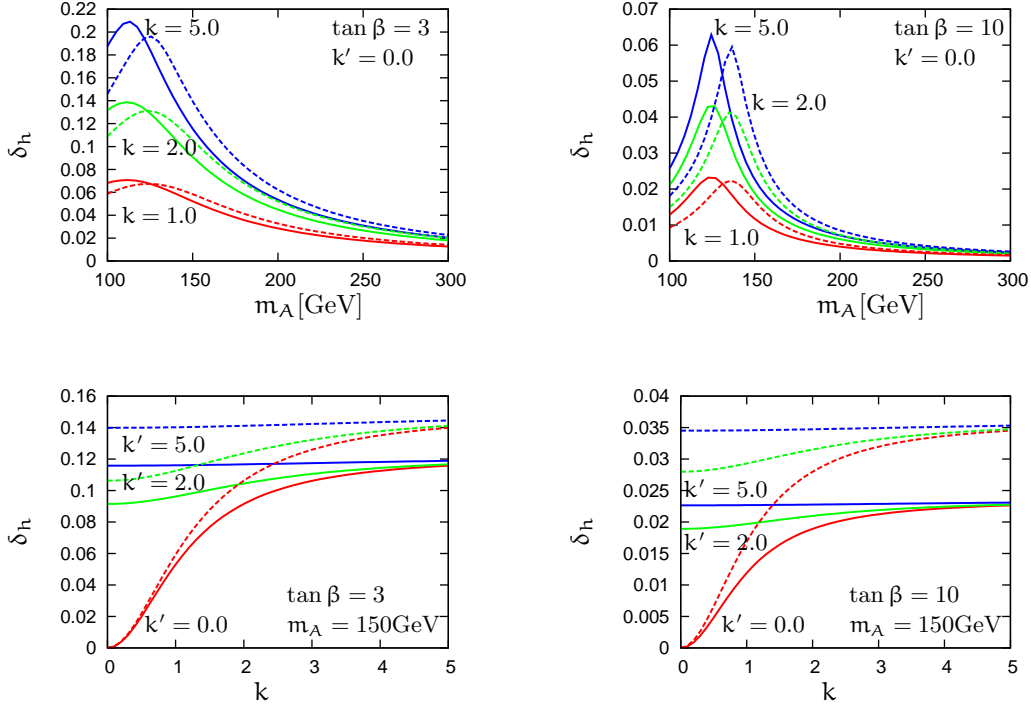


Figure 4.5: The deviation δ_h in $m_h = m_h^{\text{MSSM}}(1 + \delta_h)$ due to the quasi-nondecoupling effect of the B-term mixing parameterized by k and k' in the 4HDM, where m_h^{MSSM} is the renormalized mass of h . We here take $M = 500$ GeV, $r = 1$ and $\bar{\theta} = 0$. The SUSY soft-breaking scale for the MSSM particles is taken to be 1 TeV (solid curves) and 2 TeV (dotted curves), and the trilinear soft-breaking parameters A_t and A_b as well as the μ parameter are taken to be zero. The upper figures: δ_h as a function of m_A for $\tan \beta = 3$ (left) and $\tan \beta = 10$ (right) for $k = 1.0, 2.0$ and 5.0 with fixed $k' (= 0.0)$. The lower figures: δ_h as a function of k for $\tan \beta = 3$ (left) and $\tan \beta = 10$ (right) for $k' = 0.0, 2.0$ and 5.0 with the fixed $m_A (= 150$ GeV) [68].

Next, the CP-even scalar mass matrix \bar{M}_H^2 can also be diagonalized. We first define \hat{M}_H^2 by

$$\hat{M}_H^2 = \begin{pmatrix} 1 & 0 & 0 & 0 \\ 0 & 1 & 0 & 0 \\ 0 & 0 & c_{\bar{\theta}} & -s_{\bar{\theta}} \\ 0 & 0 & s_{\bar{\theta}} & c_{\bar{\theta}} \end{pmatrix} \bar{M}_H^2 \begin{pmatrix} 1 & 0 & 0 & 0 \\ 0 & 1 & 0 & 0 \\ 0 & 0 & c_{\bar{\theta}} & s_{\bar{\theta}} \\ 0 & 0 & -s_{\bar{\theta}} & c_{\bar{\theta}} \end{pmatrix}, \quad (4.79)$$

and according to the usual mathematical procedure \hat{M}_H^2 can be block-diagonalized by rotating the basis with an appropriate orthogonal matrix O_{MH} as

$$O_{MH}^T \hat{M}_H^2 O_{MH} = \begin{pmatrix} m_Z^2 c_{2\beta}^2 & -m_Z^2 c_{2\beta} s_{2\beta} R & 0 & 0 \\ -m_Z^2 c_{2\beta} s_{2\beta} R & m_A^2 + m_Z^2 s_{2\beta}^2 R^2 & 0 & 0 \\ 0 & 0 & a_1 M^2 & 0 \\ 0 & 0 & 0 & a_2 M^2 \end{pmatrix} + \mathcal{O}\left(\frac{m_A^2}{M^2}\right), \quad (4.80)$$

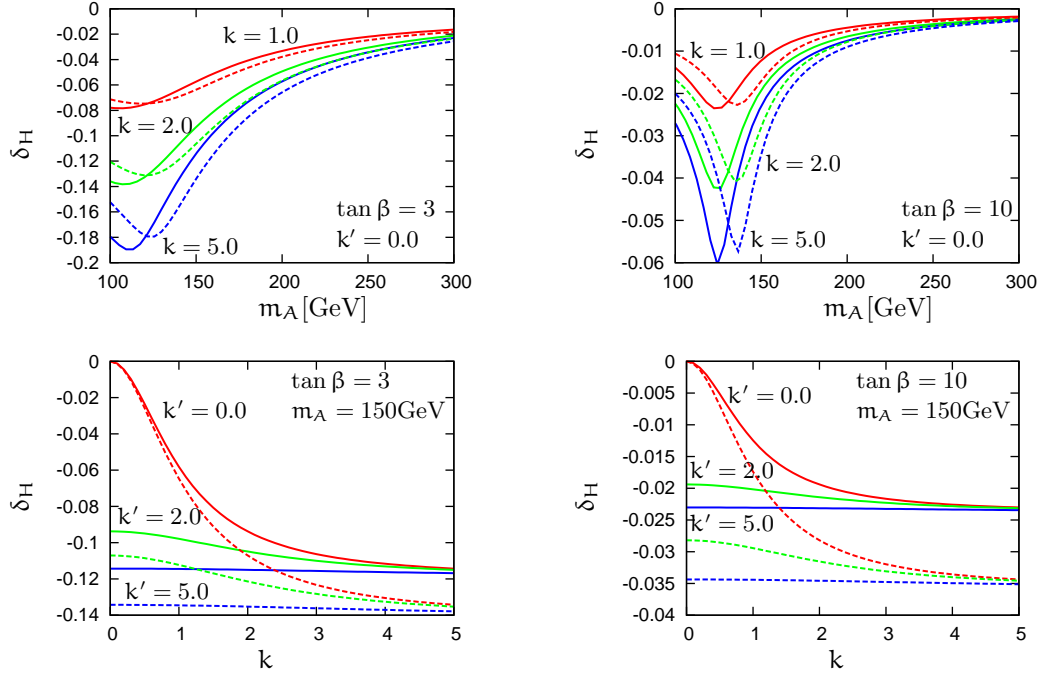


Figure 4.6: The deviation δ_H in $m_H = m_H^{\text{MSSM}}(1 + \delta_H)$ of the renormalized mass of the second lightest CP-even Higgs boson H due to the quasi-nondecoupling effect of the B-term mixing parameterized by k and k' in the 4HDM. We here take $M = 500$ GeV, $r = 1$ and $\bar{\theta} = 0$. The SUSY soft-breaking scale of the MSSM particles is taken to be 1 TeV (solid curves) and 2 TeV (dotted curves), and the trilinear soft-breaking parameters A_t and A_b as well as the μ parameter are taken to be zero. The upper figures: δ_H as a function of m_A for $\tan \beta = 3$ (left) and $\tan \beta = 10$ (right) for $k = 1.0, 2.0$ and 5.0 with fixed $k' (= 0.0)$. The lower figures: δ_H as a function of k for $\tan \beta = 3$ (left) and $\tan \beta = 10$ (right) for $k' = 0.0, 2.0$ and 5.0 with the fixed $m_A (= 150$ GeV) [68].

where R is defined as

$$R = \frac{1}{\sqrt{1 + \frac{k^2}{r^2} + k'^2}}. \quad (4.81)$$

The upper 2×2 submatrix coincides to the mass matrix of the two light scalar bosons H and h of the MSSM when $M \rightarrow \infty$ if $k = k' = 0$. For the case with nonzero k and k' , after diagonalizing the 2×2 submatrix by the mixing angle α_{eff} the mass eigenvalues of the CP-even Higgs bosons are obtained as

$$\begin{aligned} m_h^2 &= \frac{1}{2} \left[m_A^2 + m_Z^2 (c_{2\beta}^2 + R^2 s_{2\beta}^2) - \sqrt{\{(m_A^2 - m_Z^2 (1 - (1 - R^2)s_{2\beta}^2)\}^2 + 4m_A^2 m_Z^2 s_{2\beta}^2 R^2} \right. \\ &\quad \left. + m_A^2 \mathcal{O}\left(\frac{m_A^2}{M^2}\right) + \Delta_h^{\text{loop}} \right], \\ m_H^2 &= \frac{1}{2} \left[m_A^2 + m_Z^2 (c_{2\beta}^2 + R^2 s_{2\beta}^2) + \sqrt{\{m_A^2 - m_Z^2 (1 - (1 - R^2)s_{2\beta}^2)\}^2 + 4m_A^2 m_Z^2 s_{2\beta}^2 R^2} \right. \\ &\quad \left. + m_A^2 \mathcal{O}\left(\frac{m_A^2}{M^2}\right) + \Delta_H^{\text{loop}} \right], \end{aligned} \quad (4.82)$$

where Δ_h^{loop} and Δ_H^{loop} represent the one-loop corrections in the MSSM. The masses of heavier states H'_1 and H'_2 are given by $m_{H'_1}^2 \simeq a_1 M^2 \{1 + \mathcal{O}(m_A^2/M^2)\}$ and $m_{H'_2}^2 \simeq a_2 M^2 \{1 + \mathcal{O}(m_A^2/M^2)\}$. The mixing angle α_{eff} satisfies the relation

$$\tan(\beta - \alpha_{\text{eff}}) = \frac{m_h^2 - m_A^2 - m_Z^2 s_{2\beta}^2 R^2}{m_Z^2 c_{2\beta} s_{2\beta} R} \left\{ 1 + \mathcal{O}\left(\frac{m_A^2}{M^2}\right) + \Delta_{\tan(\beta - \alpha)}^{\text{loop}} \right\}, \quad (4.83)$$

where $\Delta_{\tan(\beta - \alpha)}^{\text{loop}}$ is the one-loop correction in the MSSM. Notice that m_h and m_H given in Eq. (4.82) and $\tan(\beta - \alpha_{\text{eff}})$ in Eq. (4.83) do not depend on the sign of k and k' . We note that the effective mixing angle α_{eff} contains information of the B-term quasi-nondecoupling effects between Φ_1 and Φ'_1 or between Φ_2 and Φ'_2 by k and k' , but for $m_A^2 \ll M^2$ the tree level formula with the angle α in the MSSM can still hold by replacing α by α_{eff} in a good approximation. For example, the coupling constants of the two light CP-even Higgs bosons with the weak gauge bosons V ($V = W^\pm$ and Z^0) in the case with nonzero k and k' are given by

$$\Gamma_{VVh} = -\frac{m_V^2}{v} \{c_\beta(O_H)_{12} + s_\beta(O_H)_{22}\} = \frac{m_V^2}{v} \sin(\beta - \alpha_{\text{eff}}) \left(1 + \Delta_{hVV}^{\text{loop}}\right), \quad (4.84)$$

$$\Gamma_{VVH} = -\frac{m_V^2}{v} \{c_\beta(O_H)_{11} + s_\beta(O_H)_{21}\} = \frac{m_V^2}{v} \cos(\beta - \alpha_{\text{eff}}) \left(1 + \Delta_{HVV}^{\text{loop}}\right), \quad (4.85)$$

where $\Delta_{hVV}^{\text{loop}}$ and $\Delta_{HVV}^{\text{loop}}$ represent radiative corrections in the MSSM. Finally, in general, magnitudes of k and k' are not necessarily smaller than 1, still it is helpful to deduce the approximate

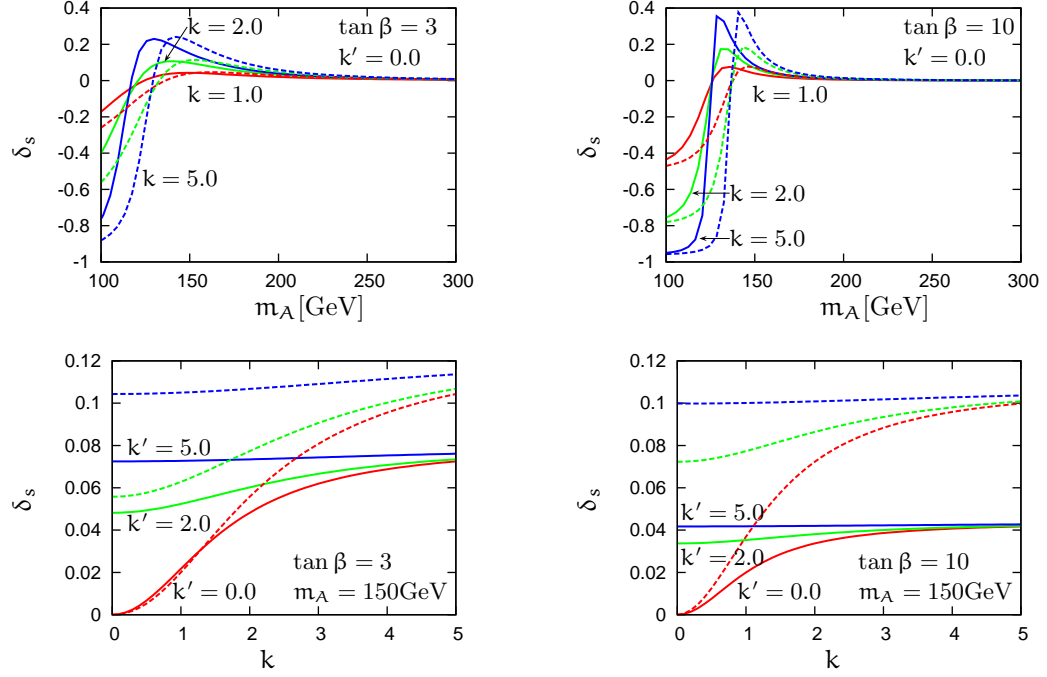


Figure 4.7: The deviation δ_s in Eq. (4.28). due to the quasi-nondecoupling effect of extra doublet fields via the B-term mixing parameterized by k and k' in the 4HDM. We here take $M = 500$ GeV, $r = 1$ and $\bar{\theta} = 0$. The SUSY soft-breaking scale of the MSSM particles is taken to be 1 TeV (solid curves) and 2 TeV (dotted curves), and the trilinear soft-breaking parameters A_t and A_b as well as the μ parameter are taken to be zero. The upper figures: δ_s as a function of m_A for $\tan \beta = 3$ (left) and $\tan \beta = 10$ (right) for $k = 1.0, 2.0$ and 5.0 with fixed $k' (= 0.0)$. The lower figures: δ_s as a function of k for $\tan \beta = 3$ (left) and $\tan \beta = 10$ (right) for $k' = 0.0, 2.0$ and 5.0 with the fixed $m_A (= 150$ GeV) [68].

formulae assuming that they are small;

$$m_h^2 = (m_h^2)^{\text{MSSM}} \left(1 + \frac{m_Z^2 s_{2\beta}^2 (\frac{k^2}{r^2} + k'^2)}{\sqrt{(m_A^2 - m_Z^2)^2 + 4m_Z^2 m_A^2 s_{2\beta}^2}} + \mathcal{O}(k^4, k'^4, k^2 k'^2) + \mathcal{O}\left(\frac{m_A^2}{M^2}\right) \right), \quad (4.86)$$

$$m_H^2 = (m_H^2)^{\text{MSSM}} \left(1 - \frac{m_Z^2 s_{2\beta}^2 (\frac{k^2}{r^2} + k'^2)}{\sqrt{(m_A^2 - m_Z^2)^2 + 4m_Z^2 m_A^2 s_{2\beta}^2}} + \mathcal{O}(k^4, k'^4, k^2 k'^2) + \mathcal{O}\left(\frac{m_A^2}{M^2}\right) \right), \quad (4.87)$$

$$\tan(\beta - \alpha_{\text{eff}}) = [\tan(\beta - \alpha)]^{\text{MSSM}} \left(1 + \frac{(m_A^2 - 2m_h^2 - m_Z^2 s_{2\beta}^2)(\frac{k^2}{r^2} + k'^2)}{2(m_A^2 - m_h^2 + m_Z^2 s_{2\beta}^2)} + \mathcal{O}(k^4, k'^4, k^2 k'^2) + \mathcal{O}\left(\frac{m_A^2}{M^2}\right) \right), \quad (4.88)$$

where $(m_h^2)^{\text{MSSM}}$, $(m_H^2)^{\text{MSSM}}$ and $[\tan(\beta - \alpha)]^{\text{MSSM}}$ are the corresponding parameters evaluated at the one-loop level assuming the MSSM. In this paper, we have used the approximate one-loop formula given in Ref. [66] in evaluating $(m_h^2)^{\text{MSSM}}$, $(m_H^2)^{\text{MSSM}}$ and $[\tan(\beta - \alpha)]^{\text{MSSM}}$.

In Fig. 2, we show the numerical results for the deviation δ_h in $m_h = m_h^{\text{MSSM}}(1 + \delta_h)$, where m_h^{MSSM} is the one-loop corrected mass of h , due to the quasi-nondecoupling effect of the B-term mixing parameterized by k and k' in the 4HDM. The SUSY soft-breaking scale of the MSSM is taken to be 1 TeV and 2 TeV, and the trilinear soft-breaking parameters A_t and A_b and the μ are taken to be zero. It is found that δ_h is always positive. This is understood from Eq. (4.80). The parameter R is unity for $k = k' = 0$, and is smaller for larger values of k and k' . A smaller value of R ($R < 1$) reduces the value of the off-diagonal term in Eq. (4.80), which makes the mixing between the first two CP-even states weaker. Consequently, the mass difference between h and H becomes smaller than the case with the MSSM case with the same value of m_A and $\tan\beta$. The deviation takes its maximal values (6-20 % for $\tan\beta = 3$ and 2-5 % for $\tan\beta = 10$) around the crossing point ($m_A \sim 130$ -150 GeV) where the role of h and H are exchanged. For larger values of m_A the magnitude of δ_h is smaller, but it can be still 3-6 % (about 1 %) at $m_A = 200$ GeV for $\tan\beta = 3$ (10). These values are substantial and can be tested by the precise measurement of m_h at the LHC (the ILC), where m_h is expected to be determined with about 0.1% [183] accuracy at the LHC, while at the ILC it is expected to be measured within less than 70 MeV [184]) error. The prediction on m_h (not on δ_h) in the 4HDM is shown in Fig. 5 with the comparison of the result in the MSSM. We can see that in the 4HDM m_h reaches its maximal value at a smaller m_A than that in the MSSM, although the predicted upper bound on the m_h is the same in both models.

In Fig. 3, we show the deviation δ_H in $m_H = m_H^{\text{MSSM}}(1 + \delta_H)$, where m_H^{MSSM} is the one-loop corrected mass of H , due to the quasi-nondecoupling effect of the B-term mixing parameterized by k and k' in the 4HDM. The SUSY parameters are taken as in the same way as Fig. 2. As we discussed, the mixing of the light two CP-even states is weakened by non-zero values of k and k' , so that m_H is smaller than the prediction in the MSSM. Therefore, δ_H is negative as we expect. The behavior of δ_H as a function of m_A and $\tan\beta$ are similar to the case of δ_h except for the sign. The magnitude is maximal around the crossing point ($m_A = 130$ -150 GeV), and

amounts to -18% (-5%) for $\tan\beta = 3$ (10). At the LHC and the ILC, the mass of H can be determined with the similar precision to that of A mentioned in the previous paragraph. The prediction on m_H (not on δ_H) in the 4HDM is shown in Fig. 5 with the comparison with the result in the MSSM.

In Fig. 4, we show the numerical results for the deviation δ_s defined in Eq. (4.75), in which $[\sin^2(\beta - \alpha)]^{\text{MSSM}}$ is the one-loop corrected mixing factor $\sin^2(\beta - \alpha)$ evaluated in the MSSM. δ_s is the net deviation from the MSSM prediction due to the quasi-nondecoupling effect of the B-term mixing parameterized by k and k' in the 4HDM. The SUSY soft-breaking scale of the MSSM is taken to be 1 TeV and 2 TeV, and the trilinear soft-breaking parameters A_t and A_b and the μ parameter are taken to be zero. In the figures, we can see that δ_s is negative when m_A is smaller than the crossing point at $m_A \sim 130\text{-}150$ GeV, while it is positive for larger m_A . The deviation can be as large as $\mathcal{O}(10)\%$ ($\tan\beta = 3$) and $\mathcal{O}(20)\%$ ($\tan\beta = 10$) just above the crossing point; i.e., at around $m_A \sim 140\text{-}150$ GeV. It is rapidly close to unity for larger values of m_A . Notice that for larger soft-SUSY-breaking scale, a larger δ_s is possible. The prediction on $\sin^2(\beta - \alpha_{\text{eff}})$ (not on δ_s) in the 4HDM is shown in Fig. 5 with the comparison with the result in the MSSM.

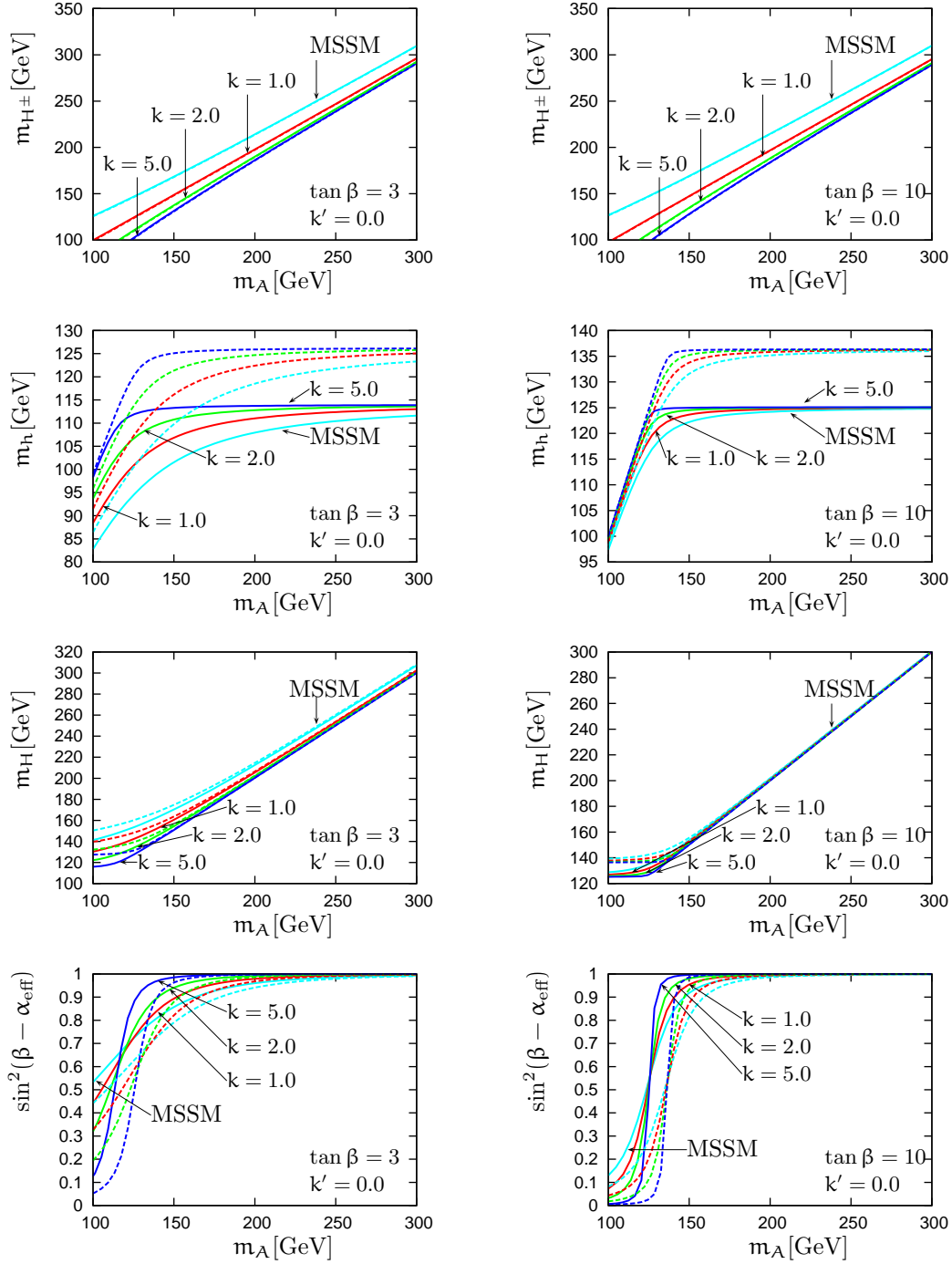


Figure 4.8: The values of m_{H^\pm}, m_h, m_H and $\sin^2(\beta - \alpha_{\text{eff}})$ in the 4HDM and the MSSM as a function of m_A for $k = 1.0, 2.0$ and 5.0 . The soft-SUSY-breaking scale of the MSSM is set to be 1 TeV (solid curves) and 2 TeV (dotted curves). The trilinear soft-breaking parameters A_t and A_b as well as the μ parameter are taken to be zero. The other parameters are taken as $M = 500$ GeV, $r = 1$, $\bar{\theta} = 0$ and $k' = 0$. Figures in the left column are for $\tan \beta = 3$ and those in the right are for $\tan \beta = 10$ [68].

Part II

Models which can explain the
phenomena beyond the SM at the
TeV scale

Chapter 5

Review of radiative seesaw models

The neutrino oscillation has been established by experiments. This suggest that neutrinos have tiny masses as compared to the electroweak scale. This is clear evidence for physics beyond the SM. If neutrinos are the Majorana fermion, then the tiny masses of left-handed neutrinos are generated from the dimension-five effective operators

$$\mathcal{L} = \frac{c_{ij}}{2\Lambda} \overline{\nu_L^{ci}} \nu_L^j \phi^0 \phi^0, \quad (5.1)$$

where Λ represents a mass scale for new physics, c_{ij} are dimensionless coefficients, and ϕ^0 is the Higgs boson. After electroweak symmetry breaking due to the VEV of the Higgs boson $\langle \phi^0 \rangle = v$, the mass matrix M_ν^{ij} for left-handed neutrinos are generated as

$$M_\nu^{ij} = \frac{c_{ij}}{2\Lambda} v^2. \quad (5.2)$$

Since we have already known $v \simeq 246$ GeV via the muon decay experiments, the coefficient c_{ij}/Λ has to be of order 10^{-14} GeV $^{-1}$ to reproduce the observed tiny neutrino masses which are around $\mathcal{O}(0.1)$ eV. The seesaw mechanism is the simple scenario to obtain the operator in Eq. (5.1) in the low energy effective theory from the tree level diagram, where right-handed neutrinos [163] are added to the SM. At the same time, the baryon asymmetry can be generated via the lepton number violation in the CP violating decays of right-handed Majorana neutrinos. In addition, in a SUSY extension of the model with such a heavy Majorana neutrinos, the lightest SUSY partner particle can be a candidate of the dark matter. In this model, if we assume the magnitude of the coefficient c_{ij} to be $\mathcal{O}(1)$, then the mass of right-handed neutrinos has to be of $\mathcal{O}(10^{14})$ GeV to obtain the scale of left-handed neutrino masses. Although this scenario is simple, it requires another hierarchy between the mass of right-handed neutrinos and the electroweak scale. In addition, physics at such a large mass scale is difficult to be tested at collider experiments.

As the other way to obtain the dimension six operator, radiative seesaw models [16–21] have been proposed, where neutrino masses are generated at the loop level. In this class of models, the coefficient c_{ij} is naturally suppressed by the loop factor, so that masses of new particles in these models can be as low as the TeV scale. Therefore, they are expected to be directly testable at current and future collider experiments. One of the characteristic features of these models is an extended Higgs sector. Another feature is the Majorana nature, either introducing lepton number violating couplings or introducing right-handed neutrinos.

The original model for radiative neutrino mass generation was first proposed by A. Zee [16], where neutrino masses are generated at the one-loop level by adding an extra $SU(2)_L$ doublet scalar field and a charged singlet scalar field with lepton number violating couplings to the SM particle entries. Phenomenology of this model has been studied in Ref. [185, 186]. However, it turned out that it was difficult to reproduce the current data for neutrino oscillation in this original model [187]. Some extensions have been discussed in Ref. [188].

The simplest successful model today may be the one proposed by A. Zee [17] and K. S. Babu [18], in which two kinds of $SU(2)_L$ singlet scalar fields are introduced; i.e., a singly charged scalar boson and a doubly charged one. These fields carry lepton number of two unit. In this model, which we refer to as the Zee-Babu model, the neutrino masses are generated at the two-loop level. Phenomenology of this model has been discussed in Refs. [189–193]. Although the Zee-Babu model can explain neutrino data, this model has not a dark matter candidate, because there are no new neutral particles in the particle content.

Apart from the Zee-Babu model, there is also another type of radiative seesaw models [19–21], where TeV-scale right-handed neutrinos are introduced with the odd charge under the exact discrete Z_2 symmetry. In these models, the Z_2 symmetry protects the tree level Dirac Yukawa coupling among the lepton doublet, Higgs doublet and right-handed neutrino. At the same time, this Z_2 symmetry also protect the decay of the lightest Z_2 odd particle, which can be a candidate of dark matter. This is an advantage of this class of models [194–196]. In addition to the explanation of neutrino masses and dark matter, baryon asymmetry of the Universe may also be able to explain in the model proposed in Ref. [21]. In Ref. [197], detailed phenomenological study of this model has been analyzed.

These models give an explanation for tiny masses of neutrino, give a candidate for dark matter and/or explain baryon asymmetry of the Universe. However, the origin of masses of neutrinos and dark matter comes from different mass scales. In Refs. [198, 199], it has been proposed that both of these masses can be explained by the spontaneous breakdown of the gauged $U(1)_{B-L}$ symmetry.

In the above discussion, we consider the case where neutrinos are the Majorana fermion, while we can also consider the case where those are the Dirac fermion. A model which can generate the Dirac masses of neutrinos is invariant under the $U(1)$ lepton number such as the SM. Up to the present, phenomena suggesting lepton number violation have not been confirmed yet by experiments such as neutrino less double beta decay. Therefore, it is valuable to investigate a possibility that kind of models. In Refs. [200–207], radiative generation of masses for Dirac neutrinos has been proposed.

In Part II, we first discuss the theoretical and experimental bounds of the model proposed in Ref. [21]. Second, we discuss the supersymmetric extension of the Zee-Babu model, and its phenomenology at the LHC. Finally, we discuss the model with an isospin doublet with $Y = 3/2$ field $\Phi_{3/2}$. We study the phenomenology of the simple model which includes $\Phi_{3/2}$ at the LHC, and then we show the model with $\Phi_{3/2}$ can apply to the radiative seesaw model, where neutrino masses can generate at one-loop level as well as the dark matter candidate exists.

Chapter 6

Three-loop neutrino mass model

In this chapter, we discuss a TeV-scale model has been proposed by M. Aoki, S. Kanemura and O. Seto [21], in which 1) tiny neutrino masses are generated without excessive fine tuning at the three-loop level by the dynamics of an extended Higgs sector and right-handed neutrinos under an unbroken Z_2 parity, 2) the Z_2 parity also guaranties the stability of a dark matter candidate which is a Z_2 odd scalar boson, and 3) the strongly first order phase transition for successful electroweak baryogenesis can be realized by the nondecoupling effect in the Higgs sector. Phenomenology of this model has been discussed in Ref. [197], and the related collider physics [38, 193, 208] and dark matter properties [196] have also been studied. In these papers, phenomenologically allowed parameter regions have been mainly discussed.

We investigate the theoretical constraint on the parameter regions in this model [21] from the requirement of vacuum stability and perturbativity up to a given cutoff scale Λ of the model [74]. In the present model, there is no mechanism for cancellation of the quadratic divergences which appear in the renormalization calculation for the Higgs boson mass, so that a huge fine tuning is required if Λ is much higher than the electroweak scale. To avoid such an unnatural situation, we need to consider Λ to be at most $\mathcal{O}(10)$ TeV, above which the model would be replaced by a more fundamental theory [209]. Hence, we have to study the theoretical consistency of the model up to such values for Λ . In particular, some of the neutrino Yukawa coupling constants are of order one in magnitude, as the scale of tiny neutrino masses is generated by loop dynamics so that we do not need fine tuning for the size of the coupling constants. In addition, some of the coupling constants in the Higgs potential are of order one to realize the nondecoupling one-loop effect for strongly first order phase transition. Although the parameters discussed in the previous works satisfy the bound from tree-level unitarity [89, 90], it is non-trivial that the model can be consistent at the quantum level with the theoretical requirements up to $\Lambda \sim 10$ TeV. Theoretical bounds from vacuum stability and perturbativity have been used to constrain parameters in extended Higgs sectors such as the THDM [86, 87] and the Zee model [88]. Here we apply the similar analysis to the model. We prepare a full set of the renormalization group equations (RGEs) for dimensionless coupling constants in the model at the one-loop level, and analyze the behavior of running coupling constants.

We also calculate the phenomenological constraint from lepton flavor violation (LFV) in the model. In the previous analysis [21, 197] only the constraint from $\mu \rightarrow e\gamma$ data has been taken into account. Here, we also analyze the one-loop induced $\mu \rightarrow eee$ process, whose current experimental data [210] turn out to give a stronger bound on the parameter space than those of $\mu \rightarrow e\gamma$ [211].

	Q_L^i	u_R^i	d_R^i	L_L^i	e_R^i	Φ_1	Φ_2	S^\pm	η	N_R^α
$Z_2(\text{exact})$	+	+	+	+	+	+	+	-	-	-
$\tilde{Z}_2(\text{softly broken})$	+	-	-	+	+	+	-	+	-	+

Table 6.1: Particle properties under the discrete symmetries [21].

6.1 Model

In this model, two Higgs doublets (Φ_1 and Φ_2) with hypercharge $Y = 1/2$, charged scalar singlets (S^\pm), a real scalar singlet (η) and right-handed neutrinos (N_R^α with $\alpha = 1, 2$) are introduced. We impose two kinds of discrete symmetries; i.e., Z_2 and \tilde{Z}_2 to the model. The former, which is exact, is introduced in order to forbid the tree-level Dirac neutrino mass term and at the same time to guarantee the stability of dark matter. The latter one, which is softly broken, is introduced to avoid the tree-level flavor changing neutral current [29]. Under the \tilde{Z}_2 symmetry there are four types of Yukawa interactions [36, 37]. In our model [21], so-called the type-X Yukawa interaction [38, 39] is favored since the charged Higgs boson from the two doublets can be taken to be as light as around 100 GeV without contradicting the $b \rightarrow s\gamma$ data. Such a light charged Higgs boson is important to reproduce the correct magnitude of neutrino masses. The particle properties under the discrete symmetries are shown in Table 6.1, where Q_L^i , u_R^i , d_R^i , L_L^i and e_R^i are the i -th generation of the left-handed quark doublet, the right-handed up-type quark singlet, the left-handed lepton doublet and the right-handed charged lepton singlet, respectively.

The type-X Yukawa interaction is given by

$$\mathcal{L}_{\text{Yukawa}}^{\text{Type-X}} = - \sum_{i,j} [(\bar{Q}_L^i Y_{ij}^d \Phi_2 d_R^j) + (\bar{Q}_L^i Y_{ij}^u \Phi_2^c u_R^j) + (\bar{L}_L^i Y_{ij}^e \Phi_1 e_R^j)] + \text{h.c.}, \quad (6.1)$$

where Yukawa coupling matrix for leptons is diagonal, $Y_{ij}^e = \text{diag}(y_{e^1}, y_{e^2}, y_{e^3})$. The mass term and the Yukawa interaction for N_R^α are written as

$$\mathcal{L}_{N_R} = \sum_{\alpha=1}^2 \frac{1}{2} m_{N_R^\alpha} (\overline{N_R^\alpha}^c N_R^\alpha) - \sum_{i=1}^3 \sum_{\alpha=1}^2 \left[h_i^\alpha (\overline{e_R^i}^c) N_R^\alpha S^+ + \text{h.c.} \right]. \quad (6.2)$$

The scalar potential is given by

$$\begin{aligned} V = & + \mu_1^2 |\Phi_1|^2 + \mu_2^2 |\Phi_2|^2 - \left[\mu_3^2 \Phi_1^\dagger \Phi_2 + \text{h.c.} \right] \\ & + \frac{1}{2} \lambda_1 |\Phi_1|^4 + \frac{1}{2} \lambda_2 |\Phi_2|^4 + \lambda_3 |\Phi_1|^2 |\Phi_2|^2 + \lambda_4 |\Phi_1^\dagger \Phi_2|^2 + \frac{1}{2} \left[\lambda_5 (\Phi_1^\dagger \Phi_2)^2 + \text{h.c.} \right] \\ & + \mu_S^2 |S^-|^2 + \rho_1 |S^-|^2 |\Phi_1|^2 + \rho_2 |S^-|^2 |\Phi_2|^2 + \frac{1}{4} \lambda_S |S^-|^4 \\ & + \frac{1}{2} \mu_\eta^2 \eta^2 + \frac{1}{2} \sigma_1 \eta^2 |\Phi_1|^2 + \frac{1}{2} \sigma_2 \eta^2 |\Phi_2|^2 + \frac{1}{4!} \lambda_\eta \eta^4 \\ & + \sum_{a,b=1}^2 \left[\kappa \epsilon_{ab} (\Phi_a^c)^\dagger \Phi_b S^- \eta + \text{h.c.} \right] + \frac{1}{2} \xi |S^-|^2 \eta^2, \end{aligned} \quad (6.3)$$

where ϵ_{ab} are anti-symmetric matrices with $\epsilon_{12} = 1$. The parameters μ_3^2 , λ_5 , and κ are complex numbers. Two of their phases can be absorbed by rephasing the fields, and the rest is a physical one. In this paper, we neglect this CP-violating phase for simplicity. The Higgs doublets are parameterized as

$$\Phi_i = \begin{pmatrix} w_i^+ \\ \frac{1}{\sqrt{2}}(h_i + v_i + iz_i) \end{pmatrix}, \quad (6.4)$$

where v_i are vacuum expectation values (VEVs) of the Higgs fields, and these are constrained by $v(= \sqrt{v_1^2 + v_2^2}) \simeq 246$ GeV. The ratio of the two VEVs is defined by $\tan \beta = v_2/v_1$. The physical scalar states h , H , A and H^\pm in the Z_2 even sector can be obtained mixing angles α and β ,

$$\begin{pmatrix} w_1^\pm \\ w_2^\pm \end{pmatrix} = R(\beta) \begin{pmatrix} w^\pm \\ H^\pm \end{pmatrix}, \quad \begin{pmatrix} z_1 \\ z_2 \end{pmatrix} = R(\beta) \begin{pmatrix} z \\ A \end{pmatrix}, \quad \begin{pmatrix} h_1 \\ h_2 \end{pmatrix} = R(\alpha) \begin{pmatrix} H \\ h \end{pmatrix}, \quad (6.5)$$

where w^\pm and z are the NG bosons absorbed by the longitudinal weak gauge bosons, and the rotation matrix with the angle θ is given by

$$R(\theta) = \begin{pmatrix} \cos \theta & -\sin \theta \\ \sin \theta & \cos \theta \end{pmatrix}. \quad (6.6)$$

The mass formulae of physical scalar states are given by

$$m_A^2 = M^2 - v^2 \lambda_5, \quad (6.7)$$

$$m_{H^\pm}^2 = M^2 - \frac{v^2}{2}(\lambda_4 + \lambda_5), \quad (6.8)$$

$$m_H^2 = \cos^2(\alpha - \beta)M_{11}^2 + 2\sin(\alpha - \beta)\cos(\alpha - \beta)M_{12}^2 + \sin^2(\alpha - \beta)M_{22}^2, \quad (6.9)$$

$$m_h^2 = \sin^2(\alpha - \beta)M_{11}^2 - 2\sin(\alpha - \beta)\cos(\alpha - \beta)M_{12}^2 + \cos^2(\alpha - \beta)M_{22}^2, \quad (6.10)$$

$$m_S^2 = \mu_S^2 + \frac{v^2}{2}\rho_1 \cos^2 \beta + \frac{v^2}{2}\rho_2 \sin^2 \beta, \quad (6.11)$$

$$m_\eta^2 = \mu_\eta^2 + \frac{v^2}{2}\sigma_1 \cos^2 \beta + \frac{v^2}{2}\sigma_2 \sin^2 \beta, \quad (6.12)$$

where $M(= \mu_3/\sqrt{\sin \beta \cos \beta})$ is the soft breaking scale for the \tilde{Z}_2 symmetry, and

$$M_{11}^2 = v^2(\lambda_1 \cos^4 \beta + \lambda_2 \sin^4 \beta) + \frac{v^2}{2}\lambda \sin^2 2\beta, \quad (6.13)$$

$$M_{22}^2 = M^2 + v^2 \sin^2 \beta \cos^2 \beta (\lambda_1 + \lambda_2 - 2\lambda), \quad (6.14)$$

$$M_{12}^2 = v^2 \sin \beta \cos \beta (-\lambda_1 \cos^2 \beta + \lambda_2 \sin^2 \beta + \lambda \cos 2\beta), \quad (6.15)$$

with $\lambda = \lambda_3 + \lambda_4 + \lambda_5$. Notice that M , μ_S and μ_η are free mass parameters irrelevant to the electroweak symmetry breaking.

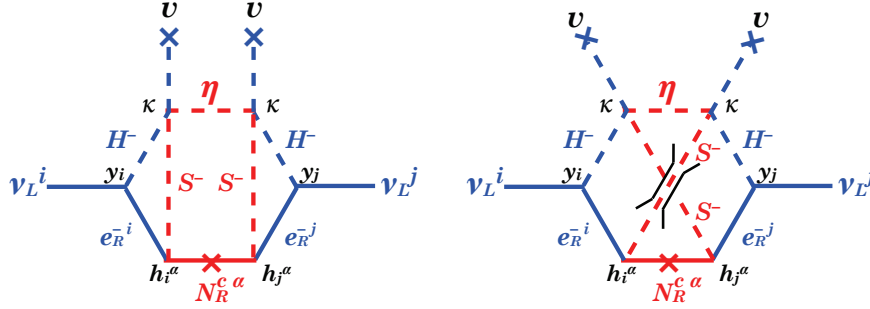


Figure 6.1: The Feynman diagrams for generating tiny neutrino masses [21].

6.2 Neutrino mass and mixing

The neutrino mass matrix M_{ij}^ν is generated by the three-loop diagrams in FIG. 6.2. The absence of lower order loop contributions is guaranteed by the Z_2 symmetry. The resulting mass matrix is calculated as

$$M_{ij}^\nu = \sum_{\alpha=1}^2 4\kappa^2 \tan^2 \beta (y_{\ell_i}^{\text{SM}} h_i^\alpha) (y_{\ell_j}^{\text{SM}} h_j^\alpha) F(m_{H^\pm}, m_S, m_{N_R^\alpha}, m_\eta), \quad (6.16)$$

where the loop integral function F is given by

$$F(m_{H^\pm}, m_S, m_N, m_\eta) = \left(\frac{1}{16\pi^2} \right)^3 \frac{(-m_N)}{m_N^2 - m_\eta^2} \frac{v^2}{m_{H^\pm}^4} \times \int_0^\infty x dx \{B_1(-x, m_{H^\pm}, m_S) - B_1(-x, 0, m_S)\}^2 \left(\frac{m_N^2}{x + m_N^2} - \frac{m_\eta^2}{x + m_\eta^2} \right), \quad (6.17)$$

with $y_{\ell_i}^{\text{SM}} = \sqrt{2}m_{\ell_i}/v$, where ℓ_1, ℓ_2 and ℓ_3 correspond to e, μ and τ , respectively. The function B_1 is the tensor coefficient in the formalism by Passarino-Veltman for one-loop integrals [212]. In the following discussion, we take $m_{N_R^1} = m_{N_R^2} \equiv m_{N_R}$, for simplicity. Numerically, the magnitude of the function F is of order 10^4 eV in the wide range of parameter regions of our interest. Since $y_{\ell_i}^{\text{SM}} < 10^{-2}$, the correct scale of neutrino masses can be naturally obtained from the three-loop diagrams.

The generated mass matrix M_{ij}^ν in Eq. (6.16) of neutrinos can be related to the neutrino oscillation data by

$$M_{ij}^\nu = U_{is} (M_{\text{diag}}^\nu)_{st} (U^T)_{tj}, \quad (6.18)$$

where $M_{\text{diag}}^\nu = \text{diag}(m_1, m_2, m_3)$. For the case of the normal hierarchy we identify the mass eigenvalues as $m_1 = 0$, $m_2 = \sqrt{\Delta m_{\text{solar}}^2}$, $m_3 = \sqrt{\Delta m_{\text{atm}}^2}$, while for inverted hierarchy $m_1 = \sqrt{\Delta m_{\text{atm}}^2}$, $m_2 = \sqrt{\Delta m_{\text{atm}}^2 + \Delta m_{\text{solar}}^2}$ and $m_3 = 0$ are taken. The Maki-Nakagawa-Sakata matrix U_{is} [213] is parameterized as

$$U = \begin{bmatrix} 1 & 0 & 0 \\ 0 & c_{23} & s_{23} \\ 0 & -s_{23} & c_{23} \end{bmatrix} \begin{bmatrix} c_{13} & 0 & s_{13}e^{i\delta} \\ 0 & 1 & 0 \\ -s_{13}e^{-i\delta} & 0 & c_{13} \end{bmatrix} \begin{bmatrix} c_{12} & s_{12} & 0 \\ -s_{12} & c_{12} & 0 \\ 0 & 0 & 1 \end{bmatrix} \begin{bmatrix} 1 & 0 & 0 \\ 0 & e^{i\tilde{\alpha}} & 0 \\ 0 & 0 & e^{i\tilde{\beta}} \end{bmatrix}, \quad (6.19)$$

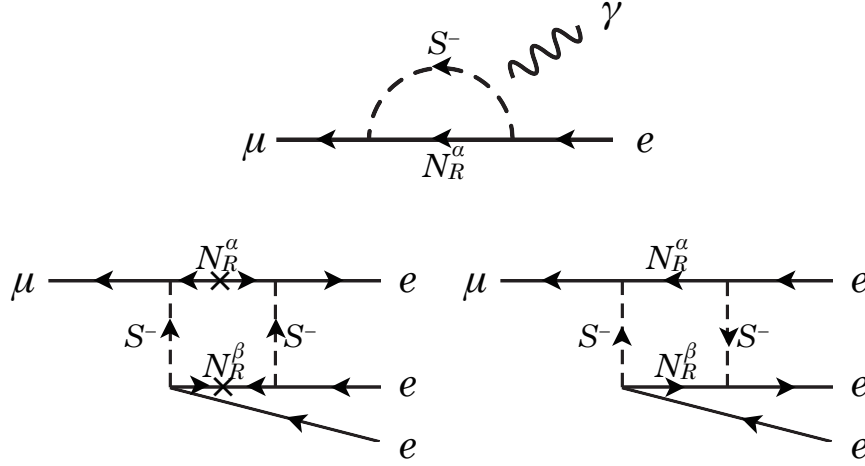


Figure 6.2: The LFV processes [69].

where s_{ij} and c_{ij} represent $\sin \theta_{ij}$ and $\cos \theta_{ij}$, respectively, with θ_{ij} to be the neutrino mixing angle between the i th and j th generations, and δ is the Dirac phase while $\tilde{\alpha}$ and $\tilde{\beta}$ are Majorana phases. For simplicity, we neglect the effects of these CP violating phases in the following analysis. Current neutrino oscillation data give the following values [26];

$$\Delta m_{\text{solar}}^2 \simeq 7.59 \times 10^{-5} \text{ eV}^2, \quad |\Delta m_{\text{atm}}^2| \simeq 2.43 \times 10^{-3} \text{ eV}^2, \quad (6.20)$$

$$\sin^2 \theta_{12} \simeq 0.32, \quad \sin^2 \theta_{23} \simeq 0.5, \quad \sin^2 \theta_{13} < 0.04. \quad (6.21)$$

In the next section, we discuss parameter regions in which both neutrino data and the LFV data are satisfied.

6.3 Lepton flavor violation

The model receives the severe constraints from the lepton-flavor violating processes of $\mu \rightarrow e\gamma$ and $\mu \rightarrow eee$: see Fig. 6.3. These processes are induced through one-loop diagrams by N_R^α and S^\pm with the Yukawa couplings h_i^α ($i = e$ and μ). The branching ratio of $\mu \rightarrow e\gamma$ is given by ¹

$$B(\mu \rightarrow e\gamma) \simeq \frac{3\alpha_{\text{em}}v^4}{32\pi m_S^4} \left| \sum_{\alpha=1}^2 h_e^{\alpha*} h_\mu^\alpha F_2 \left(\frac{m_{N_R^\alpha}^2}{m_S^2} \right) \right|^2, \quad (6.22)$$

¹The formula of Eq.(6.22) is different from Eq.(31) in Ref. [197] which includes errors. We have recalculated the values of $B(\mu \rightarrow e\gamma)$ by using the corrected formula and checked that the values of $B(\mu \rightarrow e\gamma)$ in the parameter sets in Table II in Ref. [197] are still below the experimental bound.

where $F_2(x) \equiv (1 - 6x + 3x^2 + 2x^3 - 6x^2 \ln x)/6(1 - x)^4$. For $\mu \rightarrow eee$, the branching ratio is calculated by

$$\begin{aligned}
B(\mu \rightarrow eee) = & \frac{1}{64G_F^2} \left(\frac{1}{16\pi^2} \right)^2 \times \left| \sum_{\alpha, \beta=1}^2 \left(\frac{1}{m_{N_R^\alpha}^2 - m_S^2} \right) \left(\frac{1}{m_{N_R^\beta}^2 - m_S^2} \right) \right. \\
& \times \left[h_\mu^{\alpha*} h_e^\alpha h_e^{\beta*} h_e^\beta \left(\frac{m_{N_R^\alpha}^2 m_{N_R^\beta}^2}{m_{N_R^\alpha}^2 - m_{N_R^\beta}^2} \log \frac{m_{N_R^\alpha}^2}{m_{N_R^\beta}^2} - \frac{m_{N_R^\alpha}^2 m_S^2}{m_{N_R^\alpha}^2 - m_S^2} \log \frac{m_{N_R^\alpha}^2}{m_S^2} - \frac{m_{N_R^\beta}^2 m_S^2}{m_{N_R^\beta}^2 - m_S^2} \log \frac{m_{N_R^\beta}^2}{m_S^2} + m_S^2 \right) \right. \\
& \left. \left. + h_\mu^{\alpha*} h_e^{\alpha*} h_e^\beta h_e^\beta m_{N_R^\alpha} m_{N_R^\beta} \left(\frac{m_{N_R^\alpha}^2 + m_S^2}{m_{N_R^\alpha}^2 - m_S^2} \log \frac{m_{N_R^\alpha}^2}{m_S^2} - \frac{m_{N_R^\alpha}^2 + m_{N_R^\beta}^2}{m_{N_R^\alpha}^2 - m_{N_R^\beta}^2} \log \frac{m_{N_R^\alpha}^2}{m_{N_R^\beta}^2} + \frac{m_{N_R^\beta}^2 + m_S^2}{m_{N_R^\beta}^2 - m_S^2} \log \frac{m_{N_R^\beta}^2}{m_S^2} - 2 \right) \right] \right|^2. \quad (6.23)
\end{aligned}$$

In particular, when $m_{N_R^1} = m_{N_R^2} (= m_{N_R})$, the expression in Eq. (6.23) is reduced to

$$\begin{aligned}
B(\mu \rightarrow eee) = & \frac{1}{64G_F^2} \left(\frac{1}{16\pi^2} \right)^2 \left(\frac{1}{m_N^2 - m_S^2} \right)^4 \\
& \times \left| \sum_{\alpha, \beta=1}^2 h_\mu^{\alpha*} h_e^\alpha h_e^{\beta*} h_e^\beta \left(m_N^2 + m_S^2 - \frac{2m_N^2 m_S^2}{m_N^2 - m_S^2} \log \frac{m_N^2}{m_S^2} \right) \right. \\
& \left. + 2m_N^2 \sum_{\alpha, \beta=1}^2 h_\mu^{\alpha*} h_e^{\alpha*} h_e^\beta h_e^\beta \left(\frac{m_N^2 + m_S^2}{m_N^2 - m_S^2} \log \frac{m_N^2}{m_S^2} - 2 \right) \right|^2. \quad (6.24)
\end{aligned}$$

Notice that the contributions of the two diagrams to $\mu \rightarrow eee$ are constructive for all the parameter sets in Table II. We also note that there are additional contributions to $\mu \rightarrow eee$ from penguin diagrams, which are neglected because their contributions are much smaller.

Assuming that $h_e^\alpha \sim \mathcal{O}(1)$, the masses of N_R^α and S^\pm are strongly constrained from below. In particular, if we assume that $m_S \gtrsim 400$ GeV, $m_{N_R} \gtrsim \mathcal{O}(1)$ TeV is required to satisfy the current experimental bounds, $B(\mu \rightarrow e\gamma) < 1.2 \times 10^{-11}$ [211] and $B(\mu \rightarrow eee) < 1.0 \times 10^{-12}$ [210]. Such a relatively heavier S^\pm is favored from the discussion on the dark matter relic abundance and electroweak baryogenesis [21, 197].

6.4 Typical scenarios

In Table 6.2, we show four choices for the parameter sets, and resulting values for the neutrino Yukawa coupling constants h_i^α which satisfy the neutrino data and the LFV data. For all parameter sets, $m_S = 400$ GeV and $m_{N_R} = 5$ TeV are assumed. Set A and Set B are taken as the normal hierarchy in the neutrino masses with $\sin^2 \theta_{13} = 0$ and 0.03, respectively, while Set C and Set D are for the inverted hierarchy. The predictions on $B(\mu \rightarrow e\gamma)$ and $B(\mu \rightarrow eee)$ are also shown in the table². The scenario with the inverted hierarchy requires the larger values for $\kappa \tan \beta$, so that the normal hierarchy scenarios are more natural in our model.

In Fig. 6.4, the contour plots of the branching ratio $B(\mu \rightarrow e\gamma)$ are shown in the m_S - m_{N_R} plane for the neutrino Yukawa coupling constants in Set A to Set D, while those of the branching

² In Table 6.2, we show the numbers of the h_i^α coupling constants with four digits for Set C, because the branching ratios of $\mu \rightarrow e\gamma$ and $\mu \rightarrow eee$ are sensitive to these numbers due to large cancellations.

	Yukawa couplings						LFV	
	h_e^1	h_e^2	h_μ^1	h_μ^2	h_τ^1	h_τ^2	$B(\mu \rightarrow e\gamma)$	$B(\mu \rightarrow 3e)$
A	1.2	1.3	0.024	-0.011	7.1×10^{-4}	-1.4×10^{-3}	2.8×10^{-14}	7.8×10^{-13}
B	1.1	1.1	0.0028	0.018	-5.5×10^{-4}	9.7×10^{-4}	6.1×10^{-14}	9.8×10^{-13}
C	3.500	3.474	0.01200	-0.01192	-7.136×10^{-4}	7.086×10^{-4}	4.4×10^{-17}	8.2×10^{-14}
D	2.1	2.2	6.4×10^{-3}	-8.6×10^{-3}	-5.3×10^{-4}	3.5×10^{-4}	3.5×10^{-15}	9.3×10^{-13}

Table 6.2: Values of h_i^α as well as those of branching ratios of $\mu \rightarrow e\gamma$ and $\mu \rightarrow 3e$ for $m_\eta = 50$ GeV and $m_{H^\pm} = 100$ GeV for various scenarios which satisfy neutrino data: Set A and Set B are scenarios of the normal hierarchy while Set C and Set D are those of the inverted hierarchy. For all sets, $m_S = 400$ GeV and $m_{N_R} = 5$ TeV are taken. Input parameters of $(\sin^2 \theta_{13}, \kappa \tan \beta)$ are taken to be (0, 54), (0.03, 76), (0, 80) and (0.03, 128) for Set A, Set B, Set C and Set D, respectively [69].

ratio $B(\mu \rightarrow eee)$ are shown for these scenarios in Fig. 6.4. The scale of the branching ratio of $\mu \rightarrow e\gamma$ is determined by m_{N_R} and is insensitive to m_S , while that of $\mu \rightarrow eee$ largely depend on both m_{N_R} and m_S especially for Set A, Set B and Set D. It can easily be seen that a much stronger constraint comes from $\mu \rightarrow eee$ for all scenarios.

6.5 Dark matter and electroweak phase transition

From now on, we employ Set A in Table 6.2 for further phenomenological analyses. In this scenario, masses of N_R^α are at the multi-TeV scale, so that it may be natural that the rest Z_2 -odd neutral field η is the candidate of dark matter. Since η is a singlet under the SM gauge group, the interactions with Z_2 -even particles are only through the Higgs coupling. When $m_\eta < m_W$, the η field predominantly annihilates into $b\bar{b}$ and $\tau^+\tau^-$ through s -channel Higgs boson (h and H) mediations. Strong annihilation occurs at $m_\eta \simeq m_H/2$ (and $m_\eta \simeq m_h/2$) due to the resonance of H (h) mediation in the s -channel diagrams. The pair annihilation into two photons through one-loop diagrams by H^\pm and S^\pm can also be important if κ is of the order one. The relic abundance becomes consistent with the data ($\Omega_{\text{DM}} h^2 \sim 0.11$ [9]) for $m_\eta \sim 50 - 60$ GeV, when we take $m_H = m_{H^\pm} \simeq 100$ GeV, $m_h \simeq 120$ GeV, $m_S \gtrsim 400$ GeV with $\kappa = 1.5$, $\sigma_1 = 0.05$, $\sigma_2 = 0.03$, and $\tan \beta = 36$. In such scenario, the typical spin-independent cross section for the scattering of dark matter with a proton is of order of 10^{-8} pb which is within the reach of the direct search experiments such as superCDMS and XMASS.

When $m_\eta < m_h/2$, the (SM-like) Higgs boson h can decay into a dark matter pair $\eta\eta$. The branching ratio of $h \rightarrow \eta\eta$ is evaluated as 34 % (22 %) for $m_h = 120$ GeV and $m_\eta = 48$ (55) GeV when $\sigma_1 = 0.05$, $\sigma_2 = 0.03$ and $\tan \beta > 10$. The invisible decay of h can be tested at the LHC when $B(h \rightarrow \eta\eta) > 25$ % [214]. At the ILC, it is expected that the branching ratio for the invisible decay of a few % can be detected [215]. Therefore, the invisible decay in this model can be tested at the collider experiments.

Our model [21] satisfies the conditions for baryogenesis [10]. The B number violating interaction is the sphaleron interaction. The additional CP violating phases are in the Higgs sector and in the Yukawa interaction. The condition of departure from thermal equilibrium can be realized by the strong first order electroweak phase transition, which requires a large tri-linear

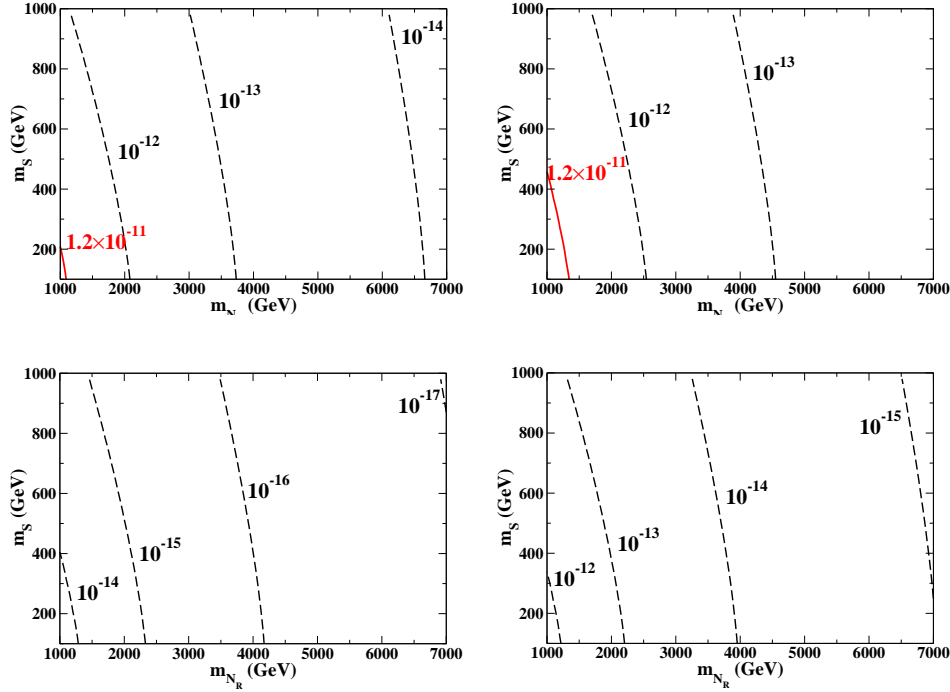


Figure 6.3: Contour plots for the branching ratio of $\mu \rightarrow e\gamma$ for the neutrino Yukawa coupling constants in Set A (top-left), Set B (top-right), Set C (bottom-left) and Set D (bottom-right). The contour for the upper limit from the data is given as the (red) solid curve [69].

coupling of the order parameter in the expression of the high temperature expansion [220] where only the bosonic loop can contribute³. In our model, there are many additional scalars running in the loop so that the large coupling can be easily realized [25]. The strong first order phase transition is possible for large m_S and/or m_A with the large nondecoupling effect: *e.g.* $m_S \sim 400$ GeV, $m_A \sim 100$ GeV, $M = 100$ GeV and $\mu_S = 200$ GeV, where M and μ_S are the invariant masses in Eq.(6.7) and Eq.(6.11), respectively. The result is not sensitive to $\tan\beta$.

6.6 Bounds from triviality and vacuum stability

There are scalar bosons in this model, so that quadratic divergences appear in the one-loop calculation for their masses. Because there is no mechanism by which such quadratic divergences are eliminated, enormous fine tuning is required to realize the renormalized Higgs boson mass being at the weak scale with a very high cutoff scale. Allowing the 1 % fine tuning, the cutoff scale is at most $\Lambda \sim O(10)$ TeV, above which the theory would be replaced by a more fundamental one [209]. Unless a mechanism of cancellation of the quadratic divergences such as supersymmetry is implemented, to avoid excessive fine tuning the model should be regarded as an effective theory, whose cutoff scale Λ is between $m_{N_R^\alpha}$ and $O(10)$ TeV. We then need to confirm the theoretical consistency of the model up to Λ [74]. We here evaluate bounds on the

³We note that such a nondecoupling effect due to the bosonic loop can also affect the quantum correction to the triple Higgs boson coupling [25, 92]. Such a large correction to the Higgs self-coupling can be an important signature for successful electroweak baryogenesis at collider experiments.

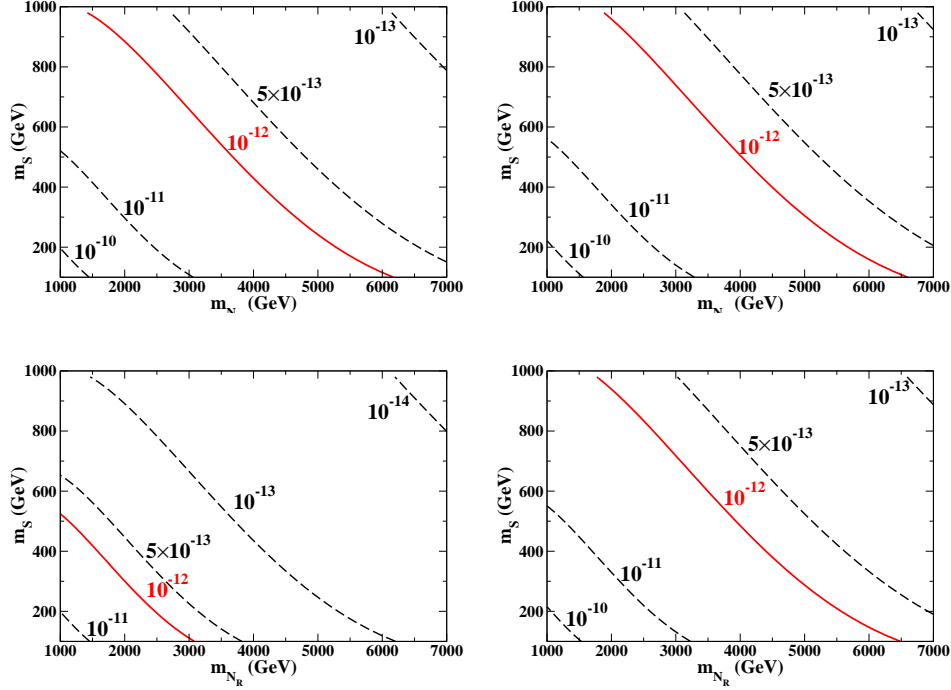


Figure 6.4: Contour plots for the branching ratio of $\mu \rightarrow eee$ for the neutrino Yukawa coupling constants in Set A (top-left), Set B (top-right), Set C (bottom-left) and Set D (bottom-right). The contour for the upper limit from the data is given as the (red) solid curve [69].

parameter space from vacuum stability and perturbativity, and examine whether the theoretically allowed parameter region is consistent with that by the experimental data discussed in the previous sections.

We have to consider these two bounds seriously because of the following reasons. First, this model includes many scalar fields, *e.g.*, h , H , A , H^\pm , S^\pm and η , so that the scale dependent dimensionless coupling constants would be drastically changed by the loop corrections due to the scalar bosons. Second, some of the Yukawa coupling constants for right-handed neutrinos are necessarily of order one for a radiative generation of the tiny mass scale of the neutrinos at the three-loop level. Finally, to realize the first order electroweak phase transition, some of the scalar self-coupling constants has to be as large as of order one.

In order to evaluate the vacuum stability bound and the triviality bound, we estimate the scale dependences of the dimensionless coupling constants by using the RGEs at the one-loop level. We have calculated the one-loop beta functions for all the coupling constants in this model. The full set of the beta functions is listed in Appendix. We take into account the threshold effects in the calculation of the scale dependent coupling constants. In the scale below the mass of S^\pm , we treat the theory without N_R and S^\pm . In the scale between the masses of the S^\pm and N_R , we treat the theory without N_R . In the scale higher than the mass of the N_R , we treat the theory with full particle contents.

6.7 The conditions

In this model, there are scalar fields Φ_i ($i = 1, 2$), S^\pm and η , which contain eleven degrees of freedom which would share the order parameter. The four of them are eliminated because of the $SU(2)_L \times U(1)_Y$ gauge symmetry. In the remaining seven dimensional parameter space, we require that for any direction the potential is bounded from below with keeping positiveness [86]. In the SM, this requirement is satisfied when the Higgs self-coupling constant is positive. In this model, we put the following conditions on the dimensionless coupling constants:

$$\lambda_1(\mu) > 0, \quad \lambda_2(\mu) > 0, \quad \lambda_S(\mu) > 0, \quad \lambda_\eta(\mu) > 0, \quad (6.25)$$

$$\begin{aligned} & \sqrt{\lambda_1(\mu)\lambda_2(\mu)} + \lambda_3(\mu) + \text{MIN}[0, (\lambda_4(\mu) + \lambda_5(\mu)), (\lambda_4(\mu) - \lambda_5(\mu))] > 0, \\ & \sqrt{\lambda_1(\mu)\lambda_S(\mu)/2} + \rho_1(\mu) > 0, \quad \sqrt{\lambda_1(\mu)\lambda_\eta(\mu)/3} + \sigma_1(\mu) > 0, \quad \sqrt{\lambda_2(\mu)\lambda_S(\mu)/2} + \rho_2(\mu) > 0, \\ & \sqrt{\lambda_2(\mu)\lambda_\eta(\mu)/3} + \sigma_2(\mu) > 0, \quad \sqrt{\lambda_S(\mu)\lambda_\eta(\mu)/6} + \xi(\mu) > 0, \end{aligned} \quad (6.26)$$

$$\begin{aligned} & 2\lambda_1(\mu) + 2\lambda_2(\mu) + 4\lambda_3(\mu) + 4\rho_1(\mu) + 4\rho_2(\mu) + \lambda_S(\mu) + 4\sigma_1(\mu) + 4\sigma_2(\mu) \\ & + \frac{2}{3}\lambda_\eta(\mu) + 4\xi(\mu) - 16\sqrt{2}|\kappa(\mu)| > 0. \end{aligned} \quad (6.27)$$

The conditions in Eqs. (6.25) and (6.26) are obtained by the similar way as in Ref. [88], while the last condition in Eq. (6.27) is derived such that the term with the coupling constant κ in the potential satisfies the positivity condition for the direction where the VEVs of the fields Φ_1 , Φ_2 , S^\pm and η are a common value.

We require that all the dimensionless running coupling constants do not blow up below Λ . Since we discuss the model within the scale where the perturbation calculation remains reliable, we here require that the running coupling constants do not exceed some critical value. In this paper, we impose the following criterion in the coupling constants in the Higgs potential Eq. (6.3) and the Yukawa interaction in Eqs. (6.1) and (6.2):

$$\begin{aligned} & |\lambda_i(\mu)|, |\sigma_i(\mu)|, |\rho_i(\mu)|, |\kappa(\mu)|, |\xi(\mu)| < 8\pi, \\ & y_t^2(\mu), y_b^2(\mu), y_\tau^2(\mu), (h_i^\alpha)^2(\mu) < 4\pi. \end{aligned} \quad (6.28)$$

The similar critical value has been adopted in the analyses in the two Higgs doublet model [87, 88] and in the Zee model [186].

6.8 Allowed regions in the parameter space

In this section, we evaluate allowed regions in parameter space, which satisfy the conditions of triviality and vacuum stability for each fixed cutoff scale Λ . For the scenarios of the neutrino Yukawa coupling constants as well as the masses of right-handed neutrinos, we choose Set A in Table 6.2. We investigate the allowed regions in the m_S - m_A plane, and the rest of the mass parameters in the scalar sector is fixed as

$$\begin{aligned} & m_{H^+} = 100 \text{ GeV}, \quad m_H = 100 \text{ GeV}, \quad m_h = 120 \text{ GeV}, \quad m_\eta = 50 \text{ GeV}, \\ & M = 100 \text{ GeV}, \quad \mu_S = 200 \text{ GeV}, \quad \mu_\eta = 30 \text{ GeV}. \end{aligned} \quad (6.29)$$

The initial values for the scalar coupling constants in the Higgs sector are taken to be

$$\begin{aligned} \lambda_1(m_Z) &= 0.24, & \lambda_2(m_Z) &= 0.24, & \lambda_3(m_Z) &= 0.24, & \kappa(m_S) \tan \beta &= 54, \\ \rho_1(m_S) &= 0.1, & \lambda_S(m_S) &= 2, & \sigma_1(m_Z) &= 0.05, & \sigma_2(m_Z) &= 0.05, & \lambda_\eta &= 3, \end{aligned} \quad (6.30)$$

and the mixing angle are set on $\sin(\beta - \alpha) = 1$. We note that the initial value of λ_4 , λ_5 and ρ_2 are determined by given values for the masses of A and S^\pm using Eqs. (6.7), (6.8) and (6.11). The rest parameter ξ (the coupling constant for $|S^-|^2\eta^2$) is taken as $\xi = 3$ and 5. The results in the case with $\xi = 3$ is shown in Fig. 6.5 for $\kappa = 1.2$ (left figure) and $\kappa = 1.5$ (right figure), while those with $\xi = 5$ is in Fig. 6.6 for the same values of κ .

In Fig. 6.5, the shaded area in the figure is excluded due to the vacuum stability condition in Eq. (6.27). In this area, the condition is not satisfied already at the electroweak scale, so that the excluded region is independent of Λ . The vacuum stability bound become stronger for a larger value of κ , although the area compatible with both theoretical conditions with $\Lambda = 10$ TeV still exists for $\kappa = 1.5$. On the other hand, the bound from perturbativity depends on Λ . In Fig. 6.5, the contour plots for $\Lambda = 6, 10$ and 15 TeV, the scales where one of the coupling constants blows up and breaks the condition of perturbativity are shown for the case of $\xi = 3$ in the m_S - m_A plane. We find that there is the parameter region which satisfies both the conditions of vacuum stability and perturbativity with the blow-up scale to be above $\Lambda = 10$ TeV. The area of the vicinity of $m_S \sim 400$ GeV and $m_A < 350$ GeV can also be consistent from the theoretical bounds. We stress that this parameter region is favored for phenomenologically successful scenarios for neutrino masses, relic abundance for the dark matter, and the strongly first order phase transition.

The similar figures but with $\xi = 5$ are shown in Fig. 6.6. The contour plots are for $\Lambda = 6, 10, 12$ and 14 TeV in the m_S - m_A plane. We find that there is the parameter region which satisfies both the conditions of vacuum stability and perturbativity with the blow-up scale to be above $\Lambda = 10$ TeV. The vacuum stability bound is more relaxed as compared to that for $\xi = 3$, while the bound from perturbativity becomes rather strict. In the regions with $m_S < 400$ GeV, the running coupling constants blow up earlier than the case with $\xi = 3$, because of the threshold effect at the scale $\mu = m_S$, above which the running of λ_η becomes enhanced by the loop contribution of S^\pm . In the area of $300 \text{ GeV} < m_S < 400 \text{ GeV}$ and $m_A < 350 \text{ GeV}$, Λ can be above 10 TeV.

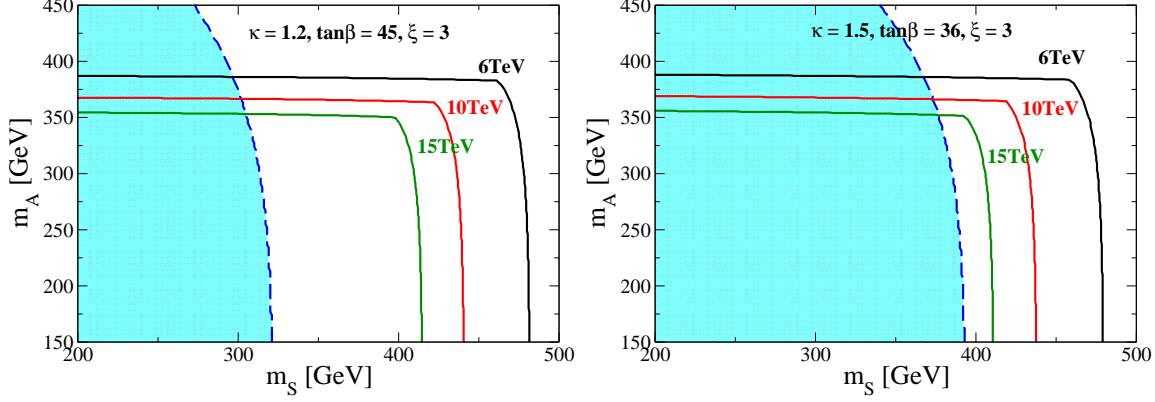


Figure 6.5: Contour plots for the scale where condition of perturbativity is broken are shown in the m_S - m_A plane in the case of $(\kappa, \tan \beta) = (1.2, 45)$ (left figure), and $(\kappa, \tan \beta) = (1.5, 36)$ (right figure). The region excluded by the vacuum stability condition is also shown as the shaded area. The constant ξ is taken to be 3 at the scale of m_S [69].

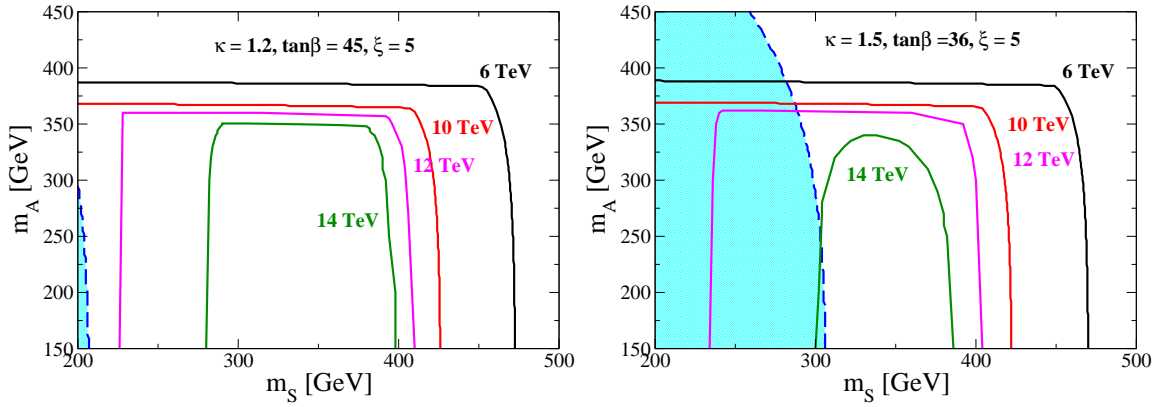


Figure 6.6: Contour plots for the scale where condition of perturbativity is broken are shown in the m_S - m_A plane in the case of $(\kappa, \tan \beta) = (1.2, 45)$ (left figure), and $(\kappa, \tan \beta) = (1.5, 36)$ (right figure). The region excluded by the vacuum stability condition is also shown as the shaded area. The constant ξ is taken to be 5 at the scale of m_S [69].

Chapter 7

Supersymmetric extension of the Zee-Babu model

The Zee-Babu model may be the simplest successful model which can be generated tiny neutrino masses at the two-loop level. In this model, isospin $SU(2)$ singlet singly- and doubly-charged scalar bosons which carry lepton number of two unit are added to the SM. Although this model can explain neutrino oscillation data, this model cannot explain the hierarchy problem because there is no symmetry to forbid the quadratic divergence in radiative corrections to the Higgs boson mass. In addition to the hierarchy problem, this model does not have a dark matter candidate.

In this section, we investigate a supersymmetric extension of the Zee-Babu model. By introducing SUSY, the quadratic divergence in the one-loop correction to the mass of the Higgs boson can be eliminated automatically. In addition, a discrete symmetry, which is so called the R-parity, is imposed in our model to forbid the term which causes the dangerous proton decay. The R-parity also guarantees the stability of the lightest super partner particle (LSP) such as the neutralino, which may be identified as a candidate of DM.

We find that there are allowed parameter regions in which the current neutrino oscillation data can be reproduced under the constraint from the lepton flavour violation (LFV) data. In addition, this model provides quite interesting phenomenological signals in the collider physics; i.e., the existence of singly as well as doubly charged singlet scalar bosons and their SUSY partner fermions. Such an allowed parameter region also appears even when new particles and their partners are as light as the electroweak scale. We also discuss the outline of phenomenology for these particles at the LHC.

7.1 Model

In the original (non-SUSY) Zee-Babu model [17, 18], two kinds of $SU(2)_L$ singlet fields ω^- ($Y = -1$) and κ^{--} ($Y = -2$) are introduced. The Yukawa interaction and the scalar potential are given by

$$\mathcal{L} = - \sum_{i,j=1}^3 f_{ij} \bar{L}_L^{ic} \cdot L_L^j \omega^+ - \sum_{i,j=1}^3 g_{ij} \bar{e}_R^i e_R^{jc} \kappa^{--} - \mu_B \omega^- \omega^- \kappa^{++} + \text{h.c.} - V' - V_{\text{SM}}, \quad (7.1)$$

where V_{SM} is the Higgs potential of the SM, the indices i, j are the flavour indices and all the scalar couplings with respect to ω^- and κ^{--} other than $\omega^- \omega^- \kappa^{++}$ are in V' . Notice that lepton

number conservation is broken only by the term of μ_B . The neutrino mass matrix is generated via two-loop diagrams as shown in Fig. 7.1. The induced neutrino mass matrix is computed as¹

$$(m_\nu)_{ij} = \sum_{k,l=1}^3 16\mu_B f_{ik}(m_e)_k g_{kl}(m_e)_l f_{jl} I(m_\omega, (m_e)_k | m_\omega, (m_e)_l | m_\kappa), \quad (7.2)$$

where $(m_e)_i$ are charged lepton masses, and the induced mass matrix $(m_\nu)_{ij}$ is defined in the effective Lagrangian as

$$\mathcal{L}_\nu = - \sum_{i,j=1}^3 \frac{1}{2} (\bar{\nu}_L^c)_i (m_\nu)_{ij} (\nu_L)_j + \text{h.c.}, \quad (7.3)$$

and $I(m_{11}, m_{12} | m_{21}, m_{22} | M)$ is the two-loop integral function defined as

$$\begin{aligned} & I(m_{11}, m_{12} | m_{21}, m_{22} | M) \\ &= \int \frac{d^4 p}{(2\pi)^4} \int \frac{d^4 q}{(2\pi)^4} \frac{1}{(p^2 + m_{11}^2)} \frac{1}{(p^2 + m_{12}^2)} \frac{1}{(q^2 + m_{21}^2)} \frac{1}{(q^2 + m_{22}^2)} \frac{1}{((p+q)^2 + M^2)}. \end{aligned} \quad (7.4)$$

Following Refs. [216], one can evaluate the function $I(m_{11}, m_{12} | m_{21}, m_{22} | M)$ as

$$\begin{aligned} & I(m_{11}, m_{12} | m_{21}, m_{22} | M) \\ &= \frac{I(m_{12} | m_{22} | M) - I(m_{11} | m_{22} | M) - I(m_{12} | m_{21} | M) + I(m_{11} | m_{21} | M)}{(m_{11}^2 - m_{12}^2)(m_{21}^2 - m_{22}^2)}, \end{aligned} \quad (7.5)$$

where

$$I(m_1 | m_2 | M) = -m_1^2 f\left(\frac{m_2^2}{m_1^2}, \frac{M^2}{m_1^2}\right) - m_2^2 f\left(\frac{m_1^2}{m_2^2}, \frac{M^2}{m_2^2}\right) - M^2 f\left(\frac{m_1^2}{M^2}, \frac{m_2^2}{M^2}\right). \quad (7.6)$$

The function $f(x, y)$ is given by

$$\begin{aligned} f(x, y) = & -\frac{1}{2} \ln x \ln y - \frac{1}{2} \left(\frac{x+y-1}{D} \right) \\ & \times \left\{ \text{Li}_2\left(\frac{-\sigma_-}{\tau_+}\right) + \text{Li}_2\left(\frac{-\tau_-}{\sigma_+}\right) - \text{Li}_2\left(\frac{-\sigma_+}{\tau_-}\right) - \text{Li}_2\left(\frac{-\tau_+}{\sigma_-}\right) \right. \\ & \left. + \text{Li}_2\left(\frac{y-x}{\sigma_-}\right) + \text{Li}_2\left(\frac{x-y}{\tau_-}\right) - \text{Li}_2\left(\frac{y-x}{\sigma_+}\right) - \text{Li}_2\left(\frac{x-y}{\tau_+}\right) \right\}, \end{aligned} \quad (7.7)$$

where D , σ_\pm and τ_\pm are

$$D = \sqrt{1 - 2(x+y) + (x-y)^2}, \quad \sigma_\pm = \frac{1}{2}(1 - x + y \pm D), \quad \tau_\pm = \frac{1}{2}(1 + x - y \pm D), \quad (7.8)$$

and $\text{Li}_2(x)$ is the dilogarithm function defined as

$$\text{Li}_2(x) = - \int_0^x \frac{\ln(1-t)}{t} dt. \quad (7.9)$$

¹Our result for the neutrino mass matrix is consistent with that in Ref. [191] including the factor.

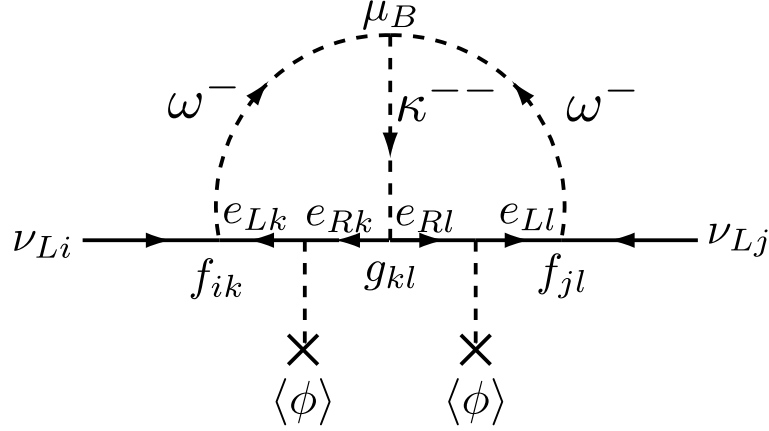


Figure 7.1: The two-loop diagram relevant to the neutrino mass matrix [70].

	Spin 0	Spin 1/2	SU(3) _C	SU(2) _L	U(1) _Y	Electric charge	Lepton number
$\hat{\Omega}_R^c$	ω_R^*	$(\tilde{\omega}_R)^c$	1	1	1	1	-2
$\hat{\Omega}_L$	ω_L	$\tilde{\omega}_L$	1	1	-1	-1	2
\hat{K}_L	κ_L	$\tilde{\kappa}_L$	1	1	-2	-2	2
\hat{K}_R^c	κ_R^*	$(\tilde{\kappa}_R)^c$	1	1	2	2	-2

Table 7.1: Particle properties of chiral superfields [70].

We note that in the limit of $m_{12} = m_{22} = 0$ and $m_{11} = m_{21} = m_\omega$ the above function $I(m_{11}, m_{12}|m_{21}, m_{22}|M)$ has the same form as the function given in Refs. [189, 190],

$$I(m_\omega, 0|m_\omega, 0|m_\kappa) = -\frac{1}{(16\pi^2)^2} \frac{1}{m_\kappa^2} \int_0^1 dx \int_0^{1-x} dy \frac{r}{x + (r-1)y + y^2} \ln \frac{y(1-y)}{x + ry}, \quad (7.10)$$

where $r = m_\kappa^2/m_\omega^2$. Details of the Zee-Babu model have been studied in the literature [189–192]. It is known that the model can reproduce the present neutrino data with satisfying constraints from the LFV.

We turn to the SUSY extension of the Zee-Babu model. The SU(2)_L singlet chiral superfields $\hat{\Omega}_R^c$, $\hat{\Omega}_L$, \hat{K}_L , and \hat{K}_R^c are added to the superfields in the MSSM, whose details are shown in Table. 7.1. Notice that although the non-SUSY Zee-Babu model includes only two SU(2)_L singlet scalars these four chiral fields are required in the SUSY model. If only $\hat{\Omega}_R^c$ and \hat{K}_L are introduced in the model, their fermion components are massless and the model is ruled out. By introducing additional fields $\hat{\Omega}_L$ and \hat{K}_R^c such massless fermions can be massive, and furthermore the model becomes anomaly free.

The superpotential is given by²

$$W = W_{\text{MSSM}} + f_{ij} \hat{L}_i \cdot \hat{L}_j \hat{\Omega}_R^c + g_{ij} \hat{E}_i^c \hat{E}_j^c \hat{K}_L + \lambda_L \hat{K}_L \hat{\Omega}_R^c \hat{\Omega}_L^c + \lambda_R \hat{K}_R^c \hat{\Omega}_L \hat{\Omega}_L^c + \mu_\Omega \hat{\Omega}_R^c \hat{\Omega}_L + \mu_K \hat{K}_L \hat{K}_R^c, \quad (7.11)$$

where W_{MSSM} is the superpotential in the MSSM. The superfields in the superpotential are listed in Table. 7.1, and the coupling matrices f_{ij} and g_{ij} are an antisymmetric matrix $f_{ji} = -f_{ij}$ and a symmetric one $g_{ji} = g_{ij}$, respectively. It is emphasized that we here impose the exact R-parity in order to protect the decay of the LSP, so that the LSP is a candidate of the DM. The soft SUSY breaking terms are given by

$$\mathcal{L}_{\text{soft}} = \mathcal{L}_{\text{MSSM}} + \mathcal{L}_{\text{SZB}} + \mathcal{L}_C, \quad (7.12)$$

where $\mathcal{L}_{\text{MSSM}}$ represents the corresponding terms in the MSSM,

$$\begin{aligned} \mathcal{L}_{\text{SZB}} = & -M_+^2 \omega_R^* \omega_R - M_-^2 \omega_L^* \omega_L - M_{--}^2 \kappa_L^* \kappa_L - M_{++}^2 \kappa_R^* \kappa_R \\ & + \left(-m_S \tilde{f}_{ij} \omega_R^* \tilde{L}_L^i \cdot \tilde{L}_L^j - m_S \tilde{g}_{ij} \kappa_L \tilde{e}_R^{i*} \tilde{e}_R^{j*} - m_S \tilde{\lambda}_L \kappa_L \omega_R^* \omega_R - m_S \tilde{\lambda}_R \kappa_R^* \omega_L \omega_L \right. \\ & \left. - B_\omega \mu_\Omega \omega_R^* \omega_L - B_\kappa \mu_K \kappa_L \kappa_R^* + \text{h.c.} \right), \end{aligned} \quad (7.13)$$

and

$$\mathcal{L}_C = -C_u \omega_R^* H_u^\dagger H_d - C_d \omega_L H_d^\dagger H_u - (C_\omega)^{ij} \omega_L^* \tilde{L}_L^i \cdot \tilde{L}_L^j + \text{h.c.}, \quad (7.14)$$

where m_S denotes a typical SUSY mass scale, and $\tilde{f}_{ji} = -\tilde{f}_{ij}$ and $\tilde{g}_{ji} = \tilde{g}_{ij}$. \mathcal{L}_{SZB} is the standard soft-breaking terms with respect to the new charged singlet fields, $\omega_{L,R}$ and $\kappa_{L,R}$. \mathcal{L}_C contains the terms so-called the ‘‘C-terms’’ [217], where the scalar component and its conjugation are mixed³.

There are two possibilities in building a SUSY model with the charged singlet fields, depending on whether or not the C-terms are switched on in a SUSY breaking scenario⁴. If we assume that \mathcal{L}_C is absent, tiny neutrino masses are generated only by at least two loop diagrams as in the Zee-Babu model. On the other hand, with the term $\omega_R^* H_u^\dagger H_d$, tiny neutrino masses are dominated by one loop diagrams in Fig. 7.2 just like in the original Zee model [16]. Here, we focus on the case where the SUSY breaking mechanism does not lead to the soft SUSY breaking C-terms, so that all the neutrino masses are generated at the two loop level.

From the superfields $\hat{\Omega}_R^c$, $\hat{\Omega}_L$, \hat{K}_L and \hat{K}_R^c , there appear singly charged ($Y = -1$) and doubly charged ($Y = -2$) singlet scalar bosons, $\omega_{R,L}$ and $\kappa_{L,R}$, as well as their superpartner fermions, namely singly and doubly charged singlinos, $\tilde{\omega}$ and $\tilde{\kappa}$, respectively. The superpotential and the

²Hereafter we omit the summation symbol for simplicity.

³The singlet scalar C-terms break SUSY hard, while the terms listed in the \mathcal{L}_C include non-singlet scalars and the quadratic divergence does not occur.

⁴Many models derived by $N = 1$ supergravity do not lead to the C-terms and if they are absent at the cut off scale, they do not appear through the radiative corrections [218]. Thus the C-terms are usually ignored in the MSSM. On the other hand, it is known that C-terms are induced in some models of SUSY breaking such as an intersecting brane model with a flux compactification [219].

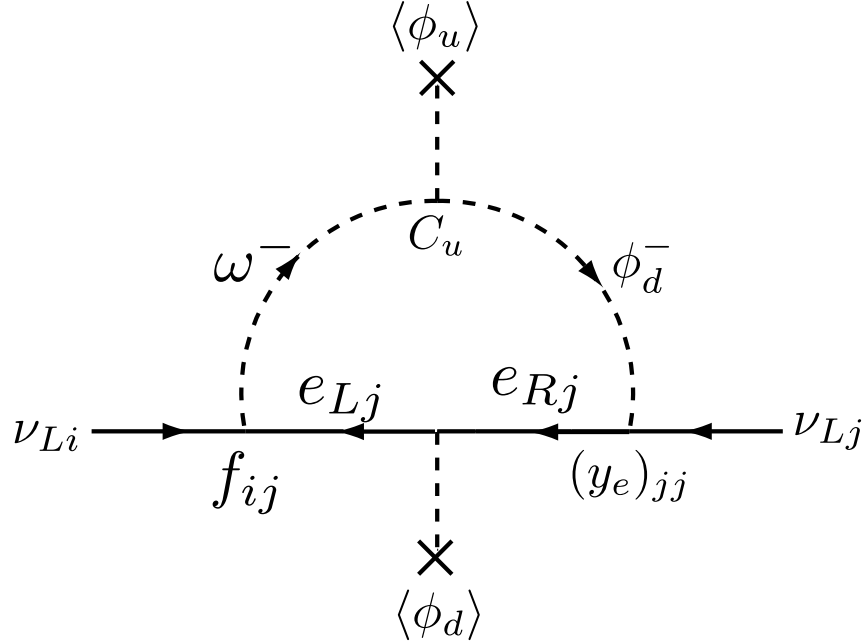


Figure 7.2: The one-loop diagram relevant to the neutrino mass matrix with the C-term $\omega^+ H_u^* H_d$. $(y_e)_{jj}$ is the charged lepton Yukawa coupling [70].

soft SUSY breaking terms lead to the mass matrix for the singly charged scalars in the basis of (ω_R, ω_L) as ,

$$M_\omega^2 = \begin{pmatrix} M_+^2 + |\mu_\Omega|^2 - m_W^2 \tan^2 \theta_W \cos 2\beta & B_\omega \mu_\Omega \\ B_\omega \mu_\Omega & M_-^2 + |\mu_\Omega|^2 + m_W^2 \tan^2 \theta_W \cos 2\beta \end{pmatrix}, \quad (7.15)$$

and the mass matrix for the doubly charged singlet scalars in the basis of (κ_L, κ_R) as

$$M_\kappa^2 = \begin{pmatrix} M_{--}^2 + |\mu_K|^2 + 2m_W^2 \tan^2 \theta_W \cos 2\beta & B_\kappa \mu_K \\ B_\kappa \mu_K & M_{++}^2 + |\mu_K|^2 - 2m_W^2 \tan^2 \theta_W \cos 2\beta \end{pmatrix}, \quad (7.16)$$

where $\tan \beta$ is a ratio of the two vacuum expectation values of the MSSM Higgs bosons as $\tan \beta = \langle \phi_u \rangle / \langle \phi_d \rangle$. As easily seen from the above expressions, ω_R and ω_L (κ_L and κ_R) can mix with each other by the soft-breaking “B-term”, $(B_\omega \mu_\Omega) \omega_R^* \omega_L$ ($(B_\kappa \mu_K) \kappa_L \kappa_R^*$). The mass eigenvalues of singly and doubly charged singlet scalar bosons are obtained after diagonalizing their mass matrices M_ω^2 and M_κ^2 by the unitary matrices U_ω and U_κ as

$$U_\omega^\dagger M_\omega^2 U_\omega = \begin{pmatrix} (m_\omega)_1^2 & 0 \\ 0 & (m_\omega)_2^2 \end{pmatrix}, \quad U_\kappa^\dagger M_\kappa^2 U_\kappa = \begin{pmatrix} (m_\kappa)_1^2 & 0 \\ 0 & (m_\kappa)_2^2 \end{pmatrix}. \quad (7.17)$$

The mass eigenstates are then given by

$$\omega_a = (U_\omega^\dagger)_{a1} \omega_R + (U_\omega^\dagger)_{a2} \omega_L, \quad \kappa_a = (U_\kappa^\dagger)_{a1} \kappa_L + (U_\kappa^\dagger)_{a2} \kappa_R, \quad (a = 1, 2). \quad (7.18)$$

The mass eigenstates of the singlinos are

$$\tilde{\omega} = \begin{pmatrix} \tilde{\omega}_L \\ \tilde{\omega}_R \end{pmatrix}, \quad \tilde{\kappa} = \begin{pmatrix} \tilde{\kappa}_L \\ \tilde{\kappa}_R \end{pmatrix}, \quad (7.19)$$

whose mass eigenvalues are given by the SUSY invariant parameters as $m_{\tilde{\omega}} = \mu_{\Omega}$ and $m_{\tilde{\kappa}} = \mu_K$, respectively.

The neutrino mass matrix is generated via the two-loop diagrams shown in Fig. 7.3, which can be written as

$$(m_{\nu})_{ij} = f_{ik}(m_e)_k H_{kl}(m_e)_l f_{jl} , \quad (7.20)$$

where the matrix H_{kl} is a symmetric matrix

$$\begin{aligned} H_{kl} = & 16(\mu_B)_{abc}(U_{\omega})_{1a}^*(U_{\omega})_{1b}^*(U_{\kappa})_{1c}g_{kl}I((m_e)_k, (m_{\omega})_a|(m_e)_l, (m_{\omega})_b|(m_{\kappa})_c) \\ & + 16\frac{\lambda_L^*m_{\tilde{\omega}}^2}{m_S}(U_{\kappa})_{1a}^*(U_{\kappa})_{1a}\left\{\frac{X_k}{m_S}\tilde{g}_{kl}\frac{X_l}{m_S}I((m_{\tilde{e}_R})_k, m_{\tilde{\omega}}|(m_{\tilde{e}_R})_l, m_{\tilde{\omega}}|(m_{\kappa})_a)\right. \\ & + \frac{X_k}{m_S}g_{kl}I((m_{\tilde{e}_R})_k, m_{\tilde{\omega}}|(m_{\tilde{e}_L})_l, m_{\tilde{\omega}}|(m_{\kappa})_a) + g_{kl}\frac{X_l}{m_S}I((m_{\tilde{e}_L})_k, m_{\tilde{\omega}}|(m_{\tilde{e}_R})_l, m_{\tilde{\omega}}|(m_{\kappa})_a)\Big\} \\ & + \frac{8\lambda_L m_{\tilde{\omega}} m_{\tilde{\kappa}}}{m_S}(U_{\omega})_{1a}(U_{\omega})_{1a}^* \\ & \times \left\{\frac{X_k}{m_S}g_{kl}I((m_{\tilde{e}_R})_k, m_{\tilde{\omega}}|(m_e)_l, (m_{\omega})_a|m_{\tilde{\kappa}}) + g_{kl}\frac{X_l}{m_S}I((m_e)_k, (m_{\omega})_a|(m_{\tilde{e}_R})_l, m_{\tilde{\omega}}|m_{\tilde{\kappa}})\right\} , \end{aligned} \quad (7.21)$$

where the indices a, b, c run from 1 to 2, the mass eigenstates of the charged singlet scalars, $(m_{\tilde{e}_R})_i$ and $(m_{\tilde{e}_L})_i$ are slepton masses, the left-right mixing term in the slepton sector is parameterized as $(m_e)_k X_k/m_S$, $I(m_{11}, m_{12}|m_{21}, m_{22}|M)$ is the loop function given in Eq. (7.4), and the other parameters are defined in the relevant Lagrangian as

$$\begin{aligned} \mathcal{L} = & -2f_{ij}(U_{\omega})_{1a}^*\tilde{\nu}^{ic}P_L e^j \omega_a^* - g_{ij}(U_{\kappa})_{1a}\bar{e}_i P_L e^j \kappa_a - 2f_{ij}\tilde{\nu}_L^{i*}\tilde{\omega}P_L e^j - 2f_{ij}\tilde{\nu}^{ic}P_L \tilde{\omega}^c \tilde{e}_L^j \\ & - 2g_{ij}\tilde{e}_R^{i*}\tilde{e}^j P_L \tilde{\kappa} - \lambda_L(U_{\kappa})_{1a}\tilde{\omega}P_L \tilde{\omega}^c \kappa_a - 2\lambda_L(U_{\omega})_{1a}^*\tilde{\omega}P_L \tilde{\kappa}\omega_a^* - g_{ij}(U_{\kappa})_{1a}(m_e)_j \tilde{e}_R^{i*}\tilde{e}_L^j \kappa_a \\ & - (\mu_B)_{abc}\omega_a\omega_b\kappa_c^* - m_S\tilde{g}_{ij}(U_{\kappa})_{1a}\tilde{e}_R^{i*}\tilde{e}_R^j \kappa_a + \text{h.c.} , \end{aligned} \quad (7.22)$$

with

$$(\mu_B)_{abc} \equiv A_L^*(U_{\omega})_{1a}(U_{\omega})_{1b}(U_{\kappa})_{1c}^* + A_R(U_{\omega})_{2a}(U_{\omega})_{2b}(U_{\kappa})_{2c}^* . \quad (7.23)$$

In the above expression, we assume that there is no flavour mixing in the slepton sector. In our model, there are two sources of the LFV processes. One is the slepton mixing which also appear in the MSSM. The other is the flavour mixing in the coupling with the charged singlet particles. In order to concentrate on the latter contribution to the lepton flavour violating phenomena, the usual slepton mixing effect is assumed to be zero. The phenomenological constraints in our discussion strongly depend on this assumption. If the assumption is relaxed, the phenomenological allowed parameters of the model can be changed to some extent. Still we think our assumption is valuable to consider in order to obtain some definite physics consequences which are relevant to the new particles in our model.

7.2 Allowed parameter region under the current constraint

It is non-trivial whether there is an allowed parameter region in our model except for the decoupling limit where masses of all the super partner particles are set to be much larger than

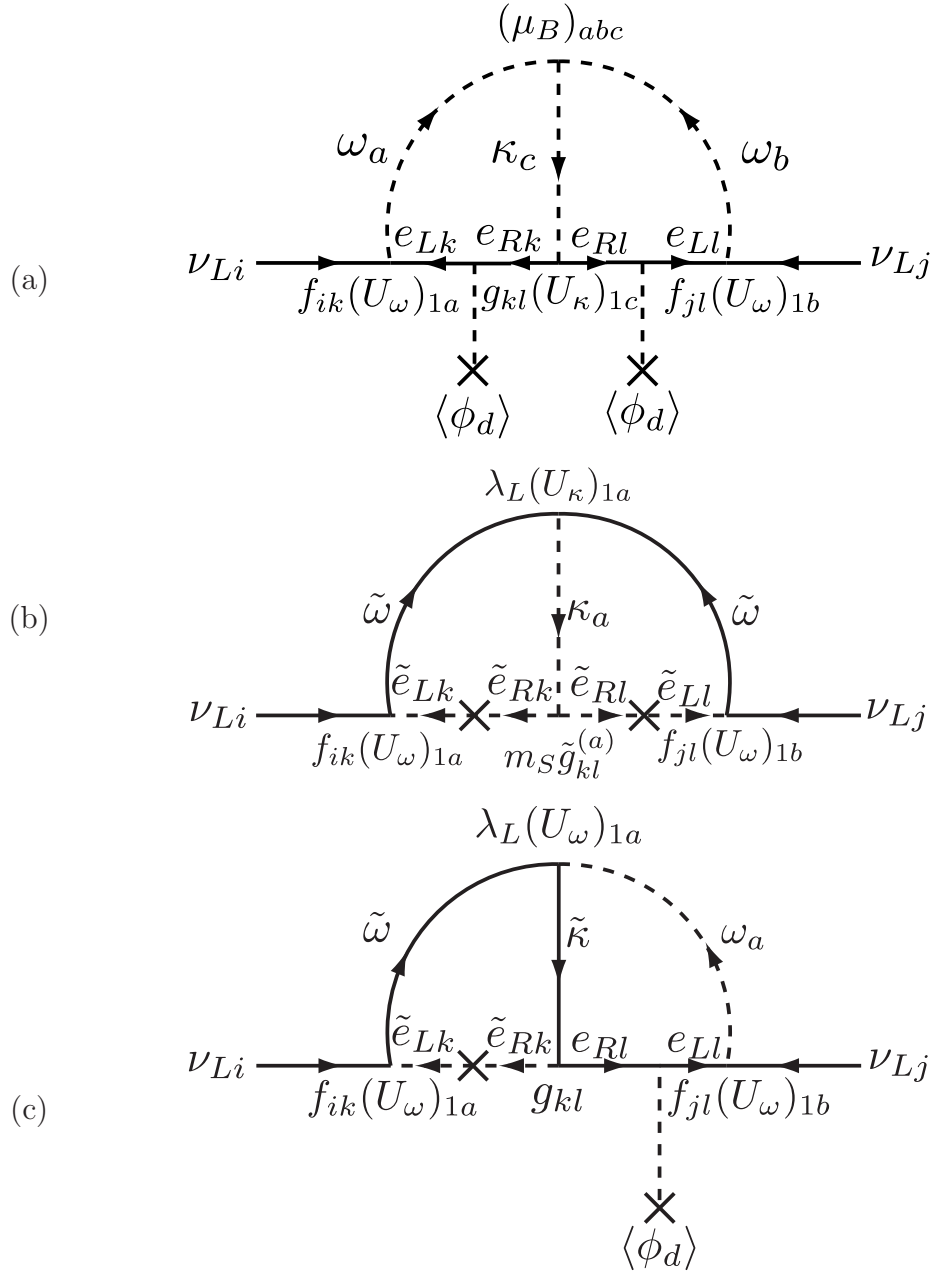


Figure 7.3: The contributions to the neutrino mass generations. A type of a diagram (a) is the corresponding diagram to the non-SUSY Zee-Babu model. Diagrams (b) and (c) are new type of diagram in the SUSY model [70].

the electroweak scale. Let us search for the parameter region where the neutrino mixing is consistent with the present oscillation data and the LFV constraints are satisfied.

Flavour violation in couplings between $SU(2)_L$ singlet fields and leptons should be large in order to generate large off-diagonal elements in the neutrino mass matrix. These large flavour violation couplings enhance the LFV processes. In particular doubly charged singlet scalar exchange tree level diagram contributes to the $e_i^+ \rightarrow e_j^+ e_k^+ e_l^-$ process. The predicted decay width of $e_i^+ \rightarrow e_j^+ e_k^+ e_l^-$ in the model is calculated as [189, 190]

$$\Gamma(e_i^+ \rightarrow e_j^+ e_k^+ e_l^-) = C_{jk} \frac{1}{8} \frac{(m_e)_i^5}{192\pi^3} \left| (U_\kappa)_{1a}^* (U_\kappa)_{1a} \frac{g_{il} g_{jk}^*}{(m_\kappa)_a^2} \right|^2, \quad (7.24)$$

where C_{jk} is a statistical factor as

$$C_{jk} = \begin{cases} 1 & (j = k) \\ 2 & (j \neq k) \end{cases}. \quad (7.25)$$

There can be still large contributions to $\mu \rightarrow e\gamma$, even if the constraint from $\mu^+ \rightarrow e^+ e^+ e^-$ can be avoided. The contribution is from one-loop diagrams. The decay width of $e_i \rightarrow e_j \gamma$ is evaluated as

$$\Gamma(e_i \rightarrow e_j \gamma) = \frac{\alpha_e}{4} (m_e)_i^5 (|A_L^{ji}|^2 + |A_R^{ji}|^2), \quad (7.26)$$

with

$$A_L^{ji} = -\frac{1}{(4\pi)^2} \left\{ (U_\omega)_{1a}^* (U_\omega)_{1a} \frac{4f_{kj}^* f_{ki}}{(m_\omega)_a^2} F_2 \left(\frac{(m_\nu)_k^2}{(m_\omega)_a^2} \right) - \frac{4f_{kj}^* f_{ki}}{(m_{\tilde{\nu}_L})_k^2} F_1 \left(\frac{m_\omega^2}{(m_{\tilde{\nu}_L})_k^2} \right) \right\}, \quad (7.27)$$

$$A_R^{ji} = -\frac{1}{(4\pi)^2} \left\{ (U_\kappa)_{1a}^* (U_\kappa)_{1a} \frac{g_{kj}^* g_{ki}}{(m_\kappa)_a^2} \left(2F_2 \left(\frac{(m_e)_k^2}{(m_\kappa)_a^2} \right) + F_1 \left(\frac{(m_e)_k^2}{(m_\kappa)_a^2} \right) \right) - \frac{g_{kj}^* g_{ki}}{(m_{\tilde{e}_R})_k^2} \left(2F_1 \left(\frac{m_\kappa^2}{(m_{\tilde{e}_R})_k^2} \right) + F_2 \left(\frac{m_\kappa^2}{(m_{\tilde{e}_R})_k^2} \right) \right) \right\}, \quad (7.28)$$

where $(m_\nu)_i$ are neutrino masses, and $(m_{\tilde{\nu}_L})_i$ are sneutrino masses. The loop functions $F_1(x)$ and $F_2(x)$ are [221]

$$F_1(x) = \frac{x^2 - 5x - 2}{12(x-1)^3} + \frac{x \ln x}{2(x-1)^4}, \quad (7.29)$$

$$F_2(x) = \frac{2x^2 + 5x - 1}{12(x-1)^3} - \frac{x^2 \ln x}{2(x-1)^4}. \quad (7.30)$$

The coupling constants f_{ij} only have nonzero values in flavour off-diagonal elements, and they tend to be large to reproduce the bi-large mixing. Then the bound from the data becomes severe.

Let us discuss how the LFV processes constrain the parameter space. First of all, the tree level diagram contributing to the $\mu \rightarrow eee$ must be suppressed. The present bound on the branching fraction is $B(\mu^+ \rightarrow e^+ e^+ e^-) < 1.0 \times 10^{-12}$ [210], which gives very strong constraint on the model parameter space. There are two possible cases to suppress the tree level contribution

to the $\mu^+ \rightarrow e^+e^+e^-$. The first possibility is considering heavy doubly charged bosons κ_1 and κ_2 . If $g_{11} \sim g_{12} \sim 0.1$ is taken, the doubly charged bosons should be heavier than 15 TeV to avoid too large contribution. The second option is suppressing a product of the couplings $|g_{12}g_{11}|$. When the doubly charged bosons are 500 GeV, the upper bound on the product $|g_{12}g_{11}|$ is obtained as $|g_{12}g_{11}| < 10^{-5}$. The contributions to $\tau^+ \rightarrow e^+e^+e^-$, $\tau^+ \rightarrow e^+e^+\mu^-$, $\tau^+ \rightarrow \mu^+\mu^+e^-$, $\tau^+ \rightarrow \mu^+\mu^+\mu^-$, $\tau^+ \rightarrow \mu^+e^+e^-$, and $\tau^+ \rightarrow e^+\mu^+\mu^-$ can be computed in the same manner. These flavour changing tau decays into three leptons are also enhanced in the model with tree level contributions. If future tau flavour experiments such as the high luminosity B factories [222] would discover a signal of such decays, it could support the model. In the phenomenological point of view, the scenario with a light doubly charged singlet scalar is attractive because the scenario with such a light exotic particle is testable at the LHC. Therefore we have searched for a solution with a suppressed $|g_{12}g_{11}|$ and we have found that the coupling g_{11} can be taken to be so small that the tree level contribution to the $\mu^+ \rightarrow e^+e^+e^-$ process is negligible with reproducing the neutrino oscillation data. In such a parameter space, the $B(\mu^+ \rightarrow e^+e^+e^-)$ is suppressed by the electromagnetic coupling constant compared with $B(\mu \rightarrow e\gamma)$, say $B(\mu^+ \rightarrow e^+e^+e^-) \sim \alpha_e B(\mu \rightarrow e\gamma)$ where the current upper limit is given by $B(\mu \rightarrow e\gamma) < 1.2 \times 10^{-11}$ [224]. The $B(\mu^+ \rightarrow e^+e^+e^-)$ is below the experimental upper bound, if the constraint of $B(\mu \rightarrow e\gamma)$ is satisfied.

In our analysis below, we work in the limit of $B_\omega \mu_\Omega \rightarrow 0$ and $B_\kappa \mu_K \rightarrow 0$ for simplicity. If these terms are switched on, the mixings in the charged singlet scalar mass eigenstates take part in the neutrino mass generation. However these mixings do not change our main results. In this limit, the mixing matrices U_ω and U_κ become the unit matrix, and only ω_1 and κ_1 contribute to the neutrino mass matrix and the LFV. Below we simply write the relevant fields as $\omega \equiv \omega_1$ and $\kappa \equiv \kappa_1$, and their masses are written as $m_\omega \equiv (m_\omega)_1$ and $m_\kappa \equiv (m_\kappa)_1$.

Following the above strategy, we search for an allowed parameter set. An example of the allowed parameter sets is

$$\begin{aligned}
f_{12} = f_{13} = \frac{f_{23}}{2} &= 3.7 \times 10^{-2}, \\
g_{11} \simeq 0, \quad g_{12} &= 4.8 \times 10^{-7}, \quad g_{13} = 2.1 \times 10^{-7}, \\
g_{22} = -0.13, \quad g_{23} &= 6.1 \times 10^{-3}, \quad g_{33} = -4.6 \times 10^{-4}, \\
\tilde{g}_{ij} = g_{ij}, \quad \lambda_a &= 1.0, \quad \mu_B = 500 \text{ GeV}, \quad \frac{X_k}{m_S} = 1.0, \\
(m_{\tilde{e}_L})_k = (m_{\tilde{e}_R})_k &= (m_{\tilde{\nu}_L})_k = m_S = 1000 \text{ GeV}, \\
m_\omega = 600 \text{ GeV}, \quad m_{\tilde{\omega}} &= 600 \text{ GeV}, \quad m_\kappa = 300 \text{ GeV}, \quad m_{\tilde{\kappa}} = 200 \text{ GeV}, \\
(m_\omega)_2 \gg m_\omega, \quad (m_\kappa)_2 &\gg m_\kappa.
\end{aligned} \tag{7.31}$$

On this benchmark point, the neutrino masses and mixing angles are given as

$$\begin{aligned}
\sin^2 \theta_{12} &= 0.33, \quad \sin^2 \theta_{23} = 0.5, \quad \sin^2 \theta_{13} = 0.0, \\
\Delta m_{21}^2 &= 7.6 \times 10^{-5} \text{ eV}^2, \quad |\Delta m_{31}^2| = 2.5 \times 10^{-3} \text{ eV}^2,
\end{aligned} \tag{7.32}$$

which are completely consistent with the present neutrino data: the global data analysis [8] of the neutrino oscillation experiments provide $\sin^2 \theta_{12} = 0.318_{-0.016}^{+0.019}$, $\sin^2 \theta_{23} = 0.50_{-0.06}^{+0.07}$, $\sin^2 \theta_{13} = 0.013_{-0.009}^{+0.013}$, $\Delta m_{21}^2 = (7.59_{-0.18}^{+0.23}) \times 10^{-5} \text{ eV}^2$, and $|\Delta m_{31}^2| = (2.40_{-0.11}^{+0.12}) \times 10^{-3} \text{ eV}^2$. Based on

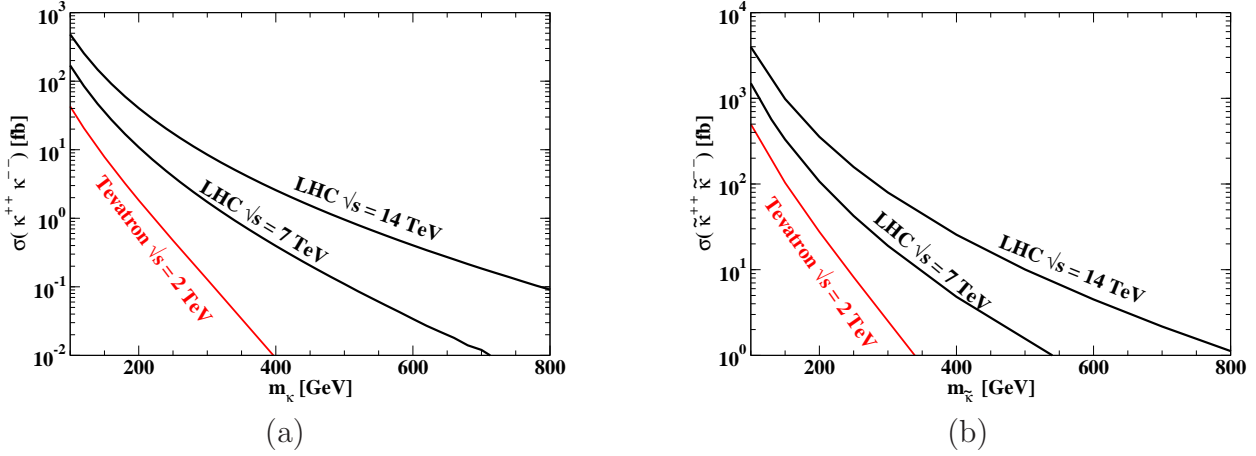


Figure 7.4: Production cross sections of (a) $\kappa^{++}\kappa^{--}$ and (b) $\tilde{\kappa}^{++}\tilde{\kappa}^{--}$, via Drell-Yan processes at the LHC (pp) and the Tevatron ($p\bar{p}$). The production cross section at the LHC is evaluated for $\sqrt{s} = 7$ TeV and $\sqrt{s} = 14$ TeV [70].

this benchmark point, our model predicts $B(\mu \rightarrow e\gamma) = 1.1 \times 10^{-11}$ and $B(\tau^+ \rightarrow \mu^+\mu^+\mu^-) = 1.3 \times 10^{-8}$, both of which are just below the present experimental bounds.

7.3 Phenomenology at the LHC

We turn to discuss collider phenomenology in the model assuming the parameters of the benchmark scenario given in Eq. (7.31). In our model, the new $SU(2)_L$ charged singlet fields are introduced, which can be accessible at collider experiments such as the LHC unless they are too heavy. In particular, the existence of the doubly charged singlet scalar boson and its SUSY partner fermion (the doubly charged singlino) provides discriminative phenomenological signals. They are produced in pair ($\kappa^{++}\kappa^{--}$ or $\tilde{\kappa}^{++}\tilde{\kappa}^{--}$) and each doubly charged boson (fermion) can be observed as a same-sign dilepton event, which would be a clear signature. In this Letter, we focus on such events including doubly charged particles. For the benchmark point given in Eq. (7.31), almost all the κ decays into the same-sign muon pair, $\kappa^{\pm\pm} \rightarrow \mu^\pm\mu^\pm$.

At hadron colliders such as the LHC and the Tevatron, the doubly charged singlet scalar κ and the doubly charged singlino $\tilde{\kappa}$ are produced dominantly in pair through the Drell-Yang processes. The production cross sections for $\kappa^{++}\kappa^{--}$ and $\tilde{\kappa}^{++}\tilde{\kappa}^{--}$ are shown as in Fig. 7.4(a) and Fig. 7.4(b), respectively. The first two plots from above correspond to the cross sections at the LHC of $\sqrt{s} = 14$ TeV and $\sqrt{s} = 7$ TeV, and the lowest one does to that at the Tevatron of $\sqrt{s} = 2$ TeV. We note that magnitudes of the production cross sections for the pair of singly-charged singlet scalars $\omega^+\omega^-$ and that of singly-charged singlinos $\tilde{\omega}^+\tilde{\omega}^-$ are $(1/4)$ smaller than those for $\kappa^{++}\kappa^{--}$ and $\tilde{\kappa}^{++}\tilde{\kappa}^{--}$ for the common mass for produced particles. At the LHC with $\sqrt{s} = 7$ TeV with the integrated luminosity \mathcal{L} of 1 fb^{-1} , about 100 of $\tilde{\kappa}^{++}\tilde{\kappa}^{--}$ pairs can be produced when $m_{\tilde{\kappa}} = 200$ GeV, while only a couple of the $\kappa^{++}\kappa^{--}$ pair is expected for $m_\kappa = 300$ GeV.

In Fig. 7.5, the distribution of the differential cross section for four muon (plus a missing transverse momentum) final states as a function of the invariant mass $M(\mu^+\mu^+)$ of the same-sign muon pair is shown assuming the bench mark scenario in Eq. (7.31) at the LHC with $\sqrt{s} = 7$

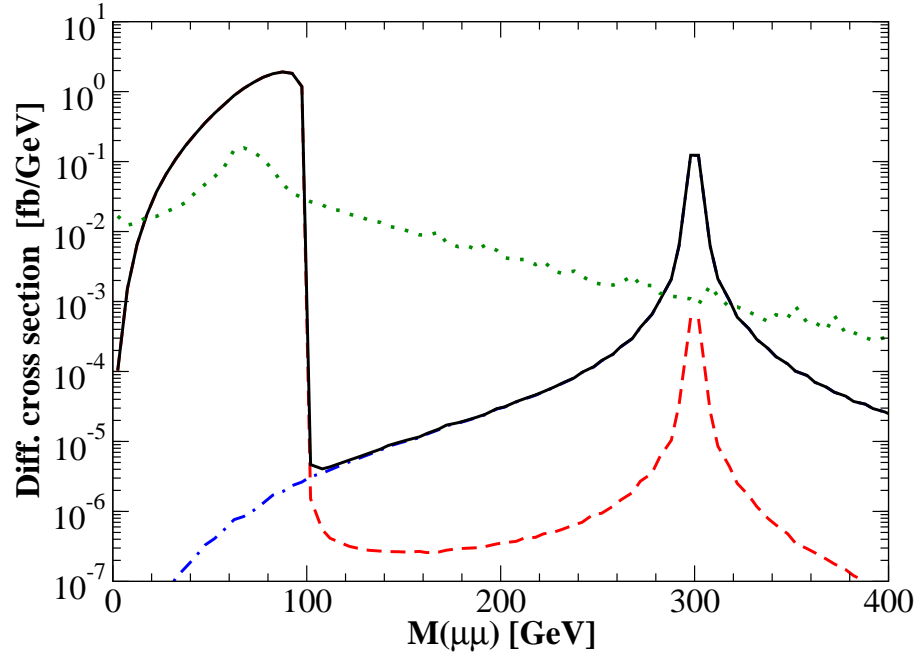


Figure 7.5: The invariant mass distribution of the same-sign dilepton event. The benchmark point in Eq. (7.31) is used and the neutralino mass is taken as $m_{\tilde{\chi}^0} = 100$ GeV. The dashed (red) curve corresponds to the events from $pp \rightarrow \tilde{\kappa}^{++}\tilde{\kappa}^{--} \rightarrow \tilde{\chi}^0\kappa_1^{++}\tilde{\chi}^0\kappa_1^{--} \rightarrow \tilde{\chi}^0\tilde{\chi}^0\mu^+\mu^+\mu^-\mu^-$. The dot-dashed (blue) curve shows the contributions from $pp \rightarrow \kappa^{++}\kappa^{--} \rightarrow \mu^+\mu^+\mu^-\mu^-$. The solid (black) curve denotes total events from the both signal processes. The dotted (green) curve shows the background events. For kinematical cut, see the text [70].

TeV. In order to suppress background events, we select the muon events with the transverse momentum larger than 20 GeV and the pseudo-rapidity less than 2.5. The signal events come from both $pp \rightarrow \kappa^{++}\kappa^{--} \rightarrow \mu^+\mu^+\mu^-\mu^-$ and $pp \rightarrow \tilde{\kappa}^{++}\tilde{\kappa}^{--} \rightarrow \tilde{\chi}^0\kappa_1^{++}\tilde{\chi}^0\kappa_1^{--} \rightarrow \tilde{\chi}^0\tilde{\chi}^0\mu^+\mu^+\mu^-\mu^-$. The $M(\mu^+\mu^+)$ distribution can be a key to explore the phenomena with the doubly charged particles. The doubly charged scalar mass and the mass difference between the doubly charged singlino and the neutralino are simultaneously determined at the LHC. A sharp peak is expected in the $M(\mu^+\mu^+)$ distribution at $M(\mu^+\mu^+) = m_{\kappa}$, because the same-sign muon pair from the κ decay is not associated with missing particles. On the other hand, the doubly charged singlino decays as $\tilde{\kappa}^{--} \rightarrow \tilde{\chi}^0\kappa^{--} \rightarrow \tilde{\chi}^0\mu^-\mu^-$ in the case that the lightest R-parity odd particle is a neutralino, $\tilde{\chi}^0$, which is a DM candidate in the model. In this Letter, we just assume that the LSP neutralino is Bino-like. In our analysis, we fix the neutralino mass as $m_{\tilde{\chi}^0} = 100$ GeV. The mass difference between $\tilde{\kappa}$ and $\tilde{\chi}^0$ can be measured by looking at a kink at $M(\mu^+\mu^+) = m_{\tilde{\kappa}} - m_{\tilde{\chi}^0}$ in the $M(\mu^+\mu^+)$ distribution. The main background comes from four muon events from the SM processes where muons are produced via the ZZ , $\gamma\gamma$ and γZ production, or a pair production of muons with the Z or γ emission. The expected background is also shown in Fig. 7.5. The events from signal dominate those from the background in the area of $M(\mu^+\mu^+) < m_{\tilde{\kappa}} - m_{\tilde{\chi}^0}$ and at around $M(\mu^+\mu^+) \sim m_{\kappa}$. The background events have been evaluated by using CalcHEP [130]. From this rough evaluation, one may expect that the event from the signal can be identified even at the LHC with $\sqrt{s} = 7$ TeV and $\mathcal{L} = 1$ fb $^{-1}$. As for the case with $\sqrt{s} = 14$ TeV, the signal to background ratio becomes larger and it will be more promising to explore our model.

There are other models in which the same-sign dilepton events are predicted. The model with the complex triplet scalar fields is an example of such a class of models [53, 59–62]. They can in principle be distinguished by looking at the decay products from doubly charged fields. In our scenario, $\kappa^{\pm\pm}$ can mainly decay into $\mu^{\pm}\mu^{\pm}$, while in the triplet models where the decay of doubly charged singlet scalars are directly connected with the neutrino mass matrix, there is no solution where only the $\mu^{\pm}\mu^{\pm}$ mode can be dominant decay mode. The difference in such decay pattern can be used to discriminate our model from the triplet models.

Chapter 8

Models with the $Y = 3/2$ doublet scalar field

In this section, we consider the extended Higgs models, in which one of the isospin doublet scalar fields carries the hypercharge $Y = 3/2$. Such a doublet field $\Phi_{3/2}$ is composed of a doubly charged scalar boson as well as a singly charged one.

Contrary to the $Y = 1$ triplet field Δ as well as the $Y = 2$ singlet S^{++} , the Yukawa coupling between $\Phi_{3/2}$ and charged leptons is protected by the chirality. In addition, the component fields of $\Phi_{3/2}$ are both charged and do not receive a vacuum expectation value (VEV) as long as electric charge is conserved. Hence, the field decays via the mixing with the other scalar representations which can decay into the SM particles or via some higher order couplings. This characteristic feature of $\Phi_{3/2}$ would give discriminative predictions at collider experiments. We therefore first study collider signatures of $\Phi_{3/2}$ at the LHC in the model (Model I) of an extension from the SM with an extra $Y = 1/2$ doublet and $\Phi_{3/2}$.

We then consider a new model for radiatively generating neutrino masses with a dark matter candidate (Model II), in which $\Phi_{3/2}$ and an extra $Y = 1/2$ doublet as well as vector-like singlet fermions carry the odd quantum number for an unbroken discrete Z_2 symmetry. We also discuss the neutrino mass model (Model III), in which the exact Z_2 parity in Model II is softly broken.

8.1 Model I

The simplest model, where $\Phi_{3/2}$ is just added to the SM, can decay into SM particles only if lepton-number violating higher order operators are introduced [223]. Thus, we here consider the model in which $\Phi_{3/2}$ is added to the model with two $Y = 1/2$ Higgs doublet fields ϕ_1 and ϕ_2 (Model I). The singly charged scalar state in $\Phi_{3/2}$ can decay into the SM particles via the mixing with the physical charged state from the $Y = 1/2$ doublets. This model can be regarded as an effective theory of Model III which we discuss later, or it may be that of the model with an additional heavier Δ , in which the gauge coupling unification would be possible. In order to avoid flavor changing neutral current, a softly-broken Z_2 symmetry is imposed [29], under which the scalar fields are transformed as $\phi_1 \rightarrow \phi_1$, $\phi_2 \rightarrow -\phi_2$, and $\Phi_{3/2} \rightarrow -\Phi_{3/2}$.

The most general scalar potential is given by

$$\begin{aligned}
 V = & \sum_{i=1}^2 \mu_i^2 |\phi_i|^2 + (\mu_3^2 \phi_1^\dagger \phi_2 + \text{h.c.}) + \sum_{i=1}^2 \frac{1}{2} \lambda_i |\phi_i|^4 + \lambda_3 |\phi_1|^2 |\phi_2|^2 + \lambda_4 |\phi_1^\dagger \phi_2|^2 + \frac{1}{2} [\lambda_5 (\phi_1^\dagger \phi_2)^2 + \text{h.c.}] \\
 & + \mu_\Phi^2 |\Phi_{3/2}|^2 + \frac{1}{2} \lambda_\Phi |\Phi_{3/2}|^4 + \sum_{i=1}^2 \rho_i |\phi_i|^2 |\Phi_{3/2}|^2 + \sum_{i=1}^2 \sigma_i |\phi_i^\dagger \Phi_{3/2}|^2 + [\kappa (\Phi_{3/2}^\dagger \phi_1) (\phi_2 \cdot \phi_1) + \text{h.c.}],
 \end{aligned} \tag{8.1}$$

where the Z_2 symmetry is softly broken at the μ_3^2 term. We neglect the CP violating phase for simplicity. The scalar doublets ϕ_1 , ϕ_2 and $\Phi_{3/2}$ are parameterized as

$$\phi_i = \begin{bmatrix} w_i^+ \\ \frac{1}{\sqrt{2}}(h_i + v_i + iz_i) \end{bmatrix} \quad (i = 1, 2), \quad \Phi_{3/2} = \begin{bmatrix} \Phi^{++} \\ \Phi^+ \end{bmatrix},$$

where the VEVs v_i satisfy $\sqrt{v_1^2 + v_2^2} = v \simeq 246$ GeV. Mass matrices for the neutral components are diagonalized as in the same way as those in the usual two Higgs doublet model (2HDM) with ϕ_1 and ϕ_2 . The mass eigenstates h and H for CP-even states are obtained by diagonalizing the mass matrix by the angle α . By the angle β ($\tan \beta \equiv v_2/v_1$), the mass eigenstates for the CP-odd states z and A are obtained, where z is the NG boson and A is the CP-odd Higgs boson. For simplicity $\sin(\beta - \alpha) = 1$ is taken such that h is the SM-like Higgs boson [91, 92]. The existence of $\Phi_{3/2}$ affects the singly charged scalar sector. The mass eigenstates are obtained by mixing angles β and χ as

$$\begin{bmatrix} w^\pm \\ H_1^\pm \\ H_2^\pm \end{bmatrix} = \begin{bmatrix} 1 & 0 & 0 \\ 0 & c_\chi & s_\chi \\ 0 & -s_\chi & c_\chi \end{bmatrix} \begin{bmatrix} c_\beta & s_\beta & 0 \\ -s_\beta & c_\beta & 0 \\ 0 & 0 & 1 \end{bmatrix} \begin{bmatrix} w_1^\pm \\ w_2^\pm \\ \Phi^\pm \end{bmatrix}, \tag{8.2}$$

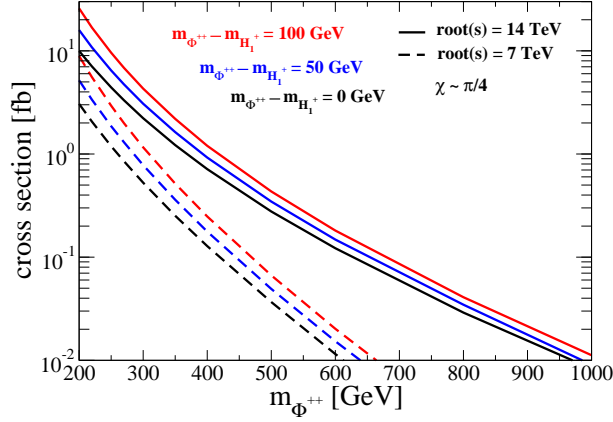
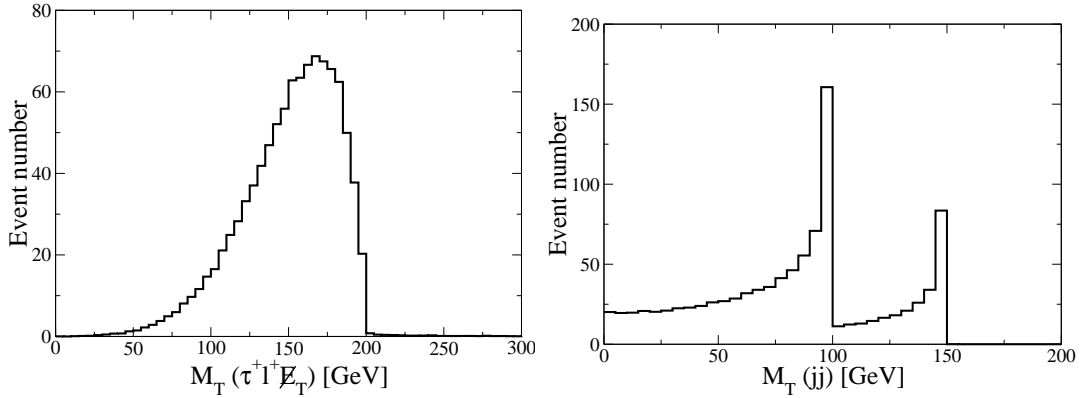
where $c_\theta = \cos \theta$ and $s_\theta = \sin \theta$, w^\pm are the NG bosons absorbed by the longitudinal component of the W^\pm bosons. H_1^\pm and H_2^\pm are physical mass eigenstates with the masses $m_{H_1^\pm}$ and $m_{H_2^\pm}$.

The Yukawa couplings for charged states are given by

$$\begin{aligned}
 \mathcal{L}_Y = & -\frac{\sqrt{2}V_{\text{KM}}^{ij}}{v} \bar{u}^i (m_{u^i} \xi_A^u d_L^j + m_{d^j} \xi_A^d d_R^j) \phi^+ \\
 & - \frac{\sqrt{2}m_{\ell^i} \xi_A^\ell}{v} \bar{\nu}^i \ell_R^i \phi^+ + \text{h.c.}, \quad (\phi^+ = H_1^+ \cos \chi - H_2^+ \sin \chi),
 \end{aligned}$$

where the coupling parameters $\xi_A^{u,d,\ell}$ [38] depend on the Z_2 charges of quarks and leptons [36, 37]. We are interested in the light charged scalar bosons such as $\mathcal{O}(100)$ GeV. To satisfy the $b \rightarrow s\gamma$ data [98–101], we choose the Type-I Yukawa interaction with $\tan \beta \gtrsim 2$. Assuming $m_{H_{1,2}^\pm} < m_t + m_b$ and $m_{H_2^\pm} - m_{H_1^\pm} < m_Z$, the branching ratios for the main decay modes are evaluated as $B(H_{1,2}^\pm \rightarrow \tau^\pm \nu) \sim 0.7$ and $B(H_{1,2}^\pm \rightarrow cs) \sim 0.3$ when $\chi \neq 0$.

At the LHC, Φ^{++} can be tested by using various processes such as the pair production and the associated production with H_1^- or H_2^- . We here discuss an interesting signal via the process $u\bar{d} \rightarrow W^{*+} \rightarrow \Phi^{++} H_{1,2}^-$. The cross section is shown in Fig. 8.1. We may examine this process, for example, by the decay $\Phi^{++} \rightarrow H_{1,2}^+ W^+ \rightarrow \tau^+ \ell^+ \nu \nu$ with $H_{1,2}^- \rightarrow jj$, when

Figure 8.1: Cross section of $pp \rightarrow XW^{+*} \rightarrow X\Phi^{++}H_1^-$ [71].Figure 8.2: (Left) The transverse mass distribution for the $\tau^+\ell^+\cancel{E}_T$ system for the signal. (Right) That for the jj system. The event number is taken to be 1000 for both figures [71].

$m_{\Phi^{\pm\pm}} > m_{H_1^\pm} + m_W$ with $m_{H_{1,2}^\pm} < m_t + m_b$ and $m_{H_2^\pm} - m_{H_1^\pm} < m_Z$, where $m_{\Phi^{\pm\pm}}$ is the mass of $\Phi^{\pm\pm}$. The signal is then $\tau^+\ell^+jj$ plus a missing transverse momentum \cancel{E}_T ($\ell^+ = e^+$ or μ^+). The signal cross section for $\tau^\pm\ell^\pm jj \cancel{E}_T$ is evaluated as 4.0 fb (1.3 fb) for $\sqrt{s} = 14$ TeV (7 TeV) for $m_{H_1^\pm} = 100$ GeV, $m_{H_2^\pm} = 150$ GeV, $m_{\Phi^{\pm\pm}} = 200$ GeV and $\chi \simeq \pi/4$.

The mass for Φ^{++} can be determined from the Jacobian peak [63] in the distribution of the transverse mass, $M_T(\tau^+\ell^+\cancel{E}_T) = \sqrt{2p_T^\tau \cancel{E}_T(1 - \cos\varphi)}$, where φ is the azimuthal angle between the transverse momentum p_T^τ of the dilepton system and \cancel{E}_T . We show numerical results for the scenario with $m_{H_1^\pm} = 100$ GeV, $m_{H_2^\pm} = 150$ GeV, $m_{\Phi^{\pm\pm}} = 200$ GeV, $\chi \simeq \pi/4$, $\tan\beta = 3$, $\sin(\beta - \alpha) = 1$ and $m_H = m_A = 127$ GeV, where m_H and m_A represent the masses of H and A , respectively. The potential is then approximately custodial symmetric, so that the rho parameter constraint is satisfied with the mass of the SM-like Higgs boson h to be 120 GeV. The end point in Fig. 8.2 (Left) indicates $m_{\Phi^{\pm\pm}}$, where the event number is taken to be 1000. One might think that the final decay products from the τ lepton should be discussed. We stress that the endpoint at $m_{\Phi^{\pm\pm}}$ also appears in the distribution of $M_T(\ell^+\ell^+\cancel{E}_T)$ obtained from the leptonic decay of the τ^+ . The cross section for the $\ell^+\ell^+jj\cancel{E}_T$ signal is about 1.3 fb for $\sqrt{s} = 14$

TeV (0.45 fb for $\sqrt{s} = 7$ TeV). Furthermore, masses of singly charged Higgs bosons can also be measured by the distribution of $M_T(jj)$. In Fig. 8.2 (Right), the two Jacobian peaks at 100 and 150 GeV correspond to $m_{H_1^\pm}$ and $m_{H_2^\pm}$, respectively, where the event number is taken to be 1000. The SM background for $\ell^+\ell^+jj\cancel{E}_T$, which mainly comes from $u\bar{d} \rightarrow W^+W^+jj$, is 3.95 fb for $\sqrt{s} = 14$ TeV (0.99 fb for $\sqrt{s} = 7$ TeV). The cross section of the background is comparable to that for the signal before kinematic cuts. There is no specific kinematical structure in the $\ell^+\ell^+$ distribution in the background. All the charged scalar states can be measured simultaneously via this process unless their masses are too heavy if sufficient number of the signal event remains after kinematic cuts. While the detection at the LHC with 300 fb $^{-1}$ may be challenging, it could be much better at the upgraded version of the LHC with 3000 fb $^{-1}$.

8.2 Model II

We here present a new model in which $\Phi_{3/2}$ is introduced to naturally generate tiny neutrino masses at one-loop level. To this end, we again consider the scalar sector with ϕ_1 , ϕ_2 and $\Phi_{3/2}$. In addition, we introduce two isospin singlet Dirac fermions ψ^a ($a = 1, 2$) with $Y = -1$. We impose the exact (unbroken) Z_2 parity, under which ϕ_2 , $\Phi_{3/2}$ and ψ^a are odd while all the SM particles including ϕ_1 are even. This Z_2 parity plays a role to forbid mixing terms of $\bar{\ell}_R\psi_L^a$ as well as couplings of $\bar{L}_L\phi_1\psi_R^a$ and $\bar{L}_L\phi_2\ell_R$, and to guarantee the stability of a dark matter candidate; i.e., the lightest neutral Z_2 odd particle. Lepton numbers $L = -2$ and $+1$ are respectively assigned to $\Phi_{3/2}$ and ψ^a .

The scalar potential coincides that in Eq. (8.1) but $\mu_3^2 = 0$ due to the exact Z_2 parity. Without $\Phi_{3/2}$, the scalar sector is that of the inert doublet model [22], in which only ϕ_1 receives the VEV yielding the SM-like Higgs boson h , while ϕ_2 gives Z_2 -odd scalar bosons H , A and H^\pm . Including $\Phi_{3/2}$, H^\pm can mix with Φ^\pm diagonalized by the angle χ in Eq. (8.2) with $\beta = 0$. Masses and interactions for ψ^a are given by

$$\mathcal{L}_Y = m_{\psi^a}\bar{\psi}_L^a\psi_R^a + f_i^a\overline{(L_L^i)^c} \cdot \Phi_{3/2}\psi_L^a + g_i^a\overline{L_L^i}\phi_2\psi_R^a + \text{h.c.} \quad (8.3)$$

The neutrino masses are generated via the one-loop diagram in Fig. 8.3. The flow of the lepton number is also indicated in the figure. The source of lepton number violation (LNV) is the coupling κ . This is similar to the model by Zee [16], although the diagram looks similar to the model by Ma [20] where Majorana masses of right-handed neutrinos ν_R is the origin of LNV. For $m_{\psi^a} \gg m_{H_1^\pm}, m_{H_2^\pm}$, the mass matrix can be calculated as

$$(\mathcal{M}_\nu)_{ij} \simeq \sum_{a=1}^2 \frac{1}{16\pi^2} \frac{1}{2m_{\psi^a}} (f_i^a g_j^{a*} + f_j^a g_i^{a*}) \frac{v^2 \kappa}{m_{H_2^\pm}^2 - m_{H_1^\pm}^2} \\ \times \left(m_{H_2^\pm}^2 \log \frac{m_{\psi^a}^2}{m_{H_2^\pm}^2} - m_{H_1^\pm}^2 \log \frac{m_{\psi^a}^2}{m_{H_1^\pm}^2} \right).$$

For $m_\psi \sim 1$ TeV, $m_{H_1^\pm} \sim m_{H_2^\pm} \sim \mathcal{O}(100)$ GeV, and $f_i^a \sim g_i^a \sim \kappa \sim \mathcal{O}(10^{-3})$, the scale of neutrino masses (~ 0.1 eV) can be generated. The bound from LFV processes such as $\mu \rightarrow e\gamma$ [224] can easily be satisfied. The neutrino data can be reproduced by introducing at least two fermions ψ^1 and ψ^2 . The lightest Z_2 odd neutral Higgs boson (either H or A) is a

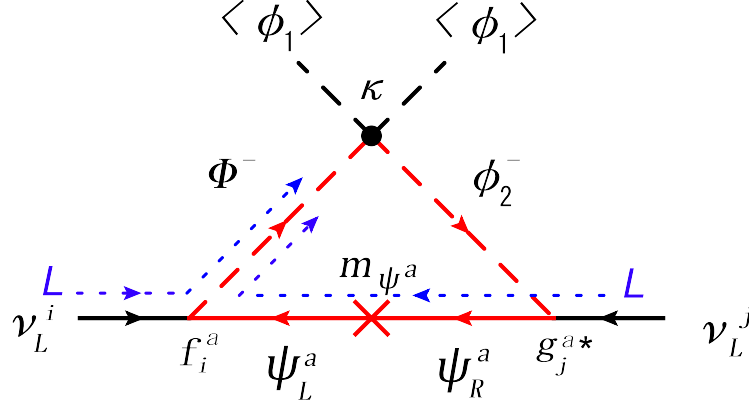


Figure 8.3: Neutrino mass diagram [71].

dark matter candidate [22]. Assuming that H is the lightest, its thermal relic abundance can explain the WMAP data [9] by the s-channel process $HH \rightarrow h \rightarrow b\bar{b}$ (or $\tau^+\tau^-$). The t-channel process $HH \rightarrow \bar{\ell}_L \ell_L$ with ψ_R mediation is negligible. The direct search results can also be satisfied.

Finally, we comment on the collider signature in Model II. $\Phi_{3/2}$ is Z_2 odd, so that its decay product includes the dark matter H . For $m_H = 50$ GeV, the mass of h would be about 115 GeV to satisfy the WMAP data [9]. We then consider the parameter set; $m_{\Phi^{++}} = 230$ GeV, $m_{H_2^+} = 150$ GeV, $m_{H_1^+} \simeq m_A = 149$ GeV and $\chi = 0.1$ to satisfy the neutrino data and the LFV data. The signal at the LHC would be $W^+W^+W^- \cancel{E}_T$ via $u\bar{d} \rightarrow \Phi^{++}H_i^- \rightarrow (H_i^+W^+)(W^-H) \rightarrow (HW^+W^+)(W^-H)$. The cross section of $W^\pm W^\pm W^\mp \cancel{E}_T$ is 23 fb for $\sqrt{s} = 14$ TeV (7.3 fb for $\sqrt{s} = 7$ TeV). The main background comes from $W^\pm W^\pm W^\mp$, and the cross section is 135 fb for $\sqrt{s} = 14$ TeV (76 fb for $\sqrt{s} = 7$ TeV). The signal background ratio is not too small at all, and we can expect the signal would be detected after appropriate kinematic cuts.

Chapter 9

Conclusion

We have discussed the phenomenology of various Higgs sectors. Extended Higgs sectors often appear in the new physics models, where problems which cannot explain within the SM such as the hierarchy problem, neutrino masses, dark matter and baryon asymmetry of the Universe, can be solved. Therefore, by studying extended Higgs sectors, we can determine the direction of new physics models.

In Part I, we have discussed the phenomenology of the THDM, the HTM and SUSY Higgs sectors as an important examples of the extended Higgs sectors.

In the THDM, we have discussed the discrimination among the types of Yukawa interaction which appear under the softly-broken discrete Z_2 symmetry to avoid the FCNC at the tree level. We have shown that the light charged Higgs boson of $\mathcal{O}(\infty'')$ GeV is allowed in the type-I and the type-X Yukawa interaction. We have discussed phenomenological discrimination of the types of Yukawa interactions in the THDM at the LHC and the ILC. In particular, we have mainly discussed the discrimination between the MSSM Higgs sector and the type-X THDM in the relatively light charged Higgs boson scenario. At the LHC, the type-X THDM can be discriminated from the MSSM by searching for the production and decays of the extra Higgs bosons A , H and H^\pm , such as $gg \rightarrow A/H \rightarrow \ell^+\ell^-$, where ℓ is e or μ when $\sin(\beta - \alpha) \simeq 1$. We have also discussed the pair production processes $pp \rightarrow AH^\pm$, HH^\pm and AH to test the type-X THDM. These processes would provide distinctive four lepton final states $\ell^+\ell^-\tau^\pm\nu$ and $\ell^+\ell^-\tau^+\tau^-$ in the type-X THDM, while the MSSM Higgs sector can be tested by $b\bar{b}\tau^\pm\nu$ and $b\bar{b}\tau^+\tau^-$. At the ILC, the type-X THDM is expected to be studied very well by the pair production $e^+e^- \rightarrow AH$. The signal should be four leptons ($\ell\ell\tau^+\tau^-$).

In the HTM, a characteristic mass spectrum $m_{H^{++}}^2 - m_{H^+}^2 \simeq m_{H^+}^2 - m_{\phi^0}^2 (\equiv \xi)$ is predicted when $v_\Delta \ll v$. Therefore, by measuring this mass spectrum of the triplet-like scalar bosons, the model can be tested at the LHC. We have investigated the collider signature in the HTM with $\xi > 0$ at the LHC. In this case, H^{++} is the heaviest of all the triplet-like scalar bosons. When $v_\Delta > 10^{-4}$ - 10^{-3} GeV, H^{++} does not decay into the same sign dilepton so that the limit of the mass of H^{++} from the recent results at the LHC cannot be applied. We thus mainly have discussed the case of light triplet-like scalar bosons whose masses are of $\mathcal{O}(100)$ GeV. In such a case, triplet-like scalar bosons mainly decay into $H^{++} \rightarrow H^+W^{+(*)}$, $H^+ \rightarrow \phi^0W^{+(*)}$ and $\phi^0 \rightarrow b\bar{b}$. We have found that all the masses of the triplet-like scalar bosons may be able to be reconstructed by measuring the endpoint in the transverse mass distribution and the invariant mass distribution of the systems which are produced via the decay of the triplet-like scalar bosons.

We have investigated decoupling properties of SUSY Higgs sectors. The SUSY Higgs sectors can be separated into the models with additional F-term contributions to the interaction terms in the Higgs potential and those without such F-term contributions. The former models have a nondecoupling property due to the F-term contribution. As an concrete examples of the former model, we have discussed the NMSSM, the TMSSM and the model with two additional Higgs doublets and the charged singlet fields (4D Ω). While m_h is at most 120-130 GeV in the MSSM, that in the NMSSM and the TMSSM can be much larger. The deviation of hhh coupling from the prediction in the SM can be significant as large as 30%-60% in the 4D Ω . Therefore, even when only h is observed in future, precision measurements of m_h and the hhh coupling can help discriminate the SUSY Higgs sectors. We have also discussed the latter SUSY models, where there are no additional F-term contributions in the Higgs potential at the tree level. We have considered the 4HDM as a simplest example. Even without interaction terms from the tree-level F-term contribution, significant quasi-nondecoupling effects of extra scalar fields can occur at the tree level due to the B-term mixing among the Higgs bosons. We have deduced formulae for deviations in the MSSM observables in the decoupling region for the extra heavy fields. The possible modifications in the Higgs sector from the MSSM predictions have been studied numerically. We have found that the quasi-nondecoupling effect from the B-term mixing can be significant in the 4HDSSM, which can change the MSSM observables m_{H^+} , m_h , m_H and $\sin^2(\beta - \alpha)$ to a considerable extent. Detecting the deviations from the MSSM predictions on these MSSM observables, the MSSM Higgs sector can be tested, and at the same time the possibility of extended SUSY Higgs sectors including the 4HDM can be explored even when only the MSSM particles are discovered in near future at the LHC and at the ILC.

In Part II, we discuss new physics models at the TeV scale, where neutrino masses, dark matter and/or baryon asymmetry of the Universe can be explained.

First, we have discussed theoretical constraints on the parameter space under the conditions from vacuum stability and triviality in the three-loop radiative seesaw model with TeV-scale right-handed neutrinos which are odd under the Z_2 parity. It has been found that the model can be consistent up to the scale above 10 TeV in the parameter region which satisfies the neutrino data, the LFV data, the thermal relic abundance of dark matter as well as the requirement from the strongly first order phase transition. We also reanalyzed the constraint from the LFV data. The data from $\mu \rightarrow eee$ is found to be more severer than that from $\mu \rightarrow e\gamma$.

Second, we have discussed the SUSY extension of the Zee-Babu model under R-parity conservation. In the model, it is not necessary to introduce very high energy scale as compared to the TeV scale, and the model lies in the reach of the collider experiments and the flavour measurements. We have found that the neutrino data can be reproduced with satisfying the current bounds from the LFV even in the scenario where not all the superpartner particles are heavy. The LSP can be a dark matter candidate. Phenomenology of doubly charged singlet fields has also been discussed at the LHC.

Finally, we have studied various aspects of $\Phi_{3/2}$ including the signature at the LHC in a few models. New TeV-scale models with $\Phi_{3/2}$ have been presented for generating tiny neutrino masses, one of which also contains dark matter candidates. We have found that $\Phi_{3/2}$ in these models shows discriminative and testable aspects at the LHC and its luminosity upgraded version, so that models with $\Phi_{3/2}$ would be distinguishable from the other models with doubly charged scalar states.

Appendix A

$W_L W_L \rightarrow W_L W_L$ scattering amplitude

In this appendix, we calculate the scattering amplitude of the process $W_L W_L \rightarrow W_L W_L$. Feynman diagrams of this process is shown in Fig. A.1. In section 2.3, we have discussed the perturbative unitarity to obtain the upper bound of the Higgs boson, and we have calculated the $W_L W_L \rightarrow W_L W_L$ scattering amplitude in the high energy limit. Here, we calculate the amplitude up to the order E^0 , where E is the energy of each W_L . The amplitude of the s-channel photon exchange diagram is

$$\mathcal{M}(W_L^+ W_L^- \rightarrow \gamma \rightarrow W_L^+ W_L^-)_s = \frac{e^2}{m_W^4} \cos \theta (4E^4 - 3m_W^4) + \mathcal{O}(E^{-2}), \quad (\text{A.1})$$

where θ is the scattering angle. The amplitude of the s-channel Z boson exchange diagram is

$$\mathcal{M}(W_L^+ W_L^- \rightarrow Z \rightarrow W_L^+ W_L^-)_s = \frac{g^2 \cos^2 \theta_W}{m_W^4} \cos \theta (4E^4 + m_Z^2 E^2 - 3m_W^4) + \mathcal{O}(E^{-2}). \quad (\text{A.2})$$

The amplitudes of the t-channel contributions of photon and Z boson exchange diagrams are

$$\begin{aligned} & \mathcal{M}(W_L^+ W_L^- \rightarrow \gamma \rightarrow W_L^+ W_L^-)_t \\ &= \frac{-e^2}{2m_W^4} \left[(\cos 2\theta - 4 \cos \theta - 5)E^4 + 16 \cos \theta E^2 m_W^2 + \left(-\cos 2\theta + 11 - \frac{8}{1 + \cos \theta} \right) m_W^4 \right] + \mathcal{O}(E^{-2}), \end{aligned} \quad (\text{A.3})$$

$$\begin{aligned} & \mathcal{M}(W_L^+ W_L^- \rightarrow Z \rightarrow W_L^+ W_L^-)_t \\ &= \frac{-g^2 \cos^2 \theta_W}{2m_W^4} \left[(\cos 2\theta - 4 \cos \theta - 5)E^4 + (3m_Z^2 + (16m_W^2 - m_Z^2) \cos \theta)E^2 \right. \\ & \quad \left. + \left(-\cos 2\theta + 11 - \frac{8}{1 + \cos \theta} \right) m_W^4 - (-\cos 2\theta + 20 \cos \theta + 5) \frac{m_W^2 m_Z^2}{2(1 + \cos \theta)} \right]. \end{aligned} \quad (\text{A.4})$$

The amplitude of the contact interaction diagram is

$$\mathcal{M}(W_L^+ W_L^- \rightarrow W_L^+ W_L^-) = \frac{g^2}{2m_W^4} [(\cos 2\theta - 12 \cos \theta - 5)E^4 + 4(1 + 3 \cos \theta)E^2 m_W^2]. \quad (\text{A.5})$$

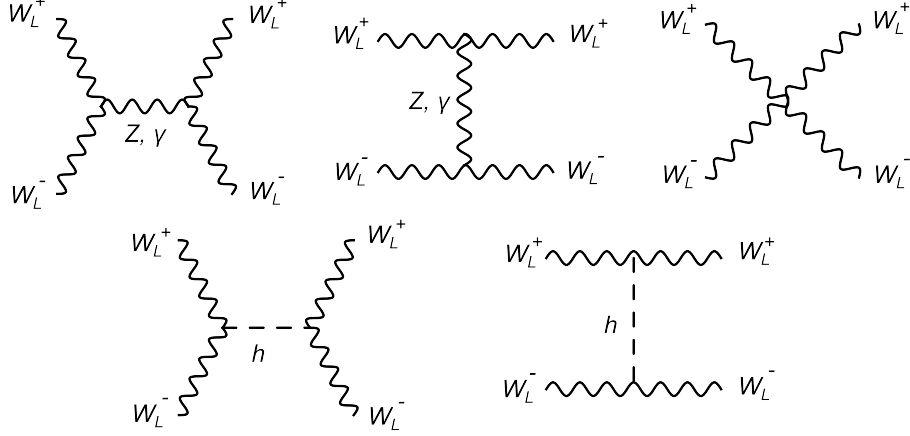


Figure A.1: Feynman diagrams for $W_L^+ W_L^- \rightarrow W_L^+ W_L^-$ scattering processes.

Therefore, the amplitude of $W_L^+ W_L^- \rightarrow W_L^+ W_L^-$ without Higgs boson exchange diagram is

$$\begin{aligned}
 & i\mathcal{M}(W_L^+ W_L^- \rightarrow W_L^+ W_L^-)_{\text{w/o Higgs}} \\
 &= \frac{g^2}{m_W^4} \left[\frac{1}{2}(1 - \cos \theta) E^2 m_W^2 + \left(\cos^2 \theta - 3 \cos \theta - 6 + \frac{-\cos 2\theta + 20 \cos \theta + 21}{4(1 + \cos \theta)} \right) m_W^4 \right] + \mathcal{O}(E^{-2}).
 \end{aligned} \tag{A.6}$$

This result shows that the $\mathcal{O}(E^4)$ dependence of the amplitude is cancelled but the $\mathcal{O}(E^2)$ dependence remains. The 0th partial wave amplitude can be calculated as

$$\begin{aligned}
 a_0(W_L^+ W_L^- \rightarrow W_L^+ W_L^-)_{\text{w/o Higgs}} &= \frac{1}{32\pi} \int_{-1}^1 d \cos \theta \mathcal{M}(W_L^+ W_L^- \rightarrow W_L^+ W_L^-)_{\text{w/o Higgs}} \\
 &= \frac{\sqrt{2} G_F E_{\text{cm}}^2}{32\pi} + \mathcal{O}(E^0),
 \end{aligned} \tag{A.7}$$

where $E_{\text{cm}} = 2E$ is the center of mass energy. By the condition in Eq. (2.21), unitarity is violated around $E_{\text{cm}} \simeq 1.7$ TeV.

Next, we take into account the Higgs boson exchange diagrams. The amplitudes of s-channel and t-channel contributions are, respectively

$$i\mathcal{M}(W_L^+ W_L^- \rightarrow h \rightarrow W_L^+ W_L^-)_s = -i \frac{g^2}{m_W^2} \left[E^2 - m_W^2 + \frac{1}{4} m_h^2 \right] + \mathcal{O}(E^{-2}), \tag{A.8}$$

$$i\mathcal{M}(W_L^+ W_L^- \rightarrow h \rightarrow W_L^+ W_L^-)_t = i \frac{g^2}{2m_W^2} \left[E^2(1 + \cos \theta) - \frac{1}{2} m_h^2 + m_W^2 \cos \theta \right] + \mathcal{O}(E^{-2}). \tag{A.9}$$

The total amplitude of $W_L^+ W_L^- \rightarrow W_L^+ W_L^-$ is

$$i\mathcal{M}(W_L^+ W_L^- \rightarrow W_L^+ W_L^-) = -i \frac{g^2 m_h^2}{2m_W^2} + g^2 \left[\cos^2 \theta - \frac{5}{2} \cos \theta - 6 + \frac{-\cos 2\theta + 20 \cos \theta + 21}{4(1 + \cos \theta)} \right] + \mathcal{O}(E^{-2}). \tag{A.10}$$

The E^2 dependence of the amplitude is cancelled by the Higgs boson exchange diagram.

Appendix B

Renormalization group equations

In this appendix, we list one-loop level renormalization group equations (RGEs) in the SM, the THDM, the model by Aoki, Kanemura and Seto [21] and several SUSY Higgs models. The beta function for the dimension less coupling constant c is defined by

$$\beta(c) \equiv \frac{dc}{d \log Q} = Q \frac{dc}{dQ}, \quad (\text{B.1})$$

where Q is an arbitrary scale. First, RGEs for the gauge couplings g_i are written as

$$\beta(g_i) = \frac{g_i^3}{16\pi^2} \left[-\frac{11}{3}C(G) + \sum_{\text{fermions}} \frac{2}{3}C(F) + \sum_{\text{scalars}} \frac{1}{3}C(S) \right], \quad (\text{B.2})$$

where $C(G)$ is defined by the structure constant f^{abc} for the gauge group G , while $C(F)$ is defined by the generator t^a which appears in fermion-fermion-gauge boson vertex as

$$C(G)\delta^{ab} = f^{acd}f^{bcd}, \quad (\text{B.3})$$

$$C(F)\delta^{ab} = \text{Tr}(t^a t^b), \quad (\text{B.4})$$

and $C(S)$ is also defined in the same way as $C(F)$.

B.1 Beta functions in the SM

Beta functions for the gauge couplings in the model with the number of the generation N_g and that of the Higgs doublet N_H are given by

$$\beta(g_s) = \frac{g_s^3}{16\pi^2} \left[-11 + \frac{4}{3}N_g \right], \quad (\text{B.5a})$$

$$\beta(g) = \frac{g^3}{16\pi^2} \left[-\frac{22}{3} + \frac{4}{3}N_g + \frac{1}{6}N_H \right], \quad (\text{B.5b})$$

$$\beta(g') = \frac{g'^3}{16\pi^2} \left[\frac{20}{9}N_g + \frac{1}{6}N_H \right]. \quad (\text{B.5c})$$

In the SM, (N_g, N_H) is $(3, 1)$. We note that Eq. (B.5) is valid in the model whose Higgs sector is composed of only doublet fields with $Y = 1/2$ and singlet fields with $Y = 0$. The beta

functions for the Higgs self-coupling λ and the top Yukawa coupling y_t are given by

$$\beta(\lambda) = \frac{1}{16\pi^2} \left[24\lambda^2 + 12y_t^2\lambda - 6y_t^4 + \frac{9}{8}g^4 + \frac{3}{4}g^2g'^2 + \frac{3}{8}g'^4 - 9\lambda g^2 - 3\lambda g'^2 \right], \quad (\text{B.6})$$

$$\beta(y_t) = \frac{y_t}{16\pi^2} \left[\frac{9}{2}y_t^2 - 8g_s^2 - \frac{9}{4}g^2 - \frac{17}{12}g'^2 \right]. \quad (\text{B.7})$$

B.2 Beta functions in the THDM

The beta functions for the Higgs self-couplings in the THDM and that for the top Yukawa coupling are given by

$$\beta(\lambda_1) = \frac{1}{16\pi^2} \left[12\lambda_1^2 + 4\lambda_3^2 + 2\lambda_4^2 + 2\lambda_5^2 + 4\lambda_3\lambda_4 + \frac{9}{4}g^4 + \frac{6}{4}g^2g'^2 + \frac{3}{4}g'^4 - 9\lambda_1g^2 - 3\lambda_1g'^2 \right], \quad (\text{B.8})$$

$$\begin{aligned} \beta(\lambda_2) = \frac{1}{16\pi^2} & \left[12\lambda_2^2 + 4\lambda_3^2 + 2\lambda_4^2 + 2\lambda_5^2 + 4\lambda_3\lambda_4 - 12y_t^4 + 12y_t^2\lambda_2 \right. \\ & \left. + \frac{9}{4}g^4 + \frac{6}{4}g^2g'^2 + \frac{3}{4}g'^4 - 9\lambda_2g^2 - 3\lambda_2g'^2 \right], \end{aligned} \quad (\text{B.9})$$

$$\begin{aligned} \beta(\lambda_3) = \frac{1}{16\pi^2} & \left[6\lambda_1\lambda_3 + 2\lambda_1\lambda_4 + 6\lambda_2\lambda_3 + 2\lambda_2\lambda_4 + 4\lambda_3^2 + 2\lambda_4^2 + 2\lambda_5^2 \right. \\ & \left. + \frac{9}{4}g^4 + \frac{3}{4}g'^4 - \frac{6}{4}g^2g'^2 - 9\lambda_3g^2 - 3\lambda_3g'^2 + 6\lambda_3y_t^2 \right], \end{aligned} \quad (\text{B.10})$$

$$\beta(\lambda_4) = \frac{1}{16\pi^2} \left[2\lambda_4(\lambda_1 + \lambda_2 + 4\lambda_3 + 2\lambda_4) + 8\lambda_5^2 + 3g^2g'^2 + \lambda_4(-9g^2 - 3g'^2) + 6\lambda_4y_t^2 \right], \quad (\text{B.11})$$

$$\beta(\lambda_5) = \frac{1}{16\pi^2} \left[2\lambda_5(\lambda_1 + \lambda_2 + 4\lambda_3 + 6\lambda_4) + \lambda_5(-9g^2 - 3g'^2) + 6\lambda_5y_t^2 \right], \quad (\text{B.12})$$

$$\beta(y_t) = \frac{y_t}{16\pi^2} \left[\frac{9}{2}y_t^2 - 8g_s^2 - \frac{9}{4}g^2 - \frac{17}{12}g'^2 \right]. \quad (\text{B.13})$$

The coupling constants λ_1 - λ_5 are defined in Eq. (3.12). The beta functions for the gauge couplings are given in Eq. (B.5) with (N_g, N_H) to be $(3, 2)$.

B.3 Beta functions in the three-loop neutrino mass model

The beta functions for dimension less couplings in the model [21] are given as

$$\beta(g_s) = \frac{1}{16\pi^2} [-7g_s^3], \quad (\text{B.14})$$

$$\beta(g) = \frac{1}{16\pi^2} [-3g^3], \quad (\text{B.15})$$

$$\beta(g') = \frac{1}{16\pi^2} \left[-\frac{22}{3}g'^3 \right], \quad (\text{B.16})$$

$$\beta(y_t) = \frac{y_t}{16\pi^2} \left[\frac{9}{2}y_t^2 - 8g_s^2 - \frac{9}{4}g^2 - \frac{17}{12}g'^2 \right], \quad (\text{B.17})$$

$$\beta(h_i^\alpha) = \frac{1}{16\pi^2} \left[-5g'^2 h_i^\alpha + \frac{1}{2}h_i^\alpha \sum_j (h_j^\alpha)^2 + \frac{1}{2}h_i^\alpha \sum_\beta (h_i^\beta)^2 + h_i^\alpha \sum_{j,\beta} (h_j^\beta)^2 \right], \quad (\text{B.18})$$

$$\begin{aligned} \beta(\lambda_1) = \frac{1}{16\pi^2} & \left[12\lambda_1^2 + 4\lambda_3^2 + 2\lambda_4^2 + 2\lambda_5^2 + 4\lambda_3\lambda_4 + 2\rho_1^2 + \sigma_1^2 + \frac{9}{4}g^4 + \frac{6}{4}g^2g'^2 + \frac{3}{4}g'^4 \right. \\ & \left. - 4y_\tau^4 + (4y_\tau^2 - 9g^2 - 3g'^2)\lambda_1 \right], \end{aligned} \quad (\text{B.19})$$

$$\begin{aligned} \beta(\lambda_2) = \frac{1}{16\pi^2} & \left[12\lambda_2^2 + 4\lambda_3^2 + 2\lambda_4^2 + 2\lambda_5^2 + 4\lambda_3\lambda_4 + 2\rho_2^2 + \sigma_2^2 + \frac{9}{4}g^4 + \frac{6}{4}g^2g'^2 + \frac{3}{4}g'^4 \right. \\ & \left. - 12y_t^4 - 12y_b^4 + (12y_t^2 + 12y_b^2 - 9g^2 - 3g'^2)\lambda_2 \right], \end{aligned} \quad (\text{B.20})$$

$$\begin{aligned} \beta(\lambda_3) = \frac{1}{16\pi^2} & \left[6\lambda_1\lambda_3 + 2\lambda_1\lambda_4 + 6\lambda_2\lambda_3 + 2\lambda_2\lambda_4 + 4\lambda_3^2 + 2\lambda_4^2 + 2\lambda_5^2 + 2\rho_1\rho_2 + \sigma_1\sigma_2 + 4\kappa^2 \right. \\ & \left. + \frac{9}{4}g^4 + \frac{3}{4}g'^4 - \frac{6}{4}g^2g'^2 + (6y_t^2 + 6y_b^2 + 2y_\tau^2 - 9g^2 - 3g'^2)\lambda_3 \right], \end{aligned} \quad (\text{B.21})$$

$$\begin{aligned} \beta(\lambda_4) = \frac{1}{16\pi^2} & \left[2(\lambda_1 + \lambda_2 + 4\lambda_3 + 2\lambda_4)\lambda_4 + 8\lambda_5^2 - 8\kappa^2 + 3g^2g'^2 \right. \\ & \left. + (6y_t^2 + 6y_b^2 + 2y_\tau^2 - 9g^2 - 3g'^2)\lambda_4 \right], \end{aligned} \quad (\text{B.22})$$

$$\beta(\lambda_5) = \frac{1}{16\pi^2} \left[2(\lambda_1 + \lambda_2 + 4\lambda_3 + 6\lambda_4)\lambda_5 + (6y_t^2 + 6y_b^2 + 2y_\tau^2 - 9g^2 - 3g'^2)\lambda_5 \right], \quad (\text{B.23})$$

$$\begin{aligned} \beta(\rho_1) = \frac{1}{16\pi^2} & \left[6\lambda_1\rho_1 + 4\lambda_3\rho_2 + 2\lambda_4\rho_2 + 2\rho_1\lambda_S + 4\rho_1^2 + \sigma_1\xi + 8\kappa^2 + 3g'^4 \right. \\ & \left. + \left(-\frac{15}{2}g'^2 - \frac{9}{2}g^2 + 2 \sum_{i,\alpha} (h_i^\alpha)^2 + 2y_\tau^2\right)\rho_1 \right], \end{aligned} \quad (\text{B.24})$$

$$\begin{aligned} \beta(\rho_2) = \frac{1}{16\pi^2} & \left[6\lambda_2\rho_2 + 4\lambda_3\rho_1 + 2\lambda_4\rho_1 + 2\rho_2\lambda_S + 4\rho_2^2 + \sigma_2\xi + 8\kappa^2 + 3g'^4 \right. \\ & \left. + \left(-\frac{15}{2}g'^2 - \frac{9}{2}g^2 + 2 \sum_{i,\alpha} (h_i^\alpha)^2 + 6y_t^2 + 6y_b^2\right)\rho_2 \right], \end{aligned} \quad (\text{B.25})$$

$$\begin{aligned} \beta(\lambda_S) = \frac{1}{16\pi^2} & \left[8\rho_1^2 + 8\rho_2^2 + 5\lambda_S^2 + 2\xi^2 + 24g'^4 - 12g'^2\lambda_S \right. \\ & \left. + 4 \sum_{i,\alpha} (h_i^\alpha)^2\lambda_S - 8 \sum_{i,j} \sum_{\alpha,\beta} h_i^\alpha h_i^\beta h_j^\beta h_j^\alpha \right], \end{aligned} \quad (\text{B.26})$$

$$\beta(\sigma_1) = \frac{1}{16\pi^2} \left[6\lambda_1\sigma_1 + (4\lambda_3 + 2\lambda_4)\sigma_2 + \sigma_1\lambda_\eta + 2\rho_1\xi + 16\kappa^2 + \left(-\frac{9}{2}g^2 - \frac{3}{2}g'^2 + 2y_\tau^2\right)\sigma_1 \right], \quad (\text{B.27})$$

$$\begin{aligned} \beta(\sigma_2) = \frac{1}{16\pi^2} & \left[6\lambda_2\sigma_2 + (4\lambda_3 + 2\lambda_4)\sigma_1 + \sigma_2\lambda_\eta + 2\rho_2\xi + 16\kappa^2 \right. \\ & \left. + \left(-\frac{9}{2}g^2 - \frac{3}{2}g'^2 + 6y_t^2 + 6y_b^2\right)\sigma_2 \right], \end{aligned} \quad (\text{B.28})$$

$$\beta(\lambda_\eta) = \frac{1}{16\pi^2} \left[12(\sigma_1^2 + \sigma_2^2) + 3\lambda_\eta^2 + 6\xi^2 \right], \quad (\text{B.29})$$

$$\beta(\kappa) = \frac{1}{16\pi^2} \kappa \left[2\lambda_3 - 2\lambda_4 + 2\xi + 2\sigma_1 + 2\sigma_2 + 2\rho_1 + 2\rho_2 + \sum_{\alpha,i} (h_i^\alpha)^2 - \frac{9}{2}g^2 - \frac{9}{2}g'^2 + 3y_t^2 + 3y_b^2 + y_\tau^2 \right], \quad (\text{B.30})$$

$$\beta(\xi) = \frac{1}{16\pi^2} \left[4\rho_1\sigma_1 + 4\rho_2\sigma_2 + 2\lambda_S\xi + \lambda_\eta\xi + 4\xi^2 - 6g'^2\xi + 2 \sum_{\alpha,i} (h_i^\alpha)^2 \xi \right], \quad (\text{B.31})$$

where definitions of these coupling constants are given in Eq. (6.3).

B.4 Beta functions in SUSY models

In the SUSY standard model, beta functions for the gauge couplings given in Eq. (B.5) are replaced by

$$\beta(g_s) = \frac{g_s^3}{16\pi^2} [-9 + 2N_g], \quad (\text{B.32a})$$

$$\beta(g) = \frac{g^3}{16\pi^2} \left[-6 + 2N_g + \frac{1}{2}N_H \right], \quad (\text{B.32b})$$

$$\beta(g') = \frac{g'^3}{16\pi^2} \left[\frac{10}{3}N_g + \frac{1}{2}N_H \right]. \quad (\text{B.32c})$$

We note that Eq. (B.32) is valid in the model whose superpotential is composed of the MSSM chiral superfields with or without extra doublet chiral superfields with $Y = 1/2$ and extra neutral chiral superfields.

B.4.1 MSSM

In the MSSM, beta functions for the gauge couplings are obtained by Eq. (B.32) with (N_g, N_H) is $(3, 2)$, and that for the top Yukawa coupling is expressed as

$$\beta(y_t) = \frac{y_t}{16\pi^2} \left[6y_t^2 - \frac{16}{3}g_s^2 - 3g^2 - \frac{13}{9}g'^2 \right]. \quad (\text{B.33})$$

B.4.2 NMSSM

In the NMSSM, beta functions for the gauge couplings are the same as those in the MSSM. The other beta functions are given as

$$\beta(y_t) = \frac{y_t}{16\pi^2} \left[6y_t^2 - \frac{16}{3}g_s^2 - 3g^2 - \frac{13}{9}g'^2 + \lambda_{HHS}^2 \right], \quad (\text{B.34})$$

$$\beta(\lambda_{HHS}) = \frac{\lambda_{HHS}}{16\pi^2} \left[4\lambda_{HHS}^2 + 2\kappa^2 + 3y_t^2 - 3g^2 - g'^2 \right], \quad (\text{B.35})$$

$$\beta(\kappa) = \frac{\kappa}{16\pi^2} \left[6\lambda_{HHS}^2 + 6\kappa^2 \right]. \quad (\text{B.36})$$

B.4.3 TMSSM

In the TMSSM, beta functions for the gauge couplings are given as

$$\beta(g_s) = -\frac{3g_s^3}{16\pi^2}, \quad (\text{B.37})$$

$$\beta(g) = \frac{4g^3}{16\pi^2}, \quad (\text{B.38})$$

$$\beta(g') = \frac{17g'^3}{16\pi^2}. \quad (\text{B.39})$$

The other beta functions are given by

$$\beta(y_t) = \left[6y_t^2 - \frac{16}{3}g_s^2 - 3g^2 - \frac{13}{9}g'^2 + 6\lambda_{HH\Delta_R}^2 \right], \quad (\text{B.40})$$

$$\beta(\lambda_{HH\Delta_L}) = \frac{\lambda_{HH\Delta_L}}{16\pi^2} \left[14\lambda_{HH\Delta_L}^2 - 7g^2 - 3g'^2 \right], \quad (\text{B.41})$$

$$\beta(\lambda_{HH\Delta_R}) = \frac{\lambda_{HH\Delta_R}}{16\pi^2} \left[14\lambda_{HH\Delta_R}^2 - 7g^2 - 3g'^2 \right]. \quad (\text{B.42})$$

B.4.4 4D Ω

In the 4D Ω , beta functions for the gauge couplings are given as

$$\beta(g_s) = -\frac{3g_s^3}{16\pi^2}, \quad (\text{B.43})$$

$$\beta(g) = \frac{g^3}{16\pi^2}, \quad (\text{B.44})$$

$$\beta(g') = \frac{13g'^3}{16\pi^2}. \quad (\text{B.45})$$

The other beta functions are given by

$$\beta(y_t) = \left[6y_t^2 - \frac{16}{3}g_s^2 - 3g^2 - \frac{13}{9}g'^2 + \lambda_{HH\Omega_L}^2 \right], \quad (\text{B.46})$$

$$\beta(\lambda_{HH\Omega_R}) = \frac{\lambda_{HH\Omega_R}}{16\pi^2} \left[4\lambda_{HH\Omega_R}^2 - 3g^2 - 3g'^2 \right], \quad (\text{B.47})$$

$$\beta(\lambda_{HH\Omega_L}) = \frac{\lambda_{HH\Omega_L}}{16\pi^2} \left[4\lambda_{HH\Omega_L}^2 - 3g^2 - 3g'^2 \right]. \quad (\text{B.48})$$

Appendix C

Decay rates

In this appendix, we list the analytic fomulae for decay rates of Higgs bosons in the SM, the THDM and the HTM.

C.1 Decay rates of the Higgs boson in the SM

The decay rates of the Higgs boson decaying into the fermion pair are given by

$$\Gamma(h \rightarrow f\bar{f}) = \sqrt{2}G_F \frac{m_h m_f^2}{8\pi} N_c^f \beta \left(\frac{m_f^2}{m_h^2} \right)^3, \quad (\text{C.1})$$

where N_c^f is the color factor with $N_c^q = 3$, $N_c^\ell = 1$ and

$$\beta(x) = \sqrt{1 - 4x}. \quad (\text{C.2})$$

The decay rates of the Higgs boson decaying into the gauge boson V pair ($V = W$ or Z) are given by

$$\Gamma(h \rightarrow VV) = \sqrt{2}G_F \frac{m_h^3}{32\pi} \delta_V \left[1 - \frac{4m_V^2}{m_h^2} + \frac{12m_V^4}{m_h^4} \right] \beta \left(\frac{m_V^2}{m_h^2} \right), \quad (\text{C.3})$$

where $\delta_W = 2$ and $\delta_Z = 1$. The decay rates of the three body decay modes can be calculated as

$$\Gamma(h \rightarrow W^+W^{*-} \rightarrow W^+f\bar{f}') = \frac{G_F^2 m_W^4 m_h}{96\pi^3} F \left(\frac{m_W^2}{m_h^2} \right), \quad (\text{C.4})$$

where the function $F(x)$ is given as

$$F(x) = -|1 - x| \left(\frac{47}{2}x - \frac{13}{2} + \frac{1}{x} \right) + 3(1 - 6x + 4x^2) |\log \sqrt{x}| \\ + \frac{3(1 - 8x + 20x^2)}{\sqrt{4x - 1}} \cos^{-1} \left(\frac{3x - 1}{2x^{3/2}} \right). \quad (\text{C.5})$$

In this decay mode, fermion pair $f\bar{f}'$ in the final state can be $(e^-\bar{\nu}_e)$, $(\mu^-\bar{\nu}_\mu)$, $(\tau^-\bar{\nu}_\tau)$, $(d\bar{u})$ and $(s\bar{c})$. By summing all these final states, we obtain

$$\Gamma(h \rightarrow W^+W^{*-}) \equiv \sum_f \Gamma(h \rightarrow W^+W^{*-} \rightarrow W^+f\bar{f}') = \frac{3G_F^2 m_W^4 m_h}{32\pi^3} F \left(\frac{m_W^2}{m_h^2} \right). \quad (\text{C.6})$$

The decay rate of $h \rightarrow ZZ^* \rightarrow Zf\bar{f}$ mode can be calculated as

$$\Gamma(h \rightarrow ZZ^* \rightarrow Zf\bar{f}) = \frac{G_F^2 m_Z^4 m_h}{48\pi^3} F\left(\frac{m_Z^2}{m_h^2}\right) (I_f^2 + 2\sin^4 \theta_W Q_f^2 - 2I_f \sin^2 \theta_W Q_f), \quad (\text{C.7})$$

where I_f and Q_f are the third component of the isospin and the electromagnetic charge of the final state fermion f . In this decay mode, fermion pair $f\bar{f}$ in the final state can be $(\ell^+ \ell^-)$, $(\nu_\ell \bar{\nu}_\ell)$, $(u\bar{u})$, $(d\bar{d})$, $(c\bar{c})$, $(s\bar{s})$ and $(b\bar{b})$ with $\ell^\pm = e^\pm, \mu^\pm$ or τ^\pm . By summimg all these final states, we obtain

$$\begin{aligned} \Gamma(h \rightarrow ZZ^*) &\equiv \sum_f \Gamma(h \rightarrow ZZ^* \rightarrow Zf\bar{f}) = \frac{G_F^2 m_Z^4 m_h}{64\pi^3} F\left(\frac{m_Z^2}{m_h^2}\right) \\ &\times \left(7 - \frac{40}{3} \sin^2 \theta_W + \frac{160}{9} \sin^4 \theta_W\right). \end{aligned} \quad (\text{C.8})$$

There are one-loop induced decay processes, e.g., $h \rightarrow \gamma\gamma$, $h \rightarrow gg$ and $h \rightarrow \gamma Z$. These decay rates can be expressed by

$$\Gamma(h \rightarrow \gamma\gamma) = \frac{\sqrt{2} G_F \alpha_{\text{em}}^2 m_h^3}{64\pi^3} \left| \sum_f Q_f^2 N_c^f I_f(m_h) + I_W(m_h) \right|^2, \quad (\text{C.9})$$

$$\Gamma(h \rightarrow gg) = \frac{\sqrt{2} G_F \alpha_s^2 m_h^3}{128\pi^3} \left| \sum_{f=q} I_f \right|^2, \quad (\text{C.10})$$

$$\Gamma(h \rightarrow Z\gamma) = \frac{\sqrt{2} G_F \alpha_{\text{em}}^2 m_h^3}{128\pi^3} \left(1 - \frac{m_Z^2}{m_h^2}\right)^3 \left| \sum_f Q_f J_f(m_h) + J_W(m_h) \right|^2, \quad (\text{C.11})$$

where the loop functions are

$$I_f(m_h) = -\frac{4m_f^2}{m_h^2} \left[1 - \frac{m_h^2}{2} \left(1 - \frac{4m_f^2}{m_h^2} \right) C_0(0, 0, m_h^2, m_f, m_f, m_f) \right], \quad (\text{C.12a})$$

$$I_W(m_h) = 1 + \frac{6m_W^2}{m_h^2} - 6m_W^2 \left(1 - \frac{2m_W^2}{m_h^2} \right) C_0(0, 0, m_h^2, m_f, m_f, m_f), \quad (\text{C.12b})$$

$$J_f(m_h) = -\frac{2N_c^f}{\sin \theta_W \cos \theta_W} (I_f(m_h) - 2Q_f \sin^2 \theta_W) [J_1(m_f) - J_2(m_f)], \quad (\text{C.12c})$$

$$\begin{aligned} J_W(m_h) &= -\cot \theta_W \\ &\times \left\{ 4(3 - \tan^2 \theta_W) J_2(m_W) + \left[\left(1 + \frac{m_h^2}{2m_W^2} \right) \tan^2 \theta_W - \left(5 + \frac{m_h^2}{2m_W^2} \right) \right] J_1(m_W) \right\}, \end{aligned} \quad (\text{C.12d})$$

$$\begin{aligned} J_1(m) &= \frac{2m^2}{m_h^2 - m_Z^2} \left[1 + 2m^2 C_0(0, m_Z^2, m_h^2, m, m, m) \right. \\ &\quad \left. + \frac{m_Z^2}{m_h^2 - m_Z^2} \{ B_0(m_h^2, m, m) - B_0(m_Z^2, m, m) \} \right], \end{aligned} \quad (\text{C.12e})$$

$$J_2(m) = m^2 C_0(0, m_Z^2, m_h^2, m, m, m). \quad (\text{C.12f})$$

In Eq. (C.12), C_0 and B_0 functions are Passarino-Veltman function [212]. The analytic formula for the B_0 function is given in Appendix D. Here, we give expressions for the special case of the C_0 function which is used in the above decay rates:

$$C_0(0, 0, m_h^2, m, m, m) = \frac{-2}{m_h^2} f\left(\frac{4m^2}{m_h^2}\right), \quad (\text{C.13})$$

$$C_0(0, m_Z^2, m_h^2, m, m, m) = \frac{-2}{m_h^2 - m_Z^2} \left[f\left(\frac{4m^2}{m_h^2}\right) - f\left(\frac{4m^2}{m_Z^2}\right) \right], \quad (\text{C.14})$$

with

$$f(x) = \begin{cases} [\arcsin(1/\sqrt{x})]^2, & \text{if } x \geq 1, \\ -\frac{1}{4}[\ln \frac{1+\sqrt{1-x}}{1-\sqrt{1-x}} - i\pi]^2, & \text{if } x < 1 \end{cases}. \quad (\text{C.15})$$

C.2 Decay rates of the Higgs bosons in the THDM

In the THDM, there are five physical scalar bosons, i.e., the CP-even scalar bosons h and H , the CP-odd scalar boson A and the charged scalar bosons H^\pm . When we take $\sin(\beta - \alpha) = 1$, then h behaves the SM-like Higgs boson.

First, decay rates for neutral scalar bosons decaying into fermions are given as

$$\Gamma(\mathcal{H} \rightarrow f\bar{f}) = \sqrt{2}G_F(\xi_{\mathcal{H}}^f)^2 \frac{m_f^2 m_{\mathcal{H}}}{8\pi} N_c^f \beta\left(\frac{m_f^2}{m_{\mathcal{H}}^2}\right)^3, \quad (\text{C.16})$$

$$\Gamma(A \rightarrow f\bar{f}) = \sqrt{2}G_F(\xi_A^f)^2 \frac{m_f^2 m_A}{8\pi} N_c^f \beta\left(\frac{m_f^2}{m_A^2}\right), \quad (\text{C.17})$$

where \mathcal{H} is h or H and $\xi_{\mathcal{H},A}^f$ are listed in Table 3.2.

Decay rates for neutral scalar bosons decaying into gauge bosons are given as

$$\Gamma(\mathcal{H} \rightarrow VV) = \eta_{\mathcal{H}}^2 \sqrt{2}G_F \frac{m_{\mathcal{H}}^3}{32\pi} \delta_V \left[1 - \frac{4m_V^2}{m_{\mathcal{H}}^2} + \frac{12m_V^4}{m_{\mathcal{H}}^4} \right] \beta\left(\frac{m_V^2}{m_{\mathcal{H}}^2}\right), \quad (\text{C.18})$$

$$\text{with } \eta_{\mathcal{H}} = \begin{cases} \sin(\beta - \alpha) & \text{for } \mathcal{H} = h, \\ \cos(\beta - \alpha) & \text{for } \mathcal{H} = H \end{cases}. \quad (\text{C.19})$$

In the CP conserving THDM, the decay rate for A decaying into gauge bosons are zero at the tree level, since $AV_\mu V^\mu$ vertex is absent.

If the mass of H^\pm is larger than $m_t + m_b$, H^+ can decay into $t\bar{b}$ according to the decay rate:

$$\begin{aligned} \Gamma(H^+ \rightarrow t\bar{b}) &= \sqrt{2}G_F \frac{m_{H^+}}{8\pi} \lambda\left(\frac{m_t^2}{m_{H^+}^2}, \frac{m_b^2}{m_{H^+}^2}\right)^{1/2} \\ &\times \left\{ [m_b^2(\xi_A^d)^2 + m_t^2(\xi_A^u)^2] \left(1 - \frac{m_t^2 + m_b^2}{m_{H^+}^2} \right) - \frac{4m_b^2 m_t^2 \xi_A^d \xi_A^u}{m_{H^+}^2} \right\}, \end{aligned} \quad (\text{C.20})$$

where the function $\lambda(x, y)$ is given by

$$\lambda(x, y) = 1 + x^2 + y^2 - 2xy - 2x - 2y, \quad (\text{C.21})$$

and $\xi_A^{u,d}$ are listed in Table 3.2.

if kinematically allowed, a scalar boson (S_0) can decay into the other scalar boson (S_1) plus a vector boson V . When $m_{S_0} > m_{S_1} + m_V$ where m_{S_0} , m_{S_1} and m_V are the masses of S_0 , S_1 and V , respectively, this type of decay rates is evaluated as

$$\Gamma(\mathcal{H} \rightarrow H^\pm W^\mp) = \sqrt{2}G_F \frac{m_{\mathcal{H}}^3 \bar{\eta}_{\mathcal{H}}^2}{8\pi} \lambda^{3/2} \left(\frac{m_{H^\pm}^2}{m_{\mathcal{H}}^2}, \frac{m_W^2}{m_{\mathcal{H}}^2} \right), \quad (\text{C.22})$$

$$\Gamma(A \rightarrow H^\pm W^\mp) = \sqrt{2}G_F \frac{m_A^3}{8\pi} \lambda^{3/2} \left(\frac{m_{H^\pm}^2}{m_A^2}, \frac{m_W^2}{m_A^2} \right), \quad (\text{C.23})$$

$$\Gamma(H^\pm \rightarrow \mathcal{H} W^\pm) = \sqrt{2}G_F \frac{m_{H^\pm}^3 \bar{\eta}_{\mathcal{H}}^2}{8\pi} \lambda^{3/2} \left(\frac{m_{\mathcal{H}}^2}{m_{H^\pm}^2}, \frac{m_W^2}{m_{H^\pm}^2} \right), \quad (\text{C.24})$$

$$\Gamma(H^\pm \rightarrow A W^\pm) = \sqrt{2}G_F \frac{m_{H^\pm}^3}{8\pi} \lambda^{3/2} \left(\frac{m_A^2}{m_{H^\pm}^2}, \frac{m_W^2}{m_{H^\pm}^2} \right), \quad (\text{C.25})$$

$$\Gamma(\mathcal{H} \rightarrow AZ) = \sqrt{2}G_F \frac{m_{\mathcal{H}}^3 \bar{\eta}_{\mathcal{H}}^2}{8\pi} \lambda^{3/2} \left(\frac{m_A^2}{m_{\mathcal{H}}^2}, \frac{m_Z^2}{m_{\mathcal{H}}^2} \right), \quad (\text{C.26})$$

$$\Gamma(A \rightarrow \mathcal{H} Z) = \sqrt{2}G_F \frac{m_A^3 \bar{\eta}_{\mathcal{H}}^2}{8\pi} \lambda^{3/2} \left(\frac{m_{\mathcal{H}}^2}{m_A^2}, \frac{m_Z^2}{m_A^2} \right), \quad (\text{C.27})$$

$$\text{with } \bar{\eta}_{\mathcal{H}} = \begin{cases} \sin(\beta - \alpha) & \text{for } \mathcal{H} = H, \\ \cos(\beta - \alpha) & \text{for } \mathcal{H} = h. \end{cases} \quad (\text{C.28})$$

When $m_{S_1} + m_V > m_{S_0} > m_{S_1}$, S_0 can also decay into S_1 and the off-shell V . These decay rates are given by

$$\Gamma(\mathcal{H} \rightarrow H^\pm W^{\pm*}) = \frac{9G_F^2 m_W^4}{16\pi^3} \bar{\eta}_{\mathcal{H}}^2 m_{\mathcal{H}} G \left(\frac{m_{H^\pm}^2}{m_{\mathcal{H}}^2}, \frac{m_W^2}{m_{\mathcal{H}}^2} \right), \quad (\text{C.29})$$

$$\Gamma(A \rightarrow H^\pm W^{\pm*}) = \frac{9G_F^2 m_W^4}{16\pi^3} m_A G \left(\frac{m_{H^\pm}^2}{m_A^2}, \frac{m_W^2}{m_A^2} \right), \quad (\text{C.30})$$

$$\Gamma(H^\pm \rightarrow \mathcal{H} W^{\pm*}) = \frac{9G_F^2 m_W^4}{16\pi^3} \bar{\eta}_{\mathcal{H}}^2 m_{H^\pm} G \left(\frac{m_{\mathcal{H}}^2}{m_{H^\pm}^2}, \frac{m_W^2}{m_{H^\pm}^2} \right), \quad (\text{C.31})$$

$$\Gamma(H^\pm \rightarrow A W^{\pm*}) = \frac{9G_F^2 m_W^4}{16\pi^3} m_{H^\pm} G \left(\frac{m_A^2}{m_{H^\pm}^2}, \frac{m_W^2}{m_{H^\pm}^2} \right), \quad (\text{C.32})$$

$$\Gamma(\mathcal{H} \rightarrow AZ^*) = \frac{3G_F^2 m_Z^4}{32\pi^3} \bar{\eta}_{\mathcal{H}}^2 m_{\mathcal{H}} \left(7 - \frac{40}{3} \sin^2 \theta_W + \frac{160}{9} \sin^4 \theta_W \right) G \left(\frac{m_A^2}{m_{\mathcal{H}}^2}, \frac{m_Z^2}{m_{\mathcal{H}}^2} \right), \quad (\text{C.33})$$

$$\Gamma(A \rightarrow \mathcal{H} Z^*) = \frac{3G_F^2 m_Z^4}{32\pi^3} \bar{\eta}_{\mathcal{H}}^2 m_A \left(7 - \frac{40}{3} \sin^2 \theta_W + \frac{160}{9} \sin^4 \theta_W \right) G \left(\frac{m_{\mathcal{H}}^2}{m_A^2}, \frac{m_Z^2}{m_A^2} \right), \quad (\text{C.34})$$

where the function $G(x, y)$ is given as

$$G(x, y) = \frac{1}{12y} \left\{ 2(-1+x)^3 - 9(-1+x^2)y + 6(-1+x)y^2 \right. \\ \left. + 6(1+x-y)y\sqrt{-\lambda(x, y)} \left[\tan^{-1} \left(\frac{-1+x-y}{\sqrt{-\lambda(x, y)}} \right) + \tan^{-1} \left(\frac{-1+x+y}{\sqrt{-\lambda(x, y)}} \right) \right] \right. \\ \left. - 3[1+(x-y)^2-2y]y \log x \right\}. \quad (\text{C.35})$$

If kinematically allowed, there also are (Scalar \rightarrow Scalar' + Scalar'') type decay modes whose decay rates can be expressed as

$$\Gamma(\phi_i \rightarrow \phi_j \phi_k) = (1 + \delta_{jk}) \frac{\lambda_{\phi_i \phi_j \phi_k}^2}{16\pi m_{\phi_1}} \lambda^{1/2} \left(\frac{m_{\phi_j}^2}{m_{\phi_i}^2}, \frac{m_{\phi_k}^2}{m_{\phi_i}^2} \right), \quad (\text{C.36})$$

where $\lambda_{\phi_i \phi_j \phi_k}$ is the coefficient of the scalar three-point vertices which are defined by

$$\mathcal{L} = -\lambda_{\phi_i \phi_j \phi_k} \phi_i \phi_j \phi_k + \dots. \quad (\text{C.37})$$

In Ref. [92], $\lambda_{\phi_i \phi_j \phi_k}$ are listed.

The decay rates for the loop-induced decay modes can be calculated as

$$\Gamma(\mathcal{H} \rightarrow \gamma\gamma) = \frac{\sqrt{2}G_F\alpha_{\text{em}}^2 m_{\mathcal{H}}^3}{64\pi^3} |I_{H^\pm}(m_{\mathcal{H}}) + \sum_f Q_f^2 N_c^f \xi_{\mathcal{H}}^f I_f(m_{\mathcal{H}}) + \eta_{\mathcal{H}} I_W(m_{\mathcal{H}})|^2, \quad (\text{C.38})$$

$$\Gamma(A \rightarrow \gamma\gamma) = \frac{\sqrt{2}G_F\alpha_{\text{em}}^2 m_A^3}{64\pi^3} \left| \sum_f Q_f^2 N_c^f \xi_A^f I_f^A(m_A) \right|^2, \quad (\text{C.39})$$

$$\Gamma(\mathcal{H} \rightarrow gg) = \frac{\sqrt{2}G_F\alpha_s^2 m_{\mathcal{H}}^3}{128\pi^3} \left| \sum_{f=q} \xi_{\mathcal{H}}^f I_f(m_{\mathcal{H}}) \right|^2, \quad (\text{C.40})$$

$$\Gamma(A \rightarrow gg) = \frac{\sqrt{2}G_F\alpha_s^2 m_A^3}{128\pi^3} \left| \sum_{f=q} \xi_A^f I_f^A(m_A) \right|^2, \quad (\text{C.41})$$

where

$$I_{H^\pm}(m_{\mathcal{H}}) = \frac{v\lambda_{\varphi H^+ H^-}}{m_{\mathcal{H}}^2} [1 + 2m_{H^+}^2 C_0(0, 0, m_{\mathcal{H}}^2; m_{H^+}^2, m_{H^+}^2, m_{H^+}^2)], \quad (\text{C.42})$$

$$I_f^A(m_A) = 2m_f^2 C_0(0, 0, m_h^2; m_f^2, m_f^2, m_f^2), \quad (\text{C.43})$$

In the THDM, the $W^\pm H^\mp Z$ vertex does not appear at the tree-level, but it appears at the one-loop level as we have discussed in section 3.3. The effective $W^\pm H^\mp Z$ vertex can be expressed in Eq. (3.92) and in Fig. 3.28. We can calculate the decay rate of $H^\pm \rightarrow ZH^\pm$ process

in terms of F , G and H as

$$\begin{aligned} \Gamma(H^\pm \rightarrow W^\pm Z) &= \frac{g^2 m_{H^\pm}}{16\pi} \lambda \left(\frac{m_W^2}{m_{H^\pm}^2}, \frac{m_Z^2}{m_{H^\pm}^2} \right)^{1/2} \\ &\times \left[\frac{m_{H^\pm}^2}{4m_Z^2} \left| F^* \left(1 - \frac{m_W^2}{m_{H^\pm}^2} - \frac{m_Z^2}{m_{H^\pm}^2} \right) + \frac{G^* m_{H^\pm}^2}{2m_W^2} \lambda \left(\frac{m_W^2}{m_{H^\pm}^2}, \frac{m_W^2}{m_{H^\pm}^2} \right) \right|^2 \right. \\ &\left. + \frac{2m_W^2}{m_{H^\pm}^2} |F|^2 + \frac{m_{H^\pm}^2}{2m_W^2} |H|^2 \lambda \left(\frac{m_W^2}{m_{H^\pm}^2}, \frac{m_Z^2}{m_{H^\pm}^2} \right) \right]. \end{aligned} \quad (\text{C.44})$$

C.3 Decay rates of the Higgs bosons in the HTM

In the HTM, in addition to the SM-like Higgs boson h , there are the doubly-charged scalar bosons H^\pm , the singly-charged scalar bosons H^\pm , the neutral CP-even (odd) scalar boson H (A). Here we list the formulae of decay rates for $H^{\pm\pm}$, H^\pm , H and A in order.

C.3.1 Decay rates of $H^{\pm\pm}$

The decay rates for $H^{\pm\pm}$ can be evaluated as

$$\Gamma(H^{\pm\pm} \rightarrow \ell_i^\pm \ell_j^\pm) = S_{ij} |h_{ij}|^2 \frac{m_{H^{\pm\pm}}}{4\pi} \left(1 - \frac{m_i^2}{m_{H^{\pm\pm}}^2} - \frac{m_j^2}{m_{H^{\pm\pm}}^2} \right) \left[\lambda \left(\frac{m_i^2}{m_{H^{\pm\pm}}^2}, \frac{m_j^2}{m_{H^{\pm\pm}}^2} \right) \right]^{1/2}, \quad (\text{C.45})$$

$$\Gamma(H^{\pm\pm} \rightarrow W^\pm W^\pm) = \frac{g^4 v_\Delta^2 m_{H^{\pm\pm}}^3}{64\pi m_W^4} \left(1 - \frac{4m_W^2}{m_{H^{\pm\pm}}^2} + \frac{12m_W^4}{m_{H^{\pm\pm}}^4} \right) \beta \left(\frac{m_W^2}{m_{H^{\pm\pm}}^2} \right), \quad (\text{C.46})$$

$$\Gamma(H^{\pm\pm} \rightarrow H^\pm W^\pm) = \frac{g^2 m_{H^{\pm\pm}}^3}{16\pi m_W^2} \cos^2 \beta_\pm \left[\lambda \left(\frac{m_W^2}{m_{H^{\pm\pm}}^2}, \frac{m_{H^\pm}^2}{m_{H^{\pm\pm}}^2} \right) \right]^{3/2}, \quad (\text{C.47})$$

$$\Gamma(H^{\pm\pm} \rightarrow W^\pm W^{\pm*}) = \frac{3g^6 m_{H^{\pm\pm}}}{512\pi^3} \frac{v_\Delta^2}{m_W^2} F \left(\frac{m_W^2}{m_{H^{\pm\pm}}^2} \right), \quad (\text{C.48})$$

$$\Gamma(H^{\pm\pm} \rightarrow H^\pm W^{\pm*}) = \frac{9g^4 m_{H^{\pm\pm}}}{128\pi^3} \cos^2 \beta_\pm G \left(\frac{m_{H^\pm}^2}{m_{H^{\pm\pm}}^2}, \frac{m_W^2}{m_{H^{\pm\pm}}^2} \right), \quad (\text{C.49})$$

where m_i is the lepton mass ($i = e, \mu$ or τ) and $S_{ij} = 1, (1/2)$ for $i \neq j, (i = j)$. The functions $\beta(x)$, $\lambda(x, y)$, $F(x)$ and $G(x, y)$ are given in Eqs. (C.2), (C.21), (C.5) and (C.35), respectively. Although the expression in Eq. (C.35) is different from that in Ref. [225], we have confirmed that the numerical value by using Eq. (C.35) coincides with that by using CalcHEP.

C.3.2 Decay rates of H^\pm

The decay rates for H^\pm can be evaluated as

$$\Gamma(H^\pm \rightarrow q\bar{q}') = \frac{3m_{H^+}^3}{8\pi v^2} \sin^2 \beta_\pm \left[\left(\frac{m_q^2}{m_{H^+}^2} + \frac{m_{q'}^2}{m_{H^+}^2} \right) \left(1 - \frac{m_q^2}{m_{H^+}^2} - \frac{m_{q'}^2}{m_{H^+}^2} \right) - 4 \frac{m_q^2}{m_{H^+}^2} \frac{m_{q'}^2}{m_{H^+}^2} \right] \times \left[\lambda \left(\frac{m_q^2}{m_{H^+}^2}, \frac{m_{q'}^2}{m_{H^+}^2} \right) \right]^{1/2}, \quad (\text{C.50})$$

$$\Gamma(H^\pm \rightarrow \ell_i^\pm \nu_j) = \delta_{ij} \frac{m_i^2 m_{H^+}}{8\pi v^2} \sin^2 \beta_\pm \left(1 - \frac{m_i^2}{m_{H^+}^2} \right)^2 + |h_{ij}|^2 \frac{m_{H^+}}{8\pi} \cos^2 \beta_\pm \left(1 - \frac{m_i^2}{m_{H^+}^2} \right)^2, \quad (\text{C.51})$$

$$\Gamma(H^\pm \rightarrow W^\pm Z) = \frac{g^2 g_Z^2}{32\pi m_{H^+}} v_\Delta^2 \cos^2 \beta_\pm \left[\lambda \left(\frac{m_W^2}{m_{H^+}^2}, \frac{m_Z^2}{m_{H^+}^2} \right) \right]^{1/2} \times \left[2 + \frac{m_{H^+}^4}{4m_W^2 m_Z^2} \left(1 - \frac{m_W^2}{m_{H^+}^2} - \frac{m_Z^2}{m_{H^+}^2} \right)^2 \right], \quad (\text{C.52})$$

$$\Gamma(H^\pm \rightarrow W^\pm Z^*) = \frac{3g^2 g_Z^4}{1024\pi^3 m_{H^+}} v_\Delta^2 \cos^2 \beta_\pm H \left(\frac{m_W^2}{m_{H^+}^2}, \frac{m_Z^2}{m_{H^+}^2} \right) \times \left(7 - \frac{40}{3} \sin^2 \theta_W + \frac{160}{9} \sin^4 \theta_W \right), \quad (\text{C.53})$$

$$\Gamma(H^\pm \rightarrow W^{\pm*} Z) = \frac{9g^4 g_Z^2}{512\pi^3 m_{H^+}} v_\Delta^2 \cos^2 \beta_\pm H \left(\frac{m_Z^2}{m_{H^+}^2}, \frac{m_W^2}{m_{H^+}^2} \right), \quad (\text{C.54})$$

$$\Gamma(H^\pm \rightarrow \hat{\varphi} W^\pm) = \frac{g^2 m_{H^+}^3}{64\pi^2 m_W^2} \xi_{H^+ W^- \hat{\varphi}}^2 \left[\lambda \left(\frac{m_W^2}{m_{H^+}^2}, \frac{m_{\hat{\varphi}}^2}{m_{H^+}^2} \right) \right]^{3/2}, \quad (\text{C.55})$$

$$\Gamma(H^\pm \rightarrow \hat{\varphi} W^{\pm*}) = \frac{9g^4 m_{H^+}}{512\pi^3} \xi_{H^+ W^- \hat{\varphi}}^2 G \left(\frac{m_{\hat{\varphi}}^2}{m_{H^+}^2}, \frac{m_W^2}{m_{H^+}^2} \right), \quad (\text{C.56})$$

where $g_Z = g / \cos \theta_W$. The function $H(x, y)$ is

$$H(x, y) = \frac{\tan^{-1} \left[\frac{1-x+y}{\sqrt{-\lambda(x, y)}} \right] + \tan^{-1} \left[\frac{1-x-y}{\sqrt{-\lambda(x, y)}} \right]}{4x\sqrt{-\lambda(x, y)}} \left[-3x^3 + (9y+7)x^2 - 5(1-y)^2 x + (1-y)^3 \right] + \frac{1}{24xy} \left\{ (-1+x)[6y^2 + y(39x-9) + 2(1-x)^2] - y[y^2 + 2y(3x-1) - x(3x+4) + 1] \log x \right\}. \quad (\text{C.57})$$

We have confirmed that the numerical value by using Eq. (C.57) coincides with that by using CalcHEP. In Eq. (C.55) and Eq. (C.56), $\hat{\varphi}$ denotes h , H or A and $\xi_{H^+ W^- \hat{\varphi}}$ is expressed as

$$\begin{aligned} \xi_{H^+ W^- h} &= \cos \alpha \sin \beta_\pm - \sqrt{2} \sin \alpha \cos \beta_\pm, \\ \xi_{H^+ W^- H} &= \sin \alpha \sin \beta_\pm + \sqrt{2} \cos \alpha \cos \beta_\pm, \\ \xi_{H^+ W^- A} &= \sin \beta_0 \sin \beta_\pm + \sqrt{2} \cos \beta_0 \cos \beta_\pm. \end{aligned} \quad (\text{C.58})$$

C.3.3 Decay rates of H

The decay rates for H can be evaluated as

$$\Gamma(H \rightarrow f\bar{f}) = \frac{N_c^f m_f^2 m_H}{8\pi v^2} \sin^2 \alpha \left[\beta \left(\frac{m_f^2}{m_H^2} \right) \right]^3, \quad (\text{C.59})$$

$$\Gamma(H \rightarrow \nu\nu) = \Gamma(H \rightarrow \nu^c \bar{\nu}) + \Gamma(H \rightarrow \bar{\nu}^c \nu) = \sum_{i,j=1}^3 S_{ij} |h_{ij}|^2 \frac{m_H}{4\pi} \cos^2 \alpha, \quad (\text{C.60})$$

$$\Gamma(H \rightarrow W^+ W^-) = \frac{g^4 m_H^3}{16\pi m_W^4} \left(\frac{v}{2} \sin \alpha - v_\Delta \cos \alpha \right)^2 \left(\frac{1}{4} - \frac{m_W^2}{m_H^2} + \frac{3m_W^4}{m_H^4} \right) \beta \left(\frac{m_W^2}{m_H^2} \right), \quad (\text{C.61})$$

$$\Gamma(H \rightarrow ZZ) = \frac{g_Z^4 m_H^3}{32\pi m_Z^4} \left(\frac{v}{2} \sin \alpha - 2v_\Delta \cos \alpha \right)^2 \left(\frac{1}{4} - \frac{m_Z^2}{m_H^2} + \frac{3m_Z^4}{m_H^4} \right) \beta \left(\frac{m_Z^2}{m_H^2} \right), \quad (\text{C.62})$$

$$\Gamma(H \rightarrow WW^*) = \frac{3g^6 m_H}{512\pi^3} \frac{\left(\frac{v}{2} \sin \alpha - v_\Delta \cos \alpha \right)^2}{m_W^2} F \left(\frac{m_W^2}{m_H^2} \right), \quad (\text{C.63})$$

$$\begin{aligned} \Gamma(H \rightarrow ZZ^*) &= \frac{g_Z^6 m_H}{2048\pi^3} \frac{\left(\frac{v}{2} \sin \alpha - 2v_\Delta \cos \alpha \right)^2}{m_Z^2} \\ &\times \left(7 - \frac{40}{3} \sin^2 \theta_W + \frac{160}{9} \sin^4 \theta_W \right) F \left(\frac{m_Z^2}{m_H^2} \right), \end{aligned} \quad (\text{C.64})$$

$$\Gamma(H \rightarrow hh) = \frac{\lambda_{Hhh}^2}{8\pi m_H} \beta \left(\frac{m_h^2}{m_H^2} \right), \quad (\text{C.65})$$

where

$$\begin{aligned} \lambda_{Hhh} &= \frac{1}{4v^2} \left\{ 2v_\Delta \left[-2M_\Delta^2 + v^2(\lambda_4 + \lambda_5) \right] \cos^3 \alpha + v^3 \left[-12\lambda_1 + 4(\lambda_4 + \lambda_5) \right] \cos^2 \alpha \sin \alpha \right. \\ &\quad \left. + 4v_\Delta \left[2M_\Delta^2 + v^2(3\lambda_2 + 3\lambda_3 - \lambda_4 - \lambda_5) \right] \cos \alpha \sin^2 \alpha - 2v^3(\lambda_4 + \lambda_5) \sin^3 \alpha \right\} \\ &\simeq \frac{1}{4v^2} \left\{ 2v_\Delta \left[-2M_\Delta^2 + v^2(\lambda_4 + \lambda_5) \right] \cos^3 \alpha + v^3 \left[-12\lambda_1 + 4(\lambda_4 + \lambda_5) \right] \cos^2 \alpha \sin \alpha \right\}. \end{aligned} \quad (\text{C.66})$$

C.3.4 Decay rates of A

The decay rates for A can be evaluated as

$$\Gamma(A \rightarrow f\bar{f}) = \sin^2 \beta_0 \frac{N_c^f m_f^2 m_A}{8\pi v^2} \beta \left(\frac{m_f^2}{m_A^2} \right), \quad (\text{C.67})$$

$$\Gamma(A \rightarrow \nu\nu) = \Gamma(A \rightarrow \nu^c \bar{\nu}) + \Gamma(A \rightarrow \bar{\nu}^c \nu) = \sum_{i,j=1}^3 S_{ij} |h_{ij}|^2 \frac{m_A}{4\pi} \cos^2 \beta_0, \quad (\text{C.68})$$

$$\Gamma(A \rightarrow hZ) = \frac{g_Z^2 m_A^3}{64\pi m_Z^2} (\cos \alpha \sin \beta_0 - 2 \sin \alpha \cos \beta_0)^2 \left[\lambda \left(\frac{m_h^2}{m_A^2}, \frac{m_Z^2}{m_A^2} \right) \right]^{3/2}, \quad (\text{C.69})$$

$$\begin{aligned} \Gamma(A \rightarrow hZ^*) &= \frac{3g_Z^4 m_A}{1024\pi^3} (\cos \alpha \sin \beta_0 - 2 \sin \alpha \cos \beta_0)^2 \\ &\times G \left(\frac{m_h^2}{m_A^2}, \frac{m_Z^2}{m_A^2} \right) \left(7 - \frac{40}{3} \sin^2 \theta_W + \frac{160}{9} \sin^4 \theta_W \right). \end{aligned} \quad (\text{C.70})$$

Appendix D

One-loop functions

In this appendix, we introduce the one-loop functions according to Passarino and Veltman [212] and Ref. [137]. First, we define A and B functions:

$$A(m_1) = \int \frac{\overline{d^D k}}{i\pi^2} \frac{1}{D_1}, \quad (\text{D.1})$$

$$[B_0, B^\mu, B^{\mu\nu}](p^2, m_1, m_2) = \int \frac{\overline{d^D k}}{i\pi^2} \frac{[1, k^\mu, k^\mu k^\nu]}{D_1 D_2}, \quad (\text{D.2})$$

where $D = 4 - 2\epsilon$,

$$\overline{d^D k} = \Gamma(1 - \epsilon)(\pi\mu^2)^\epsilon d^D k, \quad (\text{D.3})$$

is the $\overline{\text{MS}}$ regularization [226, 227], and the propagator factors are

$$D_1 = k^2 - m_1^2 + i\epsilon, \quad D_2 = (k + p)^2 - m_2^2 + i\epsilon. \quad (\text{D.4})$$

The A function is given by

$$A(m) = m^2(\Delta + 1 - \ln m^2). \quad (\text{D.5})$$

The vector and the tensor functions are reduced to the scalar functions as

$$B^\mu(p^2, m_1, m_2) = p^\mu B_1(p^2, m_1, m_2), \quad (\text{D.6})$$

$$B^{\mu\nu}(p^2, m_1, m_2) = p^\mu p^\nu B_{21}(p^2, m_1, m_2) + g^{\mu\nu} B_{22}(p^2, m_1, m_2). \quad (\text{D.7})$$

The coefficients of the vector and tensor functions (B_1 , B_{21} and B_{22}) can be expressed in terms of the functions B_0 and A_0 as

$$B_1 = \frac{1}{2p^2} [A(m_1) - A(m_2) + f_1 B_0(p^2, m_1, m_2)], \quad (\text{D.8a})$$

$$B_{21} = \frac{1}{p^2(D-1)} \left[\frac{D}{2} f_1 B_1(p^2, m_1, m_2) + \left(\frac{D}{2} - 1 \right) A(m_2) - m_1^2 B_0(p^2, m_1, m_2) \right], \quad (\text{D.8b})$$

$$B_{22} = \frac{1}{D-1} \left[\frac{1}{2} A(m_2) + m_1^2 B_0(p^2, m_1, m_2) - \frac{1}{2} f_1 B_1(p^2, m_1, m_2) \right], \quad (\text{D.8c})$$

where $f_1 = m_2^2 - m_1^2 - p^2$. By plugging $D = 4 - 2\epsilon$ to the above two expression, we obtain

$$B_{21} = \frac{1}{3p^2} \left[2f_1 B_1(p^2, m_1, m_2) + A(m_2) - m_1^2 B_0(p^2, m_1, m_2) + \frac{f_1}{2} - m_2^2 + \frac{2}{3}p^2 \right] + \mathcal{O}(\epsilon), \quad (\text{D.9a})$$

$$B_{22} = \frac{1}{3} \left[\frac{1}{2} A(m_2) + m_1^2 B_0(p^2, m_1, m_2) - \frac{1}{2} f_1 B_1(p^2, m_1, m_2) \right] + \frac{1}{6} (m_1^2 + m_2^2) - \frac{p^2}{18} + \mathcal{O}(\epsilon). \quad (\text{D.9b})$$

It is convenient to introduce the following four B functions in addition to B_0 and B_1 as

$$B_2(p^2, m_1, m_2) = B_{21}(p^2, m_1, m_2), \quad (\text{D.10a})$$

$$B_3(p^2, m_1, m_2) = -B_1(p^2, m_1, m_2) - B_2(p^2, m_1, m_2), \quad (\text{D.10b})$$

$$B_4(p^2, m_1, m_2) = -m_1^2 B_1(p^2, m_2, m_1) - m_2^2 B_1(p^2, m_1, m_2), \quad (\text{D.10c})$$

$$B_5(p^2, m_1, m_2) = A(m_1) + A(m_2) - 4B_{22}(p^2, m_1, m_2). \quad (\text{D.10d})$$

The B_n ($n = 0, 1, \dots, 5$) function can be decomposed into the infinite part Δ and the finite part as

$$B_0(p^2, m_1, m_2) = \Delta - F_0(p^2, m_1, m_2), \quad (\text{D.11a})$$

$$B_1(p^2, m_1, m_2) = -\frac{1}{2}\Delta + F_1(p^2, m_1, m_2), \quad (\text{D.11b})$$

$$B_2(p^2, m_1, m_2) = \frac{1}{3}\Delta - F_2(p^2, m_1, m_2), \quad (\text{D.11c})$$

$$B_3(p^2, m_1, m_2) = \frac{1}{6}\Delta - F_3(p^2, m_1, m_2), \quad (\text{D.11d})$$

$$B_4(p^2, m_1, m_2) = \frac{m_1^2 + m_2^2}{2}\Delta - F_4(p^2, m_1, m_2), \quad (\text{D.11e})$$

$$B_5(p^2, m_1, m_2) = \frac{p^2}{3}\Delta - F_5(p^2, m_1, m_2). \quad (\text{D.11f})$$

In the $\overline{\text{MS}}$ renormalization scheme the singular piece Δ in these function is simply replaced by a logarithm of the unit of mass μ :

$$\Delta \rightarrow \ln \mu^2. \quad (\text{D.12})$$

The F_0 , F_3 and F_A functions are given by

$$F_0(p^2, m_1, m_2) = \ln(m_1 m_2) - \delta \ln \frac{m_2}{m_1} - 2 + \beta L, \quad (\text{D.13})$$

$$F_3(p^2, m_1, m_2) = \frac{1}{6} \ln(m_1 m_2) - \frac{3\sigma - 2\delta^2}{6} \delta \ln \frac{m_2}{m_1} - \frac{5}{18} - \frac{\sigma - \delta^2}{3} + \frac{1 + \sigma - 2\delta^2}{6} \beta L, \quad (\text{D.14})$$

$$F_A(p^2, m_1, m_2) = -(\sigma - \delta^2) \ln \frac{m_2}{m_1} + \delta(1 - \beta L), \quad (\text{D.15})$$

where

$$\sigma = \frac{m_1^2 + m_2^2}{p^2}, \quad \delta = \frac{m_1^2 - m_2^2}{p^2}, \quad (\text{D.16})$$

$$\beta = \begin{cases} \sqrt{1 - 2\sigma + \delta^2} & \text{for } p^2 < (m_1 - m_2)^2 \text{ or } p^2 > (m_1 + m_2)^2, \\ i\sqrt{2\sigma - \delta^2 - 1} & \text{for } (m_1 - m_2)^2 < p^2 < (m_1 + m_2)^2, \end{cases} \quad (\text{D.17})$$

$$L = \begin{cases} \frac{1}{2} \ln \frac{1+\beta-\sigma}{1-\beta-\sigma} - i\pi & \text{for } p^2 > (m_1 + m_2)^2, \\ \frac{1}{2} \ln \frac{1+\beta-\sigma}{1-\beta-\sigma} & \text{for } p^2 < (m_1 - m_2)^2, \\ -i \left(\arctan \frac{1-\delta}{|\beta|} + \arctan \frac{1+\delta}{|\beta|} \right) & \text{for } (m_1 - m_2)^2 < p^2 < (m_1 + m_2)^2. \end{cases} \quad (\text{D.18})$$

The other F_1 , F_2 , F_4 and F_5 functions can be written in terms of the F_0 , F_3 and F_A functions as:

$$F_1(p^2, m_1, m_2) = \frac{1}{2}[F_0 - F_A](p^2, m_1, m_2), \quad (\text{D.19a})$$

$$F_2(p^2, m_1, m_2) = \left[\frac{1}{2}(F_0 - F_A) - F_3 \right](p^2, m_1, m_2), \quad (\text{D.19b})$$

$$F_4(p^2, m_1, m_2) = \left[\frac{m_1^2 + m_2^2}{2} F_0 + \frac{m_1^2 - m_2^2}{2} F_A \right](p^2, m_1, m_2), \quad (\text{D.19c})$$

$$F_5(p^2, m_1, m_2) = \left[p^2(F_0 - 4F_3) + (m_1^2 - m_2^2)F_A \right](p^2, m_1, m_2). \quad (\text{D.19d})$$

In the case with $m_1^2 = m^2 > p^2$ and $m_2^2 \simeq 0$, we obtain

$$F_0(p^2, m, 0) = \ln p^2 + R \ln R - 2 - (R - 1) \ln(R - 1), \quad (\text{D.20a})$$

$$F_3(p^2, m, 0) = \frac{1}{6} \ln p^2 + \frac{R^2}{6} (3 - 2R) \ln R - \frac{5}{18} - R \frac{1 - R}{3} + \frac{1}{6} (1 - 3R^2 + 2R^3) \ln(R - 1), \quad (\text{D.20b})$$

$$F_A(p^2, m, 0) = R(1 - R) \ln R + R + R(R - 1) \ln(R - 1), \quad (\text{D.20c})$$

where $R \equiv m^2/p^2$. In the case with $m_1 = m_2 = m$, these expressions are reduced to

$$F_0(p^2, m, m) = 2 \ln m - 2 + \beta L, \quad (\text{D.21a})$$

$$F_1(p^2, m, m) = \ln m - 1 + \frac{1}{2} \beta L, \quad (\text{D.21b})$$

$$F_2(p^2, m, m) = \frac{2}{3} \ln m - \frac{13}{18} + \frac{2m^2}{3p^2} + \frac{p^2 - m^2}{p^2} \beta L, \quad (\text{D.21c})$$

$$F_3(p^2, m, m) = \frac{1}{3} \ln m - \frac{5}{18} - \frac{2m^2}{3p^2} + \frac{p^2 + 2m^2}{6p^2} \beta L, \quad (\text{D.21d})$$

$$F_4(p^2, m, m) = 2m^2 \ln m - 2m^2 + m^2 \beta L, \quad (\text{D.21e})$$

$$F_5(p^2, m, m) = \frac{2}{3} p^2 \ln m - \frac{8}{9} p^2 + \frac{8}{3} m^2 + \frac{p^2 - 4m^2}{3} \beta L, \quad (\text{D.21f})$$

$$F_A(p^2, m, m) = 0, \quad (\text{D.21g})$$

with

$$\beta = \sqrt{1 - \frac{4m^2}{p^2}}, \quad L = \begin{cases} \frac{1}{2} \ln \frac{1+\beta-\sigma}{1-\beta-\sigma} - i\pi & \text{for } p^2 > 4m^2, \\ -2i \arctan \frac{1}{|\beta|} & \text{for } p^2 < 4m^2. \end{cases} \quad (\text{D.22})$$

In the case with $p^2 = 0$, F_0 , F_3 and F_A functions are given by

$$F_0(0, m_1, m_2) = \ln(m_1 m_2) - \frac{m_1^2 + m_2^2}{m_1^2 - m_2^2} \ln \frac{m_2}{m_1} - 1, \quad (\text{D.23a})$$

$$F_1(0, m_1, m_2) = \frac{1}{2} \ln(m_1 m_2) - \frac{1}{2} - \frac{1}{4} \frac{m_1^2 + m_2^2}{m_1^2 - m_2^2} + \frac{-m_1^4 + m_2^4 - 2m_1^2 m_2^2}{2(m_1^2 - m_2^2)^2} \ln \frac{m_2}{m_1}, \quad (\text{D.23b})$$

$$F_2(0, m_1, m_2) = \frac{1}{3} \ln(m_1 m_2) - \frac{13}{36} - \frac{3m_1^4 - 3m_2^4 + 4m_1^2 m_2^2}{12(m_1^2 - m_2^2)^2} + \frac{m_1^6 + 3m_1^4 m_2^2 - 3m_1^2 m_2^4 + m_2^6}{3(m_1^2 - m_2^2)^3}, \quad (\text{D.23c})$$

$$F_3(0, m_1, m_2) = \frac{1}{6} \ln(m_1 m_2) - \frac{5}{36} + \frac{1}{3} \frac{m_1^2 m_2^2}{(m_1^2 - m_2^2)^2} - \frac{1}{6} \frac{(m_1^2 + m_2^2)(m_1^4 + m_2^4 - 4m_1^2 m_2^2)}{(m_1^2 - m_2^2)^3} \ln \frac{m_2}{m_1}, \quad (\text{D.23d})$$

$$F_4(0, m_1, m_2) = -\frac{1}{4}(m_1^2 + m_2^2) - \frac{1}{2} \frac{m_1^4 + m_2^4}{m_1^2 - m_2^2} \ln \frac{m_2}{m_1} + \frac{m_1^2 + m_2^2}{2} \ln(m_1 m_2), \quad (\text{D.23e})$$

$$F_5(0, m_1, m_2) = \frac{1}{2}(m_1^2 + m_2^2) + \frac{2m_1^2 m_2^2}{(m_1^2 - m_2^2)} \ln \frac{m_2}{m_1}, \quad (\text{D.23f})$$

$$F_A(0, m_1, m_2) = \frac{1}{2} \frac{m_1^2 + m_2^2}{m_1^2 - m_2^2} + \frac{2m_1^2 m_2^2}{(m_1^2 - m_2^2)^2} \ln \frac{m_2}{m_1}. \quad (\text{D.23g})$$

In the limit of $p^2 \rightarrow 0$ and $m_1 = m_2 = m$, we obtain

$$F_0(0, m, m) = \ln m^2, \quad (\text{D.24a})$$

$$F_1(0, m, m) = \frac{1}{2} \ln m^2, \quad (\text{D.24b})$$

$$F_2(0, m, m) = \frac{1}{3} \ln m^2, \quad (\text{D.24c})$$

$$F_3(0, m, m) = \frac{1}{6} \ln m^2, \quad (\text{D.24d})$$

$$F_4(0, m, m) = m^2 \ln m^2, \quad (\text{D.24e})$$

$$F_5(0, m, m) = F_A(0, m, m) = 0. \quad (\text{D.24f})$$

Appendix E

Gauge boson self-energies and vertex corrections

In this appendix, analytic expressions for the gauge boson self-energies at the one-loop level are listed in terms of the Passarino-Veltman functions [212]. The gauge boson propagators $D_{\mu\nu}^V(p)$ ($V = \gamma, Z$ and W) and the photon- Z boson mixing can be expressed as [136]

$$D_{\mu\nu}^V(p^2) = -ig_{\mu\nu} \left(\frac{1}{p^2 - m_V^2} - \frac{1}{p^2 - m_V^2} \Pi_{\mu\nu}^{VV}(p^2) \frac{1}{p^2 - m_V^2} \right), \quad (\text{E.1})$$

$$D_{\mu\nu}^{\gamma Z}(p^2) = +ig_{\mu\nu} \frac{1}{p^2 - m_Z^2} \Pi_{\mu\nu}^{\gamma Z} \frac{1}{p^2}, \quad (\text{E.2})$$

where $\Pi_{\mu\nu}^{VV}(p^2)$ is the amplitude of the gauge boson two-point functions at the one-loop level. The functions $\Pi_{\mu\nu}^{VV}(p^2)$ can be decomposed into the transverse part and the longitudinal part as

$$(\Pi^{VV})^{\mu\nu}(p^2) = \left(-g^{\mu\nu} + \frac{p^\mu p^\nu}{p^2} \right) \Pi_T^{VV}(p^2) + \frac{p^\mu p^\nu}{p^2} \Pi_L^{VV}(p^2). \quad (\text{E.3})$$

The transverse part of the gauge boson two point functions Π_T^{VV} are composed of the fermionic-loop contributions and the bosonic-loop contributions as

$$\Pi_T^{VV}(p^2) = \Pi_{T,F}^{VV}(p^2) + \Pi_{T,B}^{VV}(p^2). \quad (\text{E.4})$$

E.1 Fermionic-loop contributions

The fermionic-loop contributions to the transverse part of the gauge boson two point functions are calculated as

$$\Pi_{T,F}^{WW}(p^2) = \frac{g^2}{16\pi^2} \sum_f N_c^f [-B_4 + 2p^2 B_3](p^2, m_f, m_{f'}), \quad (\text{E.5})$$

$$\Pi_{T,F}^{\gamma\gamma}(p^2) = \frac{e^2}{16\pi^2} \sum_f N_c^f Q_f^2 [8p^2 B_3](p^2, m_f, m_f), \quad (\text{E.6})$$

$$\Pi_{T,F}^{\gamma Z}(p^2) = -\frac{g^2}{16\pi^2} \frac{\hat{s}_W}{\hat{c}_W} \sum_f N_c^f 2p^2 [-4\hat{s}_W^2 Q_f^2 + 2I_f Q_f] B_3(p^2, m_f, m_f), \quad (\text{E.7})$$

$$\Pi_{T,F}^{ZZ}(p^2) = \frac{g_Z^2}{16\pi^2} \sum_f N_c^f \left[2p^2 (4\hat{s}_W^4 Q_f^2 - 4\hat{s}_W^2 Q_f I_f + 2I_f^2) B_3 - 2I_f^2 m_f^2 B_0 \right] (p^2, m_f, m_f). \quad (\text{E.8})$$

E.2 Bosonic-loop contributions

In the HTM, the bosonic-loop contributions to the transverse part of the gauge boson two point functions are listed below. The W boson two-point function is calculated as

$$\begin{aligned} \left(\frac{1}{16\pi^2} \right)^{-1} \Pi_{T,B}^{WW}(p^2) &= \left(\frac{1}{16\pi^2} \right)^{-1} \Pi_{T,B}^{WW}(p^2)_{\text{SM}} \\ &+ g^4 \left(\frac{v_\Phi}{2} c_\alpha + v_\Delta s_\alpha \right)^2 B_0(p^2, m_h, m_W) + g^4 \left(-\frac{v_\Phi}{2} s_\alpha + v_\Delta c_\alpha \right)^2 B_0(p^2, m_H, m_W) \\ &+ 2g^4 v_\Delta^2 B_0(p^2, m_{H^{++}}, m_W) \\ &+ \frac{g^4}{2\hat{c}_W^2} v_\Delta^2 c_{\beta_\pm}^2 B_0(p^2, m_{H^+}, m_W) + \frac{g^4}{\hat{c}_W^2} \left[\frac{v_\Phi}{2} \hat{s}_W^2 c_{\beta_\pm} + \frac{v_\Delta}{\sqrt{2}} (1 + \hat{s}_W^2) s_{\beta_\pm} \right]^2 B_0(p^2, m_Z, m_W) \\ &+ \frac{g^2 e^2}{4} (v_\Phi^2 + 2v_\Delta^2) B_0(p^2, 0, m_W) \\ &+ g^2 c_{\beta_\pm}^2 B_5(p^2, m_{H^{++}}, m_{H^+}) + g^2 s_{\beta_\pm}^2 B_5(p^2, m_{H^{++}}, m_W) \\ &+ \frac{g^2}{4} (c_\alpha s_{\beta_\pm} - \sqrt{2} s_\alpha c_{\beta_\pm})^2 B_5(p^2, m_{H^+}, m_h) + \frac{g^2}{4} (c_\alpha c_{\beta_\pm} + \sqrt{2} s_\alpha s_{\beta_\pm})^2 B_5(p^2, m_W, m_h) \\ &+ \frac{g^2}{4} (s_\alpha s_{\beta_\pm} + \sqrt{2} c_\alpha c_{\beta_\pm})^2 B_5(p^2, m_{H^+}, m_H) + \frac{g^2}{4} (s_\alpha c_{\beta_\pm} - \sqrt{2} c_\alpha s_{\beta_\pm})^2 B_5(p^2, m_W, m_H) \\ &+ \frac{g^2}{4} (s_{\beta_0} s_{\beta_\pm} + \sqrt{2} c_{\beta_0} c_{\beta_\pm})^2 B_5(p^2, m_{H^+}, m_A) + \frac{g^2}{4} (s_{\beta_0} c_{\beta_\pm} - \sqrt{2} c_{\beta_0} s_{\beta_\pm})^2 B_5(p^2, m_W, m_A) \\ &+ \frac{g^2}{4} (-c_{\beta_0} s_{\beta_\pm} + \sqrt{2} s_{\beta_0} c_{\beta_\pm})^2 B_5(p^2, m_{H^+}, m_Z) + \frac{g^2}{4} (c_{\beta_0} c_{\beta_\pm} + \sqrt{2} s_{\beta_0} s_{\beta_\pm})^2 B_5(p^2, m_W, m_Z). \end{aligned} \quad (\text{E.9})$$

The photon two-point function is calculated as

$$\begin{aligned} \left(\frac{1}{16\pi^2}\right)^{-1} \Pi_{T,B}^{\gamma\gamma}(p^2) &= \left(\frac{1}{16\pi^2}\right)^{-1} \Pi_{T,B}^{\gamma\gamma}(p^2)_{\text{SM}} \\ &+ \frac{e^2 g^2}{2} (v_\Phi^2 + 2v_\Delta^2) B_0(p^2, m_W, m_W) \\ &+ 4e^2 B_5(p^2, m_{H^{++}}, m_{H^{++}}) + e^2 B_5(p^2, m_{H^+}, m_{H^+}) + e^2 B_5(p^2, m_W, m_W). \end{aligned} \quad (\text{E.10})$$

The photon-Z boson mixing is calculated as

$$\begin{aligned} \left(\frac{1}{16\pi^2}\right)^{-1} \Pi_{T,B}^{\gamma Z}(p^2) &= \left(\frac{1}{16\pi^2}\right)^{-1} \Pi_{T,B}^{\gamma Z}(p^2)_{\text{SM}} \\ &+ g^4 \frac{\hat{s}_W}{\hat{c}_W} \sqrt{v_\Phi^2 + 2v_\Delta^2} \left[\frac{v_\Phi}{2} \hat{s}_W^2 c_{\beta_\pm} + \frac{v_\Delta}{\sqrt{2}} (1 + \hat{s}_W^2) s_{\beta_\pm} \right] B_0(p^2, m_W, m_W) \\ &- 2g^2 \frac{\hat{s}_W (\hat{c}_W^2 - \hat{s}_W^2)}{\hat{c}_W} B_5(p^2, m_{H^{++}}, m_{H^{++}}) \\ &- \frac{g^2}{2} \frac{\hat{s}_W}{\hat{c}_W} (\hat{c}_W^2 - \hat{s}_W^2 - c_{\beta_\pm}^2) B_5(p^2, m_{H^+}, m_{H^+}) \\ &- \frac{g^2}{2} \frac{\hat{s}_W}{\hat{c}_W} (\hat{c}_W^2 - \hat{s}_W^2 - s_{\beta_\pm}^2) B_5(p^2, m_W, m_W), \end{aligned} \quad (\text{E.11})$$

where $\Pi_{T,B}^{VV}(p^2)_{\text{SM}}$ are the SM gauge boson loop contributions. These are calculated as

$$\begin{aligned} \left(\frac{1}{16\pi^2}\right)^{-1} \Pi_{T,B}^{WW}(p^2)_{\text{SM}} &= -g^2 \hat{s}_W^2 [6(D-1)B_{22} + p^2(2B_{21} + 2B_1 + 5B_0)](p^2, 0, m_W) \\ &- g^2 \hat{c}_W^2 [6(D-1)B_{22} + p^2(2B_{21} + 2B_1 + 5B_0)](p^2, m_Z, m_W) \\ &+ g^2 (D-1) [\hat{c}_W^2 A(m_Z) + A(m_W)] \\ &+ 2e^2 \left[B_{22}(p^2, 0, m_W) + \frac{\hat{c}_W^2}{\hat{s}_W^2} B_{22}(p^2, m_Z, m_W) \right] \\ &- 4g^2 (p^2 - m_W^2) [\hat{c}_W^2 B_0(p^2, m_W, m_Z) + \hat{s}_W^2 B_0(p^2, m_W, 0)], \end{aligned} \quad (\text{E.12})$$

$$\begin{aligned} \left(\frac{1}{16\pi^2}\right)^{-1} \Pi_{T,B}^{\gamma\gamma}(p^2)_{\text{SM}} &= -e^2 [6(D-1)B_{22} + p^2(2B_{21} + 2B_1 + 5B_0)](p^2, m_W, m_W) \\ &+ 2e^2 (D-1) A(m_W) + 2e^2 B_{22}(p^2, m_W, m_W) \\ &- 4e^2 p^2 B_0(p^2, m_W, m_W), \end{aligned} \quad (\text{E.13})$$

$$\begin{aligned} \left(\frac{1}{16\pi^2}\right)^{-1} \Pi_{T,B}^{\gamma Z}(p^2)_{\text{SM}} &= +e^2 \frac{\hat{c}_W}{\hat{s}_W} [6(D-1)B_{22} + p^2(2B_{21} + 2B_1 + 5B_0)](p^2, m_W, m_W) \\ &- 2e^2 \frac{\hat{c}_W}{\hat{s}_W} (D-1) A(m_W), \\ &- 2e^2 \frac{\hat{c}_W}{\hat{s}_W} B_{22}(p^2, m_W, m_W) \\ &+ 4g^2 \frac{\hat{s}_W}{\hat{c}_W} \left(p^2 - \frac{m_W^2}{2} \right) B_0(p^2, m_W, m_W). \end{aligned} \quad (\text{E.14})$$

E.3 Vertex correction

The form factors $\Gamma_{V,A}^{Z\bar{f}f}(p^2)$ of the $Z\bar{f}f$ vertex can be calculated as [137]

$$\Gamma_V^{Z\bar{f}f}(p^2) = \Gamma_L^{Z\bar{f}f}(p^2) + \Gamma_R^{Z\bar{f}f}(p^2), \quad \Gamma_A^{Z\bar{f}f}(p^2) = \Gamma_L^{Z\bar{f}f}(p^2) - \Gamma_R^{Z\bar{f}f}(p^2), \quad (\text{E.15})$$

where $\Gamma_L^{Z\bar{f}f}(p^2)$ ($\Gamma_R^{Z\bar{f}f}(p^2)$) is $Z\bar{f}_L f_L$ ($Z\bar{f}_R f_R$) vertex form factor. These are given as

$$\begin{aligned} \Gamma_L^{Z\bar{f}f}(p^2) = & -\frac{1}{16\pi^2} \left\{ (I_f - Q_f \hat{s}_W^2) \left[\frac{g^2}{\hat{c}_W^2} (I_f - Q_f \hat{s}_W^2)^2 \Gamma_{1Z}^f(p^2) + \frac{g^2}{2} \Gamma_{1W}^{f'}(p^2) \right] \right. \\ & \left. + I_f \left[-\hat{c}_W^2 g^2 \bar{\Gamma}_{2W}^{f'}(p^2) + \frac{g^2}{2} \Gamma_{mW}^{f'}(p^2) \right] \right\}, \end{aligned} \quad (\text{E.16})$$

$$\Gamma_R^{Z\bar{f}f}(p^2) = \frac{1}{16\pi^2} \frac{g^2}{\hat{c}_W^2} Q_f^3 \hat{s}_W^6 \Gamma_{1Z}^f(p^2), \quad (\text{E.17})$$

where

$$\Gamma_{1Z}^f(p^2) = \Gamma_1(p^2, m_f, m_Z, m_f) - \Sigma'(m_f^2, m_f, m_Z), \quad (\text{E.18})$$

$$\Gamma_{1W}^{f'}(p^2) = [\Gamma_1 + \Gamma_{1m}](p^2, m_{f'}, m_W, m_{f'}) - \Sigma'(m_{f'}^2, m_{f'}, m_W), \quad (\text{E.19})$$

$$\bar{\Gamma}_{2W}^{f'}(p^2) = [\Gamma_1 + \Gamma_{1m}](p^2, m_{f'}, m_W, m_{f'}) - \Gamma_2(p^2, m_W, m_{f'}, m_W) + 2\text{Re}B_0(p^2, m_W, m_W), \quad (\text{E.20})$$

$$\Gamma_{mW}^{f'}(p^2) = \Gamma_{1m}(p^2, m_{f'}, m_W, m_{f'}) + \Gamma_{2m}(p^2, m_W, m_{f'}, m_W), \quad (\text{E.21})$$

with

$$\Sigma'(p^2, m, M) = - \left(2 + \frac{m^2}{M^2} \right) B_1(p^2, m, M) - 1, \quad (\text{E.22})$$

$$\Gamma_1(p^2, m, M, m) = \left[2p^2(C_{11} + C_{23}) + 4C_{24} - \frac{m^4}{M^2} C_0 \right] (0, 0, p^2, m, M, m) - 2, \quad (\text{E.23})$$

$$\Gamma_2(p^2, M, m, M) = 2 \left[p^2(C_{11} + C_{23}) + \left(6 + \frac{m^2}{M^2} \right) C_{24} + (p^2 - m^2) C_0 \right] (0, 0, p^2, M, m, M) - 2, \quad (\text{E.24})$$

$$\Gamma_{1m}(p^2, m, M, m) = \frac{m^2}{M^2} \left\{ [p^2(C_{12} + C_{23}) + 2C_{24} - 2M^2 C_0] (0, 0, p^2, m, M, m) - \frac{1}{2} \right\}, \quad (\text{E.25})$$

$$\Gamma_{2m}(p^2, M, m, M) = \frac{2m^2}{M^2} [2M^2 C_0 - C_{24}] (0, 0, p^2, M, m, M). \quad (\text{E.26})$$

Bibliography

- [1] B. W. Lee, C. Quigg and H. B. Thacker, Phys. Rev. D **16**, 1519 (1977).
- [2] H. M. Georgi, S. L. Glashow, M. E. Machacek and D. V. Nanopoulos, Phys. Rev. Lett. **40**, 692 (1978).
- [3] D. R. T. Jones and S. T. Petcov, Phys. Lett. B **84**, 440 (1979); R.N. Cahn and S. Dawson, Phys. Lett. B **136**, 196 (1984); D. Dicus and S. Willenbrock, Phys. Rev. D **32**, 1642 (1985); G. Altarelli, B. Mele and F. Pitolli, Nucl. Phys. B **287**, 205 (1987); W. Kilian, M. Kramer and P.M. Zerwas, Phys. Lett. B **373**, 135 (1996).
- [4] S.L. Glashow, D. Nanopoulos and A. Yildiz, Phys. Rev. D **18**, 1724 (1978); J. Finjord, G. Girardi and P. Sorba, Phys. Lett. B **89**, 99 (1979); E. Eichten, I. Hinchliffe, K. Lane and C. Quigg, Rev. Mod. Phys. **56**, 579 (1984).
- [5] R. Raitio and W.W. Wada, Phys. Rev. D **19**, 941 (1979); Z. Kunszt, Nucl. Phys. B **247**, 339 (1984); A.S. Bagdasaryan *et al.*, Sov. J. Nucl. Phys. **46**, 315 (1987); J. Ng and P. Zakarauskas, Phys. Rev. D **29**, 876 (1984).
- [6] Update of the combination of Higgs boson searches in 1.0 to 2.3 fb⁻¹ of *pp* collisions data taken at $\sqrt{s} = 7$ TeV with the ATLAS experiment at the LHC, ATLAS-CONF-2011-135; Search for standard model Higgs boson in *pp* collisions at $\sqrt{s} = 7$ TeV and integrated luminosity up to 1.7 fb⁻¹, CMS PAS HIG-11-022.
- [7] S. Weinberg, Phys. Rev. D **13**, 974 (1976), Phys. Rev. D **19**, 1277 (1979); E. Gildener, Phys. Rev. D **14**, 1667 (1976); L. Susskind, Phys. Rev. D **20**, 2619 (1979); G. 't Hooft, in *Recent developments in gauge theories*, Proceedings of the NATO Advanced Summer Institute, Cargese 1979, (Plenum, 1980).973].
- [8] T. Schwetz, M. A. Tortola, J. W. F. Valle, New J. Phys. **10**, 113011 (2008).
- [9] E. Komatsu *et al.* [WMAP Collaboration], Astrophys. J. Suppl. **192**, 18 (2011).
- [10] A. D. Sakharov, Pisma Zh. Eksp. Teor. Fiz. **5**, 32-35 (1967).
- [11] L. Susskind, Phys. Rev. D **20**, 2619 (1979); S. Weinberg, Phys. Rev. D **13**, 974 (1976); S. Weinberg, Phys. Rev. D **19**, 1277 (1979).
- [12] N. Arkani-Hamed, A. G. Cohen and H. Georgi, Phys. Lett. B **513**, 232 (2001).
- [13] N. S. Manton, Nucl. Phys. B **158**, 141 (1979); D. B. Fairlie, Phys. Lett. B **82**, 97 (1979); J. Phys. G **5**, L55 (1979).

- [14] Y. Hosotani, *Annals Phys.* **190**, 233 (1989); *Phys. Lett. B* **126**, 309 (1983); *Phys. Lett. B* **129**, 193 (1983).
- [15] T. P. Cheng and L. F. Li, *Phys. Rev. D* **22**, 2860 (1980); J. Schechter and J. W. F. Valle, *Phys. Rev. D* **22**, 2227 (1980); G. Lazarides, Q. Shafi and C. Wetterich, *Nucl. Phys. B* **181**, 287 (1981); R. N. Mohapatra and G. Senjanovic, *Phys. Rev. D* **23**, 165 (1981); M. Magg and C. Wetterich, *Phys. Lett. B* **94**, 61 (1980).
- [16] A. Zee, *Phys. Lett. B* **93** (1980) 389 [Erratum-ibid. *B* **95** (1980) 461]; A. Zee, *Phys. Lett. B* **161** (1985) 141.
- [17] A. Zee, *Nucl. Phys. B* **264** (1986) 99.
- [18] K. S. Babu, *Phys. Lett. B* **203** (1988) 132.
- [19] L. M. Krauss, S. Nasri and M. Trodden, *Phys. Rev. D* **67** (2003) 085002.
- [20] E. Ma, *Phys. Rev. D* **73** (2006) 077301.
- [21] M. Aoki, S. Kanemura and O. Seto, *Phys. Rev. Lett.* **102**, 051805 (2009).
- [22] R. Barbieri, L. J. Hall and V. S. Rychkov, *Phys. Rev. D* **74**, 015007 (2006); E. Ma, *Phys. Rev. D* **73**, 077301 (2006); J. Kubo, E. Ma and D. Suematsu, *Phys. Lett. B* **642**, 18 (2006).
- [23] S. Kanemura, Y. Okada and E. Senaha, *Phys. Lett. B* **606**, 361 (2005).
- [24] A. I. Bochkarev, S. V. Kuzmin and M. E. Shaposhnikov, *Phys. Lett. B* **244** (1990) 275; A. E. Nelson, D. B. Kaplan and A. G. Cohen, *Nucl. Phys. B* **373**, 453 (1992); N. Turok and J. Zadrozny, *Nucl. Phys. B* **369**, 729 (1992); K. Funakubo, A. Kakuto and K. Takenaga, *Prog. Theor. Phys.* **91**, 341 (1994); A. T. Davies, C. D. Froggatt, G. Jenkins and R. G. Moorhouse, *Phys. Lett. B* **336**, 464 (1994); J. M. Cline, K. Kainulainen and A. P. Vischer, *Phys. Rev. D* **54**, 2451 (1996).
- [25] L. Fromme, S. J. Huber and M. Seniuch, *JHEP* **0611**, 038 (2006).
- [26] K. Nakamura, et al., (Particle Data Group), *J. Phys. G* **37**, 075021 (2010).
- [27] J. F. Gunion, H. E. Haber, G. L. Kane and S. Dawson, “THE HIGGS HUNTER’S GUIDE,” *Front. Phys.* **80**, 1 (2000).
- [28] S. L. Glashow, J. Iliopoulos and L. Maiani, *Phys. Rev. D* **2**, 1285 (1970).
- [29] S. L. Glashow and S. Weinberg, *Phys. Rev. D* **15**, 1958 (1977).
- [30] J. A. Grifols and A. Mendez, *Phys. Rev. D* **22**, 1725 (1980); A.A. Iogansen, N.G. Uraltsev, V.A. Khoze, *Sov. J. Nucl. Phys.* **36** (1982) 717.
- [31] A. Mendez and A. Pomarol, *Nucl. Phys. B* **349**, 369 (1991); M. C. Peyranere, H. E. Haber and P. Irulegui, *Phys. Rev. D* **44**, 191 (1991); J.L. Díaz-Cruz, J. Hernández-Sánchez, J.J. Toscano, *Phys. Lett. B* **512**, 339 (2001).

- [32] S. Kanemura, Phys. Rev. D **61**, 095001 (2000).
- [33] H. Haber, H. Logan, Phys. Rev. D **62**, 015011 (2000).
- [34] P. Fayet, Nucl. Phys. B **90**, 104 (1975); Phys. Lett. B **64**, 159 (1976); Phys. Lett. B **69**, 489 (1977); Phys. Lett. B **84**, 416 (1979).
- [35] G. C. Branco, P. M. Ferreira, L. Lavoura, M. N. Rebelo, M. Sher and J. P. Silva, arXiv:1106.0034 [hep-ph].
- [36] V. D. Barger, J. L. Hewett and R. J. N. Phillips, Phys. Rev. D **41**, 3421 (1990).
- [37] Y. Grossman, Nucl. Phys. B **426**, 355 (1994).
- [38] M. Aoki, S. Kanemura, K. Tsumura and K. Yagyu, Phys. Rev. D **80**, 015017 (2009).
- [39] H. S. Goh, L. J. Hall and P. Kumar, JHEP **0905**, 097 (2009); S. Su and B. Thomas, Phys. Rev. D **79**, 095014 (2009); H. E. Logan and D. MacLennan, Phys. Rev. D **79**, 115022 (2009).
- [40] M. Ciuchini, G. Degrassi, P. Gambino and G. F. Giudice, Nucl. Phys. B **527**, 21 (1998); P. Ciafaloni, A. Romanino and A. Strumia, Nucl. Phys. B **524**, 361 (1998); F. Borzumati and C. Greub, Phys. Rev. D **58**, 074004 (1998); T. M. Aliev and E. O. Iltan, Phys. Rev. D **58**, 095014 (1998).
- [41] A. G. Akeroyd and S. Recksiegel, J. Phys. G **29**, 2311 (2003).
- [42] M. Krawczyk and D. Sokolowska, arXiv:0711.4900 [hep-ph].
- [43] D. s. Du, arXiv:0709.1315 [hep-ph].
- [44] M. Misiak and M. Steinhauser, Nucl. Phys. B **764**, 62 (2007).
- [45] M. Misiak *et al.*, Phys. Rev. Lett. **98**, 022002 (2007); T. Becher and M. Neubert, Phys. Rev. Lett. **98**, 022003 (2007).
- [46] S. Kanemura, K. Tsumura and H. Yokoya, arXiv:1111.6089 [hep-ph]; S. Kanemura, K. Tsumura and H. Yokoya, arXiv:1201.6489 [hep-ph].
- [47] S. Kanemura and H. Sugiyama, arXiv:1202.5231 [hep-ph].
- [48] S. Kanemura and K. Yagyu, arXiv:1201.6287 [hep-ph].
- [49] T. Blank and W. Hollik, Nucl. Phys. B **514**, 113 (1998).
- [50] M. Czakon, J. Gluza, F. Jegerlehner and M. Zralek, Eur. Phys. J. C **13**, 275 (2000); J. R. Forshaw, D. A. Ross and B. E. White, JHEP **0110**, 007 (2001); J. R. Forshaw, A. Sabio Vera and B. E. White, JHEP **0306**, 059 (2003); M. C. Chen, S. Dawson and T. Krupovnickas, Phys. Rev. D **74**, 035001 (2006); M. C. Chen and S. Dawson, Phys. Rev. D **70**, 015003 (2004); P. H. Chankowski, S. Pokorski and J. Wagner, Eur. Phys. J. C **50**, 919 (2007); M. C. Chen, S. Dawson and C. B. Jackson, Phys. Rev. D **78**, 093001

- (2008); P. H. Chankowski and J. Wagner, Phys. Rev. D **77**, 025033 (2008); R. S. Chivukula, N. D. Christensen and E. H. Simmons, Phys. Rev. D **77**, 035001 (2008).
- [51] M. C. Chen, S. Dawson and T. Krupovnickas, Int. J. Mod. Phys. A **21**, 4045 (2006).
- [52] E. J. Chun, K. Y. Lee and S. C. Park, Phys. Lett. B **566**, 142 (2003); M. Kakizaki, Y. Ogura and F. Shima, Phys. Lett. B **566** (2003) 210; A. G. Akeroyd and M. Aoki, Phys. Rev. D **72**, 035011 (2005).
- [53] P. Fileviez Perez, T. Han, G. -y. Huang, T. Li, K. Wang, Phys. Rev. **D78**, 015018 (2008).
- [54] A. G. Akeroyd, H. Sugiyama, Phys. Rev. **D84**, 035010 (2011).
- [55] A. Melfo, M. Nemevsek, F. Nesti, G. Senjanovic and Y. Zhang, arXiv:1108.4416 [hep-ph].
- [56] S. Chakrabarti, D. Choudhury, R. M. Godbole and B. Mukhopadhyaya, Phys. Lett. B **434**, 347 (1998).
- [57] M. Aoki, S. Kanemura and K. Yagyu, Phys. Rev. D **85**, 055007 (2012).
- [58] C. -W. Chiang, T. Nomura and K. Tsumura, arXiv:1202.2014 [hep-ph].
- [59] J. F. Gunion, C. Loomis and K. T. Pitts, *In the Proceedings of 1996 DPF / DPB Summer Study on New Directions for High-Energy Physics (Snowmass 96), Snowmass, Colorado, 25 Jun - 12 Jul 1996, pp LTH096* [arXiv:hep-ph/9610237].
- [60] M. Muhlleitner and M. Spira, 4-lepton Phys. Rev. D **68**, 117701 (2003); T. Han, B. Mukhopadhyaya, Z. Si and K. Wang, Phys. Rev. D **76**, 075013 (2007); A. G. Akeroyd, C. W. Chiang and N. Gaur, JHEP **1011**, 005 (2010).
- [61] J. Garayoa and T. Schwetz, JHEP **0803**, 009 (2008); A. G. Akeroyd, M. Aoki and H. Sugiyama, Phys. Rev. D **77**, 075010 (2008); F. del Aguila and J. A. Aguilar Saavedra, Nucl. Phys. B **813**, 22 (2009); A. G. Akeroyd and C. W. Chiang, Phys. Rev. D **80**, 113010 (2009).
- [62] M. Kadastik, M. Raidal and L. Rebane, Phys. Rev. D **77**, 115023 (2008).
- [63] J. Smith, W. L. van Neerven, and J. A. M. Vermaseren, Phys. Rev. Lett. **50**, 1738 (1983).
- [64] Y. Okada, M. Yamaguchi, T. Yanagida, Prog. Theor. Phys. **85**, 1-6 (1991); J. R. Ellis, G. Ridolfi, F. Zwirner, Phys. Lett. **B257**, 83-91 (1991); H. E. Haber, R. Hempfling, Phys. Rev. Lett. **66**, 1815-1818 (1991).
- [65] P. H. Chankowski, S. Pokorski and J. Rosiek, Phys. Lett. B **274**, 191 (1992); A. Brignole, Phys. Lett. B **281**, 284 (1992); D. M. Pierce, J. A. Bagger, K. T. Matchev and R. j. Zhang, Nucl. Phys. B **491**, 3 (1997).
- [66] A. Dabelstein, Z. Phys. C **67**, 495 (1995); Nucl. Phys. B **456**, 25 (1995).
- [67] S. Kanemura, T. Shindou and K. Yagyu, Phys. Lett. B **699**, 258 (2011).

- [68] M. Aoki, S. Kanemura, T. Shindou and K. Yagyu, JHEP **1111**, 038 (2011).
- [69] M. Aoki, S. Kanemura and K. Yagyu, Phys. Rev. D **83**, 075016 (2011).
- [70] M. Aoki, S. Kanemura, T. Shindou and K. Yagyu, JHEP **1007**, 084 (2010).
- [71] M. Aoki, S. Kanemura and K. Yagyu, Phys. Lett. B **702**, 355 (2011).
- [72] N. Cabibbo, Phys. Rev. Lett. **10**, 531 (1963); M. Kobayashi and T. Maskawa, Prog. Theor. Phys. **49**, 652 (1973).
- [73] J. M. Cornwall, D. N. Levin and G. Tiktopoulos, Phys. Rev. Lett. **30**, 1268 (1973); J. M. Cornwall, D. N. Levin and G. Tiktopoulos, Phys. Rev. D **10**, 1145 (1974).
- [74] L. Maiani, G. Parisi and R. Petronzio, Nucl. Phys. B **136**, 115 (1978); N. Cabibbo, L. Maiani, G. Parisi and R. Petronzio, Nucl. Phys. B **158**, 295 (1979); R. F. Dashen and H. Neuberger, Phys. Rev. Lett. **50**, 1897 (1983); D. J. E. Callaway, Nucl. Phys. B **233**, 189 (1984); M. A. B. Beg, C. Panagiotakopoulos and A. Sirlin, Phys. Rev. Lett. **52**, 883 (1984).
- [75] H. Komatsu, Prog. Theor. Phys. **67**, 1177 (1982).
- [76] K. Inoue, A. Kakuto, H. Komatsu and S. Takeshita, Prog. Theor. Phys. **67**, 1889 (1982).
- [77] M. Lindner, Z. Phys. C **31**, 295 (1986).
- [78] B. Grzadkowski and M. Lindner, Phys. Lett. **178B**, 81 (1986).
- [79] L. D. Landau, *in Niels Bohr and the Development of Physics*, edited by W. Pauli (Pergamon Press, London, 1955).
- [80] T. Hambye and K. Riesselmann, Phys. Rev. D **55**, 7255 (1997).
- [81] H. Georgi and D. V. Nanopoulos, Phys. Lett. B **82**, 95 (1979).
- [82] T. P. Cheng and M. Sher, Phys. Rev. D **35**, 3484 (1987); J. L. Diaz-Cruz, R. Noriega-Papaqui and A. Rosado, Phys. Rev. D **69**, 095002 (2004).
- [83] A. Pich and P. Tuzon, Phys. Rev. D **80**, 091702 (2009).
- [84] D. Atwood, L. Reina and A. Soni, Phys. Rev. D **55**, 3156 (1997).
- [85] P. Ko, Y. Omura and C. Yu, arXiv:1108.4005 [hep-ph].
- [86] N. G. Deshpande and E. Ma, Phys. Rev. D **18**, 2574 (1978); M. Sher, Phys. Rept. **179**, 273 (1989).
- [87] S. Nie and M. Sher, Phys. Lett. B **449**, 89 (1999).
- [88] S. Kanemura, T. Kasai and Y. Okada, Phys. Lett. B **471**, 182 (1999).
- [89] S. Kanemura, T. Kubota and E. Takasugi, Phys. Lett. B **313**, 155 (1993).

- [90] H. Huffer and G. Pocsik, Z. Phys. C **8**, 13 (1981); J. Maalampi, J. Sirkka and I. Vilja, Phys. Lett. B **265**, 371 (1991); A. G. Akeroyd, A. Arhrib and E. M. Naimi, Phys. Lett. B **490**, 119 (2000); I. F. Ginzburg and I. P. Ivanov, arXiv:hep-ph/0312374, Phys. Rev. D **72**, 115010 (2005).
- [91] J. F. Gunion and H. E. Haber, Phys. Rev. D **67**, 075019 (2003).
- [92] S. Kanemura, Y. Okada, E. Senaha and C. P. Yuan, Phys. Rev. D **70**, 115002 (2004).
- [93] S. Kanemura, S. Moretti, Y. Mukai, R. Santos and K. Yagyu, Phys. Rev. D **79**, 055017 (2009).
- [94] ALEPH, DELPHI, L3 and OPAL Collaborations, The LEP Working Group for Higgs Boson Searches, Phys. Lett. B **565**, 61 (2003); Eur. Phys. J. C **47**, 547 (2006).
- [95] A. Abulencia *et al.* [CDF Collaboration], Phys. Rev. Lett. **96**, 042003 (2006); V. M. Abazov *et al.* [D0 Collaboration], Phys. Rev. Lett. **88**, 151803 (2002).
- [96] H. E. Haber and A. Pomarol, Phys. Lett. B **302**, 435 (1993); A. Pomarol and R. Vega, Nucl. Phys. B **413**, 3 (1994).
- [97] P. H. Chankowski, M. Krawczyk and J. Zochowski, Eur. Phys. J. C **11**, 661 (1999); Phys. Rev. Lett. **98**, 251802 (2007); W. Grimus, L. Lavoura, O. M. Ogreid and P. Osland, Nucl. Phys. B **801**, 81 (2008); J. M. Gerard and M. Herquet, S. de Visscher, J. M. Gerard, M. Herquet, V. Lemaître and F. Maltoni, JHEP **0908**, 042 (2009).
- [98] K. Abe *et al.* [Belle Collaboration], AIP Conf. Proc. **1078**, 342 (2009).
- [99] B. Aubert *et al.* [BABAR Collaboration], Phys. Rev. D **77**, 051103 (2008).
- [100] S. Chen *et al.* [CLEO Collaboration], Phys. Rev. Lett. **87**, 251807 (2001).
- [101] D. Asner *et al.*, arXiv:1010.1589 [hep-ex].
- [102] T. Goto and Y. Okada, Prog. Theor. Phys. **94**, 407 (1995); M. Ciuchini, G. Degrandi, P. Gambino and G. F. Giudice, Nucl. Phys. B **534**, 3 (1998).
- [103] B. Aubert *et al.* [BABAR Collaboration], Phys. Rev. D **77**, 011107 (2008).
- [104] G. Isidori and P. Paradisi, Phys. Lett. B **639**, 499 (2006).
- [105] M. Krawczyk and D. Temes, Eur. Phys. J. **C44**, 435 (2005).
- [106] R. Jackiw and S. Weinberg, Phys. Rev. D **5**, 2396 (1972); K. Fujikawa, B. W. Lee and A. I. Sanda, Phys. Rev. D **6**, 2923 (1972).
- [107] J. P. Leveille, Nucl. Phys. B **137**, 63 (1978); H. E. Haber, G. L. Kane and T. Sterling, Nucl. Phys. B **161**, 493 (1979); M. Krawczyk and J. Zochowski, Phys. Rev. D **55**, 6968 (1997); A. Dedes and H. E. Haber, JHEP **0105**, 006 (2001).
- [108] S. M. Barr and A. Zee, Phys. Rev. Lett. **65**, 21 (1990) [Erratum-ibid. **65**, 2920 (1990)].

- [109] D. Chang, W. F. Chang, C. H. Chou and W. Y. Keung, Phys. Rev. D **63**, 091301 (2001); K. m. Cheung, C. H. Chou and O. C. W. Kong, Phys. Rev. D **64**, 111301 (2001); K. Cheung and O. C. W. Kong, Phys. Rev. D **68**, 053003 (2003).
- [110] A. Abulencia *et al.* [CDF Collaboration], Phys. Rev. Lett. **96**, 042003 (2006); M. Baarmand, M. Hashemi and A. Nikitenko, J. Phys. G **32**, N21 (2006).
- [111] A. C. Bawa, C. S. Kim and A. D. Martin, Z. Phys. C **47**, 75 (1990); J. L. Diaz-Cruz and O. A. Sampayo, Phys. Rev. D **50**, 6820 (1994); V. D. Barger, R. J. N. Phillips and D. P. Roy, Phys. Lett. B **324**, 236 (1994); L. G. Jin, C. S. Li, R. J. Oakes and S. H. Zhu, Eur. Phys. J. C **14**, 91 (2000); A. Belyaev, D. Garcia, J. Guasch and J. Sola, JHEP **0206**, 059 (2002); T. Plehn, Phys. Rev. D **67**, 014018 (2003); J. Alwall and J. Rathsmann, JHEP **0412**, 050 (2004); S. h. Zhu, Phys. Rev. D **67**, 075006 (2003); E. L. Berger, T. Han, J. Jiang and T. Plehn, Phys. Rev. D **71**, 115012 (2005); K. A. Assamagan and N. Gollub, Eur. Phys. J. C **39S2**, 25 (2005).
- [112] M. Aoki, R. Guedes, S. Kanemura, S. Moretti, R. Santos and K. Yagyu, Phys. Rev. D **84**, 055028 (2011).
- [113] G. Aad *et al.* [The ATLAS Collaboration], arXiv:0901.0512 [hep-ex]; K. A. Assamagan, Y. Coadou and A. Deandrea, Eur. Phys. J. direct C **4**, 9 (2002).
- [114] J. F. Gunion, H. E. Haber, F. E. Paige, W. K. Tung and S. S. D. Willenbrock, Nucl. Phys. B **294**, 621 (1987).
- [115] S. S. D. Willenbrock, Phys. Rev. D **35**, 173 (1987); O. Brein and W. Hollik, Eur. Phys. J. C **13**, 175 (2000); A. A. Barrientos Bendezu and B. A. Kniehl, Phys. Rev. D **64**, 035006 (2001).
- [116] J. F. Gunion and H. E. Haber, Nucl. Phys. B **278**, 449 (1986).
- [117] D. A. Dicus, J. L. Hewett, C. Kao and T. G. Rizzo, Phys. Rev. D **40**, 787 (1989); S. Moretti and K. Odagiri, Phys. Rev. D **59**, 055008 (1999); A. A. Barrientos Bendezu and B. A. Kniehl, Phys. Rev. D **59**, 015009 (1998); O. Brein, W. Hollik and S. Kanemura, Phys. Rev. D **63**, 095001 (2001); W. Hollik and S. h. Zhu, Phys. Rev. D **65**, 075015 (2002); E. Asakawa, O. Brein and S. Kanemura, Phys. Rev. D **72**, 055017 (2005); D. Eriksson, S. Hesselbach and J. Rathsmann, Eur. Phys. J. C **53**, 267 (2008).
- [118] H. M. Georgi, S. L. Glashow, M. E. Machacek and D. V. Nanopoulos, Phys. Rev. Lett. **40**, 692 (1978).
- [119] R. N. Cahn and S. Dawson, Phys. Lett. B **136**, 196 (1984) [Erratum-ibid. B **138**, 464 (1984)]; D. A. Dicus and S. S. D. Willenbrock, Phys. Rev. D **32**, 1642 (1985); G. Altarelli, B. Mele and F. Pitolli, Nucl. Phys. B **287**, 205 (1987).
- [120] D. L. Rainwater and D. Zeppenfeld, JHEP **9712**, 005 (1997); D. L. Rainwater, D. Zeppenfeld and K. Hagiwara, Phys. Rev. D **59**, 014037 (1998).

- [121] S. Dawson, C. B. Jackson, L. Reina and D. Wackerroth, Phys. Rev. D **69**, 074027 (2004); S. Dittmaier, M. I. Kramer and M. Spira, Phys. Rev. D **70**, 074010 (2004); J. M. Campbell *et al.*, arXiv:hep-ph/0405302.
- [122] R. Raitio and W. W. Wada, Phys. Rev. D **19**, 941 (1979); J. N. Ng and P. Zakarauskas, Phys. Rev. D **29**, 876 (1984); A. S. Bagdasaryan, R. S. Egorian, S. G. Grigorian and S. G. Matinyan, Sov. J. Nucl. Phys. **46**, 315 (1987) [Yad. Fiz. **46**, 572 (1987)]; D. A. Dicus, C. Kao and S. S. D. Willenbrock, Phys. Lett. B **203**, 457 (1988).
- [123] Z. Kunszt, Nucl. Phys. B **247**, 339 (1984).
- [124] “ATLAS detector and physics performance. Technical Design Report. Vol. 2,” ATLAS-TDR-015, CERN-LHCC-99-015; G. Aad *et al.* [The ATLAS Collaboration], arXiv:0901.0512.
- [125] T. Han and B. McElrath, Phys. Lett. B **528**, 81 (2002).
- [126] S. Kanemura and C. P. Yuan, Phys. Lett. B **530** 188 (2002).
- [127] A. G. Akeroyd, Phys. Rev. D **68** (2003) 077701.
- [128] Q. H. Cao, S. Kanemura and C. P. Yuan, Phys. Rev. D **69**, 075008 (2004).
- [129] Q. H. Cao, D. Nomura, K. Tobe and C. P. Yuan, Phys. Lett. B **632**, 688 (2006); A. Belyaev, Q. H. Cao, D. Nomura, K. Tobe and C. P. Yuan, Phys. Rev. Lett. **100**, 061801 (2008).
- [130] A. Pukhov, arXiv:hep-ph/0412191.
- [131] J. F. Gunion *et al.*, Phys. Rev. D **38**, 3444 (1988); A. Djouadi, J. Kalinowski and P. M. Zerwas, Z. Phys. C **57**, 569 (1993).
- [132] J. C. Pati and A. Salam, Phys. Rev. D **10**, 275 (1974) R. N. Mohapatra and J. C. Pati, Phys. Rev. D **11**, 2558 (1975); G. Senjanovic and R. N. Mohapatra, Phys. Rev. D **12**, 1502 (1975).
- [133] P. Dey, A. Kundu and B. Mukhopadhyaya, J. Phys. G **36**, 025002 (2009); A. Arhrib, R. Benbrik, M. Chabab, G. Moultaqa, M. C. Peyranere, L. Rahili and J. Ramadan, Phys. Rev. D **84**, 095005 (2011).
- [134] M. Aoki, S. Kanemura, M. Kikuchi, K. Yagyu, in preparation.
- [135] K. I. Aoki, Z. Hioki, M. Konuma, R. Kawabe and T. Muta, Prog. Theor. Phys. Suppl. **73**, 1 (1982).
- [136] W. F. L. Hollik, Fortsch. Phys. **38**, 165 (1990).
- [137] K. Hagiwara, S. Matsumoto, D. Haidt and C. S. Kim, Z. Phys. C **64**, 559 (1994).
- [138] M. E. Peskin and T. Takeuchi, Phys. Rev. Lett. **65**, 964 (1990); M. E. Peskin and T. Takeuchi, Phys. Rev. D **46**, 381 (1992).

- [139] U. Amaldi *et al.*, Phys. Rev. D **36**, 1385 (1987).
- [140] D. Toussaint, Phys. Rev. D **18**, 1626 (1978).
- [141] S. Bertolini, Nucl. Phys. B **272**, 77 (1986).
- [142] M. E. Peskin and J. D. Wells, Phys. Rev. D **64**, 093003 (2001).
- [143] W. Grimus, L. Lavoura, O. M. Ogreid and P. Osland, Nucl. Phys. B **801**, 81 (2008).
- [144] S. Kanemura, Y. Okada, H. Taniguchi and K. Tsumura, Phys. Lett. B **704**, 303 (2011).
- [145] E. Asakawa, S. Kanemura, Phys. Lett. **B626**, 111-119 (2005); E. Asakawa, S. Kanemura, J. Kanzaki, Phys. Rev. **D75**, 075022 (2007); M. Battaglia, A. Ferrari, A. Kiiskinen, T. Maki, [hep-ex/0112015]; S. Godfrey, K. Moats, Phys. Rev. **D81**, 075026 (2010).
- [146] K. -m. Cheung, R. J. N. Phillips, A. Pilaftsis, Phys. Rev. **D51**, 4731-4737 (1995).
- [147] S. Kanemura, K. Yagyu and K. Yanase, Phys. Rev. D **83**, 075018 (2011).
- [148] A. Arhrib, R. Benbrik, M. Chabab, G. Moulhaka and L. Rahili, arXiv:1112.5453 [hep-ph].
- [149] J. R. Ellis, M. K. Gaillard and D. V. Nanopoulos, Nucl. Phys. B **106**, 292 (1976); B. L. Ioffe and V. A. Khoze, Sov. J. Part. Nucl. **9**, 50 (1978) [Fiz. Elem. Chast. Atom. Yadra **9**, 118 (1978)]; M. A. Shifman, A. I. Vainshtein, M. B. Voloshin and V. I. Zakharov, Sov. J. Nucl. Phys. **30**, 711 (1979) [Yad. Fiz. **30**, 1368 (1979)].
- [150] T. Appelquist and J. Carazzone, Phys. Rev. D **11**, 2856 (1975).
- [151] R. Godbole, B. Mukhopadhyaya and M. Nowakowski, Phys. Lett. B **352**, 388 (1995).
- [152] S. Kanemura, Eur. Phys. J. C **17**, 473 (2000).
- [153] S.-H. Zhu, hep-ph/9901221; A. Arhrib, et al., Nucl. Phys. B **581**, 34 (2000); H.E. Logan, S. Su, Phys. Rev. D **66**, 035001 (2002); Phys. Rev. D **67**, 017703, (2003); O. Brein and T. Hahn, Eur. Phys. J. C **52**, 397 (2007); D.K. Ghosh, R.M. Godbole, B. Mukhopadhyaya, Phys. Rev. D **55**, 3150 (1997).
- [154] S. Kanemura, S. Moretti and K. Odagiri, JHEP **0102**, 011 (2001).
- [155] J. R. Ellis, M. K. Gaillard, D. V. Nanopoulos, Nucl. Phys. **B106**, 292 (1976); J. D. Bjorken, SLAC Report, 198 (1976); B. L. Ioffe, V. A. Khoze, Sov. J. Part. Nucl. **9**, 50 (1978); D. R. T. Jones, S. T. Petcov, Phys. Lett. **B84**, 440 (1979).
- [156] W. Lohmann, M. Ohlerich, A. Raspereza and A. Schalicke, *In the Proceedings of 2007 International Linear Collider Workshop (LCWS07 and ILC07), Hamburg, Germany, 30 May - 3 Jun 2007, pp TIG13* [arXiv:0710.2602 [hep-ex]]; H. Li, F. Richard, R. Poeschl and Z. Zhang, arXiv:0901.4893 [hep-ex].
- [157] H. Georgi and M. Machacek, Nucl. Phys. B **262**, 463 (1985); M. S. Chanowitz and M. Golden, Phys. Lett. B **165**, 105 (1985).

- [158] J. F. Gunion, R. Vega and J. Wudka, Phys. Rev. D **42**, 1673 (1990); R. Vega and D. A. Dicus, Nucl. Phys. B **329**, 533 (1990); J. F. Gunion, R. Vega and J. Wudka, Phys. Rev. D **43**, 2322 (1991).
- [159] M. Aoki and S. Kanemura, Phys. Rev. D **77**, 095009 (2008); H. E. Logan, M. -A. Roy, Phys. Rev. **D82**, 115011 (2010).
- [160] J. Brau, (Ed.) *et al.* [ILC Collaboration], arXiv:0712.1950 [physics.acc-ph]; G. Aarons *et al.* [ILC Collaboration], arXiv:0709.1893 [hep-ph]; T. Behnke, (Ed.) *et al.* [ILC Collaboration], arXiv:0712.2356 [physics.ins-det].
- [161] A. Salam, J. A. Strathdee, Phys. Rev. **D11**, 1521-1535 (1975); M. T. Grisaru, W. Siegel, M. Rocek, Nucl. Phys. **B159**, 429 (1979).
- [162] H. Goldberg, Phys. Rev. Lett. **50**, 1419 (1983); J. R. Ellis, J. S. Hagelin, D. V. Nanopoulos, K. A. Olive, M. Srednicki, Nucl. Phys. **B238**, 453-476 (1984).
- [163] P. Minkowski, Phys. Lett. B **67** (1977) 421; M. Gell-Mann, P. Ramond, and R. Slansky in *Supergravity*, p. 315, edited by F. Nieuwenhuizen and D. Friedman, North Holland, Amsterdam, 1979; T. Yanagida, Proc. of the *Workshop on Unified Theories and the Baryon Number of the Universe*, edited by O. Sawada and A. Sugamoto, KEK, Japan 1979; Prog. Theor. Phys. **64** (1980) 1103; S. L. Glashow, in *Proc. of the Cargèse Summer Institute on Quarks and Leptons*, Cargèse, July 9-29, 1979, eds. M. Lévy et al. , (Plenum, 1980, New York), p707; R. N. Mohapatra and G. Senjanovic, Phys. Rev. Lett. **44**, (1980) 912.
- [164] R. Foot, H. Lew, X. G. He and G. C. Joshi, Z. Phys. C **44** (1989) 441; E. Ma, Phys. Rev. Lett. **81** (1998) 1171.
- [165] I. Affleck, M. Dine, Nucl. Phys. **B249**, 361 (1985).
- [166] M. Fukugita, T. Yanagida, Phys. Lett. **B174**, 45 (1986).
- [167] M. Drees and M. M. Nojiri, Phys. Rev. D **45**, 2482 (1992); M. S. Carena, J. R. Espinosa, M. Quiros, C. E. M. Wagner, Phys. Lett. **B355**, 209-221 (1995); M. S. Carena, M. Quiros, C. E. M. Wagner, Nucl. Phys. **B461**, 407-436 (1996); H. E. Haber, R. Hempfling, A. H. Hoang, Z. Phys. **C75**, 539-554 (1997).
- [168] R. Hempfling and A. H. Hoang, Phys. Lett. B **331**, 99 (1994); S. Heinemeyer, W. Hollik and G. Weiglein, Phys. Rev. D **58**, 091701 (1998); Eur. Phys. J. **C9**, 343-366 (1999); J. R. Espinosa, R. -J. Zhang, Nucl. Phys. **B586**, 3-38 (2000); G. Degrandi, P. Slavich, F. Zwirner, Nucl. Phys. **B611**, 403-422 (2001); A. Brignole, G. Degrandi, P. Slavich, F. Zwirner, Nucl. Phys. **B643**, 79-92 (2002); Nucl. Phys. **B631**, 195-218 (2002); S. Heinemeyer, W. Hollik, H. Rzehak and G. Weiglein, Eur. Phys. J. C **39**, 465 (2005).
- [169] S. P. Martin, Phys. Rev. D **75**, 055005 (2007); R. V. Harlander, P. Kant, L. Mihaila and M. Steinhauser, Phys. Rev. Lett. **100**, 191602 (2008) [Phys. Rev. Lett. **101**, 039901 (2008)]; P. Kant, R. V. Harlander, L. Mihaila and M. Steinhauser, JHEP **1008**, 104 (2010).

- [170] J. R. Ellis, J. F. Gunion, H. E. Haber, L. Roszkowski and F. Zwirner, Phys. Rev. D **39**, 844 (1989); M. Drees, Int. J. Mod. Phys. A **4**, 3635 (1989); J. R. Espinosa and M. Quiros, Phys. Lett. B **279**, 92 (1992).
- [171] T. Moroi and Y. Okada, Phys. Lett. B **295** 73 (1992); U. Ellwanger, Phys. Lett. B **303**, 271 (1993); G. L. Kane, C. F. Kolda and J. D. Wells, Phys. Rev. Lett. **70**, 2686 (1993).
- [172] U. Ellwanger, C. Hugonie and A. M. Teixeira, Phys. Rept. **496**, 1 (2010).
- [173] J. E. Kim and H. P. Nilles, Phys. Lett. B **138**, 150 (1984).
- [174] A. Rossi, Phys. Rev. D **66**, 075003 (2002); M. Hirsch, S. Kaneko and W. Porod, Phys. Rev. D **78**, 093004 (2008).
- [175] L. Calibbi, M. Frigerio, S. Lavignac and A. Romanino, JHEP **0912**, 057 (2009);
- [176] T. Goto, T. Kubo and Y. Okada, Phys. Lett. B **687**, 349 (2010).
- [177] S. Kanemura, E. Senaha and T. Shindou, Phys. Lett. B **706**, 40 (2011).
- [178] R. S. Gupta and J. D. Wells, Phys. Rev. D **81**, 055012 (2010).
- [179] G. Marshall and M. Sher, Phys. Rev. D **83**, 015005 (2011).
- [180] H. Kawase, JHEP **1112**, 094 (2011).
- [181] K. A. Assamagan and Y. Coadou, Acta Phys. Polon. B **33**, 707 (2002).
- [182] A. Djouadi, Phys. Rept. **459**, 1 (2008).
- [183] F. Gianotti and M. Pepe-Altarelli, Nucl. Phys. Proc. Suppl. **89**, 177 (2000).
- [184] P. Garcia-Abia and W. Lohmann, Eur. Phys. J. direct C **2**, 2 (2000); P. Garcia-Abia, W. Lohmann and A. Raspereza, Eur. Phys. J. C **44**, 481 (2005).
- [185] S. T. Petcov, Phys. Lett. B **115** (1982) 401.
- [186] S. Kanemura, T. Kasai, G. L. Lin, Y. Okada, J. J. Tseng and C. P. Yuan, Phys. Rev. D **64** (2001) 053007.
- [187] C. Jarlskog, M. Matsuda, S. Skadhauge and M. Tanimoto, Phys. Lett. B **449** (1999) 240; P. H. Frampton and S. L. Glashow, Phys. Lett. B **461** (1999) 95; Y. Koide, Phys. Rev. D **64** (2001) 077301; N. Haba, K. Hamaguchi and T. Suzuki, Phys. Lett. B **519** (2001) 243; X. G. He, Eur. Phys. J. C **34** (2004) 371.
- [188] P. H. Frampton, M. C. Oh and T. Yoshikawa, Phys. Rev. D **65** (2002) 073014; K. Hasegawa, C. S. Lim and K. Ogure, Phys. Rev. D **68** (2003) 053006.
- [189] K. S. Babu and C. Macesanu, Phys. Rev. D **67** (2003) 073010.
- [190] D. Aristizabal Sierra and M. Hirsch, JHEP **0612** (2006) 052.

- [191] M. Nebot, J. F. Oliver, D. Palao and A. Santamaria, Phys. Rev. D **77** (2008) 093013.
- [192] T. Ohlsson, T. Schwetz and H. Zhang, Phys. Lett. B **681** (2009) 269.
- [193] M. Aoki and S. Kanemura, Phys. Lett. B **689** (2010) 28.
- [194] K. Cheung and O. Seto, Phys. Rev. D **69** (2004) 113009; K. Cheung, P. Y. Tseng and T. C. Yuan, Phys. Lett. B **678** (2009) 293.
- [195] J. Kubo, E. Ma and D. Suematsu, Phys. Lett. B **642** (2006) 18; T. Hambye, K. Kannike, E. Ma and M. Raidal, Phys. Rev. D **75** (2007) 095003; D. Aristizabal Sierra, J. Kubo, D. Restrepo, D. Suematsu and O. Zapata, Phys. Rev. D **79** (2009) 013011; D. Suematsu, T. Toma and T. Yoshida, Phys. Rev. D **79** (2009) 093004.
- [196] M. Aoki, S. Kanemura and O. Seto, Phys. Lett. B **685** (2010) 313.
- [197] M. Aoki, S. Kanemura and O. Seto, Phys. Rev. D **80** (2009) 033007.
- [198] S. Kanemura, O. Seto and T. Shimomura, Phys. Rev. D **84**, 016004 (2011).
- [199] S. Kanemura, T. Nabeshima and H. Sugiyama, Phys. Rev. D **85**, 033004 (2012).
- [200] R. N. Mohapatra, Phys. Lett. B **198**, 69 (1987).
- [201] G. C. Branco and C. Q. Geng, Phys. Rev. Lett. **58**, 969 (1987).
- [202] E. Ma, Phys. Rev. D **39**, 1922 (1989).
- [203] B. S. Balakrishna and R. N. Mohapatra, Phys. Lett. B **216**, 349 (1989).
- [204] R. N. Mohapatra, Phys. Lett. B **201**, 517 (1988).
- [205] D. Chang and R. N. Mohapatra, Phys. Rev. Lett. **58**, 1600 (1987).
- [206] K. S. Babu and X. G. He, Mod. Phys. Lett. A **4**, 61 (1989).
- [207] S. Kanemura, T. Nabeshima and H. Sugiyama, Phys. Lett. B **703**, 66 (2011).
- [208] A. Belyaev, R. Guedes, S. Moretti and R. Santos, JHEP **1007**, 051 (2010).
- [209] C. F. Kolda, and H. Murayama, JHEP **0007**, 035 (2000).
- [210] U. Bellgardt *et al.* [SINDRUM Collaboration], Nucl. Phys. B **299**, 1 (1988).
- [211] M. L. Brooks *et al.* [MEGA Collaboration], Phys. Rev. Lett. **83**, 1521 (1999).
- [212] G. Passarino and M. J. G. Veltman, Nucl. Phys. B **160**, 151 (1979).
- [213] Z. Maki, M. Nakagawa and S. Sakata, Prog. Theor. Phys. **28**, 870 (1962).
- [214] Di Girolamo and B. Neukermans, L 2003 *Atlas Note* ATL-PHYS-2003-006; M. Warsinsky [ATLAS Collaboration], J. Phys. Conf. Ser. **110**, 072046 (2008).

- [215] M. Schumacher, Repot No. LC-PHSM-2003-096.
- [216] J. van der Bij and M. J. G. Veltman, Nucl. Phys. B **231** (1984) 205; K. L. McDonald and B. H. J. McKellar, arXiv:hep-ph/0309270.
- [217] L. J. Hall and L. Randall, Phys. Rev. Lett. **65** (1990) 2939.
- [218] I. Jack, D. R. T. Jones and A. F. Kord, Phys. Lett. B **588** (2004) 127.
- [219] P. G. Camara, L. E. Ibanez and A. M. Uranga, Nucl. Phys. B **689** (2004) 195.
- [220] G. W. Anderson and L. J. Hall, Phys. Rev. D **45**, 2685 (1992); M. Dine, R. G. Leigh, P. Y. Huet, A. D. Linde and D. A. Linde, Phys. Rev. D **46**, 550 (1992).
- [221] T. Inami and C. S. Lim, Prog. Theor. Phys. **65** (1981) 297 [Erratum-ibid. **65** (1981) 1772].
- [222] T. Aushev *et al.*, arXiv:1002.5012 [hep-ex]; M. Bona *et al.*, arXiv:0709.0451 [hep-ex].
- [223] J. F. Gunion, C. Loomis and K. T. Pitts, arXiv:hep-ph/9610237.
- [224] J. Adam *et al.*, Nucl. Phys. B **834**, 1 (2010).
- [225] A. Djouadi, J. Kalinowski, P. M. Zerwas, Z. Phys. **C70**, 435-448 (1996).
- [226] O. V. Tarasov, A. A. Vladimirov and A. Y. Zharkov, Phys. Lett. B **93**, 429 (1980).
- [227] K. G. Chetyrkin, A. L. Kataev and F. V. Tkachov, Nucl. Phys. B **174**, 345 (1980).